Flow Control of Low-Reynolds Number Airfoils Using Morphing Surface

By

Behrooz Afra

A thesis presented to the Faculty of Graduate Studies,
Lakehead University, Thunder Bay, Ontario

A dissertation submitted in partial fulfillment of the
requirements for the degree of
Doctor of Philosophy in Biotechnology

April 2025

Abstract

This thesis investigates the application of traveling wave surface morphing as an advanced active flow control method to enhance the aerodynamic performance of airfoils operating at low Reynolds numbers of 1000 and 20,000. The motivation for this study stems from the need to address flow separation and improve aerodynamic efficiency in low-speed applications, such as micro air vehicles (MAVs) and unmanned aerial vehicles (UAVs). The study focuses on the NACA 0018 airfoil, analyzing its aerodynamic behavior under various traveling wave configurations (frequency, amplitude, and wavelength) across different angles of attack, ranging from 7 to 15 degrees. Through a combination of computational fluid dynamics (CFD) methods, including the Immersed Boundary-Lattice Boltzmann Method (IB-LBM) and Large Eddy Simulation (LES), and simulations conducted using OpenFOAM, along with machine learning (ML) techniques, the research provides comprehensive insights into the optimization of traveling wave parameters for enhanced lift-to-drag ratios and delayed flow separation. The findings at a Reynolds number of 1,000 demonstrate that backward traveling waves significantly improve the aerodynamic performance of the NACA 0018 airfoil. Numerical simulations show that, for wavelengths between 0.1 and 0.4, the lift-to-drag ratio increases 12% from 3.21 to 3.55, compared to the baseline unactuated case where the ratio remains at 2.83. In contrast, forward traveling waves are shown to decrease the lift-to-drag ratio due to the induction of reverse flows on the suction side, highlighting the superiority of backward traveling wave actuation. The results show that amplitudes and frequencies play a crucial role in achieving optimal flow control. At an amplitude of 0.003 and a frequency of 1.5, backward traveling waves generate a lift coefficient four times higher than those at a low frequency of 0.25. At a higher Reynolds number of 20,000, traveling wave actuation continues to exhibit remarkable effects on flow separation control and turbulence management. Results reveal that

backward traveling waves not only enhance lift but also reduce drag by controlling the turbulent kinetic energy (TKE) and generating coherent flow structures such as quasi-streamwise vortices and reverse horseshoe vortices. A parametric study shows that a wavelength of 0.3, an amplitude of 0.003, and a frequency of 1.0 yield the maximum lift-to-drag ratio of 5.47, compared to 2.91 (i.e. by approx. 88%) for the unactuated airfoil. Furthermore, large coherent structures (LCS) analysis demonstrates the ability of traveling waves to stabilize boundary layer dynamics and delay flow separation, especially at higher angles of attack. For example, at an angle of attack of 11°, the suction peak reduces from −2.15 in the unactuated case to −1.27 with traveling wave actuation, significantly shrinking the separation bubble. This study also analyzes TWM's effects on boundary layer stability, flow separation, and vortex structures across angles of attack (7°, 11°, and 14°). The results show that TWM organizes vortex structures, enhances boundary layer mixing, and delays flow separation, significantly reducing drag and stall effects. Higher amplitude TWM (a=0.02) achieves the best results, stabilizing the boundary layer and creating a quasi-laminar flow even at high angles of attack. These findings highlight TWM as a promising technique for improving lift and reducing drag in aerodynamic applications. These findings demonstrate the novelty of applying advanced flow control techniques to a thicker airfoil profile, broadening the scope of aerodynamic research.

The integration of CFD simulations with machine learning models, such as Gaussian Process Regression (GPR), Support Vector Machines (SVM), and Decision Trees (DT), enables efficient prediction and optimization of aerodynamic coefficients. Machine learning techniques are applied to analyze 93 simulation cases, revealing strong correlations between wave parameters (frequency, amplitude, and wavelength) and aerodynamic forces. For instance, the optimal wave configuration at an angle of attack of 11° achieves a drag reduction of 40% and

a lift increase of 20%, reducing computational time significantly compared to traditional CFD methods.

The thesis highlights the transformative potential of traveling wave surface morphing in advancing airfoil design for low Reynolds number applications. By bridging numerical methods and machine learning, this study introduces a practical framework for real-time optimization of aerodynamic performance. The research establishes that backward traveling waves are highly effective in mitigating flow separation, enhancing lift-to-drag ratios, and controlling turbulent flow structures.

Acknowledgments

I would like to sincerely thank **Dr. Ali Tarokh**, my supervisor, for his unwavering support, guidance, and encouragement throughout the course of this research. His insights and mentorship were vital to my progress and development.

A heartfelt thank you goes to my wife, **Mahsa**, whose love, patience, and encouragement were a constant source of strength. I am also deeply grateful to our son, **Samyar**, whose joy and presence brought balance and meaning to every day of this journey.

I would like to express my appreciation to **Brenda**, the Biotechnology Program Coordinator at Lakehead University, for her support, and willingness to assist whenever needed.

My sincere thanks to **Hesam Tofighian** from the Karlsruhe Institute of Technology, Germany, for sharing his expertise and helping me learn OpenFOAM. I am also grateful to **Rasoul Ameri** from National Yunlin University of Science and Technology, Taiwan, for his valuable advice on machine learning and for helping me with model setup.

To our research group, **Dr. Delouei, Soorena, Aysan, and Zahra**. thank you for the collaboration, camaraderie, and memorable moments we shared during these years. I look forward to crossing paths again in the future.

I extend my gratitude to my committee members, **Dr. Ismail, Dr. Elshaer, and Dr. Komrakova**, for their time, thoughtful feedback, and support during the thesis review process.

Special thanks also to **Lakehead University**, the **University of Calgary**, and the **Digital Research Alliance of Canada** for providing essential resources and tools that greatly contributed to this work.

Finally, I gratefully acknowledge the financial support provided by **NSERC**, which played an integral role in making this research possible.

Table of Contents

List of Tables

List of Figures

List of Abbreviations

LBM: Lattice Boltzmann Method

IB-LBM: Immersed Boundary-Lattice Boltzmann Method

LES: Large Eddy Simulation

CFD: Computational Fluid Dynamics

ML: Machine Learning

TKE: Turbulent Kinetic Energy

LCS: Large Coherent Structures

AOA: Angle of Attack

GPR: Gaussian Process Regression

SVM: Support Vector Machines

DT: Decision Trees

MAV: Micro Air Vehicles

UAV: Unmanned Aerial Vehicles

Re: Reynolds Number

PO: Parrot Optimizer

TWM: Traveling Wave Modulation

LSB: Laminar Separation Bubble

FSI: Fluid-Structure Interaction

ZNMF: Zero-Net-Mass-Flux

BGK: Bhatnagar-Gross-Krook

TVD: Total Variation Diminishing

SGS: Sub-Grid Scale

IB: Immersed Boundary

1 Chapter 1: Introduction

1.1 General overview and rationale of the study

Aerodynamic performance, particularly the lift-to-drag ratio, plays a crucial role in the design and functionality of airfoils, especially in low Reynolds number regimes. Low Reynolds numbers, typically encountered in micro-air vehicles (MAVs) [1], unmanned aerial vehicles (UAVs) [2], and certain aircraft operating at low speeds, present unique challenges due to the dominance of flow separation and the formation of laminar separation bubbles (LSB). The control of these flow phenomena is vital to enhance performance and minimize aerodynamic losses. In this context, considerable research has focused on various flow control techniques, both active and passive [3–5], to modify and optimize the boundary layer and improve the aerodynamic characteristics of airfoils operating in low Reynolds number flows.

Kitsios explored methods for delaying flow separation by modifying the boundary layer properties using aerodynamic controls, particularly through the use of zero-net-mass-flux (ZNMF) jets [6]. These methods adjust local flow characteristics at different angles of attack, enhancing lift by stabilizing the boundary layer and delaying separation. This approach is critical in mitigating the high drag and stall that often occur at higher angles of attack. Similarly, Myers and Altememe employed Fluid-Structure Interaction (FSI) simulations to predict lift and drag forces over airfoils at various angles of attack during upstroke and downstroke motions [7]. Their analysis of velocity distributions reinforced the idea that controlling flow separation and ensuring aerodynamic stability during these motions is vital for maintaining optimal performance.

Alongside these studies, Amiralaei et. al [8] examined unsteady aerodynamic coefficients during pitching oscillations at low Reynolds numbers. Their findings are summarized in

investigation of the effects of amplitude of oscillation, frequency, and Reynolds number significantly on performance of a pitching NACA0012 airfoil. Increasing the amplitude of oscillation or reduced frequency enhances the maximum lift coefficient, widens the hysteresis loops, and affects the number of vortices involved in lift generation.

In this regard, the dynamics of boundary layer separation are not only a primary challenge but also an area of significant opportunity for flow control interventions. Passive flow control techniques (Figure 1-1) offer valuable insights, especially in reducing complexity and energy consumption. Thake [9] showed that the creation of laminar separation bubbles (LSB) could enhance lift and reduce drag, particularly at angles of attack where flow separation is more pronounced. Passive techniques such as vortex generators [10] and synthetic jets [11] have been demonstrated to delay flow separation and mitigate the adverse effects of stall without requiring external energy input. These methods, which rely on manipulating the flow naturally, are advantageous for applications where energy efficiency is critical. Genç [12] investigated the effectiveness of passive flow control in delaying separation and improving aerodynamic performance in the pre-stall region. Their results indicated that controlling LSB formation significantly enhanced lift while reducing drag, offering an energy-efficient alternative to active flow control techniques. These findings are in line with other research suggesting that passive techniques can be particularly beneficial in low Reynolds number flows, where the energy required for active control methods might outweigh their benefits.

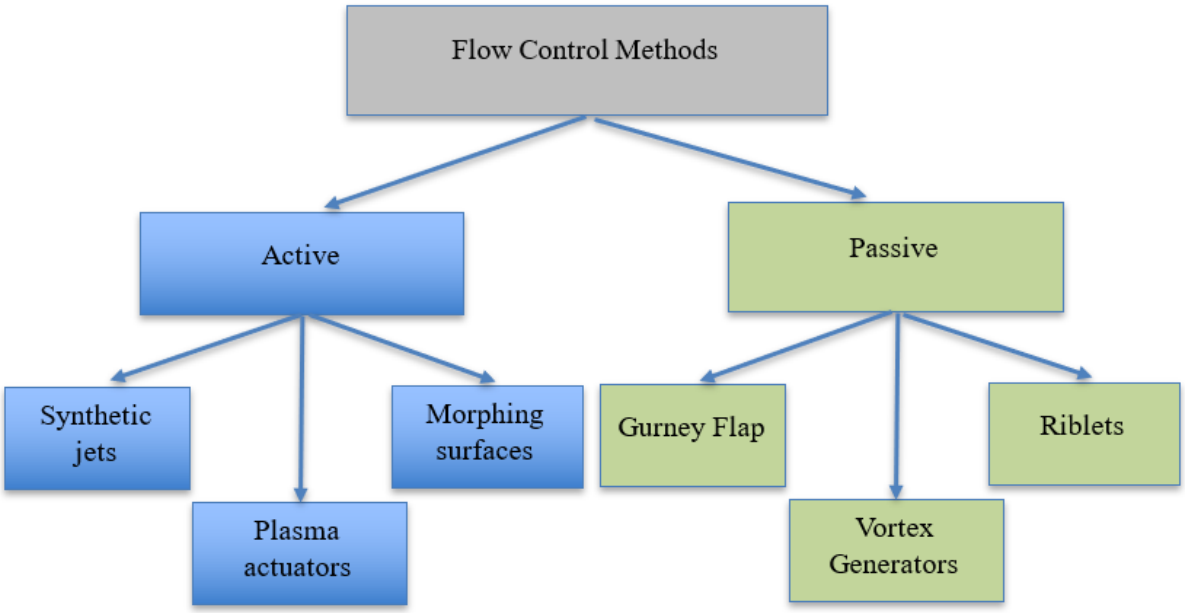

Figure 1-1- Classification of Flow Control Methods

Active flow control (AFC) methods have garnered attention for their ability to directly modify flow patterns, particularly at low Reynolds numbers, where passive methods often struggle to provide significant improvements [4,13,14]. One such method is traveling wave actuation, which has been shown to be highly effective in mitigating flow separation. Akbarzadeh [15] examined the impact of surface morphing (dynamic surface deformation) using backward traveling waves. Their study focused on the effect of actuation frequency, amplitude, and wavelength on significant reductions in drag and corresponding increases in lift. Further advancing the use of traveling waves, Ogunka and Borazjani [16] demonstrated that low-amplitude backward traveling wave actuation on the upper surface of a NACA 0018 airfoil significantly improved lift and reduced drag, with lift coefficients increasing by over 20% and drag coefficients decreasing by more than 40% within the Reynolds number range of Re = 50,000-500,000. These oscillations, mimicking natural surface movements, altered the boundary layer behavior, delaying separation and promoting reattachment, thereby enhancing aerodynamic performance.

In a more recent study, Li and Wang [17] explored the interaction between wave parameters and aerodynamic performance, noting that increasing frequency led to an initial increase in lift, followed by a decline, while drag exhibited an opposite trend. This behavior highlights the complexity of flow control at low Reynolds numbers, where an optimal frequency exists for each configuration. Their study demonstrated that identifying this optimal frequency is crucial for maximizing aerodynamic performance, as it promotes flow attachment while minimizing adverse effects such as excessive drag. An essential component of optimizing these flow control methods is the fine-tuning of wave parameters such as frequency, amplitude, and wavelength. Pujol [18] emphasized the importance of adjusting these parameters to control flow separation and improve aerodynamic performance. They found that optimizing the frequency range and amplitude could significantly enhance lift and reduce drag, offering a practical method for improving the performance of airfoils in low Reynolds number regimes. Dai [19] further explored this parameter optimization, demonstrating that different actuation frequencies and amplitudes are required at various angles of attack to achieve the best aerodynamic outcomes. This work also highlighted the impact of wave parameters on boundary layer behavior and showed that carefully chosen frequencies and amplitudes can reattach separated flow and improve overall aerodynamic performance.

While traditional numerical methods, such as computational fluid dynamics (CFD), provide highly accurate results, they are often limited by substantial computational requirements. On the other hand, the rapid growth of high-performance computing and advanced data analysis techniques has led to an explosion of data in fluid mechanics research, driving the integration of machine learning (ML) for more efficient statistical analysis of complex fluid. These traditional methods, though precise, are time-consuming and resource-heavy, emphasizing the need for alternative approaches like ML to manage and analyze large-scale data more efficiently. The combination of ML with CFD offers promising potential for enhancing flow

control techniques, including active and passive strategies such as traveling wave actuation and laminar separation bubble control, ultimately optimizing aerodynamic performance in low Reynolds number environments.

This dissertation is organized into six chapters. Chapter 1 introduces the research topic, highlighting the importance of traveling wave modulation (TWM) as an active flow control technique, identifying research gaps, and outlining the study's objectives. Chapter 2 presents preliminary simulations at Re = 1,000 using the immersed boundary lattice Boltzmann method (IB-LBM) to establish fundamental trends in TWM before applying it to higher Reynolds numbers. Chapter 3 focuses on large eddy simulations (LES) at Re = 20,000, evaluating the influence of wave parameters on flow separation, lift, and drag characteristics at a fixed angle of attack. Chapter 4 extends this investigation by analyzing the effects of TWM across multiple angles of attack (7°, 11°, and 14°) to assess its impact on boundary layer stability and turbulence modulation. Chapter 5 integrates machine learning (ML) with CFD simulations, developing a predictive model for optimizing wave parameters and enhancing aerodynamic performance. Chapter 6 concludes the dissertation by summarizing key findings, discussing their implications, and providing recommendations for future research.

1.2 Research Objectives

Previous studies have explored the effects of wave parameters on aerodynamic performance but have not thoroughly examined the underlying flow control mechanisms, particularly the role of large coherent structures (LCS) in turbulence modulation. Additionally, the impact of traveling wave modulation (TWM) at low Reynolds numbers, particularly Re = 20,000, remains underexplored, and its effects across multiple angles of attack have not been systematically analyzed. While past research has primarily relied on manual parameter tuning,

the integration of machine learning (ML) for optimizing wave characteristics has been largely overlooked. This study addresses these gaps by investigating the influence of TWM on LCS formation, analyzing its aerodynamic effects at different angles of attack, and developing an ML-based framework for efficient wave parameter optimization. By bridging these gaps, this work advances the understanding of TWM in low Reynolds number aerodynamics and provides a novel approach for enhancing aerodynamic performance. Thus, the objectives are as follows:

a) **To Investigate the Effects of Traveling Wave Method on Aerodynamic Performance at Reynolds number of 20,000:**

Previous studies have primarily focused on higher Reynolds numbers (Re > 50,000), leaving a gap in understanding how TWM influences aerodynamic performance at lower Reynolds numbers, particularly Re = 20,000, where flow separation is more pronounced. This research addresses this gap by evaluating the effectiveness of TWM in controlling turbulent flow separation over a NACA 0018 airfoil, analyzing its ability to delay separation, reduce drag, and enhance lift. Emphasis is placed on understanding how wave-induced momentum injection stabilizes the boundary layer, ensuring flow attachment at critical angles of attack.

b) **To Evaluate the Impact of Wave Parameters on Flow Structures and Aerodynamic Forces:**

While past research has examined TWM's overall aerodynamic effects, it has not provided a detailed analysis of how frequency, amplitude, and wavelength influence large coherent structures (LCS), turbulent kinetic energy (TKE) distribution, and Reynolds stress profiles. This study fills this gap by systematically investigating how these wave parameters shape flow structures, such as coherent vortical formations and turbulent eddies, and how they contribute to suppressing flow separation and reattaching the boundary layer.

c) Integrate Machine Learning with Computational Fluid Dynamics for Efficient Prediction:

Most prior studies rely on manual parameter tuning, which is computationally expensive and time-consuming. No previous research has integrated machine learning (ML) for predicting aerodynamic forces in TWM-controlled airfoils. To address this, this study explores Gaussian Process Regression (GPR), Support Vector Machines (SVM), and Decision Trees (DT) to predict drag and lift coefficients, enabling faster identification of performance trends without requiring full-scale CFD simulations.

d) To Optimize Wave Parameters Using Machine Learning:

While existing parametric studies identify optimal wave configurations through exhaustive computational testing, they lack data-driven optimization strategies for maximizing aerodynamic efficiency. This research addresses this gap by implementing machine learning-driven optimization techniques, such as the Parrot Optimizer (PO), to determine the most effective combinations of frequency, amplitude, and wavelength across different angles of attack. The results will provide practical guidelines for implementing TWM in real-world aerodynamic applications, making active flow control more efficient and feasible.

1.3 Originality of Research

The originality of this research lies in its investigation of traveling wave modulation (TWM) as an active flow control strategy at Re = 20,000, a Reynolds number where boundary layer separation and turbulence dynamics are significantly different from higher Reynolds number regimes. Most previous studies on TWM have focused on Re > 50,000, where turbulence is fully developed, and separation characteristics differ. However, many small-scale aerial vehicles, such as unmanned aerial vehicles (UAVs) and micro air vehicles (MAVs), operate at lower Reynolds numbers, making the study of TWM at Re = 20,000 particularly relevant. The

choice of NACA 0018 is motivated by its common application in low-Re aerodynamic studies and its symmetric airfoil profile, which allows for a controlled investigation of TWM effects without inherent asymmetric influencing results. Additionally, this research is the first to integrate machine learning (ML) with computational fluid dynamics (CFD) to optimize wave parameters, providing a data-driven approach to improving aerodynamic performance. By addressing these gaps, this study advances knowledge in active flow control techniques, low-Re aerodynamics, and ML-driven aerodynamic optimization.

2 Chapter 2: Aerodynamic Assessment of an Airfoil with a Travelling Wave Motion on the Suction Surface in a Low-Reynolds Number.

This chapter explores the fundamental effects of traveling wave modulation (TWM) at a low Reynolds number (Re = 1,000) before extending the study to higher Reynolds numbers. The insights gained from this analysis help in understanding how wave amplitude and frequency influence aerodynamic forces, serving as a reference for the investigations at Re = 20,000 presented in the subsequent chapters.

Abstract

In this study, active flow control via surface morphing has been investigated in the form of a traveling wave. To achieve high lift and low drag, along with postponing (or even eliminating) the separation point, a traveling wave morphing surface has recently been used to inject momentum into the boundary layer, leading to a decrease in vertical hydrodynamic forces on the suction side of the wing. This research employs the Immersed Boundary-Lattice Boltzmann (IB-LB) technique to resolve the continuity and momentum equations, as well as the interface forces between the fluid and the airfoil. Lattice Boltzmann simulations of fluid flows allow our modeling to take advantage of direct numerical simulation, achieving physically consistent accuracy in both space and time for resolving the momentum equations. In this paper, the aerodynamics of the popular NACA0018 airfoil equipped with a traveling wave in the low-Reynolds number flow regime (1,000) have been investigated. Numerical simulations have found that the forward traveling wave has negative effects on flow control when the airfoil interacts with a low-speed fluid flow in the laminar regime. However, similar to higher Reynolds-number flows reported in the literature, the backward motion of surface waves induces an increase in the lift-to-drag coefficient as surface vibrations push high-momentum

flows at the leading edge downstream. This results in a decrease in pressure around the suction side and an increase in the lift force over the airfoil.

Keywords: Flow Control Methods, Travelling Wave Morphing Surface, Lattice Boltzmann Method, Immersed Boundary Method

2.1 Introduction

Many aquatic animals are seen to induce deformation of their bodies (such as wave-like motions along their bodies or fins) to generate a larger thrust force. Such a special driver can be considered an internal biological motor called a traveling wave actuator. Inspired by this type of animal motion, the traveling wave is applied to control flow behavior over airfoil bodies [20, 21].

Stall management and control are of paramount importance for Unmanned Aerial Vehicles (UAVs) as they ensure that these vehicles operate at the margins of safe flight. Inappropriate management of stall increases the risk of a temporary (but normally recoverable) loss of aircraft control. Aerodynamic stall is an undesirable phenomenon that occurs when lift forces decrease and the wing (airfoil) can no longer produce sufficient lift to counteract the weight [22]. To delay stall, different control methods have been applied based on two categories: (a) active flow control and (b) passive flow control. The performance of passive flow control is limited around the design condition. However, active flow control can be adjusted based on different flow conditions, especially in the low Reynolds number flow regime. One common way to apply active flow control to eliminate or postpone flow separation is the injection of momentum close to the wall using different techniques. Inspired by animal locomotion, the effects of

morphing surfaces in the form of traveling waves on controlling flow separation are investigated in this research.

Studying low Reynolds number aerodynamics is becoming increasingly important as it plays a crucial role in understanding small-scale air vehicles [23,24]. Thus, simulating a Reynolds number below 1,000 is valuable for finding an optimal wing design for such low-speed aerial vehicles. Without a doubt, flow control methods determine how efficiently aerial vehicles can move and the direct effects they have on fabricating the whole-body structure. If the surface of the wing (airfoil) is changed either with vibration or slats, it is called a morphing surface. The morphing methods that have been reported are categorized into (a) vibrating surfaces using piezoelectric actuators [25], (b) changing the radius of leading and trailing edges [25,26], and (c) standing and traveling wave induction on the suction side and in either the span-wise [27] or chord-wise direction [20, 28]. The traveling waveform of morphing surfaces has been found to be successful in eliminating unfavorable behaviors over the airfoil body, such as reducing lift and increasing drag at Reynolds numbers on the order of 10^4 and 10^5 [25]. In particular, a backward traveling wave over an airfoil (from the trailing edge toward the leading edge) can either suppress or postpone flow separation. Waves that move faster with lower amplitudes have been shown to generate higher lift and lower drag coefficients [15, 29, 30]. This is because the suction side equipped with a moving wave experiences higher momentum flows compared to the unactuated airfoil, resulting in a stronger boundary layer momentum force opposite to the adverse pressure generated. Additionally, increased kinetic energy over the airfoil leads to higher pressure on the suction side and consequently a greater pressure gradient between the suction and pressure sides, resulting in a larger lift force applied over the airfoil.

In low Reynolds number flows, the lift-to-drag ratio (L/D) is particularly important to study due to the wide range of real-world applications that involve such conditions. Additionally, it is important to study the wake structure and separation points altered by manipulating the

geometry and using different flow control methods. Munday et al. [31] showed that tangential actuations influence the drag coefficients over a cylinder under the effect of a laminar cross-flow at a Reynolds number of 100 [31]. Furthermore, the effects of the aspect ratio of a wing, its actuator frequency, and body shape have been determined at a Reynolds number of 100 [23,31–33]. Traveling wave morphing surfaces have also been found to contribute to lift-to-drag ratio enhancement in low Reynolds number flows (10^2–10^3), similar to what occurs at Reynolds numbers of (10^4–10^5). In this study, an extensive parametric analysis has been employed to examine the effects of moving wave characteristics (wavelength, amplitude, and frequency) on the drag and lift forces on the wing.

In the present study, we limit the interaction to include only the frequency, amplitude, and wavelength of the backward movement of the wave over the suction side. The selected Reynolds number is in the range of 100 to 1,000 to ensure laminar flow. This paper aims to uncover the conditions under which the lift and drag forces on a NACA0018 airfoil are influenced by altering its geometry compared to the clean (unactuated) airfoil. We begin the discussion by describing the numerical methods used and then verify the proposed algorithm by simulating a benchmark problem in which a crossflow passes over a NACA0018 airfoil. We then perform numerical simulations of controlled flow to examine how the moving wave modifies the associated lift-to-drag ratio on the airfoil.

2.2 Computational Methods

In this paper, a mesh-independent hybrid model including Immersed Boundary and Lattice Boltzmann Method (LBM) has been carried out to investigate the response of fluid flows to the small vibrations on the airfoil suction side. The LB method helps to have a comprehensive understanding of special laminar structures that take place on the wings and to give appropriate emphasis to physical realism in respect to our in-house computational technology.

2.2.1 Lattice Boltzmann Method

Instead of solving the Navier-Stokes equations, the Lattice Boltzmann Method (LBM) can be used to describe the behavior of fluid flows. According to the Chapman-Enskog theory [34], the continuity and momentum equations can be derived from the LBM algorithm. Accordingly, the so-called distribution function f, which encapsulate local fluid properties, are updated using the Bhatnagar-Gross-Krook (BGK) collision model [35]. These distribution functions also transfer properties by streaming toward their neighboring nodes. Thus, it can be expressed as [36]:

$$f_i(x + e_i\Delta t, t + \Delta t) - f_i(x,t) = -\left(\frac{1}{\tau}\right)\left[f_i(x,t) - f_i^{eq}(x,t)\right] \quad \text{Equation 2-1}$$

Here, f_i represents the distribution function associated with each discrete velocity direction i, defined at a specific spatial position x and time t. This function describes the probability density of particles traveling with a particular velocity in the given direction at a specific location and time. The equilibrium distribution function, denoted as f_i^{eq}, is derived based on macroscopic quantities such as fluid density (ρ) and velocity (u). It serves as the target state that the distribution function approaches during collisions. The mathematical form of f_i^{eq} ensures consistency with the Navier-Stokes equations and is given as follows:

$$f_i^{eq} = \omega_i \rho \left[1 + 3\frac{\vec{e}_i \bullet \vec{u}}{c_s^2} + 9\frac{(\vec{e}_i \bullet \vec{u})^2}{2c_s^4} - \frac{\vec{u} \bullet \vec{u}}{2c_s^2}\right] \quad \text{Equation 2-2}$$

$w_{1-4} = \frac{1}{9}, w_{5-8} = \frac{1}{36}, and\ w_0 = \frac{4}{9}$, where if $D2Q9$ is considered as the lattice structure [36], the discrete velocity vector is defined as follows:

$$\vec{e}_i = \begin{bmatrix} (0,0) for\ i\ =\ 0; \\ (\pm c, 0), (0, \pm c) for\ i\ =\ 1,2,3,4; \\ (\pm c, \pm c) for\ i\ =\ 5,6,7,8 \end{bmatrix}$$

Equation 2-3

where $c\ =\ \delta x\ /\ \delta t$. LBM is divided into two steps, including collision and streaming. The collision method is resolved with Equation 2-1 to Equation 2-2, and the streaming method is recovered by moving each f towards their neighbors. Thus, density and velocity of the fluid flow in each position and time are introduced

$$\rho\ =\ \Sigma_i f_i\ =\ \Sigma_i f_i^{eq}$$

$$\rho\vec{u}\ =\ \Sigma_i \vec{e}_i f_i\ +\ (\delta t/2)\vec{F}$$

Equation 2-4

Also, based on Chapman-Enskog theory [37], kinematic viscosity gets the form as follows:

$$\nu\ =\ c_s^2 \left(\tau\ -\frac{1}{2}\right) \delta t$$

Equation 2-5

Where τ represents the single relaxation time, which plays a crucial role in converting macroscopic fluid properties to mesoscale Lattice Boltzmann (LB) parameters. The relaxation time determines the fluid's viscosity and the system's stability, making it a critical parameter in LB simulations.

The parameter c_s, known as the speed of sound, takes the value $c_s\ =\ 1/\sqrt{3}$ for this model. This value is important because it ensures a proper relationship between pressure and density, adhering to the requirements of the Lattice Boltzmann Method (LBM). It serves as a reference for simulating incompressible or weakly compressible flows.

To maintain the accuracy and stability of the simulation, the Mach number, defined as $Ma\ =\ U/c_s$, must be kept below 0.3, where U is the inlet velocity in the LB scale. This

condition ensures that compressibility effects, which are not accounted for in the LBM framework, remain negligible. Maintaining this limit is particularly significant when creating a range of inlet velocities for simulations, as exceeding the threshold could lead to numerical inaccuracies and invalid results. This criterion highlights the importance of carefully selecting simulation parameters to ensure realistic and accurate modeling of fluid behavior within the computational domain

2.2.2 Immersed Boundary Lattice Boltzmann Method

We employ the Immersed Boundary-Lattice Boltzmann (IB-LB) technique [36,38] to simulate fluid flow in the vicinity of a moving boundary. This method updates the velocity and pressure fields of the fluid flow on a fixed Cartesian grid using statistical distribution functions propagated in nine discrete directions. The Immersed Boundary Method significantly reduces the challenges associated with aligning solid and fluid meshes during the evaluation of fluid-solid interface forces. Specifically, the IB method uses temporal interpolation between fluid nodes (Eulerian nodes) and user-defined boundary nodes (Lagrangian nodes) to accurately transfer fluid-structure interaction forces [39].

To account for the influence of the boundary on the surrounding fluid, an external body force is incorporated into the Lattice Boltzmann equations. This external force simulates the interaction at the surface of the airfoil, ensuring accurate modeling of the coupled dynamics between the fluid and the moving boundary.

$$f_{\mathrm{i}}(\vec{r} + \vec{e}_i\delta t, t + \delta t) = f_{\mathrm{i}}(\vec{r}, t) - \tau^{-1}[f_{\mathrm{i}}(\vec{r}, t) - f_{\mathrm{i}}^{\mathrm{eq}}(\vec{r}, t)] + F_{\mathrm{i}}(\vec{r}, t)\delta t \qquad \text{Equation 2-6}$$

where

$$F_{\mathrm{i}}(\vec{r},t) \;=\; (1 \;-\; 1\,/\,2\tau)\, w_{\mathrm{i}}\; [3\frac{\vec{e}_i - \vec{u}}{c^2} \;+\; \frac{9(\vec{u}\,.\,\vec{e}_i)}{c^4}\vec{e}_i]\,.\,\vec{F}(\vec{r},t)$$ Equation 2-7

where $F(\vec{r},t)$ is the body force and is mainly the term accounting for the coupling of the fluid and the elastic membrane. In the split forcing method, the momentum exchange is affected not only by forces exerted at time *t*, but also due to forces exerted at $t + \delta t$. Based on the Immersed-Boundary Method, the boundary force $F(r,t)$ is obtained:

$$F(\vec{r}_b, t \;+\; \delta t) = \; \rho\frac{\left[\vec{U}_b^{desired} \;-\; \vec{u}_b^{nof}\right]}{\delta t/2}$$ Equation 2-8

where $\vec{U}_b^{desired}$ is the velocity at the boundary point *b* and $\vec{u}_b^{nof}$ is defined as no-forced velocity and is give as:

$$\vec{u}_b^{nof} \;=\; \Sigma_{b=1}^{n}\vec{u}^{nof}(\vec{r}_{ij},t)D(\vec{r}_{ij} \;-\; \vec{r}_b)$$ Equation 2-9

where subscripts i,j demonstrate Eulerian grid points in horizontal and vertical directions and *D* is the Dirac delta function for interpolation of Eulerian velocities on each Lagrangian nodes and given as:

$$D(x_{ij} \;-\; x_b) = \frac{1}{h^2} *\; d_h\left(\frac{(x_i \;-\; x_b)}{h}\right) *\; d_h\left(\frac{(y_i \;-\; y_b)}{h}\right)$$ Equation 2-10

where $h \;=\; \Delta x^{LB}$ equals to dx, and the function d is defined as:

$$d(|\vec{r}|) = \begin{cases} \frac{1}{8}\left(3 - 2|\vec{r}| + \sqrt{1 + 4|\vec{r}| - 4|r\vec{r}|^2}\right), & 0 \le |\vec{r}| < 1 \\ \frac{1}{8}\left(5 - 2|\vec{r}| - \sqrt{-7 + 12|\vec{r}| - 4|\vec{r}|^2}\right), & 1 \le |\vec{r}| < 2 \\ 0, & |\vec{r}| \ge 2 \end{cases}$$ Equation 2-11

This equation illustrates that the Eulerian nodes are located in distances larger than 2 LB units respected to the boundary nodes are not effective in boundary force calculation. Finally, the total force F^{total} exerted on the submerged boundary is given as:

$$\vec{F}^{total}(t) = \Sigma_b \vec{F}_b^{total}(\vec{r}_b, t)\Delta S_b$$ Equation 2-12

where ΔS_b is the arc length of boundary division over the NACA0018 airfoil surface.

2.2.3 Induction of Travelling Waves on the Airfoil Suction Side

Figure 2-1 shows a schematic of surface morphing using travelling wave induction. The motion equation of the travelling wave on the suction side of the airfoil is described as follows [15]:

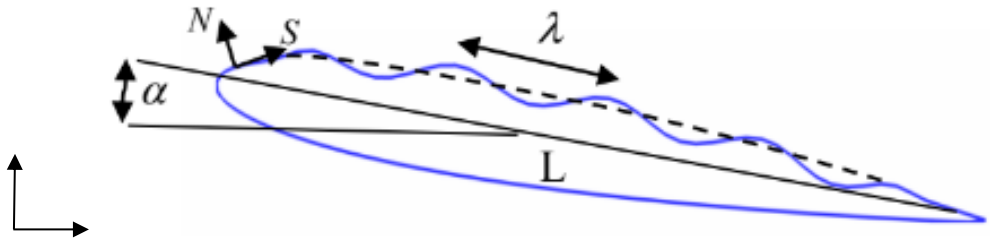

Figure 2-1- The schematic of a symmetric airfoil with a partially wavy upper surface

$$N(s) = a(s)\, sin[2\pi(f \pm s/\lambda)]$$ Equation 2-13

The s-coordinate represents the curvilinear distance along the wavy surface from the leading edge to the trailing edge of the airfoil. The N-coordinate, perpendicular to the s-coordinate, defines the normal distance from the surface, pointing outward from the airfoil. These coordinates are used to describe the wave motion and deformation of the surface relative to its baseline geometry. The negative sign indicates the direction of wave motion, specifically representing the movement of the wave either from the leading edge toward the trailing edge or vice versa. This bi-directional motion plays a critical role in determining the aerodynamic effects on the airfoil surface. The parameters y, λ, and a represent the vertical displacement of the surface nodes, the wavelength of the wave, and the vibration amplitude, respectively. It is important to note that the chord length is utilized to make non-dimensional parameters, ensuring that the analysis remains scalable and comparable across different airfoil sizes. In fact, the inlet velocity U, along with the chord length L, are used to define non-dimensional vibration frequency (f) and dimensionless wavelength (λ):

2.3 Validation of the Numerical Models and its Convergency

In this section, the impact of grid resolution on the accuracy of the average lift coefficient (C_L) for the NACA0012 airfoil (as shown in Figure 2-2) is thoroughly examined. The investigation focuses on evaluating how different grid sizes influence the computed results, ensuring that the numerical solution is both accurate and reliable. Furthermore, the average lift coefficient at an angle of attack (α=10°) is compared with values reported in previous studies to validate the numerical approach used in this work. It is important to note that the NACA0012 airfoil has been selected for this analysis due to its widespread usage in the literature. This airfoil serves as a benchmark geometry for studying fluid flow behavior because of its symmetric design and well-documented aerodynamic characteristics. Additionally, most of the studies involving the NACA0012 airfoil have been conducted at a Reynolds number of 1000, making it an ideal case

for comparing the results obtained from the current numerical simulation with established data. The availability of extensive reference data ensures that any discrepancies in the results can be thoroughly analyzed and attributed to grid resolution, numerical schemes, or boundary conditions. By conducting this study, we aim to establish confidence in the computational methodology employed, thereby providing a solid foundation for further simulations involving more complex flow scenarios or airfoil geometries.

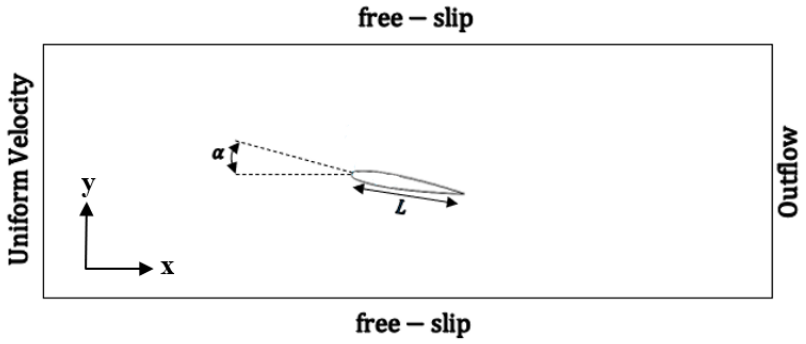

Figure 2-2-The schematic of a NACA0012 airfoil located at the middle of an unconfined channel.

Four different grid resolutions $200 \times 100, 300 \times 150, 600 \times 300$, and 900×450 (where the first and second digits represent the number of nodes in the x- and y-directions, respectively) were examined, and the results are presented in Table 2-1.The 600×300 grid resolution was found to be sufficient to produce mesh-independent results. Additionally, the average lift coefficients obtained are consistent with the values of 0.41 and 0.42 reported by Mittal et al. [40] and Gopalakrishnan Meena et al. [41].

Table 2-1- Grid Convergence Study of IB-LB

Grid Resolution	**Present**			
	200×100	300×150	600×300	900×450
$\overline{C_L}$	0.356	0.395	0.418	0.420

2.4 Numerical Results and Discussions

In this section, the implementation of the travelling wave method on a NACA0018 airfoil has been studied. The airfoil is located in the middle of the channel and surrounded by fluid flows. Figure 2-3 reveals more detailed information about the computational domain and boundary conditions. The 600×300 grid resolution has been considered for the simulation, leading to 60 LB units as the cord length. S_L and S_U respectively denote the location where the moving wave starts and finishes. Also, the interval with constant amplitude of a is shown by $[s_L^c, s_U^c]$.

In this interval, a travelling wave is generated, and the amplitude of $a(s)$ becomes dimension-less by the chord length and set as follow:

$$a(s) = \begin{cases} \frac{a}{2} sin[\pi(s - (\frac{s_L + s_L^c}{2}))/(s_L^c - s_L)] + \frac{a}{2} & 0.05 < s < 0.15 \\ \frac{a}{2} cos[\pi(s - (\frac{s_U + s_U^c}{2}))/(s_U - s_U^c)] + \frac{a}{2} & 0.85 < s < 0.95 \end{cases} \quad \text{Equation 2-14}$$

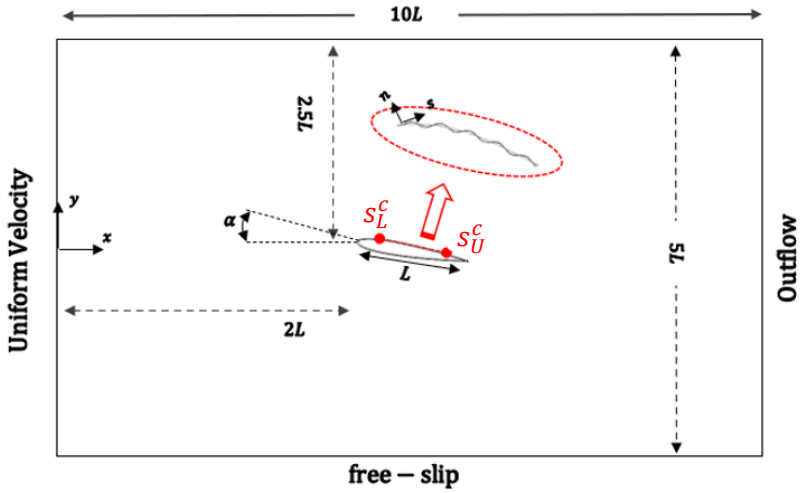

Figure 2-3- The schematic of a NACA0018 airfoil whose upper surface is under effects of travelling wave.

Equation 2-14 is utilized to make a smooth decrease of vibration amplitude from the point where the suction side fluctuates with the maximum amplitude of a to the point that has no

fluctuation. We aim to examine the influence of different wave parameters (wavelength, amplitude and frequency) on the coefficient of lift-to-drag ratio.

2.4.1 The Effect of Wavelength on Flow Control Enhancement

The enhancement ability to implement a particular wavelength can be expressed by means of a lift-to-drag coefficient. In fact, wavelength is defined as an important parameter of the travelling wave actuator that affects the flow structure close to the suction side. In this section, the maximum travelling wave amplitude gets the value of 0.003 between s (0.15, 0.85) while $s = 0.05$ and $s = 0.95$ are the positions get the minimum value of zero. We set the values of 0.5 and 10^o for the vibration frequency and angle of attack, respectively. Figure 2-4 compares the lift-to-drag ratio ($C_{L/D}$) as a function of wavelength in two-direction wave propagation (backwards and forward). The average of drag and lift coefficients are utilized and respectively defined as $C_D = F_x/\rho_f U^2 L$and $C_L = F_y/\rho_f U^2 L$. As shown in Figure 2-4, for each wavelength of λ ranging from 0.1 to 0.4, the lift-to-drag coefficient becomes greater than the unactuated case (e.g., λ=0).

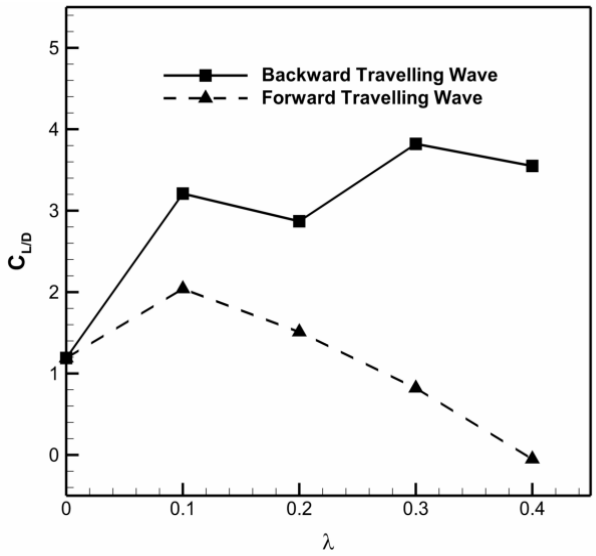

Figure 2-4-Comparison of the lift-to-drag ratio (present results) as a function of wavelength (λ) for two wave propagation directions (backward and forward). For wavelengths ranging from 0.1 to 0.4, the lift-to-drag ratio increases compared to the unactuated case (λ=0).

However, forward motion exhibits behavior that differs from expectations. It has been found to increase lift when the wavelength is shorter than 0.24; however, the lift subsequently drops below the values observed for the unactuated airfoil. Furthermore, a comparison of the two graphs in Figure 2-4 reveals that increasing the wavelength of a backward traveling wave from 0.1 to 0.4, despite minor variations in the interval, leads to a increase in $C_{L/D}$ from 3.21 to 3.55. Additionally, it is observed that increasing the wavelength in the forward movement of the wave reduces the lift-to-drag ratio to as low as 0. This occurs because the forward traveling wave actuation increases reverse flow near the suction side.

Figure 2-5 illustrates the contour of velocity magnitude over the airfoil and imply how the backward and forward motion of the wave transfers momentum along the airfoil, specifically from the leading edge toward the trailing edge. This distinct separation zones plays a critical role in bring high momentum bulk flow mainstream toward the suction surface, consequently, the aerodynamic performance of the airfoil. As depicted in Figure 2-5-b, a significantly larger laminar coherent structure—approximately 75% larger—has formed on the suction side of the actuated airfoil compared to the unactuated airfoil, as shown in Figure 2-5-a. This enlarged structure enhances the stability and coherence of the flow over the suction side, promoting a more favorable pressure distribution.

In contrast, the unactuated airfoil's upper surface (Figure 2-5-a) experiences a negative pressure gradient along the lower portion of the suction side. This adverse pressure gradient disrupts the flow, resulting in higher local pressure values on the suction side. The increased pressure adversely impacts the lift coefficient by reducing the pressure difference between the suction and pressure sides of the airfoil. This demonstrates the crucial role of wave-induced motion in controlling flow separation and enhancing aerodynamic performance through effective momentum transfer mechanisms.

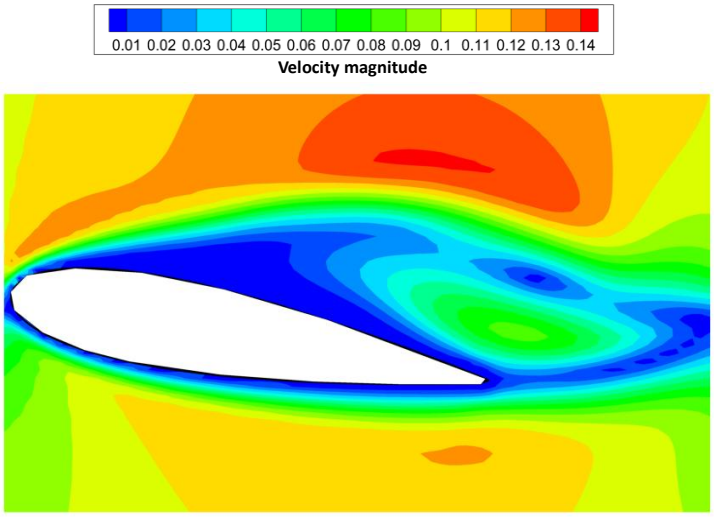

(a)

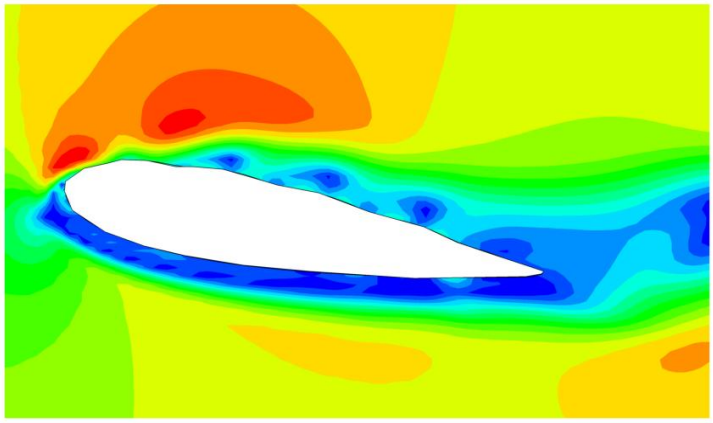

(b)

Figure 2-5-The contour of magnitude velocity around. (a) the NACA0018, (b) the NACA0018 airfoil that induced by travelling wave.

2.4.2 The Effect of Actuator Vibration Amplitude on Increasing the Lift-to-Drag Ratio

The maximum displacement of fluctuations significantly influences the flow control efficiency at Reynolds numbers on the order of 10^5 [15]. The amplitude of vibrations is a critical

parameter in designing and fabricating the experimental setup, as well as in live testing [28,42]. For instance, reducing the amplitude by just 1 mm (e.g., when induced by gears and shafts) may require altering the entire vibration mechanism, especially when actuators are driven by magnetic fields. Therefore, it is essential to determine a viable range of amplitudes based on the overall dimensions of the structure. Numerical methods play a crucial role in mitigating unintended challenges arising from improper amplitude selection during the fabrication of efficient actuators. To focus the analysis, the wavelength is kept constant, allowing for a direct comparison of how varying amplitude sizes affect the lift-to-drag ratio at different frequencies. Figure 2-6 illustrates the lift-to-drag ratio ($C_{L/D}$) as a function of dimensionless amplitude for three frequencies: 0.25, 1, and 1.5. The figure reveals that increasing the wave amplitude results in a gradual rise in the lift-to-drag ratio. The maximum values of $C_{L/D}$ are 2.87, 4.74, and 8.08 for the respective frequencies, achieved at the highest amplitudes.

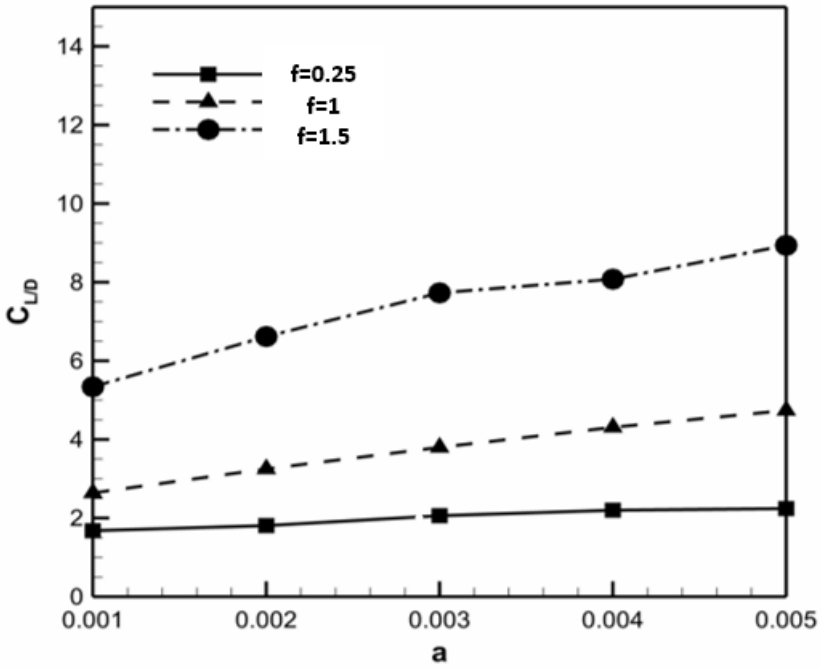

Figure 2-6- Investigating the effect of amplitude size on the ratio of lift-to-drag in three different frequencies.

2.4.3 The Effect of Frequency Variation on Flow Control Enhancement

To investigate the effect of frequency on the evolution of the forces acting on the airfoil with a backward traveling wave, the temporal evolution of the drag and lift coefficients was analyzed and plotted for three different frequencies: 0.25, 1, and 1.5. The wavelength, angle of attack, and fluctuation amplitude were fixed at 0.3, 10° and 0.003, respectively, to maintain consistency and isolate the effect of frequency. As shown in Figure 2-7-a, the drag coefficient exhibited fluctuations with increasing amplitude at a frequency of 1.5 compared to the unactuated airfoil (clean airfoil). However, the average value of the drag coefficient remained relatively unchanged across the different frequencies, suggesting that the backward traveling wave primarily influences lift without significantly affecting the overall drag performance.

Interestingly, the results demonstrate a dramatic improvement in lift performance at higher frequencies, see Figure 2-7-b. Specifically, the airfoil equipped with the fastest traveling wave ($f = 1.5$) generated a lift force approximately four times greater than that observed at a frequency of 0.25. This substantial increase in lift can be attributed to the enhanced momentum transfer caused by the higher wave frequency, which strengthens the boundary layer's resistance to separation and improves aerodynamic efficiency. Physically, this mechanism stabilizes the boundary layer by energizing near-wall flow structures, preventing the adverse pressure gradient from causing premature separation. In addition, the shedding frequency of the flow appears higher as the actuation frequency increases because the traveling wave surface morphing interacts more dynamically with the boundary layer, enhancing the generation and shedding of vortices. This interaction introduces additional unsteady flow structures at a higher rate, directly linked to the increased actuation frequency. This analysis highlights the critical role of wave frequency in optimizing flow control strategies, as it allows for significant enhancements in lift generation without compromising drag performance.

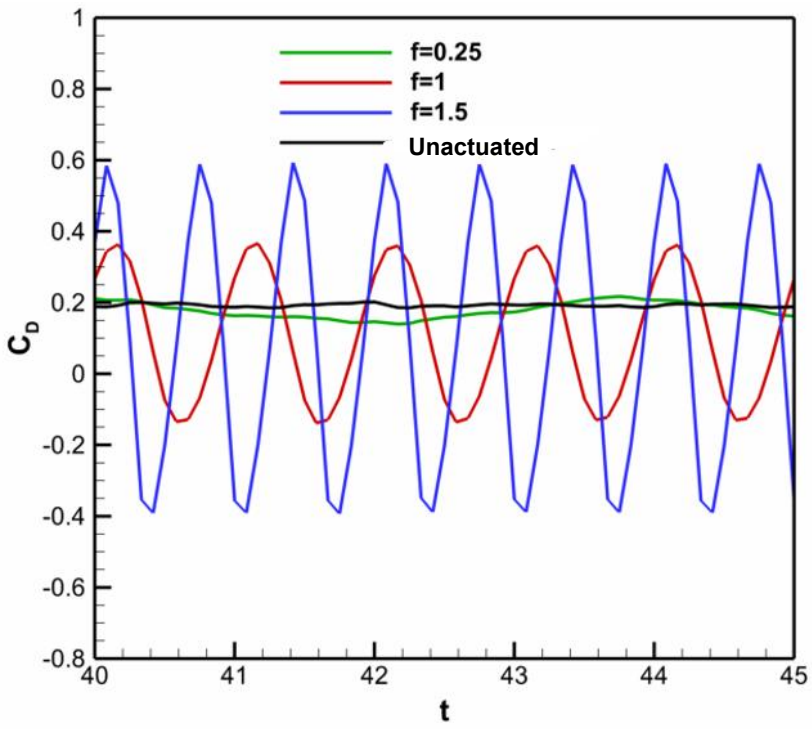

(a)

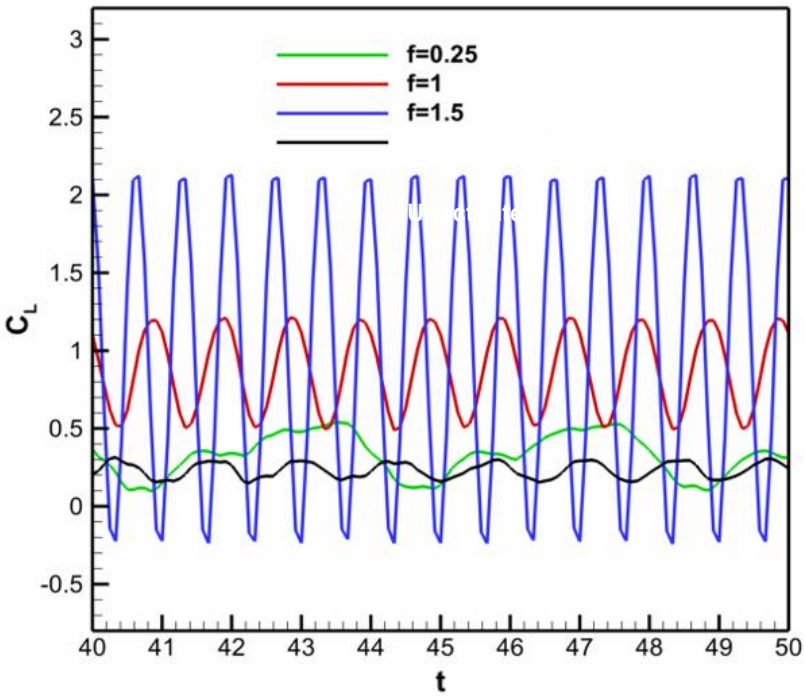

(b)

Figure 2-7-Temporal evolution of (a) drag and (b) lift coefficients for an airfoil with a wavy surface, compared to an unactuated airfoil, at three different frequencies: 0.5, 1, and 1.5.

2.5 Conclusion

This study investigated the aerodynamic performance of a NACA0018 airfoil equipped with a traveling wave actuator at low Reynolds numbers using the Immersed Boundary-Lattice Boltzmann Method (IB-LBM). Results demonstrated that backward traveling waves significantly enhanced the lift-to-drag ratio ($C_{L/D}$) by delaying flow separation and increasing momentum near the suction side. This effect was most pronounced for wavelengths between 0.1 and 0.4 and higher frequencies, with a maximum lift increase observed at $f = 1.5$.

Forward traveling waves, however, reduced flow control efficiency by promoting reverse flow and premature separation. Amplitude and frequency were critical parameters, with larger amplitudes and higher frequencies consistently improving $C_{L/D}$. The hybrid IB-LBM approach effectively captured these phenomena, providing insights into wave-induced flow control. These findings highlight the potential of traveling wave actuators to improve aerodynamic efficiency in low-speed aerial applications, offering a pathway to optimize designs for drones and micro air vehicles.

3 Chapter 3: Numerical Investigation of Travelling Wave-Induced Flow Control on a NACA-0018 airfoil at Reynolds of 20,000

Abstract

The application of traveling wave morphing surfaces has emerged as an effective approach to reducing drag and preventing stall on airfoils at low Reynolds numbers. This study specifically examines the influence of wave parameters on flow control and stall mitigation over a NACA0018 airfoil at a Reynolds number of 20,000. Large Eddy Simulation were performed to explore how traveling waves interact with the boundary layer, focusing on their ability to modify the flow dynamics and influence coherent flow structures. The results demonstrate that traveling waves can reduce turbulent kinetic energy in the region near the suction surface, promoting flow relaminarization under certain conditions, particularly with low-speed, high-amplitude waves. At the same time, faster waves enhance turbulence, aiding separation control by generating coherent structures such as quasi-streamwise vortices and horseshoe-shaped vortices. This dual mechanism, combining relaminarization and enhanced turbulence, contributes to drag reduction and lift enhancement by preventing flow separation. Overall, this study highlights the effectiveness of traveling wave-induced flow control in improving aerodynamic performance and offers new insights into the interaction between the traveling waves and boundary layer dynamics.

Keywords: Travelling Wave Method, Flow Control, Drag Reduction, Lift Enhancement, Large Coherent Structures, Reverse Horseshoe

3.1 Introduction

In various aerodynamic mechanisms over airfoils, gradual boundary shape modifications, often referred to as boundary actuation have been implemented to improve the efficiency of flow control, particularly under lower Reynolds numbers of conditions [43–46]. Studies reveal that aligning actuation frequencies with vortex shedding frequencies of the flow can enhance lift by facilitating better fluid transport and reducing flow separation zones [47]. Camber morphing airfoils, which adjust their camber thickness in real time, have demonstrated up to a 54% increase in aerodynamic efficiency [48]. This type of shape improvement allows airfoils to adapt to changing aerodynamic conditions in real-time. Another beneficial method is the wave propagation technique (Travelling Wave Method) which is used for morphing surfaces and is able to control flow separation and delay stalls at high angles of attack [29,49,50]. The traveling wave method boosts boundary layer momentum through two distinct processes. Initially, the oscillating surface generates localized fluctuations that inject momentum directly into the flow near the wall, increasing energy in the boundary layer. Additionally, the travelling wave motion induces a vortex-like effect in near wall region that pulls high-momentum fluid from the free stream into the boundary layer, promoting stronger mixing and reducing the likelihood of flow separation [51]. From another point of view, the morphing surface applications alter the configuration of large coherent structures in near-boundary regions over the airfoils, leading to a reduction or elimination of the recirculation zone. Manipulating these structures through various methods can exchange momentum between layers of airflow over airfoils.

The influence of travelling wave method is mainly attributed to two main mechanisms: firstly, by introducing stream-wise momentum into the flow and secondly, by triggering the large flow strcutures. The former is much more sensible than the latter because the stream-wise momentum increasement is a predefined and expected phenomenon while the latter is formed

in a particular situation [25]. A more complex and situational outcome is the triggering of flows inabilities, such as Kelvin-Helmholtz's instability, merging instability or formation of stream-wise vortex tubes. These instabilities are caused by primary instability mechanisms within the flow, which may not always occur under certain conditions [25]. They occur when the traveling wave induces high-shear regions specificllyin larger wave amplitudes, particularly in areas of flow separation or boundary layer instability. The instability are revealed as vortices or wave-like structures in the flow, and while these exacerbate turbulence, they can also contribute to beneficial mixing if controlled properly.

Wave charactristics including frequency, amplitude and wavelength determine the efficiency of the travelling wave method. The study of the effects of various induced wave characteristics on airfoil's aerodynamic performance has been addressed in a large number of research studies involving both numerical simulations [29,52–54] , and experimental investigations [49,55–57]). These studies investigated the effects of the induced wave characteristics on drag reduction, lift augment, and stall elimination. There are also examples that describe progression of travelling wave method development. The first insight for considering the travelling wave over a wall boundary condition was made by Kendall [58]. He revealed that the dynamic pressure distribution can be significantly reduced over wall boundary layer. Taneda and Tomonari [30] experimentally showed the streamlines and streaklines over a wavy flat plate in order to prove that the separation is highly dependent on the ratio of wave speed and free stream velocity. Also, the first observation of a laminar vorticcal structures in through of the wave made by Wu et al [59] in their experimental results, which broaded the next reseracher’s horizon to think about the laminarization of the boundary layer over the wall with travelling wave induced on. However, relaminarization may take place in certain conditions which causes turbulence levels decrease and thus a reduced resistance to fluids or drag. Akbarzadeh and Borazjani [60] numerically observed the effects of travelling wave on seaparation control

happens over an inclined plate. They used Large Eddy Simulation (LES) to model the flow behaviour in vicinity of the suction surface on which there is a traveling wave.

Baed on the consensus of various studies, the ratio between wave velocity and free flow speed is a critical parameter for shaping turbulence flows structures [61,62]. Essentially, how this ratio affects turbulence is determined by the geometry of the boundary and its flow's Reynolds number, which represents the relative balance in inertial and viscous forces. It is therefore important to understand the effect of that ratio in order to manipulate and predict turbulent flow behaviour for practical purposes.This ratio differs based on the geometry shape, and Reynolds number [21,42]. Wu [63] also developed a theory for the swimming propulsion mechanism of a plate moving at variable forward speed in an inviscid fluid. Using a laboratory fish-like vehicle, Barrett et al. [64] showed that the power required to propel a swimming body may be smaller than the power needed to tow a straight-rigid body. Beside the wave speed, the flow structures may be affected by the wave steepness. Larger steepness results in more mixing between shear layer and free stream and influences the turbulent quantities distribution between viscous and inviscid layers over the upper surface.

To the best of authors' knowledge, a deep understanding on flow structures and their effects on surface force components are still rare in the literature. The flow structures (coherent vortical structures) are identified via different sampling methods that exist in the literature among which the second largest eigenvalue of the velocity gradient tensor has been widely implemented [65]. Reynolds stresses are calculated in such studies in order to quantitatively describe flow events (like sweep and ejection) happen over the travelling wave surface [61]. In order to study the Reynolds stresses over the suction surface, several methods are used to extract the flow structures correlated with the turbulent flow [62]: the Stochastic Estimation Model, the Reynolds stress contribution (Quadrant Method), Space Averaging on Variable Intervals, and Time-Average of Variable Intervals. Different methods offer unique insight and approaches to

model large coherent structures in a precise way [66]. To the best of authors' knowledge, the more detailed analysis on flow structures and their effects on flow separation relies on studying the contribution of Reynolds stress using quadrant analysis, which clarifies the important role of bursts and sweeps in this separation elimination[67]. The analysis is further upgraded through space and time averaging techniques, which explore turbulence characteristics over a range of periods and timescales to provide an overall perception of the transient and spatial properties of instability [68,69].

In this study, we also show coherent structures over the NACA0018 airfoil suction surface along with the turbulent kinetic energy that is dominant close to the actuated boundary to prove mechanism of drag reduction in the case of Travelling wave boundary is varied in different wave characteristics. Hoepffner & Fukagata [70] observed that in the absence of sufficient wall pumping effects induced by the travelling wave, the primary mechanism for drag reduction (and lift augmentation) is the re-laminarization of the flow near the boundary. This re-laminarization, marked by a reduction in turbulent kinetic energy, plays a crucial role in reducing drag.

Prior to discussing the travelling wave concepts over an airfoil, it is worth considering how the effect of a solid actuated surface is on the flow structures. The concave shape of moving wave over a plate, compared to the flat plate, improves turbulent production and changes law of wall in layers close to the wall. In regard to travelling wave surfaces effects on flow control, Shen et al [21], Lu and Yin [71], Wu et al. [72] and Dong and Lu [73] not only confirmed previous experimental measurements, but also added a detailed instantaneous physical picture including the discovery of velocity bursts originating in the separated region, a detailed analysis of the turbulent kinetic energy budget, and instantaneous vortex structures. In a more general framework, this method allowed them to better depict the turbulence characteristics and effects of viscosity at various Reynolds numbers in order to provide deeper insight into the dynamics

of flow over travelling wave surfaces. It must be pointed out that the majority of previous experiments were conducted at low Reynolds number. But it may be raised the notice why this study has been dedicated to the low Reynolds number flows. It was proved that full strong separation and stall are likely to happen over low the thick airfoils (like NACA0018) operating in low Reynolds number flow ($10^3 < Re < 10^6$) compared to the higher ones ($10^6 < Re < 10^7$) [9]. The boundary layer over the airfoil at high Reynolds number (even in high angle of attack) are completely attached to the surface, resulting in a favorable pressure gradient and then enough lift around the airfoil. However, in low Reynolds number flow, boundary layer is susceptible to flow separation as the flow does not have enough energy to persist adverse pressure gradient specially in high angle of attacks. Previous studies have shown effects of morphing surface as an effective flow control method at Reynolds of 50,000 applied on NACA0018 both experimentally and numerically [15,51]. Although flow remains laminar at areas very close to the leading edge, the majority of suction surface experiences turbulence. It means that the separated flow is strongly driven to reattach, as it is energized by a significant amount of momentum carried within the flow [74]. In this study, the flow characteristics in low Reynolds number flow of 20,000 are numerically examined in order to test effectiveness of TWM in controlling stronger separated flow at a 15-degree angle of attack, consistent with previous studies.

3.2 Problem definition and numerical method

In this section, we define the flow configuration, and the numerical approach used to investigate the effects of traveling wave actuation on the separated turbulent flow over a NACA 0018 airfoil. Detailed explanations of the physical setup and governing equations are presented below.

3.2.1 Physical problem, mathematical formulation numerical scheme

We consider a three-dimensional incompressible turbulent flow over a NACA 0018 airfoil undergoing a 2D travelling wave over its suction surface. The assumption of incompressibility is appropriate due to the range of Reynolds numbers studied, the low-speed nature of the vehicles of interest, and the simplification it provides for computational analysis without compromising accuracy. Here the characteristic length and velocity are chord length L and uniform flow velocity U in free-shear region of the flow. Accordingly, Reynolds number is defined $\mathrm{Re} = \frac{\mathrm{UL}}{\nu}$ which equals 2×10^4 . The angle of attack is 15 as it is roughly stalled angle of attack where the flow separation is observed from trailing to leading edge over the suction side of the airfoil. Points on the suction side of airfoil have an up-down oscillation which their position are updated in rotated coordinates $(\mathrm{X}, \mathrm{Y}, \mathrm{z})$ over the surface as the following equations:

$$\left|\vec{\mathrm{h}}(\mathrm{X}, \mathrm{t})\right| = \mathrm{a}(\mathrm{x})\mathrm{sink}(\mathrm{X} - \mathrm{ct}), \qquad \text{Equation 3-1}$$

$$\vec{\mathrm{h}} = |\mathrm{h}(\mathrm{X}, \mathrm{t})|\hat{\mathrm{n}} \qquad \text{in } (\mathrm{n}, \zeta, \mathrm{z}) \text{ coordinate}$$

$$\vec{\mathrm{r}}(\mathrm{X}, \mathrm{t}) = \vec{\mathrm{r}}^{\mathrm{ua}}(\mathrm{X}, \mathrm{t}) + \vec{\mathrm{h}}(\mathrm{X}, \mathrm{t}) \qquad \text{in } (\mathrm{X}, \mathrm{Y}, \mathrm{z}) \text{ coordinate} \qquad \text{Equation 3-2}$$

Where $\left|\vec{\mathrm{h}}\right|$ is the wave-induced variation length of the wave which determines here updated positions of the suction surface in rotated coordinate system $(\mathrm{X}, \mathrm{Y}, \mathrm{z})$. The wave characteristics a (the magnitude of the variations), c (wave speed) and $\mathrm{k} = \frac{2\pi}{\lambda}$ (wave number with the wavelength λ) are in non-dimensional form based on the chord length and the uniform velocity. Wave amplitude $\mathrm{a}(\mathrm{X})$ the wave has a relation with X in positions near the leading and trailing edge [15]. Thus, to generate a continues wave from zero oscillation at the leading edge $(\mathrm{X} = \mathrm{L}_1)$

to start of high amplitude oscillation ($X = L_2$), also from $X = T_2$ to $X = T_1$ (zero oscillation) near the trailing edge, the amplitude $a(X)$ is defined:

$$a(X) = \begin{cases} 0, & X < L_1 \\ a(X - L_1)/(L_2 - L_1), & L_1 < X < L_2 \\ a, & L_2 < X < T_2 \\ a(X - T_1)/(T_2 - T_1), & T_1 < X < T_2 \\ 0, & x \geq T_1 \end{cases} \qquad \text{Equation 3-3}$$

The incompressible Navier-Stokes equations is numerically solved using Large Eddy Simulation and filtered form as follow [75]:

$$\frac{\partial \overline{u}_i}{\partial t} + \frac{\partial(\overline{u}_i \overline{u}_j)}{\partial x_j} = -\frac{1}{\rho}\frac{\partial \overline{p}}{\partial x_i} + \frac{\partial}{\partial x_j}\left[2\rho(\nu_{sgs} + \nu)\overline{S}_{ij}\right] \qquad \text{Equation 3-4}$$

where $\overline{u}_I$ describes the filtered component of velocity on the grid cells, *p* denotes the grid scale component of pressure, and ρ shows the fluid density, ν is the kinetic viscosity of fluid which breaks down eddies larger than the grid size. The ν_{sgs} is the sub grid scale eddy viscosity which is involved with breaking down the eddies are just larger than (or equal to) the grid size. $\overline{S}_{ij}$ is also filtered strain tensor which includes resolved velocity gradient in scale of the grids.

In order to close the Equation 3-4, it needs to model sub grid scale viscosity. As has been mentioned in previous section, there are different models that describe the SGS kinematic viscosity. Based on dynamic one-equation SGS kinetic energy model The generic model of ν_{sgs} is defined as follows [76]:

$$\nu_{sgs} = C_k \Delta \sqrt{k_{sgs}} \qquad \text{Equation 3-5}$$

where C_k is a non-negative coefficient that varied based on different SGS models and is smaller than unity. Also Δ is the grid characteristic length and is equal to the cubic root of a single computational cell volume. If Δ is the characteristic length of a rectangular cube with the sides of Δ_x, Δ_y and Δ_z the volume is then obtained as follows:

$$\Delta = \sqrt[3]{\Delta_x \Delta_y \Delta_z} \qquad \text{Equation 3-6}$$

Thus, the transport model of $\mathbf{k_{sgs}}$ is as follows:

$$\frac{\partial k_{sgs}}{\partial t} + \overline{u}_j \frac{\partial k_{sgs}}{\partial x_j} = \nu_{sgs}\left[2\overline{S}_{ij}\overline{S}_{ij}\right] - \varepsilon + \frac{\partial}{\partial x_j}\left(\nu_{sgs}\frac{\partial k_{sgs}}{\partial x_j}\right) \qquad \text{Equation 3-7}$$

Where the dissipation rate ε is given:

$$\varepsilon = \frac{C_\varepsilon k_{sgs}^{\frac{3}{2}}}{\Delta} \qquad \text{Equation 3-8}$$

In Equation 3-8, the constant coefficients of C_ε and ε are calculated using Kim and Menon's formulation [77].

3.2.2 Computational strategy

For numerical simulation OpenFOAM 19.6 open-source platform has been used in present study. The Pressure-Implicit with splitting of operators has been used for pressure-velocity decoupling of N-S equation. The time derivatives are discretized by backward differencing. The standard second-order central differencing has been used to discretize the diffusive terms except for the kinetic energy k that is discretized using cellLimited Gauss Linear [78]. Convection terms of N-S equation are also discretized using Gauss Linear-Upwind Stabilized Transport method via the function called Gauss limited Linear [79] in OpenFOAM and based on Total Variation Diminishing (TVD) [80]. This method is a mix of

linear/linear-Upwind. In OpenFOAM, *turbulenceProperties* controls different turbulent models added to N-S equation. In present study, LES has been selected with dynamic k-equation sub-grid model which is discretized using low-dissipation central differencing Gauss filtered Linear [81]. Initial time step of 0.0001 along with an adjustable Courant number are selected in which the maximum Courant is set 0.65.

3.2.3 Validation of numerical model

The separated flow over a NACA 0012 has been simulated to verify the numerical scheme carried out in this simulation. The results of this simulation are validated by numerical simulation of Winslow et. Al [82], experimental of Feng et. al [83] and Anyoji et. al [84]. In this simulation, the channel height, streamwise length, and spanwise length are 30L, 30L and L, respectively. The comparison of time-averaged lift and drag coefficients at Reynolds number of 2×10^4 are made at different angle of attacks between 2 and 15. Boundary conditions are mentioned in Figure 3-1. Note that free slip boundary conditions are also applied to two channel's sides that are perpendicular to the free stream direction. The lift and drag coefficients formulated as $C_L = \frac{2F_y}{\rho U^2}$ and $C_D = \frac{2F_x}{\rho U^2}$, respectively. F_x and F_y demonstrate streamwise and normal aerodynamic forces over the airfoil.

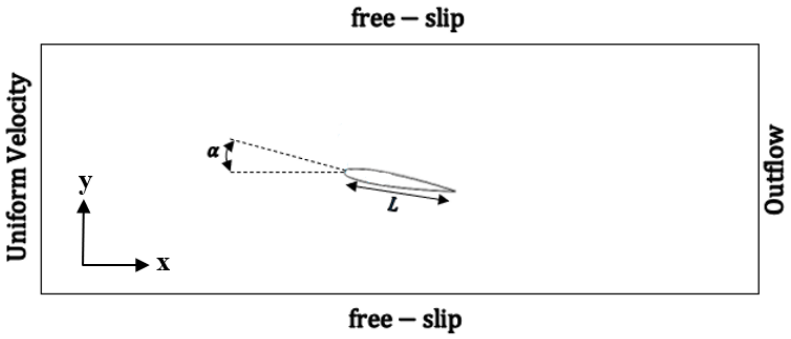

Figure 3-1-Simulation setup for the separated flow over a NACA 0012 airfoil, showing boundary conditions with uniform inflow, outflow, and free-slip boundaries on all sides.

The lift coefficient (C_L) in Figure 3-2 indicates a steady increase as the Angle of Attack (AOA) rises from 2 degrees, starting at just over 0.1 and progressively reaching a peak of approximately 0.6 at an AOA of about 14 degrees. This steady increment gives improvement in generated lift through incrementing AOA, showing the capability for the airfoil to produce attached flow over the surface and hence make this lift effectively and correctly. The red triangles are the calculated values, which seem to follow the overall trend line in good agreement with it, comparing with results of Feng et. al [83] and Anyoji et. Al [84]. These would suggest a robustness in the ability of the LES model to simulate the lift characteristics at these discrete AOAs.

The C_D graph in Figure 3-2 also shows the values from just about 0.02 at an AOA of 1-degree up to just about 0.2 at 14 degrees. This is a trend to suggest relatively low drag for increased lift unto the AOA of 14 degrees. The red triangles, the computational results, show good agreement with the trend established by comparing the work of Feng et. al [83], who gives empirical validation against the LES model prediction for drag forces.

All the more, the few data points you pick up on with LES modeling capture critical transitions in flow behavior—like the boundary layer growth and onset of flow separation that affect both lift and drag—couple with high precision through C_L. The alignment of these points with the overall trends of the data surely must illustrate the effectiveness of the LES model to capture the complex physics governing the flow over an airfoil, including the impact of turbulent eddies and vortex structures. These are critical in the correct prediction of aerodynamic forces.

Taken together, these observations would make the case stronger in this research that LES in OpenFOAM, using a dynamic one-equation SGS kinetic energy model, offers a reliable tool for simulation of the lift and drag over a NACA0018 airfoil at various AOAs and insight into the controlled flow techniques that might reduce the drag or delay flow separation, respectively, providing a complete perspective on the aerodynamic performance at low Reynolds numbers.

Additionally, the pressure coefficient on the upper and lower surfaces of the airfoil at a 5-degree angle of attack is examined. It can be observed that it matches with the results of Anyoji et. al [84]. Due to the separation tales place at 5-degree angle of attack, a strong separation region is formed on the upper surface of the airfoil, starting from the trailing edge. This separation flattens the pressure curve and even makes the upper surface pressure lower than that on the lower surface for most of the chord length (see Figure 3-3). In some areas near the trailing edge, the upper pressure curve in Figure 3-3 is not monotonic, due to vortical structures arising from the pressure surface and passing over the upper surface of the trailing edge, which then recover the pressure distribution.

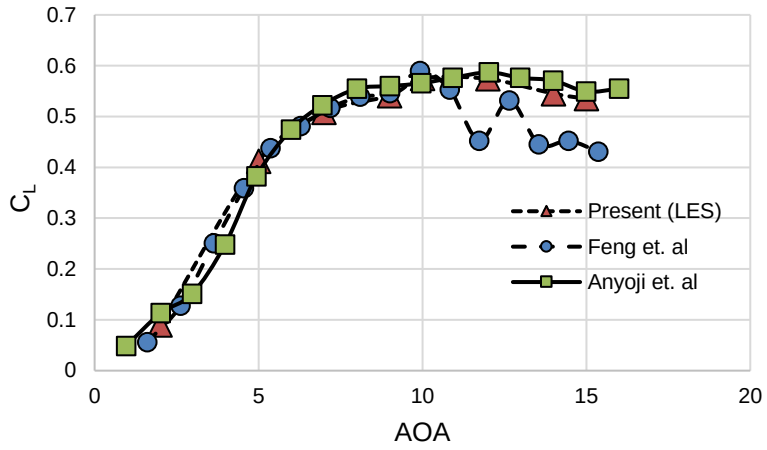

(a)

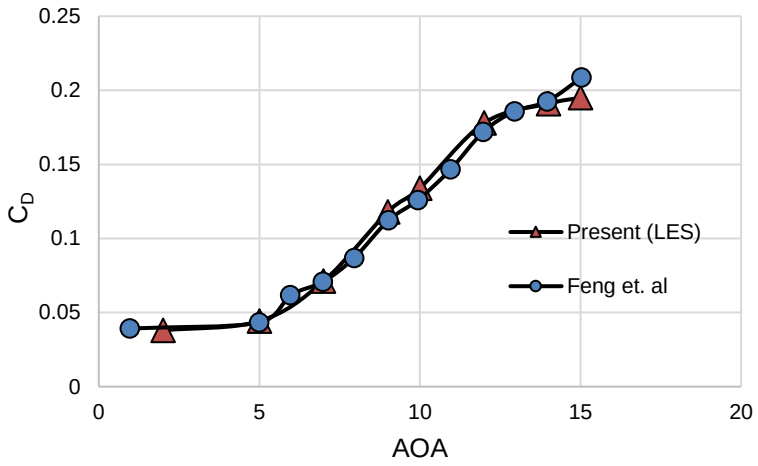

(b)

Figure 3-2-Time-averaged total (a) lift and (b) drag coefficient in varied angle of attacks ranging from 2-15 degrees for NACA0012 airfoil at Reynolds number of 20,000

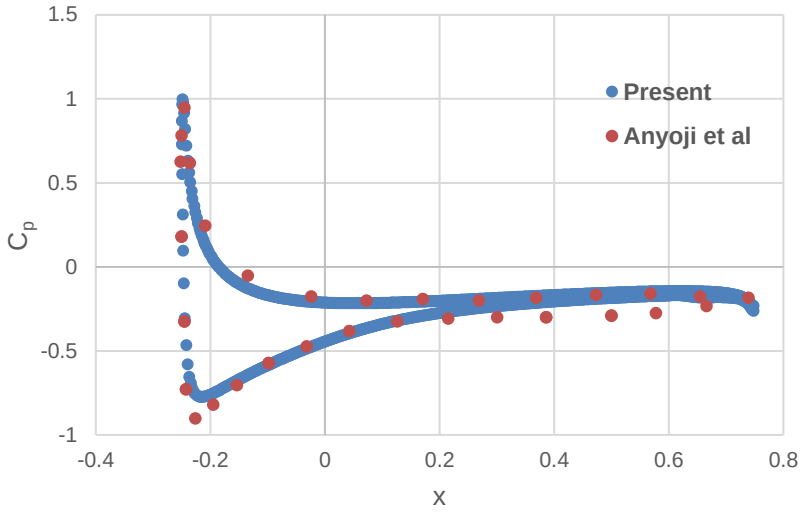

Figure 3-3- Time-averaged pressure coefficient around the NACA0012 airfoil at Reynolds number of 20,000

3.2.4 Simulation parameters and boundary conditions

The Table 3-1 presented above is the set of test cases with various parameters characterizing wave properties at the airfoil suction surface. The parameters are associated with the properties of the traveling wave, which has been used in the simulation to manipulate the boundary layer over the surface of the airfoil where c/U is non-dimensional wave speed. This parameter shows how the wave speeds over the surface of the airfoil with respect to the freestream velocity U of the fluid. It is important because it determines when and how the wave starts affecting the boundary layer and other flow regions, such as the separation or transition from laminar to turbulency.

Table 3-1-Case studies including unactuated airfoil and five controlled ones using travelling wave method

Case	$\frac{c}{U}$	λ	ak
Unactuated	—	—	—
Case 1	0.3	0.3	0.21
Case 2	0.3	0.3	0.42
Case 3	0.6	0.3	0.21
Case 4	1	0.5	0.25
Case 5	2	0.5	0.06

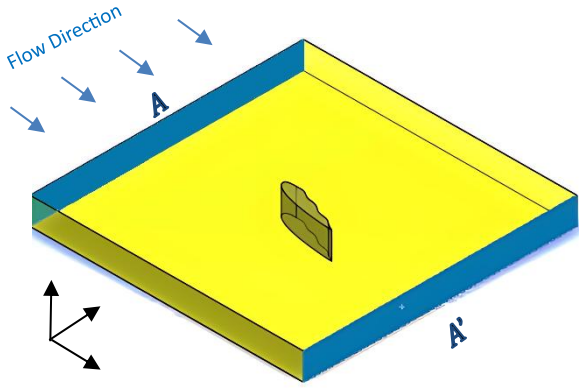

(1) Inlet (*A*) and outlet (*A'*) boundary conditions

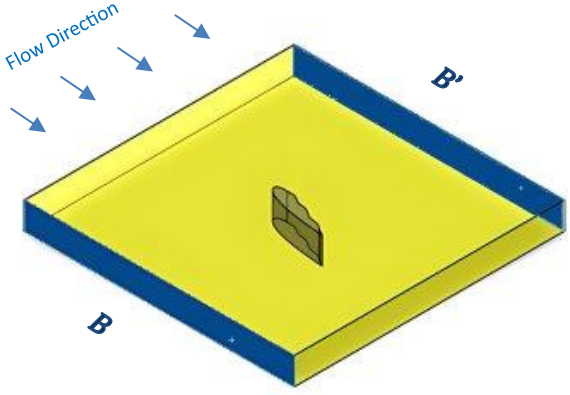

(2) top (*B*) and bottom (*B'*) free-slip boundary conditions

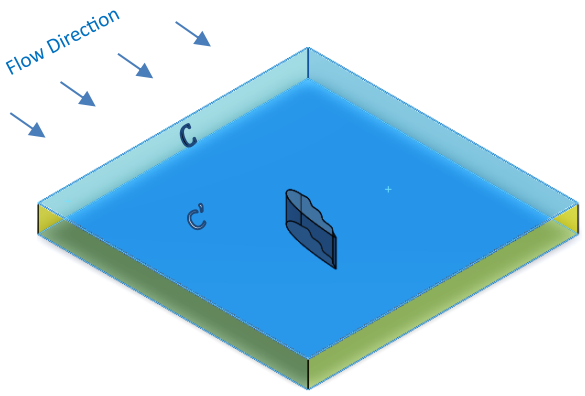

(3) front and back (C, C') cyclic boundary conditions

Figure 3-4- 3D representation of the computational domain for the NACA-0018 airfoil simulation, showcasing the airfoil within the bounded fluid region with specified boundary conditions for low-Reynolds number flow analysis.

The computational domain size is $L_x = 30L$ (streamwise) × $L_y = 30L$ (vertical) × $L_z = 1$ (spanwise). The domain is discretized with a block-structured grid comprising 6,550,000 hexahedral cells. A custom C++ code has been developed and integrated into the solution procedures of OpenFOAM to enhance its functionality for simulation of travelling wave boundary. It controls the mesh topology near the airfoil boundary, enabling adjustments to wave characteristics, including wave speed and steepness. The spanwise boundaries are set as periodic boundary conditions. It is essential to ensure correct spanwise periodicity to resolve all potential flow structures over the airfoil [6]. Different studies have already examined the spanwise length over various NACA airfoils in low-Reynolds number flows, specifically of the order $O(10^4)$ [76,85,86]. They all concur with an increase in Reynolds number and angle of attack, the minimum allowable spanwise length decreases. Studies with flow conditions and Reynolds numbers similar to ours suggest a spanwise length of L_z =0.66L in LES simulations. We compared the effects of two different spanwise lengths (e.g., 0.2 and 1) on drag and lift coefficients at angles of attack of 10 and 15 degrees. The $L_z = 1L$ configuration successfully aligned with previous studies' results at both angles, whereas $L_z = 0.2L$ exhibited a maximum deviation of 39% in the drag coefficient at an angle of 10 degrees and a maximum deviation of

25% in the lift coefficient at an angle of 15 degrees. Due to brevity, detailed values are not presented in this paper. In boundary layer regions and near-wake regions, a finer mesh is used to increase solution accuracy. In fact, the sharp velocity gradients and coherent structures that typically occur in the near boundary regions are properly resolved by this refined mesh. According to Figure 3-4, initial boundary conditions are tuned as the Table 3-2.

In Table 3-2, zero gradient conditions are commonly used where velocity, pressure, and turbulent kinetic normal to the boundary energy are expected to be stable or unaffected by the boundary. Slip conditions are applied when no shear stress is applied, and where no energy loss due to friction is desired.

Table 3-2- Boundary conditions applied on airfoil surface and boundaries of computational domain.

Airfoil (actuated)	**Airfoil (unactuated)**	***A***	***A'***	***B***	***B'***	***C***	***C'***
			Velocity				
Moving Wall	No-slip	Uniform inlet velocity	zero gradient	slip	slip	Cyclic	Cyclic
			Pressure				
zero gradient	zero gradient	zero gradient	Fixed-Value	zero gradient	zero gradient	Cyclic	Cyclic
			Turbulent Kinetic Energy				
Zero ($1e^{-8}$)	Zero	Zero	zero gradient	zero gradient	zero gradient	Cyclic	Cyclic
			Turbulent Kinematic Viscosity				
Calculated	Calculated	Calculated	Calculated	Calculated	Calculated	Cyclic	Cyclic

In terms of Turbulent kinematic viscosity, a placeholder, namely 'calculated', has been assigned to all boundaries except the front and back walls. This indicates that the value is derived from other fields like velocity, and turbulence quantities, rather than being explicitly defined.

Here are the boundary condition equations based on the table you provided:

a) Velocity Boundary Conditions

- Airfoil Surface (Actuated Case - Moving Wall Condition)

$$\vec{u} = \vec{u}_{wave}, \vec{v} = \vec{v}_{wave}$$ Equation 3-9

- Airfoil Surface (Unactuated Case - No-Slip Condition)

$$\vec{u} = 0, \vec{v} = 0, \vec{w} = 0$$ Equation 3-10

- Inlet Velocity Condition (Uniform Inlet Velocity)

$$\vec{u} = U_{\infty}, \vec{v} = 0, \vec{w} = 0$$ Equation 3-11

- Outlet Velocity Condition (Zero Gradient)

$$\frac{\partial \vec{u}}{\partial x} = 0, \frac{\partial \vec{v}}{\partial x} = 0, \frac{\partial \vec{w}}{\partial x} = 0$$ Equation 3-12

- Top & Bottom Boundaries (Slip Condition)

$$\frac{\partial \vec{u}}{\partial y} = 0, \vec{v} = 0, \vec{w} = 0$$ Equation 3-13

- Front & Back Boundaries (Cyclic Condition)

$$\vec{u}_{front} = \vec{u}_{back}, \quad \vec{v}_{front} = \vec{v}_{back}, \quad \vec{w}_{front} = \vec{w}_{back}$$ Equation 3-14

b) Pressure Boundary Conditions

- Airfoil Surface & Inlet (Zero Gradient Condition)

$$\frac{\partial p}{\partial y} = 0$$ Equation 3-15

- Outlet (Zero Gradient Condition)

$$\frac{\partial p}{\partial x} = 0$$ Equation 3-16

- Top & Bottom Boundaries (Zero Gradient Condition)

$$\frac{\partial p}{\partial y} = 0$$ Equation 3-17

- Front & Back Boundaries (Cyclic Condition)

$$p_{front} = p_{back}$$ Equation 3-18

c) Turbulent Kinetic Energy (TKE) Boundary Conditions

- Airfoil Surface (Fixed Low Value for Stability)

$$k = 1 \times 10^{-8}$$ Equation 3-19

- Inlet (Fixed Low Value for Natural Turbulence Growth)

$$k = 0$$ Equation 3-20

- Outlet (Zero Gradient Condition)

$$\frac{\partial k}{\partial x} = 0$$ Equation 3-21

- Top & Bottom Boundaries (Zero Gradient Condition)

$$\frac{\partial k}{\partial x} = 0$$ Equation 3-22

- Front & Back Boundaries (Cyclic Condition)

$$k_{front} = k_{back}$$ Equation 3-23

- Turbulent Kinematic Viscosity Boundary Conditions

$$\nu_t = calculated\ dynamically \quad \text{Equation 3-24}$$

- Inlet, Outlet, Top & Bottom Boundaries (Calculated or Zero Gradient)

$$\frac{\partial \vec{v}_t}{\partial x} = 0, \quad \frac{\partial \vec{v}_t}{\partial y} = 0, \quad \frac{\partial \vec{v}_t}{\partial z} = 0 \quad \text{Equation 3-25}$$

The computational domain used in this study is a three-dimensional box with bounding coordinates ranging from (-15, -15, 0) to (15, 15, 1). The grid is structured with three geometric and solution directions (1,1,1), ensuring a fully resolved three-dimensional representation of the flow. The total volume of the domain is 899.877 with a minimum and maximum cell volume of $4.1612\times10^{-9}$and 0.0229749, respectively.

The grid quality was evaluated using OpenFOAM's *checkMesh* utility, confirming that the boundary openness remains within an acceptable range, with a maximum value of 1.80225×10^{-15}, ensuring no significant domain leakage. The mesh aspect ratio is 9.77606, and the face areas range from 1.06539×10^{-6} to 0.0918998, indicating an appropriate variation in grid resolution across the domain.

To ensure the numerical accuracy of the solution, key mesh quality metrics were analyzed. The maximum non-orthogonality was found to be 45.06, with an average of 6.25, indicating good alignment of grid cells with flow features. The maximum skewness was 1.75587, well within the acceptable range for OpenFOAM solvers, confirming the grid's suitability for resolving flow structures. The mesh remains fully consistent, with no significant pyramid deformation and coupled point location matching errors averaging zero. These results confirm that the generated grid meets the necessary quality criteria for capturing key aerodynamic characteristics while maintaining computational efficiency.

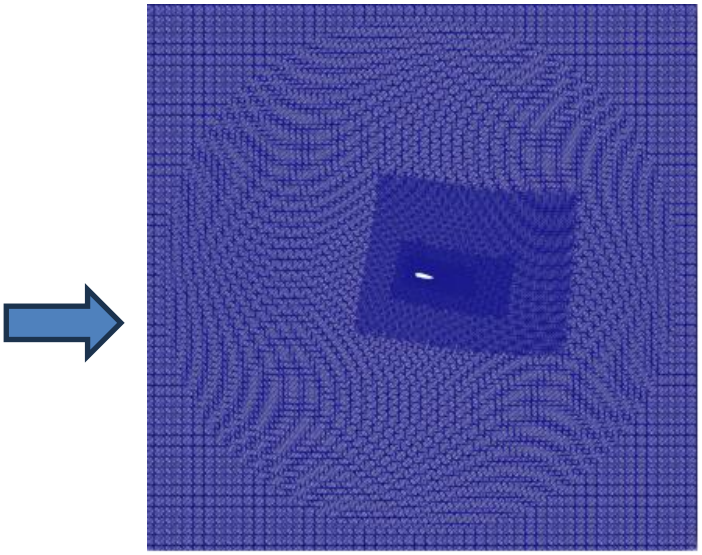

(a)

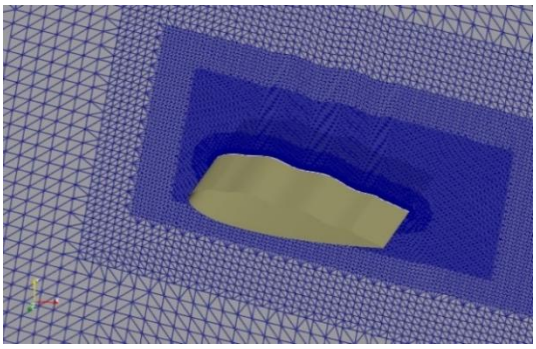

(b)

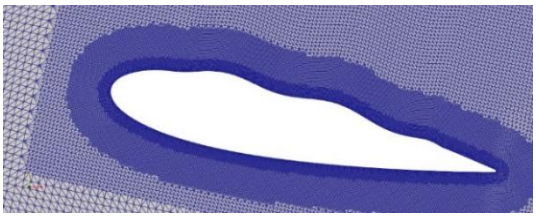

(c)

Figure 3-5-Illustration of the topology of the mesh around the airfoil, with (a) high resolution mesh near the boundary transitioning to coarser grids far from the airfoil, (b) depicting the mesh distribution in z-slice and (c) providing a zoomed-in view around the boundary

3.3 Results and discussions

In the results section, we investigated the aerodynamic effects of different wave parameters (including frequency, amplitude and wavelength) by focusing on their effects on drag, lift and separation characteristics through pressure distribution over the airfoil. Detailed analyses are then conducted on streamlines, vortical shapes and large coherent structures are then extracted to understand dynamic of flow separation and control under various wave conditions

3.3.1 Pressure, drag force and wave growth rate

By modifying the boundary layer dynamics and pressure distribution through employing a moving wall, it is possible to significantly influence both drag and lift, leading to improved overall performance of the airfoil. The instantaneous lift and drag coefficients for the above five cases (as shown in table 1) have been demonstrated in Figure 3-6. As the wave speed c/U decreases (from Case 1 to Case 5), the average drag slightly decreases, whereas the average lift significantly increases. Although the maximum reduction in average drag and the maximum increase in average lift are important criteria to choose the most effective wave parameters, they are not the only factors to consider; minimal fluctuation in these values is also important. In the drag coefficient curves in Figure 3-6, those that exhibit minimum fluctuations are considered the candidates for the most effective wave parameters. Thus, Case 1 and Case 3 are identified as the best choices for the most effective waves since their averages and fluctuations are almost the same and the smallest compared to those of the other cases. Regarding the lift coefficient in Figure 3-6 , Case 1 clearly shows the maximum average lift and minimum fluctuations, whereas Case 3 shows a lift coefficient even lower than the unactuated case. In Case 1, the slower wave speed (c/U = 0.3) provides more effective high energy transfer to the

boundary layer, enhancing lift and stabilizing the flow. However, in Case 3, the faster wave speed (c/U = 0.6) does not synchronize with the flow dynamics, potentially leading to less efficient energy utilization, resulting in reduced lift, even lower than of the unactuated case. For both lift and drag coefficients, the wave parameters of Case 4 lead to strong fluctuations, which are undesirable in the flow control of airfoils. These fluctuations can be the result of larger vortex happening due to the larger wave steepness and larger wavelength [62].

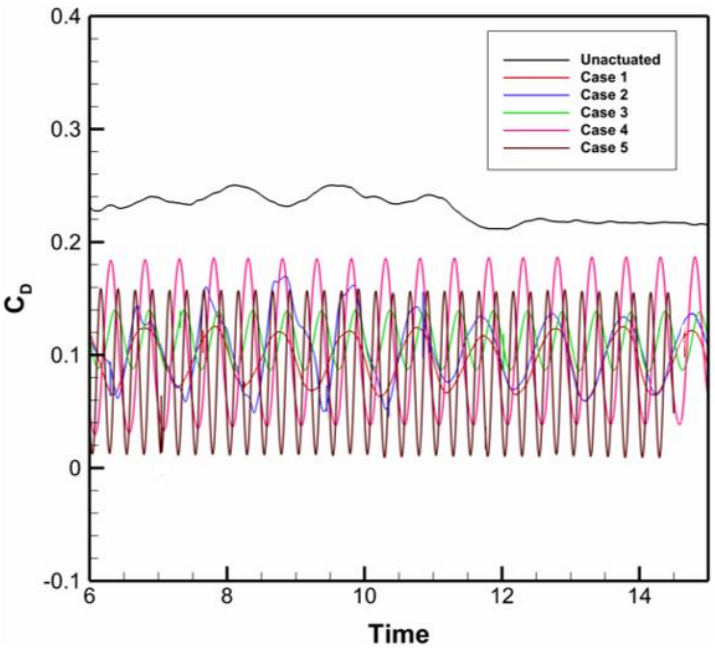

(a)

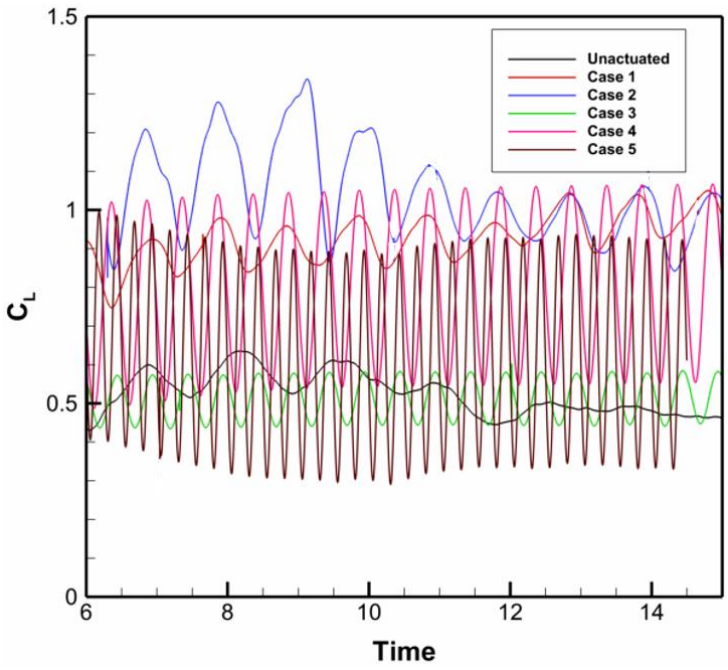

(b)

Figure 3-6- Time evolution of (a) total drag and (b) total lift exerted over the NACA0018 airfoil at Reynolds number of 20,000 at AOA of 15.

3.3.2 Time-average flow field and streamlines

This part of the paper is dedicated to simulating the time-averaged flow field and streamline patterns to provide an overall understanding of the turbulent boundary layer near the traveling wave on the upper surface of the NACA 0018 airfoil. The representative cases discussed in this section are the unactuated case, the low-speed wave (Case 1), and the faster wave (Case 3), as detailed in Table 3-1. The velocity vectors, displayed in Figure 3-7, are demonstrated along lines perpendicular to the airfoil's surface at seven representative detection positions, labeled A through G. These vectors show the time-averaged velocity, highlighting both the magnitude and the direction of the flow at these specific points. We can figure out flow separation over the suction surface based on changes in vector orientation and length. The reversal of vectors

denotes that the flow is not attached to the surface from point A, but instead moving in the opposite direction, characteristic of a separated flow that can drastically affect the airfoil's aerodynamic efficiency by increasing drag and reducing lift. This comprehensive separation from the leading-edge onward emphasizes significant aerodynamic challenges, emphasizing the need for wave parameters to mitigate such adverse effects.

The streamlines in Figure 3-8-a illustrates a strong flow separation existing over the suction surface of the unactuated case. In this case, flow separation occurs when the boundary layer flow loses its adherence to the surface of the airfoil and flows away from it. When the boundary layer moves from its leading-edge point of highest velocity, lowest pressure to a trailing edge it is frequently caused by unfavourable pressures gradients encountered. In turbulent flows, the boundary layer has more energy and is better able to cope with adverse gradients without separation, but it is not invulnerable to separation, especially at higher angles of attack. To analyze the velocity distribution and separation behavior, we evaluate the flow characteristics at seven representative points (A to G) along the suction surface, as shown in Figure 8. These points correspond to specific x-positions: A (X=−0.1), B (X=0.06), C (X=0.19), D (X=0.34), E (X=0.47), F (X=0.6), and G (X=0.70), where X represents the streamwise coordinate along the suction surface. These locations are chosen to capture the evolution of the boundary layer and the progression of separation across the airfoil.Additionally, Figure 3-8-b demonstrates the time-averaged velocity profile, indicating that the main separation starts from point A, with two small separation bubbles already formed upstream of point A. The velocity profile over the surface in the unactuated case shows fluid particles moving upstream over the suction surface, with the maximum backward velocities occurring near the trailing edge of the airfoil. The velocity profiles plotted on the right side, showing tangential velocity, are all negative (toward the leading edge), confirming separation over the suction surface.

For Case 1, the streamlines remain attached to the surface despite a separation occurring between X= -0.05 and X=0.22, and a small bubble further downstream is not depicted in the streamline pattern; instead, it is shown in the tangential velocity profile at the location of point F (X=+ 0.6). The velocity profiles on the right-hand side for Case 1 are steeper than those of the unactuated case, specifically at point G, close to the trailing edge, indicating that the flow is less affected by the counter-rotating vortices emanating from beneath the trailing edge. Thus, the parallel and attached streamlines explain why this case is more successful than others in reducing drag and increasing lift, as the flow contains higher turbulent energy that resists the adverse pressure gradient beyond the separation bubble.

In the faster wave scenario of Case 3, see Figure 3-8-c, the flow remains laminar up to X=+0.18 and then it begins transitioning into a transient and turbulent state. The streamlines are less aligned to the suction surface, indicating that the favorable pressure gradient is not as strong as in Case 1, insufficient to resist bending the streamlines. The velocity profile on the right side also shows the presence of reverse velocity vectors, although these do not display negative values close to the boundary layer, unlike in the previous two cases. The velocities are nearly zero at three points closer to the trailing edge (E,F and G), extending up to 0.1 chord length from the boundary. These nearly zero time-averaged velocity profiles in this extended region indicate frequent instantaneous long separation bubbles near the trailing edge.

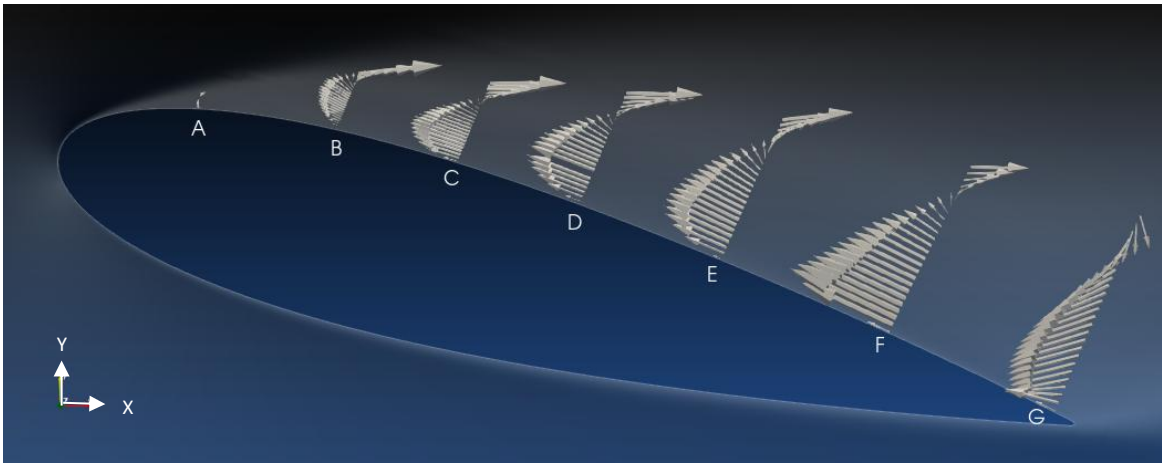

Figure 3-7- Time-averaged velocity vectors over the unactuated surface of the airfoil NACA0018. The figure shows the distribution of velocity vectors along the airfoil's surface from point A to point G, capturing key characteristics of the boundary layer and flow separation.

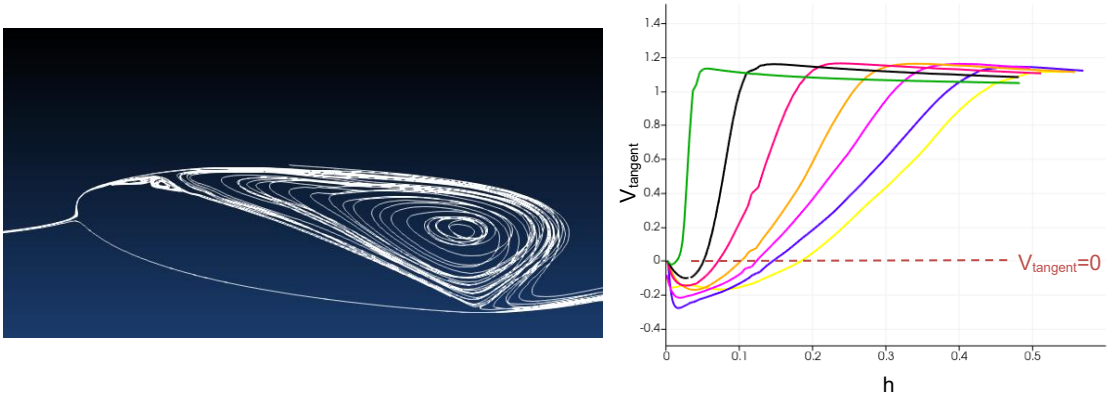

(a) Unactuated

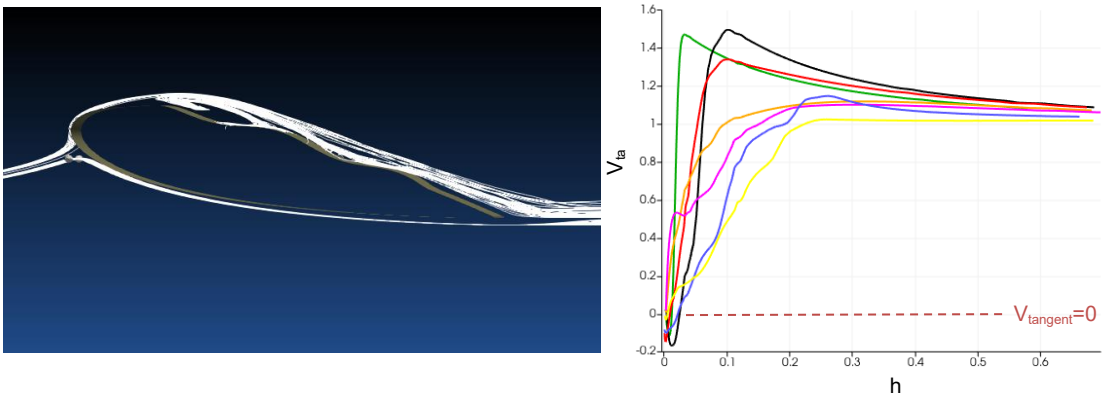

(b) Case 1

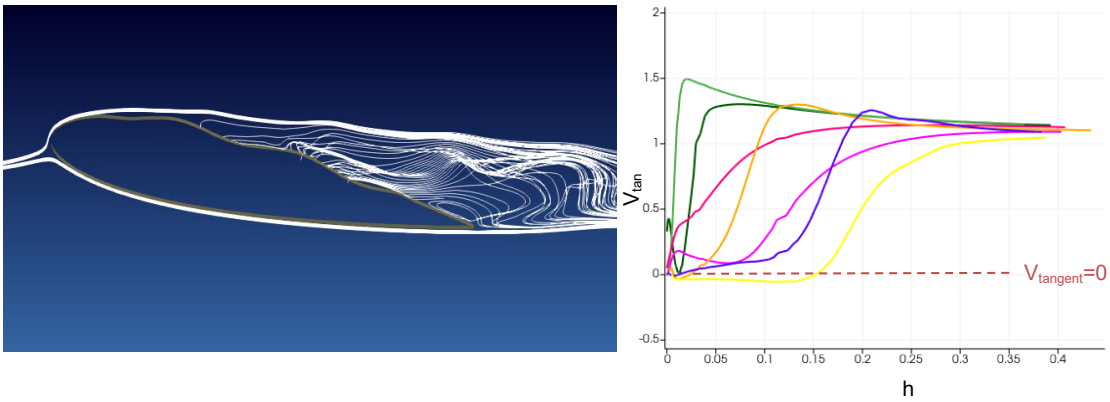

(c) Case 3

Figure 3-8- The streamlines (left figures) and the tangent velocity as a function of normal distance h from the suction surface (right figures) at 7 representative points at seven representative points over the suction surface: A(green)=-0.1, B (black)=+0.06, C (red)=+0.19, D (orange)=+0.34, E (purple)=+0.47, F (blue)=+0.6, G (yellow)=+0.70 for (a) unactuated case, (b) Case 1 and (c) Case3.

In order to understand how lift coefficient is improved using travelling wave, time-averaged pressure distribution has been plotted around the airfoil in halfway spanwise direction, see Figure 3-9-a. The pressure coefficient is defined as:

$$C_P = \frac{P - P_\infty}{\rho U^2} \qquad \text{Equation 3-26}$$

Where P_∞ represents the free-stream pressure. Time-averaged pressure distribution P means averaging the pressure over the boundary points for one cycle of the wave. In the case of the unactuated case, the averaging time becomes n times bigger than the time it takes for the free-stream flow to pass one chord length, $nT_{chractristics} = \frac{nL}{U}$. The time-averaged pressure distributions for the unactuated airfoil, as well as the five actuated cases, are plotted in Figure 3-9-b. From these plots and considering the details indicated in Figure 3-8, we perceive that the traveling wave on the suction surfaces (Case 1 through Case 5) successfully increases lift,

as the pressure at the leading edge drops more than in the unactuated case. The flat area of the pressure coefficients confirms the full stall condition over the suction surface between X = -0.15 and X = 0.55, despite a peak at X = -0.22. In the case of the traveling wave, i.e., Case1 to Case 5, C_P shows a significant negative pressure drop close to the leading edge around X = -0.22. In Case 1, a laminar separation bubble can be seen after the peak drop from X = -0.16 to X =-0.03 near the leading edge, which generates a plateau in the pressure distribution curve in this area [50]. The pressure recovers after this bubble up to the trailing edge. The lower surface (pressure side) of the airfoil experiences a favorable pressure distribution in all cases. It is evident that a higher C_P on the lower surface leads to a greater overall pressure difference across the airfoil, thereby enhancing lift. Notably, the C_P difference at the trailing edge is more substantial in the unactuated case compared to Case 1. However, the C_P difference near the leading edge, which crucially influences net lift force, is significantly more pronounced in Case 1, despite the presence of a laminar bubble. This pronounced pressure difference implies a stronger, more favorable pressure gradient induced by the traveling wave over the suction surface. This difference in C_P, visualized as the vertical distance between the upper and lower lines at each x position in the pressure coefficient plot, highlights the effectiveness of the aerodynamic modifications in Case 1. The leading-edge peak pressure coefficients decrease from Case 1 (C_P =-2.6) to Case 2 (C_P =-2.58) and then to Case 5 (C_P =-2.19), Case 3 (C_P =-1.89), and unactuated (C_P =-1.21) respectively. The observed differences in negative peak existing in pressure coefficients across different cases in Table 1 can be explained by interaction of the wave surface and flow. The slowest wave of Case 1 causes stronger suction effects near the leading edge which is due to prolonged wave interaction with the boundary layer. Conversely, faster waves in Case 2, 3 and 5 do not allow the boundary layer to interact with travelling wavy surface. These results follow the patterns extracted by Akbarzadeh et. al [15] for Reynolds of 50,000 where they report mean pressure coefficient

which is affected by TWM over a NACA0018 airfoil at AOA of 15. In this study, we do not investigate the effect of standing wave and forward wave motion because the former has negative effect on lift coefficient and the latter is less efficient than the backward wave [35].

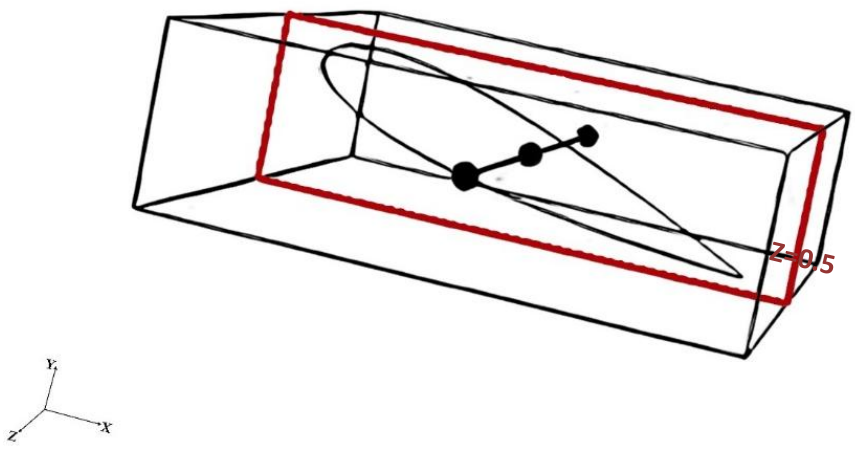

(a)

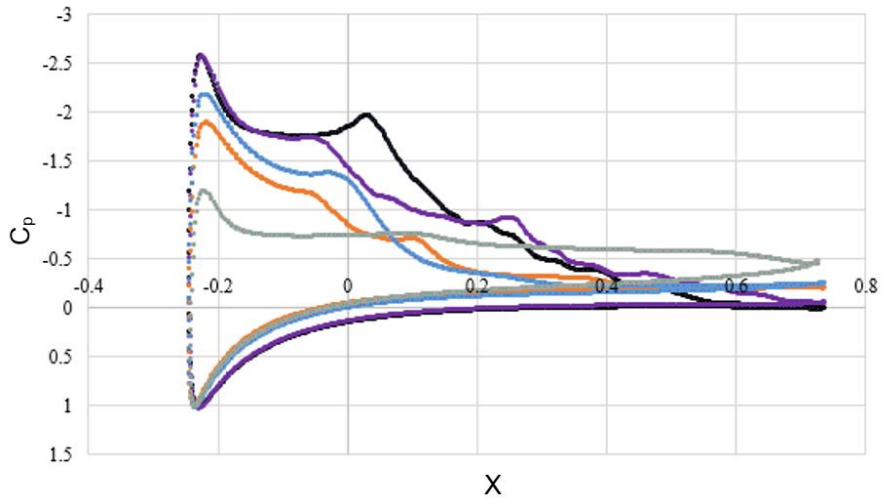

(b)

Figure 3-9- (a) A z-normal slice cut the airfoil at z=+0.5 to measure the pressure coefficient and (b) pressure coefficient for all case studies. The different case studies are represented as follows: unactuated (gray), Case 1 (black), Case 2 (purple), Case 3 (orange), and Case 5 (blue).

3.3.3 Analyzing Coherent Structures Using the Second-Invariant Eigenvalue Method

Previous studies of the turbulence boundary layer of an airfoil have indicated the existence of coherent structures of the travelling wave surface [87,88]. These structures are organized, recurring patterns in the boundary layers that considerably enhance momentum transport and, consequently, drag reduction and lift enhancement. In this study, we use second-invariant eigen value of the tensor $\Omega^2 + S^2$ [65] where $\vec{\Omega}$ and $\vec{S}$ are asymmetric and symmetric parts of the velocity gradient tensor ∇u. Thus:

$$Q = \frac{1}{2}\left(\left\|\vec{S}\right\|^2 - \left\|\vec{\Omega}\right\|^2\right) \qquad \text{Equation 3-27}$$

The asymmetric part shows the rotation rate, and symmetric tensor denotes the viscous stress tensor. Examining the definition of the second invariant, it becomes apparent that Q captures the local equilibrium between the shear strain rate and the magnitude of vorticity. This parameter defines regions where the magnitude of vorticity exceeds that of the rate-of-strain [62].

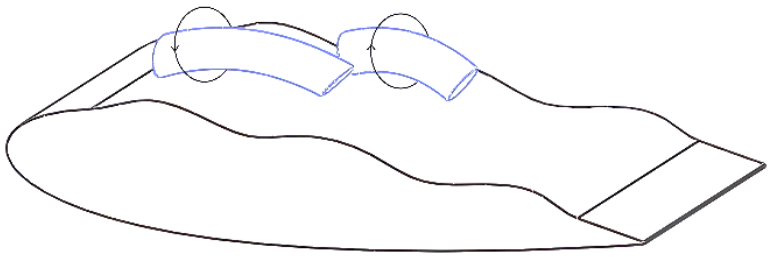

(a)

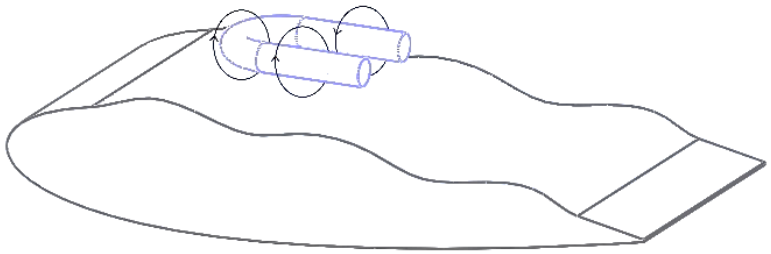

(b)

Figure 3-10- Sketch of vortical structures above a slow wave and b) faster wave.

The Q-criterion particularly demonstrates the regions where rotation effects dominate over the deformation effects of shear strain. Positive Q values are indicative of true vortical structures, as these values represent zones where the magnitude of vorticity exceeds that of the rate-of-strain. Thus, positive Q will be implemented to see the vortical structures in the areas where viscous stresses are influential. Finding a suitable Q value is a kind of trial-and-error strategy. This is generally problem-specific and needs some trial and error. The results are almost as a function of order of magnitude of Q. Because both these S and Ω quantities can vary significantly across different flow scenarios or even within different regions of the same flow, finding the right Q value that highlights the vortical structures without capturing too much noise or missing important features requires adjustments. The Q value must be sensitive enough to detect vortices without being overwhelmed by other flow characteristics.

Smaller values of Q are better in visualization of detailed vortical structures whereas higher ones usually show a general and culminative form of vortical structures [65]. The previous studies by Yang and Shen [62], used different sampling methods to illustrate coherent structures in the presence of travelling wavy boundary. They predicted the two types of vortical structures exist for slow waves which are quasi-streamwise vortices and reversed horseshoe vortices with the head upstream and legs downstream, shown in Figure 3-10-a. Quasi-streamwise vortices,

on the other hand, are parallelly aligned to the direction of the free stream. Note that a low percentage of flow structures that shaped like regular horseshoes happen in a turbulent boundary layer. Also, for faster waves, Figure 3-10-b, they showed that quasi-streamwise vortices dominate the flow structures and they come out from the through of the wave and stretched downstream are dominant in the flow structures. Figure 3-11 shows the coherent structures over the suction surface in Case 3 from different views. It is a representative of slow wave, e. g., $\frac{c}{U} = 0.6$. It is clearly shown in Figure 3-11-a that span-wise vortices, and reversed horseshoe vortical structure are dominant entire the near-surface region over the suction surface. Also, Figure 3-11-a, and Figure 3-11-b illustrate the slow-moving wave over the airfoil was successful to laminarize the flow from leading edge to $X = +0.28$ (compared to the unactuated airfoil where this point was about -0.22). This area is all filled by span-wise vortex tubes which are deformed at X=+0.28 and the head of horseshoe started to be appeared a head of this point at $X = 0.3$. Rolling the spanwise vortexes over the small legs of horseshoes stretched the legs so that the legs become 0.36 long. These stretched and thin lengths that are called vortex pairs (or streamwise vortices) which make upwelling and downwelling of the flow (eject and sweep) [61,62]. Approaching the vortical structures to the wake region close to the trailing edge of airfoil, see Figure 3-11-b and Figure 3-11-c, density of the streamwise vortices is decreased and a street of spanwise vortex is shaped, like unsteady laminar flow behind a bluff body [36,89]. The transition from streamwise (R1) to spanwise vortices (R2) near the trailing edge are associated with larger and thicker vorticities which implies a big wake region which is unfavorable especially in high angle of attack. These vorticities are mixed with other vorticities (R3) coming up from the pressure surface at the trailing edge tip, generating weaker, but larger wakes. This leads to the formation of a high-pressure region which can roll back toward the leading edge.

The Q-iso surface in Figure 3-11 is colored according to an identification parameter of I defined by Yang and Shen [62]. In order to quantify the spatial frequency of the vortex types over the airfoil, they introduced a detection I function as follows:

$$I_0(x,y,z,t) = \begin{cases} 1 & if\ Q(x,y,z,t)\ \geq 0, \\ 0 & otherwise, \end{cases} \qquad \text{Equation 3-28}$$

Where I_0 detects the vortex core. This function helps to distinguish positive values from negative ones. To identify intensity region with the most stream-wise vortices, I_x is given as follows:

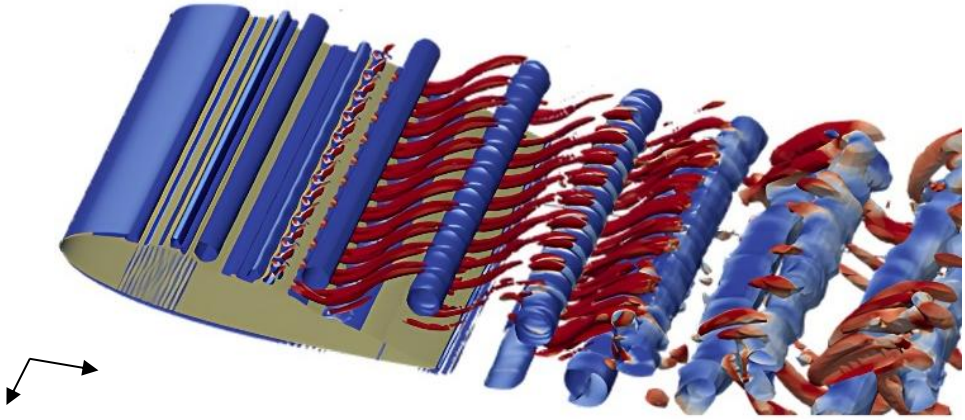

(a)

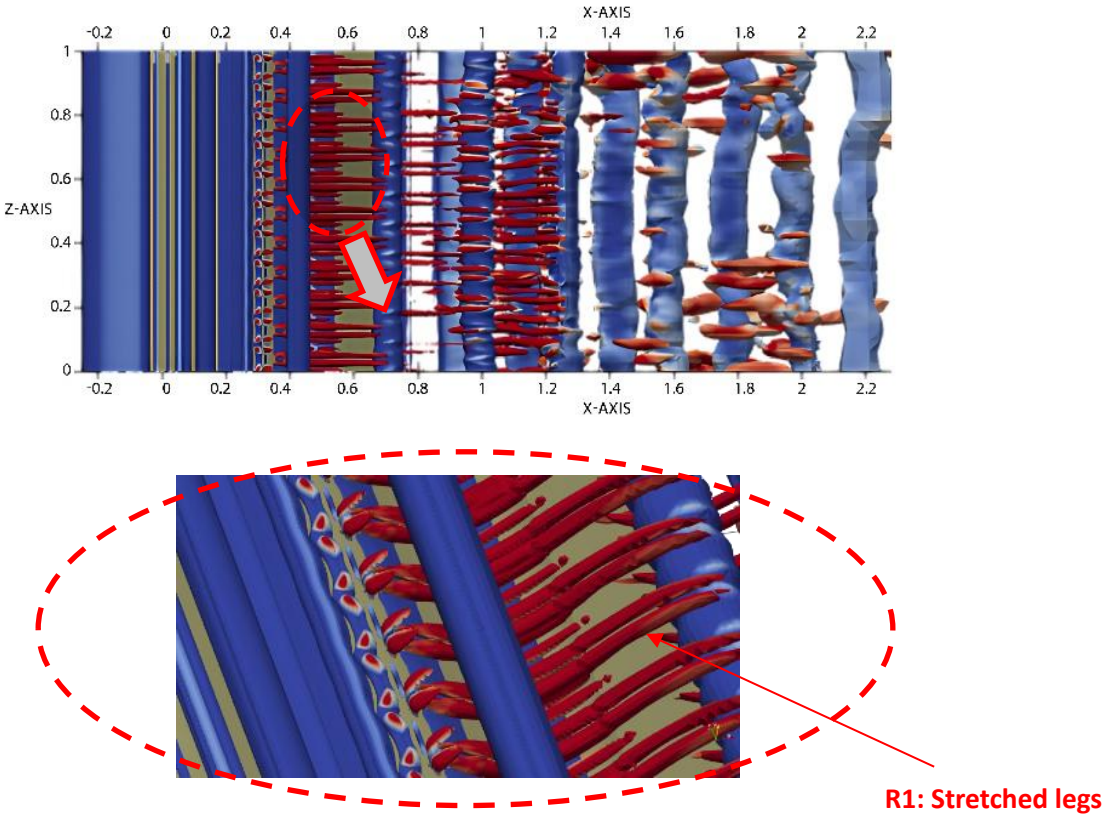

(b)

(c)

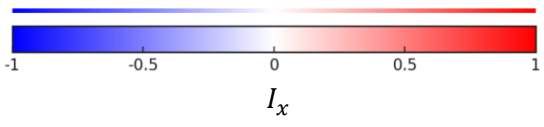

Figure 3-11- Coherent structures over the suction surface of Case 3 from different display view. The structures are resolved with Q-isosurface of +10.

$$I_x(x,y,z,t) = \sqrt{\vec{\omega}_x^2 + \vec{\omega}_y^2} - |\vec{\omega}_z| \qquad \text{Equation 3-29}$$

Vortical structures =

$$\begin{cases} streamwise\ vortex\ pairs, horsshoe\ legs & if\ \ I_x > 0\ and\ |\omega_x| \\ spanwise & if\ \ I_x < 0\ and\ |\omega_x| \end{cases}$$

Figure 3-12 serves as a validation of this method. In this analysis, the I_x values for streamwise vorticities (or stretched horseshoe legs) are positive while those for the spanwise ones appear negative which is not applicable in this identification method, as streamwise vortices inherently have positive I_x values. The negative values have been intentionally used in the contour color map to clearly distinguish streamwise structures from other types of structures.

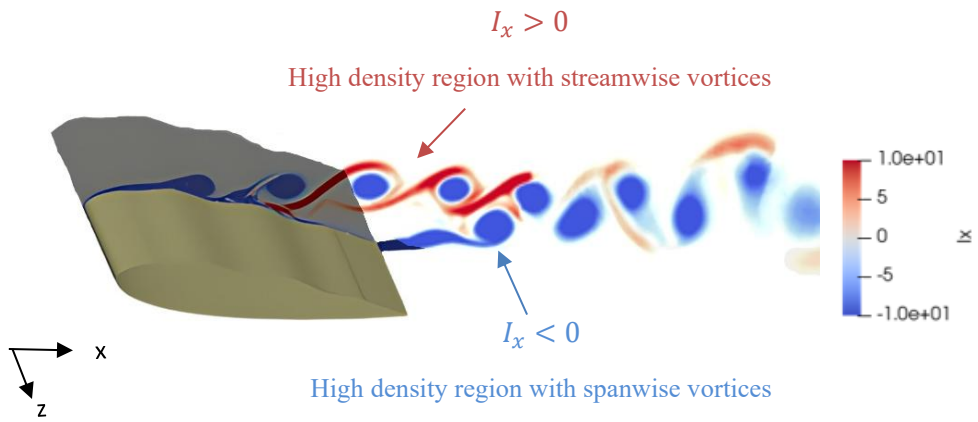

Figure 3-12- Streamwise vortex indicator I for the Case 3 which is shown on a z-normal slice at $z = 0.5$. The dark red shows the vortices that are the most stretched along the streamwise direction, while the dark blue highlights those that are primarily revolving around the spanwise axis.

Figure 3-13 shows 3D vortical structures that help identify different types of coherent structures around the airfoil. For the unactuated one, high intensity region of positive I_x, streamwise

vorticities is depicted by red color and recognized by the *I* function among the flow structures shown in the left figure (Figure 3-13-a). The right-hand side (Figure 3-13-b) has a focused view, highlighting the primary vortical structures. The blue streaks represent tube-like coherent flow structures, which are mostly transient regions near the leading edge. As shown, the bulk flow rolls downstream as it passes over the high-curvature suction surface and begins to experience instability, an early sign of horseshoe vortex formation. The red areas indicate intense streamwise vortices, which correspond to the 3D legs of these horseshoe vortices, playing a significant role in momentum transfer through upwash and downwash around the vortex legs.

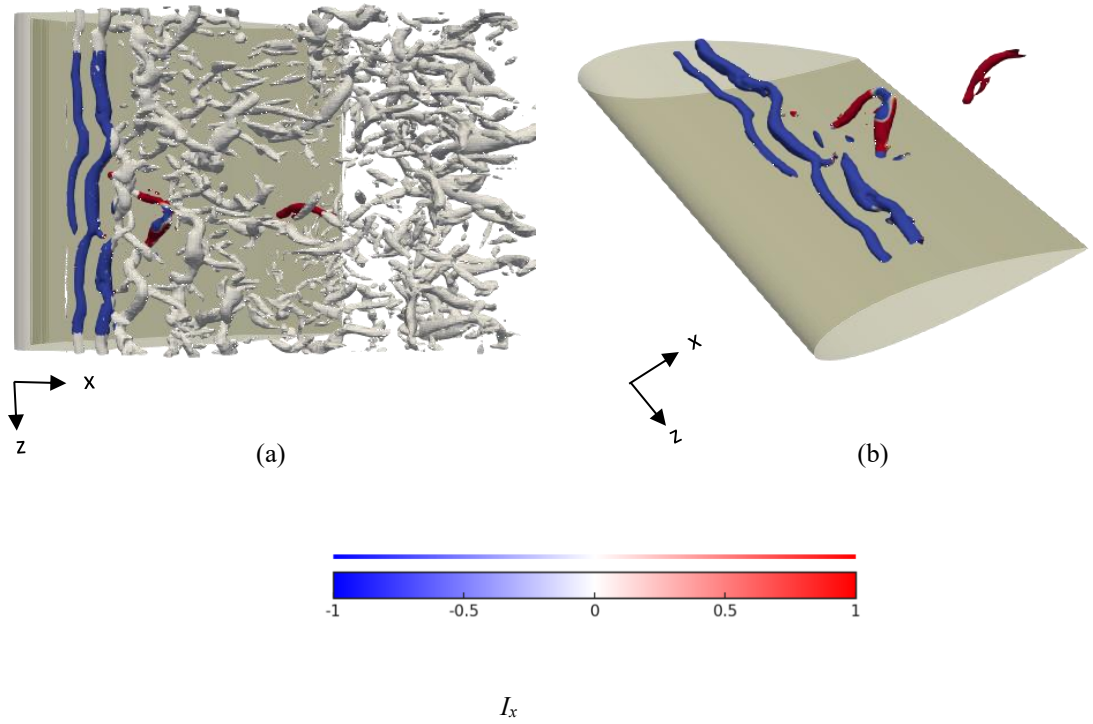

Figure 3-13- Detection of vortical structures using I function. (a) The identified horseshoe and streamwise vortex tube and (b) I function of these structures.

3.3.4 Impact of Traveling Wave on Turbulent Kinetic Energy (TKE) and Aerodynamic Performance

The intensity of turbulent kinetic energy $\frac{1}{2}\langle u'^2 + v'^2 + w'^2 \rangle$ are also affected by travelling wave parameters over the surface. The amplifying or diminishing TKE by the wave is highly dependent on specific parameters such as the wave speed and steepness. In Figure 3-14, phase-averaged velocity fluctuations have been used to compute TKE over the actuated boundary. Comparing the unactuated one airfoil vs Case 1, it is observed that the turbulent energy has been increased so that the maximum TKE of Case 1 is roughly three times more than that of unactuated case. Also, the region above the surface of unactuated airfoil with very low value of TKE, caused by the full separation, has been substituted by higher momentum. This transformation again underscores the effectiveness of TWM in enhancing momentum transfer. Additionally, the single high energy spot near the leading edge of airfoil, initially caused by the small separation bubble, is then transferred downstream via travelling wave boundary. In the other words, compared to the unactuated case, as the wave moves on the airfoil suction surface from leading edge to trailing edge, it carries this high TKE downstream which modifies local flow characteristics and leads to attached flow, as was previously shown in Figure 3-8. In Case 3, as the wave speed increases while maintaining the same steepness, the flow becomes more organized. The faster interaction between the wave and the flow reduces large turbulent eddies, and the low TKE region typically observed in fully separated flow diminishes to nearly zero. It means the flow has been relaminarized. The drag coefficient plot (in Figure 3-6) as well as pressure coefficient plot (in Figure 3-9) showed that this is successful in reducing the drag and producing favorable pressure gradient. This improvement can be partially attributed to a stabilization and smoothing of the flow, which resembles characteristics of a laminar flow (re-laminarization process) over a substantial portion of the suction surface, specifically in Case 3. "Interestingly, lift does not show a significant improvement in Case 3, while drag experiences

a noticeable reduction compared to the unactuated case. This is due to the smoother, laminar-like flow over a large portion of the airfoil surface in Case 3. The fastest wave in Case 5, with lowest steepness also decreases TKE one order of magnitude. It seems to be successful in re-laminarization, whereas the fast fluctuation makes high amplitude fluctuations forces applied over the airfoil surface.

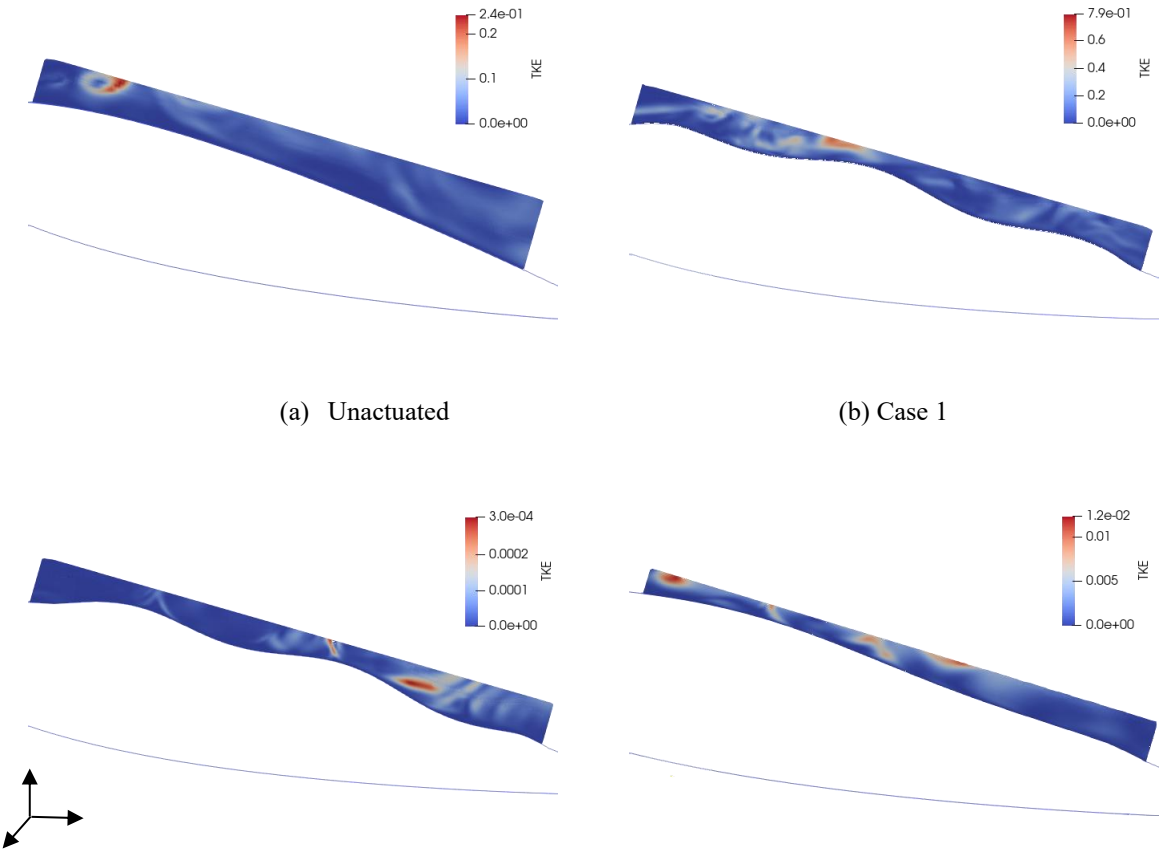

(a) Unactuated

(b) Case 1

(c) Case 3

(d) Case 5

Figure 3-14-Turbulent kinetic energy contours in the selected region above the actuated surface for different cases. (a) unactuated case highlights a minimal turbulent activity with a maximum TKE of 0.24. (b) displays Case 1 with the peak of TKE=0.79 which shows enhanced turbulence, (c) Case 3 demonstrates a trend toward diminishing turbulent eddies on most percentage of the airfoil surface and (d) Case 5 Illustrations the most significant TKE elevation to 1.2, reflecting substantial turbulence amplification at this setting.

3.3.5 The role of Reynolds stress and quadrant analysis

The travelling wave changes the mean velocity profile of the flow near boundary region which alters the velocity fluctuations values compared to those in unactuated cases. Thus, the Reynolds stress, representing the momentum flux due to velocity fluctuations in turbulent flows, behaves differently which leads to different turbulent events in crescent and though of the wave. These distinctions help figure out how turbulent energy transport is performed between the flow layers. A useful tool in the study of Reynolds stress is quadrant analysis.[90] Quadrant analysis stands out in breaking down the contributions of different turbulent structures to the total Reynolds stress. Robinson [89] mentioned that repeating patterns of coherent motion, specifically the near-surface coherent structures, are quantitatively illustrated by distribution of Reynolds stress (with its components $\mathrm{u}'$and v'). The tensor of Reynolds stress consist of four parts that determines four events that mostly happen over an actuated surface [62]. This study does not use w', the spanwise component of Reynolds Stress, since its inclusion would complicate the analysis without substantially enhancing the understanding of Reynolds stress contributions in the context of wall-bounded flows [91]. The primary Reynolds shear stress component, which is crucial for boundary layer phenomena, does not involve w'. The Reynolds stress components are categorized into four quadrants as follows:

$$R_s = \begin{bmatrix} -\mathrm{u}'\mathrm{u}' & -\mathrm{u}'\mathrm{v}' \\ -\mathrm{u}'\mathrm{v}' & -\mathrm{v}'\mathrm{v}' \end{bmatrix}$$

Q1: $\langle \mathrm{u}' \rangle > 0$, $\langle \mathrm{v}' \rangle > 0$ which show outward interactions.

Q2: $\langle \mathrm{u}' \rangle < 0$, $\langle \mathrm{v}' \rangle > 0$ which shows the ejection event.

Q3: $\langle \mathrm{u}' \rangle < 0$, $\langle \mathrm{v}' \rangle < 0$ which shows the inward interations.

Q4: $\langle \mathrm{u}' \rangle > 0$, $\langle \mathrm{v}' \rangle < 0$ which shows the sweep event.

This method directly relates to the calculation of Reynolds stress, particularly the shear stress component, $-\mathrm{u}'\mathrm{v}'$. Q1 and Q3 which have negative contribution to Reynolds stress are

customarily mentioned as the turbulence dissipation whereas Q2 and Q2 have the positive contribution (product of u' and v' is negative) to the Reynolds stress and is percepted as the turubulence production. Figure 3-15 shows the flow structures over the Case 1 airfoil. As shown in Figure 3-15-a, three distinct structures have been extracted to specify their contribution to Reynolds stresses: (1) one reversed horseshoe with head upstream and legs downstream (2) one regular horseshoe with head downstream and legs upstream, (3) and two streamwise vortex tubes (one in Figure 3-15-b and one in Figure 3-15-c). To clearly distinguish between areas of momentum transfer toward (Q1 and Q3) and away from (Q2 and Q4) the mean flow, the range of color map of shear stress component ($u'v'$) has been limited. As also shown in Figure 3-16-b, the reversed horseshoe of shape 1 shows sweep event from the leeward of the horseshoe toward the legs as the $-u'v'$ is positive, and $\langle u' \rangle$ and $\langle v' \rangle$ are respectively positive and negative. In fact, Figure 3-16-a and Figure 3-16-b show contribution of the travelling wave to downwelling motion of the high momentum flow toward the near boundary region(high-speed fluid moving downward towards the wall). The windward of the head of horseshoe shows a negative Reynolds stress component ($-u'v'$). Based on Figure 3-16-a that shows negative values for both velocities' fluctuations, this region is experiencing Q1 event that is outward interaction of the fluid from the boundary which is again consistent with Figure 3-15. Shape 2 which illustrates reversed horseshoe has been associated with positive Reynolds stress at both leeward and windward of the horseshoe. Based on Figure 3-16-c, and Figure 3-16-d, leeward is experiencing Q2 event (upwelling motion) whereas the head region is undergoing Q2 event (downwelling motion). The structure 3 shows a streamwise vortex tube which appeared as a positive component of Reynolds stress.

Figure 3-16-e and Figure 3-16-f clearly show that the top and bottom sides of the vortex tube exhibit opposite signs in velocity fluctuations, indicating that Q2 events occur on one side and Q4 events on the other. This event is also reported by Yang and Shen [62] for the turbulent flow

over a wavy wall. The last structure, shape 4, as shown in Figure 3-16-g and Figure 3-16-h, a streamwise vortex tube is experiencing Q2 events on the both sides whereas includes Q1 event at the tube center.

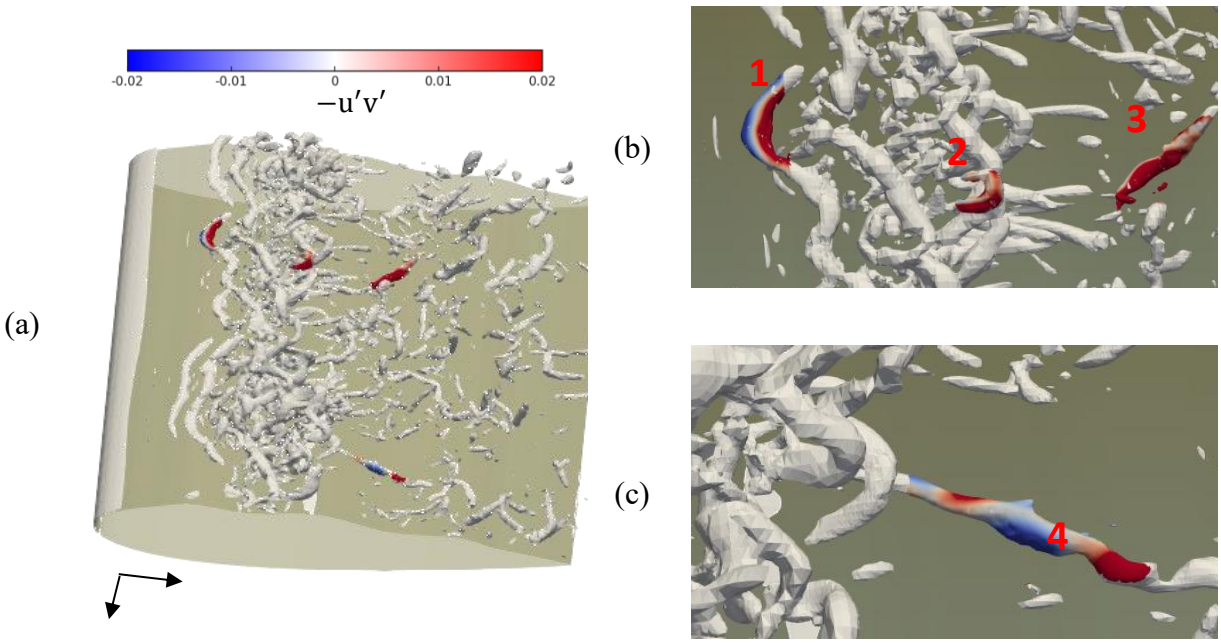

Figure 3-15-(a) Three distinct structures contributing to Reynolds stresses- (b) and (c) show the zoom-in view of the structures.

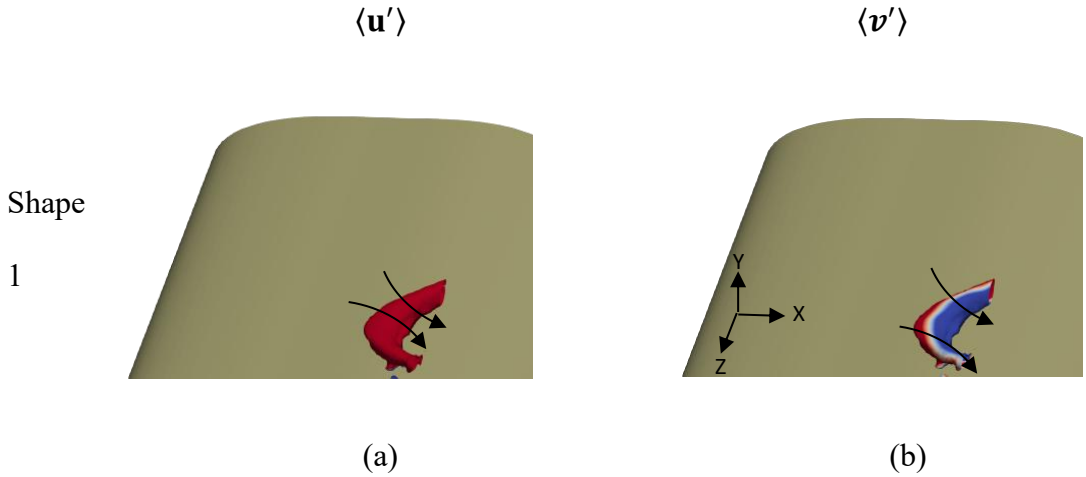

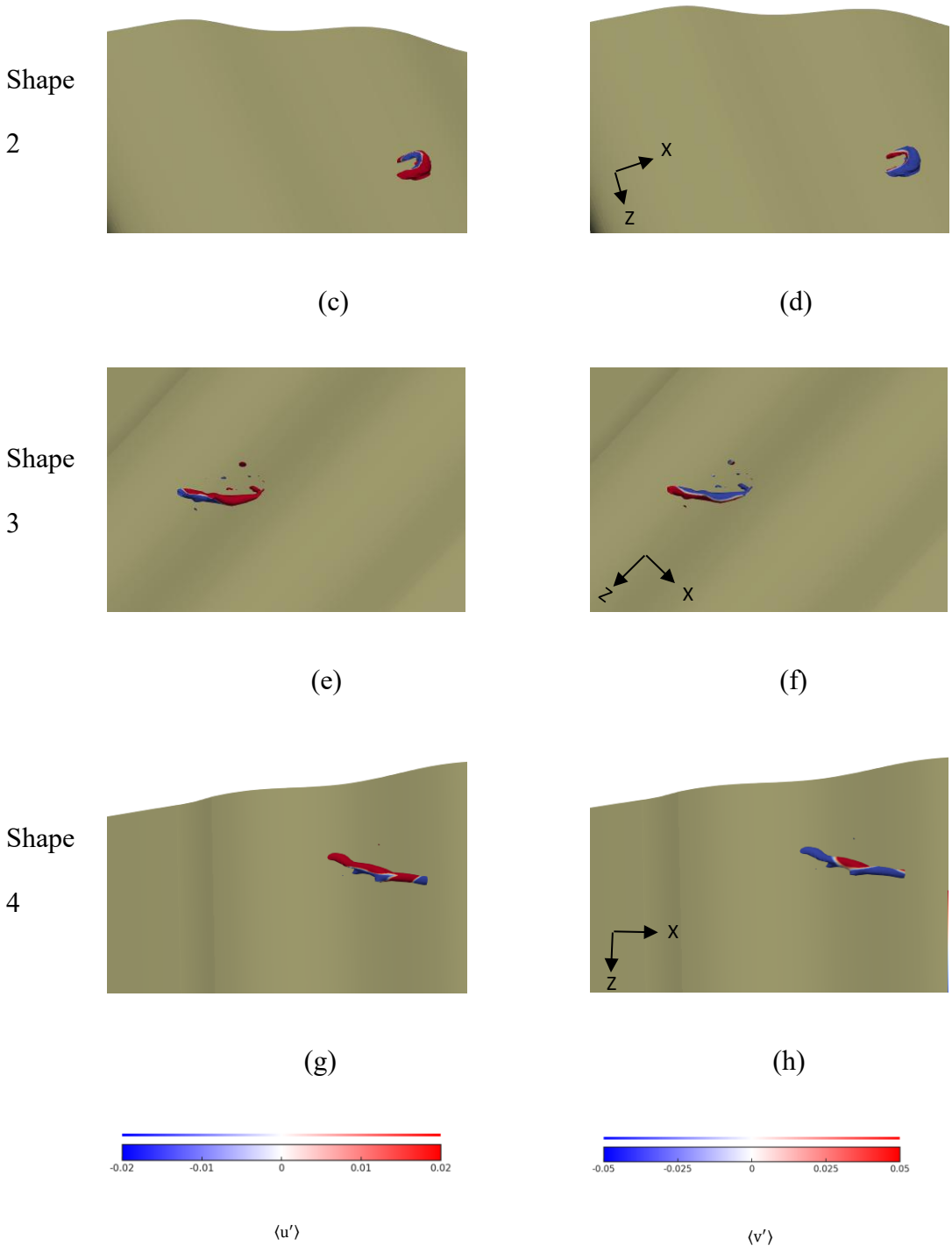

Figure 3-16- The contour of velocities fluctuations for the sake of quadrant analysis which is mapped over the four shapes extracted from Q-iso surface.

To contextualize the findings of this study at Re = 20,000, a comparison was made with the work of Akbarzadeh et al., [60] who investigated the effect of backward traveling waves on a

NACA 0018 airfoil at Re = 50,000 and an angle of attack of 15°. Both studies identified backward traveling waves as the most effective configuration for improving the lift-to-drag ratio. However, key differences in the magnitude of aerodynamic improvements were observed, reflecting the sensitivity of flow characteristics to Reynolds number.

While Akbarzadeh et al. reported a 38.3% increase in lift coefficient and a 68.4% reduction in drag, leading to a maximum lift-to-drag ratio of 10.62, the current study at Re = 20,000 observed a higher relative improvement in the lift-to-drag ratio. The stronger effects at lower Reynolds numbers are attributed to the dominance of laminar separation bubbles and weaker turbulent diffusion, allowing TWM to exert a more pronounced stabilizing influence on the boundary layer.

The amplitude sensitivity observed in both studies shows that higher amplitude traveling waves can induce shear layer instabilities, reducing aerodynamic efficiency. However, at Re = 20,000, this destabilization occurs at lower amplitude thresholds, indicating that laminar flows are more susceptible to wave-induced instabilities.

Overall, the comparative analysis confirms that while the general mechanism of flow control via TWM remains consistent across Reynolds numbers, TWM is more effective in lower Reynolds number regimes, where it can delay separation and enhance boundary layer reattachment more significantly.

In order to understand which quadrants are dominant in this case1, we plotted the contour of Reynolds stress in mid-plane (z=0.5) slice. Figure 3-17 qualitatively shows that Q2 and Q4 are dominant over the windward side toward the wave crest whereas Q1 and Q3 is mostly seen close to the leading edge, above the trailing edge, and the wake region. This can be attributed to the flow separation and reattachment processes in these areas, where outward and inward momentum fluctuations dominate as the flow transitions between different states. In Table 3-3 , the number of cell points are shown which involved in the four quadrant events (Q1: outward

interaction, Q2: ejection, Q3: inward interaction, and Q4: sweep) for different cases aplied on the airfoil. These values help recognize the most possible flow structures in each case. In the unactuated case, the number of events is relatively balanced, with Q2 (ejection) and Q4 (sweep) showing slightly higher occurrences, accounting for around 26% and 27% of the total quadrant events, respectively.In Case 1, the number of events increases significantly across all quadrants. Q4 (sweep) jumps by nearly 155%, reaching 10,850 cell points, indicating a stronger interaction between high-speed fluid sweeping toward the surface. Similarly, Q2 (ejection) also shows an increase of about 150%, rising to 10,591 cell points. Case 2 displays a different trend, where Q1 (outward interaction) and Q3 (inward interaction) become more prominent, increasing by approximately 20% compared to the Case 1, while Q2 and Q4 decrease by about 15%. In Case 5, the quadrant events experience a dramatic rise, especially in Q2 and Q4. Q4 increases by over 150%, reaching 25,221 cell points, while Q2 grows to 23,150 cell points, highlighting intense ejection and sweep events in this highly turbulent flow. These large increases suggest that the fast wave in Case 5 generates the most turbulence and energy exchange compared to other cases. Overall, faster waves, as in Case 5, significantly enhance turbulence, with Q2 and Q4 events consistently dominating ejection and sweep processes

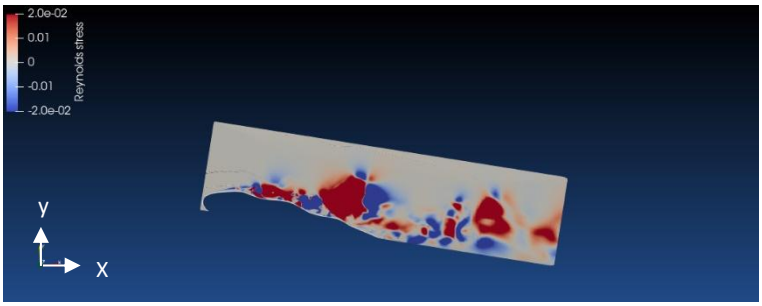

Figure 3-17- Reynolds Stress contour over the region over the suction surface and in the wake region for Case 1.

Table 3-3-The quantity of the cell points in the selected region that are involved in four possible events

Case	Q1	Q2	Q3	Q4
Unactuated	6459	6822	5998	6985
Case 1	10119	10591	10727	10850
Case 2	12351	8510	13210	7950
Case 3	3400	5102	3915	5784
Case 4	11308	13555	10523	13698
Case 5	18211	23150	16522	25221

3.4 Conclusion

This study focused on investigating the effects of traveling wave motion applied to a NACA0018 airfoil at a Reynolds number of 20,000. Specifically, it examined the changes in drag and lift coefficients over the suction surface, the improvements in pressure distribution compared to the unactuated case, the flow structures within turbulent flow over the airfoil, and the distribution of turbulent kinetic energy, as well as the re-laminarization process. To capture the complex interaction between the flow and the actuated boundary, Large Eddy Simulation (LES) was employed using the open-source OpenFOAM platform. A dynamic mesh code was integrated into the LES model to simulate the moving boundary created by the traveling wave.

The primary focus of this study was to utilize advanced sampling methods, including the III-function, the second invariant matrix of the velocity gradient, and quadrant analysis to investigate the flow structures generated by the traveling wave. The results showed that traveling waves significantly influenced the control of aerodynamic forces and turbulent kinetic energy over the airfoil surface. Among the tested cases, the slow wave with a speed of c/U=0.3

(Case 1) proved to be the most effective in improving both drag and lift. The faster wave with a speed of c/U=0.6 (Case 3), while still effective in reducing drag, was less successful in increasing lift. Both Case 1 and Case 3 exhibited similar performance in terms of pressure recovery after a small separation bubble near the leading edge, with Case 1 demonstrating slightly better performance. An important aspect of this research was the identification of dominant flow structures and their impact on local fluid motion. To achieve accurate identification, quadrant analysis, integrated with the second invariant matrix of the velocity gradient, was chosen as the main method for coherent structure identification. This allowed us to identify three typical structures present in the turbulent flow over the moving boundary of the NACA0018 airfoil at a 15-degree angle of attack: regular horseshoe vortices with the head downstream and legs upstream, reversed horseshoe vortices with the head upstream and legs downstream, and streamwise vortex tubes.

Quadrant analysis further revealed the directional behavior of fluid particles around specific flow structures based on the signs of velocity fluctuations. This method enabled a quantitative measurement of the contribution of velocity fluctuations to Reynolds stress over the airfoil surface. In Case 1, four key events—outward and inward interactions (Q1 and Q3) as well as ejection and sweep events (Q2 and Q4) were observed, playing a significant role in the overall flow dynamics around the airfoil.

4 Chapter 4: Effect of Traveling Wave on Flow Structures at Various Angles of Attack Over a NACA 0018 Airfoil at Reynolds number of 20,000

Abstract

This study explores the potential of traveling wave modulation (TWM) as an active flow control method for enhancing aerodynamic performance over a NACA 0018 airfoil at low Reynolds number (Re=20,000). TWM's impact on flow behavior, particularly in terms of boundary layer stability, separation control, and coherent structure formation, is examined across various AOA (7°, 11°, and 14°) to determine its effectiveness in delaying stall and reducing drag. The research employs large eddy simulation (LES) with a dynamic sub-grid scale model to capture the complex interactions within the turbulent boundary layer. Different TWM amplitudes are applied to analyze their effects on flow structure, vorticity distribution, and momentum transfer. The simulations focus on comparing unactuated cases with TWM at amplitudes of a=0.01, examining both 2D and 3D flow features, and visualizing large coherent structures using Q-criterion and x-vorticity contour maps. The results show that in unactuated cases, flow separation is characterized by chaotic, disorganized vortices that contribute to early stall and high drag. TWM introduces organized vortex tubes that extend along the surface, enhancing mixing and transferring high-momentum fluid to the boundary layer, effectively delaying flow separation. The higher amplitude TWM (a=0.02) proves most successful, creating a quasi-laminar flow state that reduces turbulent kinetic energy and stabilizes the boundary layer, even at higher angles of attack (14°). These findings demonstrate that TWM can effectively mitigate flow separation, improve lift, and reduce drag, making it a promising strategy for aerodynamic performance optimization.

4.1 Introduction

The relationship between Angle of Attack (AOA) and aerodynamic performance over airfoils has long been a central theme in fluid dynamics research [92–94]. As a fundamental parameter governing lift, drag, and overall flow structures around aerodynamic bodies, AOA manipulation can be fundamental for control of the stability of aircraft and maneuverability. While conventional fixed-wing designs rely on adjusting AOA to modulate lift forces, emerging technologies like traveling wave propulsion present a novel avenue for augmenting aerodynamic efficiency across a wider AOA spectrum [42,54,95].

The impact of AOA on flow structures and aerodynamic forces has been the subject of extensive research. Influential works by Anderson [96] has elucidated the fundamental relationship between AOA and lift coefficient in varying airfoils, highlighting the critical AOA beyond which flow separation and stall occur. Previous research on flow control methods at different angles of attack on airfoils have demonstrated various effective strategies. Geissler and van der Wall [97] reviewed dynamic stall control on flapping wing airfoils, focusing on techniques like dynamic shape adaptation and momentum blowing, which can significantly alleviate dynamic stall across different flow conditions. Genc et al. [12] provided a comprehensive review of both traditional and innovative passive flow control techniques, such as vortex generators and winglets, which improve aerodynamic performance by delaying flow separation and reducing drag, particularly across a broad spectrum of angles of attack . Goodarzi et. al [98] investigated active flow control using blowing techniques over a NACA 0015 airfoil, highlighting the method's effectiveness in stabilizing the boundary layer and enhancing aerodynamic performance at higher angles of attack . Kornilov et al. [99] examined the effects of combined blowing and suction on low-speed airfoils, demonstrating how these methods effectively control the turbulent boundary layer, thereby improving lift and

reducing drag across different angles of attack. Monshi Tousi et al. [100] focused on optimizing synthetic jets for active flow control on the SD7003 airfoil, showing significant improvements in aerodynamic efficiency at both pre-stall and post-stall angles. These studies collectively illustrate the potential of various flow control methods in enhancing the aerodynamic performance of airfoils across a wide range of angles of attack. Traveling wave propulsion, inspired by the elegant locomotion of biological organisms, has emerged as a promising frontier for aerodynamic innovation. Pioneering research by Fish and Lauder [101] has demonstrated the feasibility of utilizing traveling waves to control boundary layer flow and delay stall. These investigations have revealed the potential of wave propagation to energize the boundary layer, thereby mitigating flow separation and extending the operational envelope of AOAs.

The integration of traveling wave methods with an understanding of AOA effects on flow structures offers a comprehensive approach to optimizing airfoil performance. Amitay et al. [102] demonstrated that synthetic jet actuators could effectively reattach separated flow and enhance lift, particularly when combined with traveling wave actuation. The dynamic behavior of the flow during reattachment, involving the shedding and advection of vortices, highlights the complex interactions between flow structures and control mechanisms [102]. In the context of combined flow control techniques, Seifert and Pack [103] explored the synergistic effects of synthetic jets and traditional control surfaces, such as flaps, showing enhanced control authority and improved aerodynamic efficiency. This approach demonstrates the potential for integrating multiple flow control strategies to achieve optimal performance.

Traveling wave morphing surface is an active flow control method that has shown significant potential for mitigating flow separation and stall elimination which leads to increase of lift and reduction in drag forces. Recent research has demonstrated the travelling wave actuation with low amplitude on the suction side of a NACA airfoil can create negative pressure gradients and transfer high momentum from free stream region into the boundary layer [53,104,105]. These

waves eliminate strong separation and reduce drag through a combination of mechanisms, including direct streamwise momentum injection with the surface fluctuations and triggering controlled instabilities in the close boundary flow field [25,106].

In turbulence modeling of the flow over airfoils, Large-eddy simulations (LES) have been widely implemented to study the effects of traveling waves parameters including frequency, amplitude and wavelength on airfoil performance at different angles of attack. For instance, simulations by Ogunka [53] explored a NACA0018 airfoil equipped with traveling waves over the suction surface and showed enhanced aerodynamic performance and reduced flow separation, especially at higher angles of attack (10-20 degrees). Akbarzadeh et. Al [15] investigated the impact of wave characteristics, such as reduced frequency and amplitude. These wave characteristics were found to be significant, with specific surface configurations matching the flow shedding frequency in the unactuated airfoil proving particularly effective for flow control. The implementation of traveling waves is often enabled facilitated by placing smart materials, such as piezoelectric actuators embedded beneath the airfoil surface, which generate controlled oscillations. These actuations create localized vortices that function as a fluid roller bearing, reducing friction between the external flow and the airfoil surface, as noted in earlier studies [107,108]. Recent work continues to refine conventional travelling wave method, focusing on optimizing wave parameters like wavelength and wave velocity. Simulations by Ogunka and Borazjani [16] have shown that specific wavelength-to-chord ratios can significantly influence flow behavior, with some configurations promoting flow separation control comparable to baseline cases. Our research supports the broader goal of using travelling wave actuations to alter aerodynamic performance in applications such as micro air vehicles and other advanced aerodynamic systems [109,110]

This study embarks on an investigation into the nuanced effects of varying angles of attack on flow structures, with a particular focus on the potential of traveling wave mechanisms to

improve flow patterns so that adverse flow phenomena such as stall and flow separation are controlled. By strategically manipulating the boundary shape of the airfoil, specifically the suction side surface, through wave propagation, traveling wave systems offer the tantalizing prospect of maintaining attached flow and delaying stall, even at elevated AOAs where conventional designs falter. The primary goals of this study are to comprehensively analyze how different angles of attack (7°, 11°, and 14°) influence the flow structures over a NACA 0018 airfoil. This includes a detailed investigation into the onset and progression of flow separation and stall across these angles, capturing the intricate flow patterns and vortex dynamics that contribute to these phenomena. Additionally, the study aims to investigate the effectiveness of traveling wave mechanisms in controlling flow separation and maintaining attached flow. By matching or tuning the wave frequency to interact constructively with the boundary layer instabilities, the study aims to understand how traveling waves can eliminate or delay separation. This also includes studying the optimal wave parameters such as amplitude, speed, and wavelength that result in the best flow control performance at various AOAs.

4.2 Numerical Method

We consider a three-dimensional incompressible ($Ma < 0.3$) turbulent flow over a NACA 0018 airfoil undergoing a 2D traveling wave on its suction surface at various angles of attack (7°, 11°, and 14°). The characteristic length and velocity are the chord length L and the uniform flow velocity U in the free-shear region of the flow, respectively. Accordingly, the Reynolds number is defined as $\mathrm{Re} = \frac{\mathrm{UL}}{\nu}$, which equals 2×10^4

The angles of attack chosen for this study range from low to high, capturing the behavior of the flow as it transitions through different aerodynamic regimes. At 7°, the airfoil begins to

approach the stall region, with initial signs of flow separation forming near the trailing edge. At 11°, the flow separation becomes more pronounced, extending further towards the leading edge, indicating the onset of significant aerodynamic changes or stall condition. At 14°, which is post stall angle of attack, flow separation is observed from the trailing to the leading edge on the suction side of the airfoil. This condition provides a critical test case for evaluating the effectiveness of traveling wave control in delaying or preventing flow separation

The surface morphing of the airfoil, as shown in Figure 4-1, induced by a traveling wave on its suction side, is defined by the following equation:

$$N(s) = a(s)\sin\left[2\pi\left(\frac{S}{\lambda} \pm ft\right)\right] \qquad \text{Equation 4-1}$$

Where $N(s)$ represents the displacement of the vertical surface nodes, describing the height of the wave at a specific location along the airfoil. $a(s)$ is the amplitude of the wave, which may vary along the dimensionless surface coordinate s, allowing for control over the wave's intensity at different points along the airfoil. λ is the wavelength, determining the spatial frequency of the wave along the surface. s is a dimensionless position variable along the airfoil's chord, where 0 represents the leading edge and 1 represents the trailing edge. f is the non-dimensional vibration frequency, controlling the speed at which the wave oscillates. t is the non-dimensional time, scaling the wave's temporal progression.

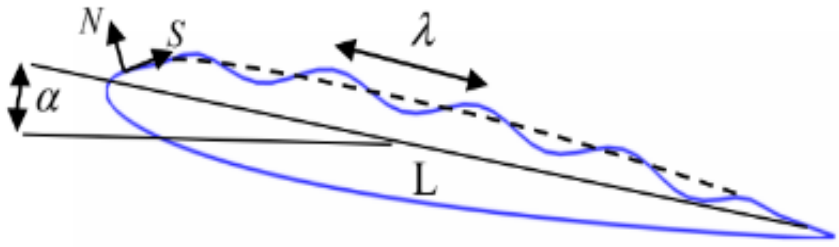

Figure 4-1-Schematic illustration of a NACA 0018 airfoil surface with a traveling wave actuation applied along the suction side. The wave parameters include wavelength (λ), amplitude (a), and frequency, which create an oscillatory motion in the normal (N) direction relative to the surface's tangent (s) direction.

Turbulence modeling in Large Eddy Simulation (LES) involves directly resolving the large-scale turbulent motions while modeling the effects of subgrid-scale (SGS) motions. This is achieved by applying a spatial filter to the Navier-Stokes equations, resulting in equations that describe the evolution of the filtered velocity field and require modeling of the SGS stresses.

The incompressible Navier-Stokes equations for a Newtonian fluid are given by:

$$\frac{\partial u_i}{\partial t} + \frac{\partial (u_i u_j)}{\partial x_j} = -\frac{1}{\rho}\partial p \over \partial x_i + \nu \frac{\partial^2 u_i}{\partial {x_j}^2} \quad \text{Equation 4-2}$$

$$\partial u_i / \partial x_i = 0 \quad \text{Equation 4-3}$$

where u_i, p, ρ and ν represent the velocity components, pressure, density of the fluid, and kinematic viscosity respectively. In LES, the velocity field is decomposed into a large-scale resolved component ($\bar{u}_i$) and a subgrid-scale component (u'_i). Applying a spatial filter to the Navier-Stokes equations results in:

$$\frac{\partial \bar{u}_i}{\partial t} + \frac{\partial (\bar{u}_i \bar{u}_j)}{\partial x_j} = -\frac{1}{\rho}\partial \bar{p} \over \partial x_i + \nu \frac{\partial^2 \bar{u}_i}{\partial {x_j}^2} - \frac{\partial \tau_{ij}}{\partial x_j} \quad \text{Equation 4-4}$$

$$\frac{\partial \bar{u}_i}{\partial x_i} = 0 \quad \text{Equation 4-5}$$

Where $\bar{u}_i$ and $\bar{p}$ are the filtered velocity and pressure, respectively. $\tau_{ij} = \bar{u}_i \bar{u}_j - \bar{u}_i \bar{u}_j$ is the subgrid-scale (SGS) stress tensor.

The SGS turbulence kinetic energy k is defined as:

$$k = \frac{1}{2} \bar{u}'_i \bar{u}'_i \quad \text{Equation 4-6}$$

To model the evolution of k, a transport equation can be derived. The filtered dynamic k-equation takes the form:

$$\frac{\partial(\rho k)}{\partial t} + \frac{\partial(\rho \bar{u}_j k)}{\partial x_j} = P - \varepsilon + T \qquad \text{Equation 4-7}$$

where P is the production of SGS kinetic energy and ε is the dissipation rate of SGS kinetic energy. Also T represents the transport of SGS kinetic energy.

The Expanded formulation takes this form:

$$\frac{\partial(\rho k)}{\partial t} + \bar{u}_j \frac{\partial(\rho k)}{\partial x_j} = -\tau_{ij} \frac{\partial \bar{u}_i}{\partial x_j} - \varepsilon + \frac{\partial}{\partial x_j}\left(\rho \nu_t \sigma_k \frac{\partial k}{\partial x_j}\right) + S \qquad \text{Equation 4-8}$$

where $\nu_t, \sigma_k, and\ S$ are respectively the SGS eddy viscosity, the model constant, and any additional source terms. To ensure adaptability of the model, a dynamic procedure can be used to compute the model coefficient C_ν based on the resolved scales. This allows the SGS viscosity ν_t to be determined dynamically:

$$\nu_t = C_\nu \Delta^2 \sqrt{2 S_{ij} S_{ij}} \qquad \text{Equation 4-9}$$

Where Δ is the filter width (typically related to the grid size). $S_{ij} = ½ \left(\frac{\partial \bar{u}_i}{\partial x_j} + \frac{\partial \bar{u}_j}{\partial x_i}\right)$ is the resolved strain rate tensor. To solve the model for the model coefficient C_ν, the dynamic procedure involves: (1) Applying a secondary filter (test filter) to the resolved scales: $\bar{U}_i = G[\bar{u}_i]$, (2) Utilizing the *Germano* identity [111] to relate the subgrid-scale stresses at different filter levels: $L_{ij} = \hat{\tau}_{ij} - \bar{\tau}_{ij} = \bar{U}_i \bar{U}_j - \bar{u}_i \bar{u}_j$, (3) Expressing both $\hat{\tau}_{ij}$ and $\bar{\tau}_{ij}$ using the dynamic model:

$$\hat{\tau}_{ij} = 2 \nu_t^{jest} \hat{S}_{ij} - \frac{1}{3} \hat{\tau}_{kk} \delta_{ij}$$

$$\bar{\tau}_{ij} = 2 \nu_t \hat{S}_{ij} - \frac{1}{3} \bar{\tau}_{kk} \delta_{ij} \qquad \text{Equation 4-10}$$

By projecting the *Germano* identity onto the model expressions and minimizing the error, C_ν can be solved dynamically at each grid point and time step. Thus, the final form of the Filtered Dynamic k-Equation becomes:

$$\frac{\partial(\rho k)}{\partial t} + \frac{\partial(\rho \bar{u}_j k)}{\partial x_j} = -2\,\nu_t\,S_{ij}\,S_{ij} + \varepsilon + \frac{\partial}{\partial x_j}\left(\rho \nu_t \sigma_k \frac{\partial k}{\partial x_j}\right) + S \qquad \text{Equation 4-11}$$

4.3 Numerical Method Validation

In this study, the numerical method is validated using a NACA 0018 airfoil at a Reynolds number of 20,000. The validation focuses on comparing the lift and drag results at various angles of attack (3°, 7°, 12°, and 14°). The results are validated using experimental data from a study by Klimas [112], showing a good agreement and demonstrating the accuracy of the simulation. The boundary conditions used in the simulations are depicted in the accompanying schematic, see Figure 4-2. As shown in Figure 4-2, the chosen boundary conditions are designed to accurately replicate realistic aerodynamic scenarios and ensure computational efficiency. The airfoil actuated with a moving wall velocity condition and a zero gradient pressure mimics the dynamic behavior of the airfoil surface under traveling wave control, while the no-slip condition for the unactuated airfoil provides a baseline for comparison. As shown in Figure 4-2, The uniform inlet velocity at the inlet (face A) represents the steady, undisturbed airflow approaching the airfoil, essential for calculating the lift and drag forces accurately. The zero gradient conditions on the opposite face (A') ensure that the outflow does not artificially influence the upstream flow, maintaining the natural development of the boundary layer.

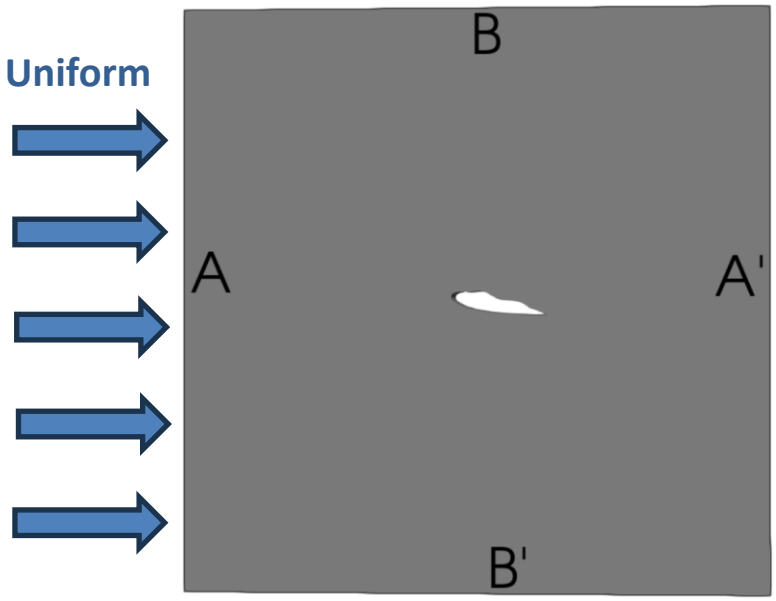

Figure 4-2- Computational domain setup for NACA 0018 airfoil simulation. Face A has a uniform velocity inlet to simulate steady, approaching airflow essential for lift and drag calculations, while face A' employs a zero-gradient condition to maintain natural outflow. Faces B and B' are set with slip conditions to allow frictionless lateral flow, simulating an unconfined environment. Faces C and C' (not shown in this view) are front and back boundaries with cyclic conditions, allowing periodic continuation of the flow, essential for traveling wave analysis and preventing boundary effects from distorting the flow field in the direction normal to the inlet velocity.

The slip conditions on the side faces (B and B') allow the airflow to slide along the boundaries without friction, which helps to simulate an unconfined flow environment and avoids unrealistic reflections of turbulence at the domain edges. The cyclic boundary conditions on the top and bottom faces (C and C') facilitate the periodic continuation of the flow, which is particularly useful in simulations involving traveling waves and ensures that the boundary effects do not distort the flow field in direction normal to the inlet velocity direction.

Table 4-1- Comparison of the lift and drag results extracted from present study and the previous experimental work [112].

Angle of Attack	Lift (Sheldahl and Klimas)	Drag (Sheldahl and Klimas)	Lift (Present)	Drag (Present)
0	0	0.0286	0	0.0198
3	0.155	0.0299	0.144	0.031
4	0.1788	0.031	----	----
5	0.1788	0.0323	0.174	0.034
6	0.1582	0.0339	----	----
7	0.1161	0.0358	0.1099	0.0341
12	-0.0602	0.123	-0.057	0.124
14	0.0172	0.158	0.0131	0.132
16	0.1114	0.196	0.1119	0.199

In Table 4-1, the comparison of simulation results ("Present") with the experimental data from Sheldahl and Klimas [112] reveals significant insights into the aerodynamic behavior of the NACA0018 airfoil at low Reynolds numbers, particularly in relation to pre-stall, stall, and post-stall conditions.

At lower angles of attack (0 to 5 degrees), the lift coefficient increases almost linearly with the angle of attack. This trend is consistent with attached flow conditions, where the boundary layer remains largely attached to the airfoil surface, promoting efficient lift generation. In this regime, both the simulation and experimental results align closely, indicating that the simulation accurately models the attached flow behavior. The slight underestimation of the

drag coefficient in the simulation at 0 degrees suggests minor discrepancies in modeling the viscous effects, but these are not significant enough to impact the overall trend.

As the angle of attack increases to around 5 degrees, the lift coefficient reaches its maximum value. This peak marks the pre-stall condition, where the boundary layer begins to exhibit early signs of separation but remains mostly attached. The drag coefficient also starts to increase due to the thicker boundary layer and the onset of flow separation. The simulation data at this stage still follows the experimental trend closely, though there are minor deviations.

Beyond 5 degrees, a significant decrease in the lift coefficient is observed in the experimental data, indicating the onset of stall. Stall occurs when the boundary layer separates from the airfoil surface, leading to a dramatic loss of lift and a sharp increase in drag. The simulation shows a less pronounced drop in lift and a corresponding increase in drag at these higher angles of attack (12 and 14 degrees). This discrepancy suggests that the simulation may not fully capture the flow separation and reattachment dynamics, which are critical in the stall and post-stall regions. The turbulent boundary layer separation and reattachment, as discussed by Winslow et. al [82] are complex phenomena that significantly influence the aerodynamic performance in these regimes. At even higher angles of attack (beyond 12 degrees), the airfoil enters the post-stall condition. In this regime, the flow is fully separated from the surface, resulting in significantly reduced lift and increased drag. The experimental data shows this behavior clearly, with a partial recovery of lift at 16 degrees due to flow reattachment at the trailing edge, a phenomenon sometimes observed in post-stall conditions.

4.4 Parametric Study on wave Parameters in different Angles of Attack

In this section, we analyze the influence of key wave parameters—Frequency, Amplitude, and Wavelength—on aerodynamic performance variables such as Lift and Drag across different angles of attack, using heatmaps to illustrate correlation coefficients. The heatmaps represent

the relationship between input wave parameters and output aerodynamic responses at angles of attack of 7°, 11°, and 14°, with the color gradients indicating the direction and strength of correlations.

Table 4-2. This heatmap illustrates the correlation coefficients between the input variables (Frequency, Amplitude, Wavelength) and the output variables (Drag, Lift) for an angle of attack of 7°. The strength and direction of the correlations are represented by the color scale, with red indicating positive correlation and blue indicating negative correlation. The numeric values in each cell display the specific correlation coefficients.

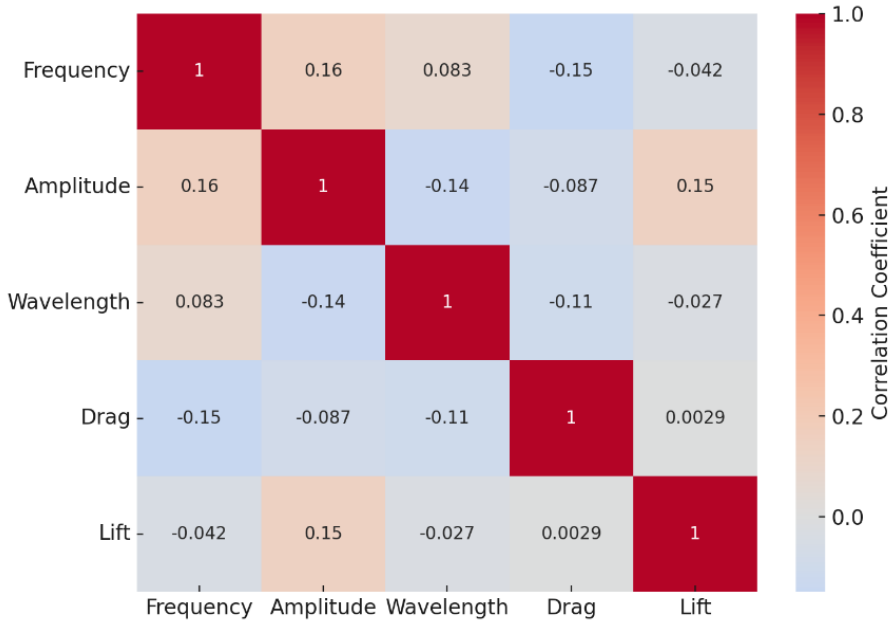

The first heatmap, Table 4-2 represents the correlation coefficients between the input variables (Frequency, Amplitude, Wavelength) and the output variables (Drag, Lift) for an angle of attack of 7°. The color scale indicates the strength and direction of the correlations, with red signifying positive correlation and blue signifying negative correlation. The exact correlation coefficients are displayed within each cell. The correlation between Frequency and Drag is -0.15, indicating a moderate negative correlation. At this angle of attack, the flow starts to experience mild separation. Higher frequencies can disrupt the separated flow regions, thereby reducing drag by promoting reattachment of the boundary layer.

Table 4-3. This heatmap shows the correlation coefficients between the input variables (Frequency, Amplitude, Wavelength) and the output variables (Drag, Lift) for an angle of attack of 11°. The color scale reflects the strength and direction of the correlation, with red representing positive correlation and blue representing negative correlation. The values within the cells represent the exact correlation coefficients.

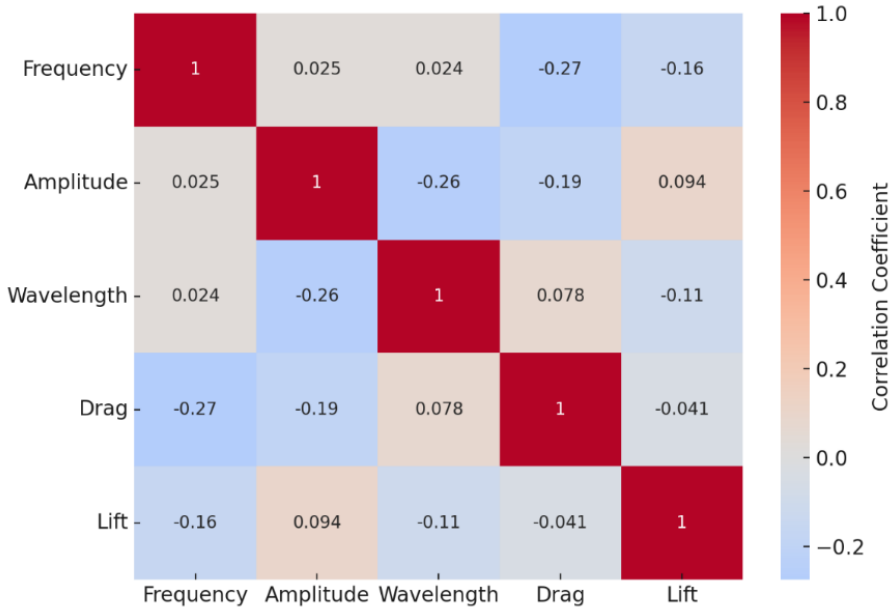

Table 4-4. This heatmap depicts the correlation coefficients between the input variables (Frequency, Amplitude, Wavelength) and the output variables (Drag, Lift) for an angle of attack of 14°. The strength and direction of the correlations are indicated by the color scale, where red denotes positive correlation and blue denotes negative correlation. The values in the cells provide the specific correlation coefficients

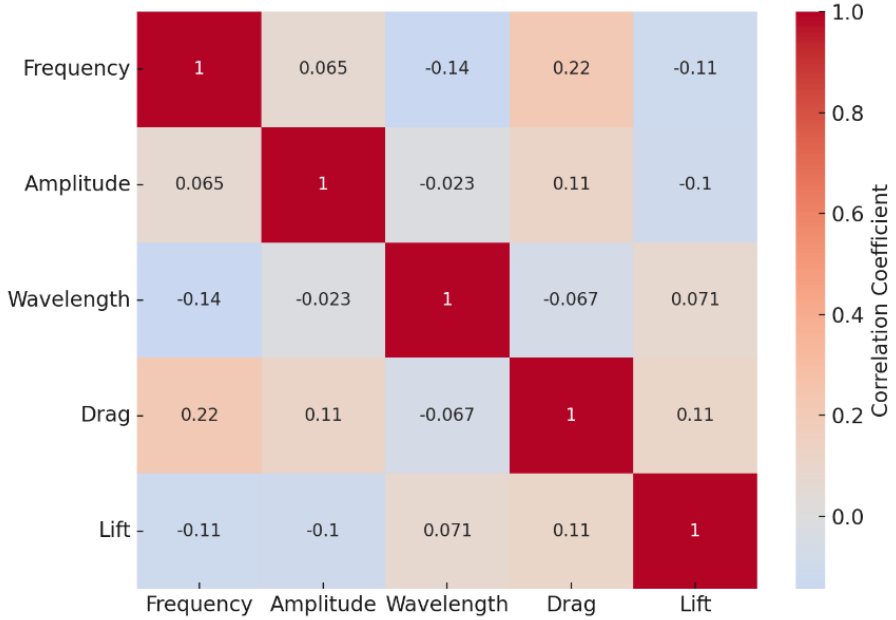

This can be attributed to the high-frequency waves energizing the boundary layer and preventing separation. The correlation between Frequency and Lift is -0.042, indicating a weak negative correlation. Changes in frequency have a small reducing effect on lift because higher frequencies can disturb the lift-generating pressure difference across the airfoil, slightly diminishing the overall lift. The correlation between Amplitude and Drag is -0.087, a weak negative correlation, suggesting that increased amplitude slightly reduces drag. Enhanced wave amplitudes might energize the boundary layer, delaying flow separation and thus reducing drag. Amplitude and Lift have a correlation of 0.15, indicating a weak positive correlation. Higher amplitudes can slightly increase lift by stabilizing the flow and preventing early separation, maintaining a higher-pressure difference between the upper and lower surfaces. Wavelength and Drag have a correlation of -0.11, indicating a weak negative correlation. Increasing wavelength reduces drag slightly, which could be due to smoother transitions in the boundary layer and less pronounced flow disturbances. Wavelength and Lift have a correlation of -0.027, indicating a very weak negative correlation, showing that wavelength changes have minimal impact on lift at this moderate angle of attack.

The second heatmap, Table 4-3 shows the correlations for an angle of attack of 11°. The correlation between Frequency and Drag is -0.27, indicating a moderate negative correlation. Higher frequencies can significantly reduce drag at this angle, likely due to more effective suppression of flow separation and turbulence control on the trailing edge. The correlation between Frequency and Lift is -0.16, indicating a weak negative correlation. Frequency changes have a slight reducing effect on lift, as high-frequency waves may disrupt the favorable pressure distribution and induce turbulence that weakens the lift force. Amplitude and Drag have a correlation of -0.19, indicating a weak negative correlation. Higher amplitudes can reduce drag by promoting more favorable flow conditions and delaying separation. The correlation between Amplitude and Lift is 0.094, indicating a weak positive correlation.

Increasing amplitude slightly increases lift by maintaining attached flow over the airfoil and enhancing the pressure difference.

Wavelength and Drag have a correlation of 0.078, indicating a very weak positive correlation. Longer wavelengths slightly increase drag, potentially due to less effective boundary layer control and increased flow instability. The correlation between Wavelength and Lift is -0.11, indicating a weak negative correlation. Longer wavelengths slightly reduce lift by causing minor flow separation or instability near the leading edge.

The third heatmap, Table 4-4 represents the correlations for an angle of attack of 14°. The correlation between Frequency and Drag is 0.22, indicating a weak positive correlation. At this higher angle of attack, increased frequencies may increase drag due to more pronounced flow disturbances and turbulence, which can enhance the adverse pressure gradient and promote flow separation. The correlation between Frequency and Lift is -0.11, indicating a weak negative correlation. Frequency changes have a slight reducing effect on lift, as high-frequency waves may induce turbulence and disrupt the favorable pressure gradient needed for lift generation.

Amplitude and Drag have a correlation of 0.11, indicating a weak positive correlation. Higher amplitudes can slightly increase drag due to increased flow disruptions and turbulence on the surface. The correlation between Amplitude and Lift is -0.1, indicating a weak negative correlation. Higher amplitudes slightly reduce lift by causing flow separation and instability, diminishing the effective pressure difference. Wavelength and Drag have a correlation of -0.067, indicating a very weak negative correlation. Longer wavelengths have minimal impact on drag at this angle, as the dominant factor is likely the overall flow separation and turbulence. The correlation between Wavelength and Lift is 0.071, indicating a very weak positive

correlation. Wavelength changes have a minimal impact on lift, as the primary effects at this high angle of attack are due to larger-scale flow separation and instability.

In summary, the effects of wave parameters on lift and drag vary depending on the angle of attack. At lower angles of attack, the boundary layer remains largely attached, and the effects of wave parameters are weak. As the angle of attack increases, the boundary layer becomes more prone to separation, and the wave parameters play a more significant role in energizing or disrupting the flow. Higher frequencies and amplitudes can energize the boundary layer, reducing drag and maintaining lift by preventing flow separation. However, at higher angles of attack, these parameters can also introduce turbulence and instability, potentially increasing drag and reducing lift. Longer wavelengths tend to have a more complex interaction with the boundary layer, sometimes smoothing transitions and other times causing instability.

4.5 Pressure Coefficient distribution in different angles of attack

This section explores the pressure coefficient distribution over the surface of a NACA 0018 airfoil at various angles of attack, highlighting the differences in flow behavior between unactuated and actuated cases. The C_P distribution is analyzed to reveal the regions of flow separation, reattachment, and their impact on aerodynamic performance. The comparisons provide insights into how traveling wave actuation (TWM) affects the boundary layer stability and the pressure recovery process at different angles of attack.

4.5.1 Pressure Distribution over the unactuated (baseline) NACA0018 at Different Angles of Attack

Figure 4-3- Pressure Coefficient distribution over a NACA 0018 airfoil at Reynolds number 20,000 for various angles of attack. Black dots: AOA=3°, Green: AOA=7°, Blue: AOA=11°, Orange: AOA=14°. compares the pressure distributions (C_P) over unactuated NACA 0018 airfoil for the various angles of attack: 3°, 7°, 11°, and 14°. The C_P plots highlight differences

in flow behavior, including regions of flow separation and reattachment, and their effects on lift and drag. We will compare these results with the effects of traveling wave actuations over each angle of attack later to evaluate the potential improvements in aerodynamic performance.

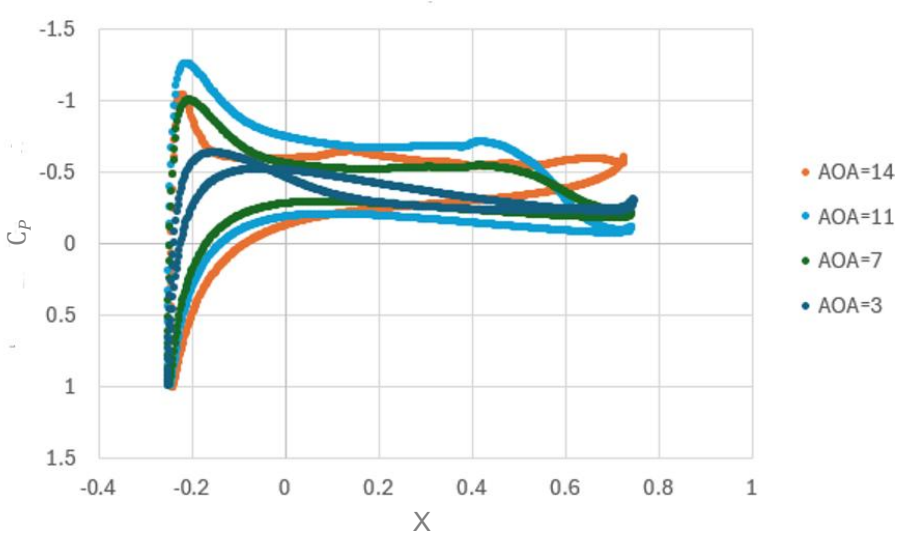

Figure 4-3- Pressure Coefficient distribution over a NACA 0018 airfoil at Reynolds number 20,000 for various angles of attack. Black dots: AOA=3°, Green: AOA=7°, Blue: AOA=11°, Orange: AOA=14°.

The pressure coefficient is defined by the formula [25]:

$$C_P(x) = \frac{P(x) - P_\infty}{\rho U^2} \qquad \text{Equation 4-12}$$

Where P represents the pressure at a specific chordwise location x on either the suction or pressure surface of the airfoil, and P_∞ is the free-stream pressure. The y coordinates are ignored as pressures on both the suction and pressure surfaces are combined. This results in two C_P values for each x location: one for the suction surface and one for the pressure surface. The spanwise averaging process in numerical method with OpenFOAM involves taking the pressure measurements at each chordwise prob points and averaging them across the span of the airfoil. This yields a mean spanwise-averaged pressure value for each chordwise point,

providing a two-dimensional representation of the pressure distribution. Mathematically, the spanwise-averaged pressure coefficient at a given chordwise location x can be expressed as:

$$C_{P_{spanwise}}(x) = \frac{1}{S}\int_{0}^{z=S} C_P(x,z)\,dz \qquad \text{Equation 4-13}$$

where S is the span of the airfoil, and $C_P(x,z)$ represents the instantaneous pressure coefficient at a specific chordwise location x and spanwise location S. After obtaining the spanwise-averaged pressure coefficients, the next step is to average these values over time. Pressure data is collected over a specified time interval, from 10 seconds to 60 seconds, to capture the dynamic behavior of the flow. At each chordwise location, the spanwise-averaged C_P values are recorded at regular time intervals of 0.02s. This combined spanwise and time-averaging process ensures that the calculated C_P values are representative of the steady-state aerodynamic performance of the airfoil, free from transient fluctuations and local spanwise variations.

At an angle of attack (AOA) of 3 degrees, the suction peak is observed at x = -0.153 with a C_P of -0.632. This mild suction peak indicates moderate aerodynamic loading, resulting in a stable and attached flow over most of the airfoil surface. The C_P values from both the pressure and suction sides cross each other. This crossing point is significant because it marks the location where the pressure differential diminishes, impacting the overall lift generation. The area between the pressure and suction side C_P curves represent the net pressure difference contributing to lift. When these curves cross, it leads to a reduction in this differential pressure, thereby affecting the lift adversely.

The increase in C_P values at the tip of the airfoil can be attributed to three-dimensional effects, such as tip vortices. These vortices cause a rise in pressure at the wingtip, leading to higher drag and reduced aerodynamic efficiency. The flow at the wingtip is more complex due to these vortices, which create a mixing of turbulent air that impacts the overall pressure distribution.

At an AOA of 7 degrees, the suction peak shifts to x = -0.205 with a C_P of -1. This indicates a higher aerodynamic loading compared to AOA=3°, resulting in increased lift. The flat area observed between x = 0 and x = 0.46 is indicative of flow separation. This region represents a laminar separation bubble where the flow has detached from the surface and is undergoing transition. In this separated flow region, the pressure remains relatively constant, signifying the presence of a bubble. The gradual pressure recovery observed after x = 0.46 towards the trailing edge indicates the reattachment of the flow. This recovery is crucial because it reduces the adverse pressure gradient, which helps in restoring some aerodynamic efficiency. The flow reattachment minimizes the wake size behind the airfoil, thus reducing drag. This reattachment point is critical for maintaining a balance between lift and drag, especially at moderate angles of attack.

For an AOA of 11 degrees, the suction peak is at x = -0.21 with a C_P of -1.25. This significant suction peak reflects a high aerodynamic loading, enhancing lifts but also increasing the risk of flow separation. The flat area between x = 0.15 and x = 0.38 indicates a prolonged region of separated flow. This extended separation zone is indicative of a large laminar separation bubble, which leads to a substantial increase in drag due to the larger wake behind the airfoil. The steep pressure gradient in the mid-chord region highlights the separation and transition of the flow, resulting in a turbulent boundary layer. This turbulent mixing within the separation bubble increases the drag significantly. The pressure recovery in this case is less effective, indicating that the separated flow does not reattach efficiently, thereby reducing the overall aerodynamic efficiency. At the highest AOA of 14 degrees, the suction peak occurs at x = -0.22 with a C_P of -1.03. Despite the high suction peak indicating a significant lift, the value is slightly lower than at AOA=11°, suggesting severe flow separation. The flat area extending from x = -0.1 to the trailing edge indicates an extensive region of separated flow, where the pressure remains nearly constant, signifying a large separation bubble.

This prolonged plateau in C_P is indicative of turbulent separation, where the flow separates early and remains detached, leading to a large turbulent wake. The adverse effects of this extensive separation are evident in the significantly increased drag and reduced aerodynamic efficiency. The sharp recovery of pressure towards the trailing edge suggests possible reattachment, but the overall impact is dominated by the large, separated flow region.

4.5.2 Pressure Distribution over Traveling Wave Actuated NACA 0018 at Different Angles of Attack and Comparison to Baseline Cases

Now we shift our focus to analyzing the effects of traveling waves on the aerodynamic performance of the airfoil. In this study, we will compare the impact of the Traveling Wave Method (TWM) on pressure coefficient distributions. To ensure a thorough investigation, we have selected a specific set of wave parameters including frequency, amplitude, and wavelength that have demonstrated good performance in preliminary tests. These parameters have been chosen carefully to maximize the effectiveness of TWM in enhancing aerodynamic characteristics. It is important to note that while a comprehensive parameter study could provide deeper insights into the optimal wave configurations, our primary goal here is to understand the general effects of TWM on fluid dynamics. Therefore, we will focus on this selected set of parameters to illustrate the potential benefits of TWM. Table 4-5 is the summary of the specific cases that were found to work well for traveling wave actuation:

Table 4-5-Summary of traveling wave actuation parameters for different cases

	Case 1	Case 2	Case 3	Case 4	Case 5	Case 6
AOA	7	7	11	11	14	14
frequency	1	1	1	1	1	1
amplitude	0.01	0.02	0.01	0.02	0.01	0.02
wavelength	0.3	0.4	0.3	0.4	0.3	0.4

We found that an amplitude of 0.01 and 0.02, and frequencies of 1 and 2, work well for traveling wave actuation on the NACA 0018 airfoil. These parameters were chosen because these amplitudes provide sufficient energy to influence the boundary layer without causing instability, while the frequencies, being in the order of magnitude of the natural flow speed, effectively generate a lock-in region. This synchronization stabilizes the boundary layer, reducing flow separation and enhancing aerodynamic performance.

At AOA=7 as shown in Figure 4-4, the C_P distribution for Case 3 (orange line) shows a smoother and less pronounced suction peak compared to the unactuated case. The suction peak reaches -1.38, indicating a higher aerodynamic loading. The flat area, which is indicative of flow separation, is considerably reduced, suggesting improved flow attachment. Additionally, the pressure recovery towards the trailing edge is more gradual and smoother, indicating that the flow remains attached over a longer chordwise distance., the TWM has effectively modified the pressure coefficient distribution by reducing the extent of flow separation and promoting a more stable boundary layer. This results in improved aerodynamic performance, with increased lift and reduced drag, demonstrating the efficacy of TWM in enhancing the aerodynamic characteristics of the airfoil.

At AOA=11, as shown in Figure 4-5*,* the C_P distribution shows a stronger impact of the traveling wave mechanism (TWM) on flow control. In the unactuated case, the suction peak reaches −2.15 at x=−0.22, with a large flat region from x=−0.04 to x=0.4 indicating extensive flow separation. This high suction value and extended separation area contribute to increased drag. In contrast, the actuated case (Case 3) has a reduced suction peak of −1.27, showing smoother pressure recovery and a much smaller separation bubble near x=−0.04. This reduction in peak suction and containment of separation demonstrates TWM's effectiveness in promoting flow attachment. The larger difference in suction peak between unactuated and actuated cases

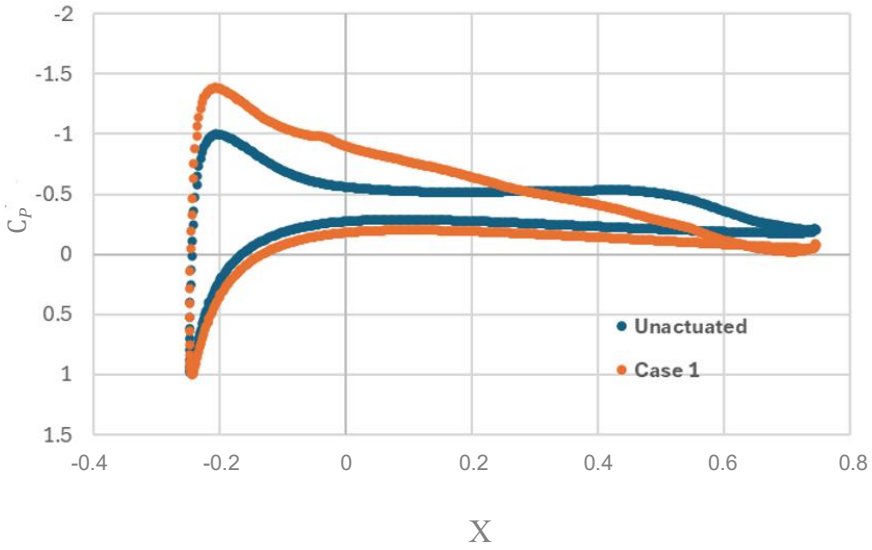

Figure 4-4- Pressure Coefficient distribution over a NACA 0018 airfoil at an angle of attack of 7 degrees. The blue dots represent the unactuated case, while the orange line represents the Traveling Wave Method (TWM) controlled case.

at AOA=11 compared to AOA=7 highlights TWM's enhanced ability to reduce separation and improve aerodynamic performance at higher angles of attack.

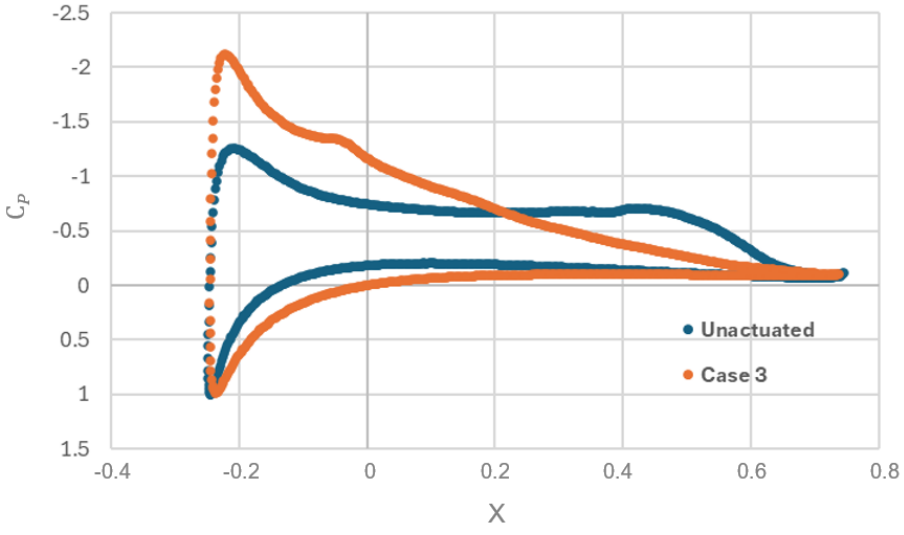

Figure 4-5- Pressure Coefficient distribution over a NACA 0018 airfoil at an angle of attack of 11 degrees. The blue dots represent the unactuated case, while the orange line represents the Traveling Wave Method (TWM) controlled case

For the angle of attack of 14 degrees, the unactuated case shows a C_P peak of −2.1, which is more negative than the C_P observed at AOA = 11, indicating stronger suction and a more pronounced adverse pressure gradient. In contrast, for Case 5, the C_P peak is reduced to −1.26, similar to the C_P observed for AOA = 11. This reduction highlights the effect of the traveling wave in mitigating the adverse pressure gradient. In the unactuated case, the flat region of C_P extends across the entire chord length from the leading edge to the trailing edge, signifying extensive flow separation. However, in Case 5, a large rotational zone with separation bubbles is observed between x=−0.18 and x=−0.03. This localized region of rotational flow indicates the partial control of separation near the leading edge due to the traveling wave actuation.

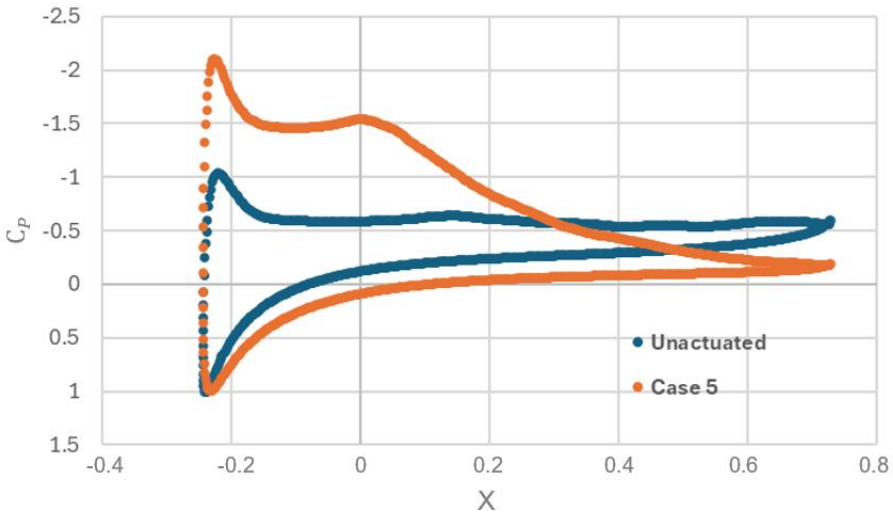

Figure 4-6-Pressure Coefficient distribution over a NACA 0018 airfoil at an angle of attack of 14 degrees. The blue dots represent the unactuated case, while the orange line represents the Traveling Wave Method (TWM) controlled case

4.6 Velocity contours and when it is controlled

In the previous section, we focused on analyzing the pressure distribution over the airfoil with and without travelling wave actuation (TWM) at various angles of attack. This analysis provided insights into how TWM influences the aerodynamic forces by altering the pressure

gradients. However, to fully understand the underlying mechanisms of flow control, it is essential to examine the flow structures directly. Therefore, we now shift our focus to the velocity vectors, which offer a more detailed view of the flow behavior around the airfoil. By assessing the velocity vectors, we aim to capture the differences in flow attachment, separation, and reattachment between the actuated and unactuated cases at four specific angles of attack: 7°, 11°, and 14°. This will allow us to comprehensively evaluate the effectiveness of TWM in controlling flow separation and improving aerodynamic performance.

Figure 4-7-a depicts the phase-averaged velocity vectors for the unactuated case at AOA=7, both in a zoomed-in and zoomed-out view, respectively. These figures reveal significant flow separation starting from $x = -0.12$, with swirling patterns and reversed flow vectors indicating areas of flow detachment. This separation leads to increased drag and reduced lift, highlighting the aerodynamic inefficiencies without TWM. In contrast, Figure 4-7-b and , Figure 4-7-c respectively illustrate the phase-averaged velocity vectors for the actuated Case 1 and Case 2, showing a smooth downstream flow direction and effective flow control. In Case 1, the vectors remain aligned with the flow direction, and while those near the boundary are smaller, they are not upstream or even surface normal directed. In Case 2, as shown in Figure 4-7-c, with higher amplitude TWM, the velocity vectors demonstrate stronger alignment with the boundary layer and an enhanced curvature toward the surface, shaped by the wave crests and troughs. This configuration avoids any upward deviation of bulk flow, further promoting attachment and boundary layer stability.

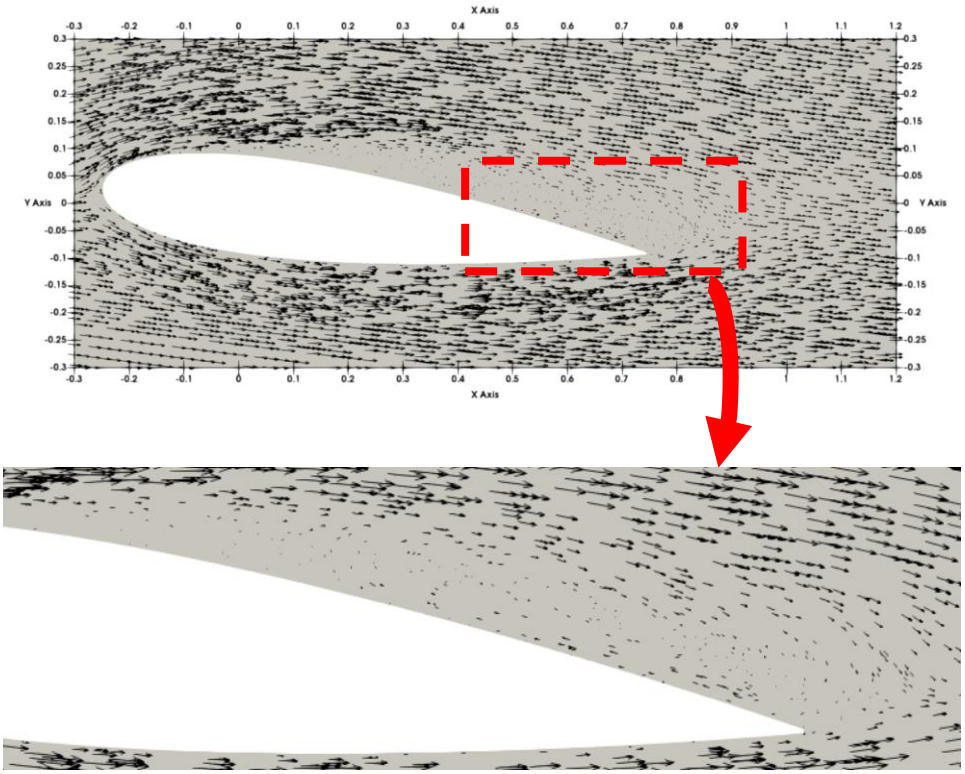

(a)

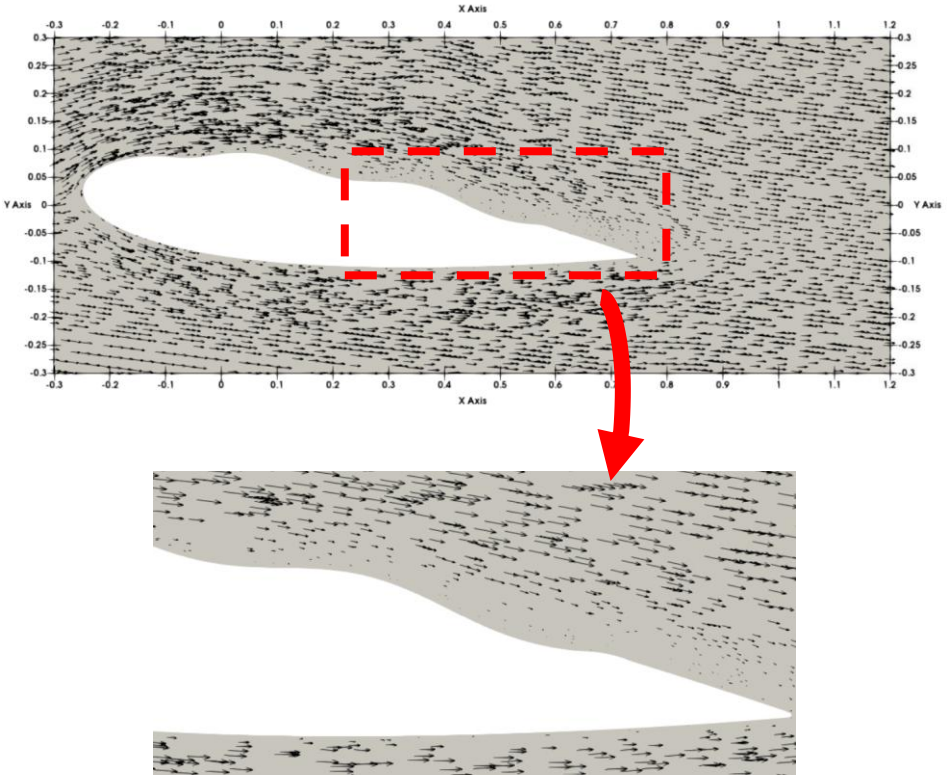

(b)

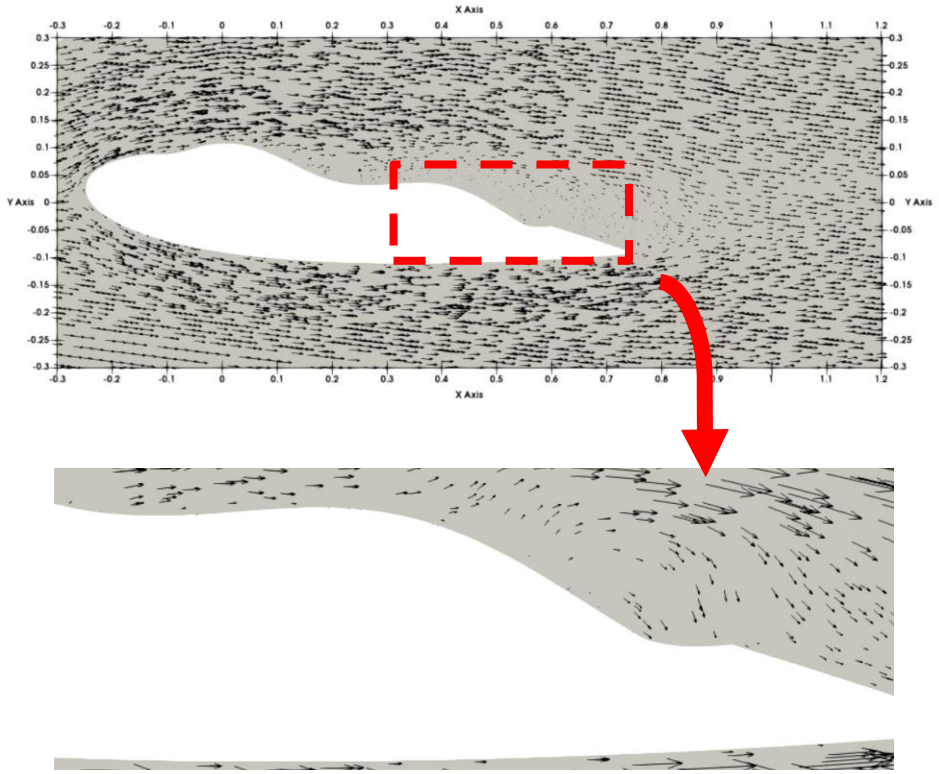

(c)

Figure 4-7-Phase-averaged velocity vectors at an angle of attack of 7° for a NACA 0018 airfoil at Reynolds number 20,000. The unactuated case (a) shows significant flow separation starting from x=0.28 with swirling patterns and reversed flow, indicating areas of flow detachment and increased drag. The actuated Case 2 (b) with TWM (amplitude 0.02) shows a smooth downstream flow direction and effective flow control, with maintained flow attachment and reduced separation.

Having analyzed the effectiveness of travelling wave actuation (TWM) at an angle of attack of 7°, where significant flow separation was mitigated, we now focus on examining how TWM performs under different flow conditions. Specifically, we will look at the challenging stall conditions at higher angles of attack (11° and 14°).

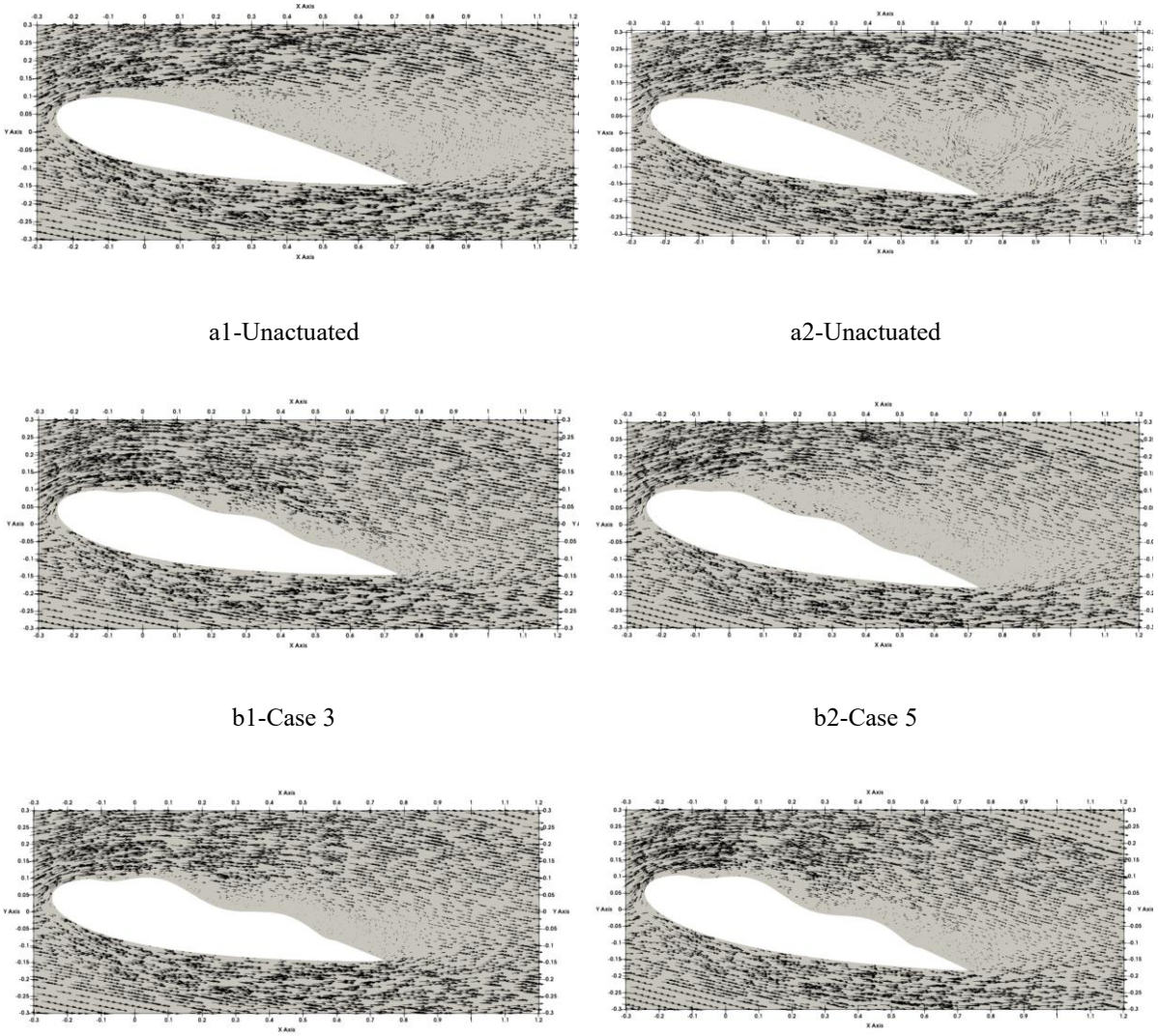

a1-Unactuated a2-Unactuated

b1-Case 3 b2-Case 5

C1-Case 4 C2-Case 6

Figure 4-8- Phase-averaged velocity vectors over the suction surface of a NACA 0018 airfoil for AOA=11 and AOA=14. Panels (a1) and (a2) represent the unactuated cases, while panels (b1) and (b2) show the results for moderate TWM amplitude, and panels (c1) and (c2) correspond to higher TWM amplitude.

For AOA=11, the phase-average velocity vectors display distinct behavior across the unactuated and actuated cases. In the unactuated case (Figure 4-8-a1), the velocity vectors are oriented fully upward from the leading edge, indicating strong flow separation and stall. In Case 3 (Figure 4-8-b1), with moderate TWM amplitude, the flow control is more effective. From x=0.2, see Figure 4-8-c1, the vectors are aligned in the downstream direction, and regions

with sparser vectors indicate reduced velocity magnitudes, suggesting a more controlled and stabilized boundary layer compared to the unactuated case. In Case 3 (Figure 4-8-c1), with a higher amplitude, the separation control is less effective than in Case 3. Here, backward-directed vectors start appearing around x=0.28, suggesting the formation of separation bubbles. The higher amplitude TWM creates stronger oscillations that, instead of enhancing flow attachment, introduce additional disturbances (separation bubbles), particularly in regions with strong adverse pressure gradients. These stronger oscillations force the boundary layer to detach intermittently, making it difficult to maintain a steady, attached flow close to the surface.

For AOA=14, the phase-averaged velocity vectors reveal the differences in flow behavior across the unactuated and actuated cases. In the unactuated case, see Figure 4-8-a2, a large separation zone is evident, spanning nearly the entire suction surface from the leading edge to the trailing edge with a strong rotating zone above x=0.75 near trailing edge. At this post-stall angle of attack, the velocity vectors show an ejection behaviour which is upward motion of the bulk flow toward the mainstream.

In Case 5, as show in Figure 4-8-b2, with moderate traveling wave amplitude of 0.01, the control over the separation is minimal. While there are slight indications of improved flow attachment near the leading edge, at x=0.14, the separation bubble extends downstream, failing to reattach the flow effectively. The velocity vectors in this case remain disorganized, and regions of reversed flow persist, demonstrating that the lower amplitude is insufficient to counteract the strong adverse pressure gradient at this high angle of attack. In contrast, Case 6 as shown in Figure 4-8-c2, with a higher amplitude traveling wave (a=0.02), successfully mitigates the flow separation. The velocity vectors near the leading edge show a more organized downstream alignment, indicating improved boundary layer attachment. The influence of the higher amplitude wave energizes the boundary layer, preventing the separation bubble from extending downstream.

4.7 Reynolds Stress Distribution

In this section, we analyze the Reynolds stress distribution for both unactuated (baseline) and travelling wave (TW) actuated cases over an airfoil at different angles of attack. The comparison of Reynolds stress distribution between the unactuated and actuated cases reveals how travelling wave actuation enhances flow control by modifying the turbulent flow structures. The focus will be on understanding how these Reynolds stress components contribute to momentum transfer within the flow and their relation to flow separation control [19]. This study investigates the contribution of Reynolds stress components to momentum transfer and flow separation control over a traveling wave airfoil compared to a baseline airfoil at various angles of attack. Using OpenFOAM, we will analyze the $< -u'v' >$ component contour, referred to as uPrime2Mean, to understand its role in turbulent momentum exchange. The focus on $< -u'v' >$ is because it captures the exchange of momentum between the upper and lower layers of the boundary layer. For each angle of attack, the Reynolds stress profiles are plotted along normal lines to the airfoil wall at specific locations: A, B, C, D, and E. These profiles are used to quantitatively compare the different cases.

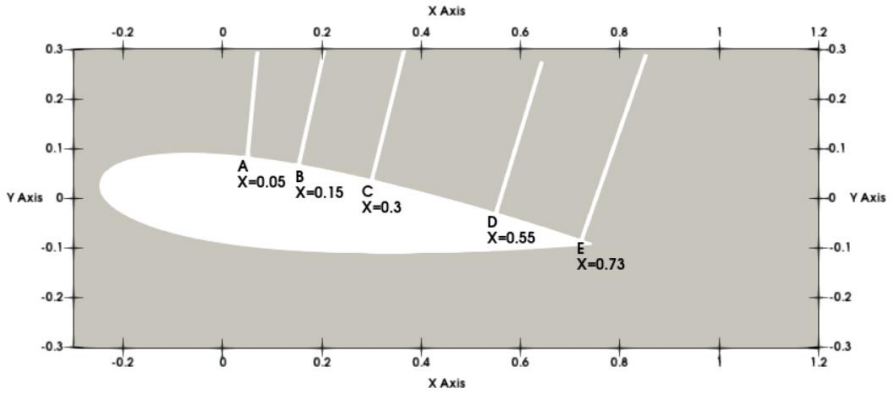

Figure 4-9- Diagram of the NACA airfoil with a 7-degree angle of attack, showing the locations of lines used for Reynolds stress profile analysis. The lines are positioned at specific x-coordinates along the airfoil surface.

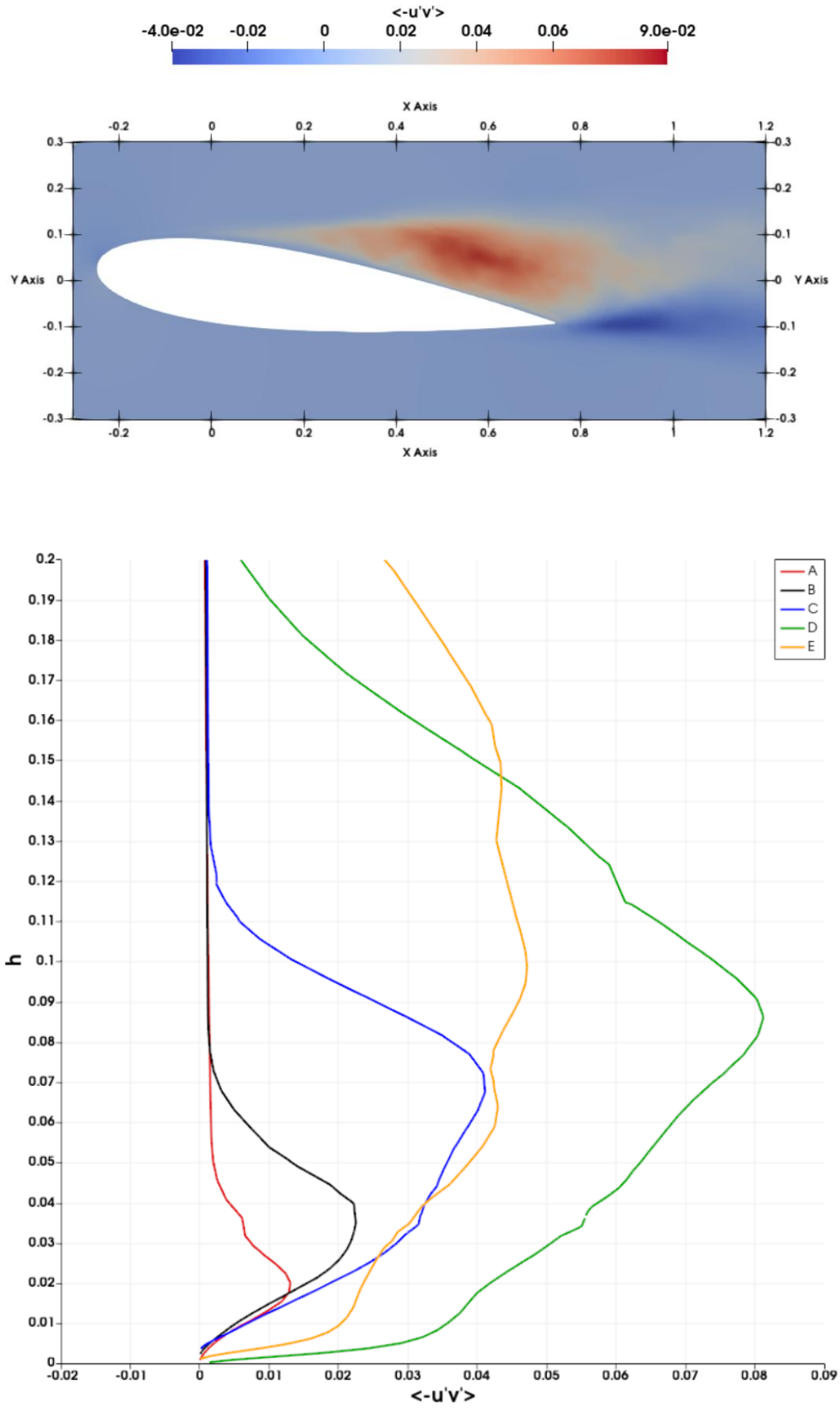

(a) Unactuated

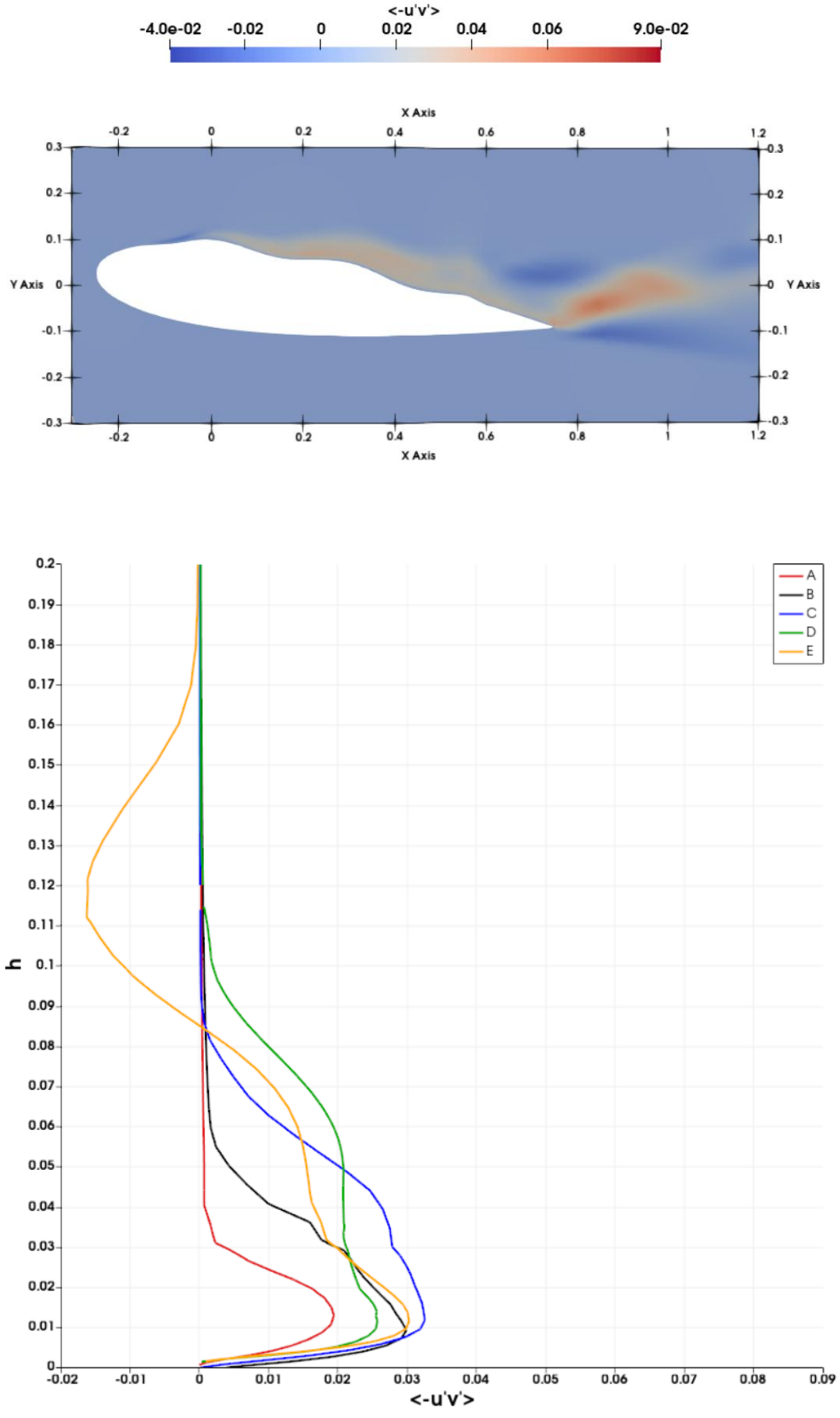

(b) Case 1

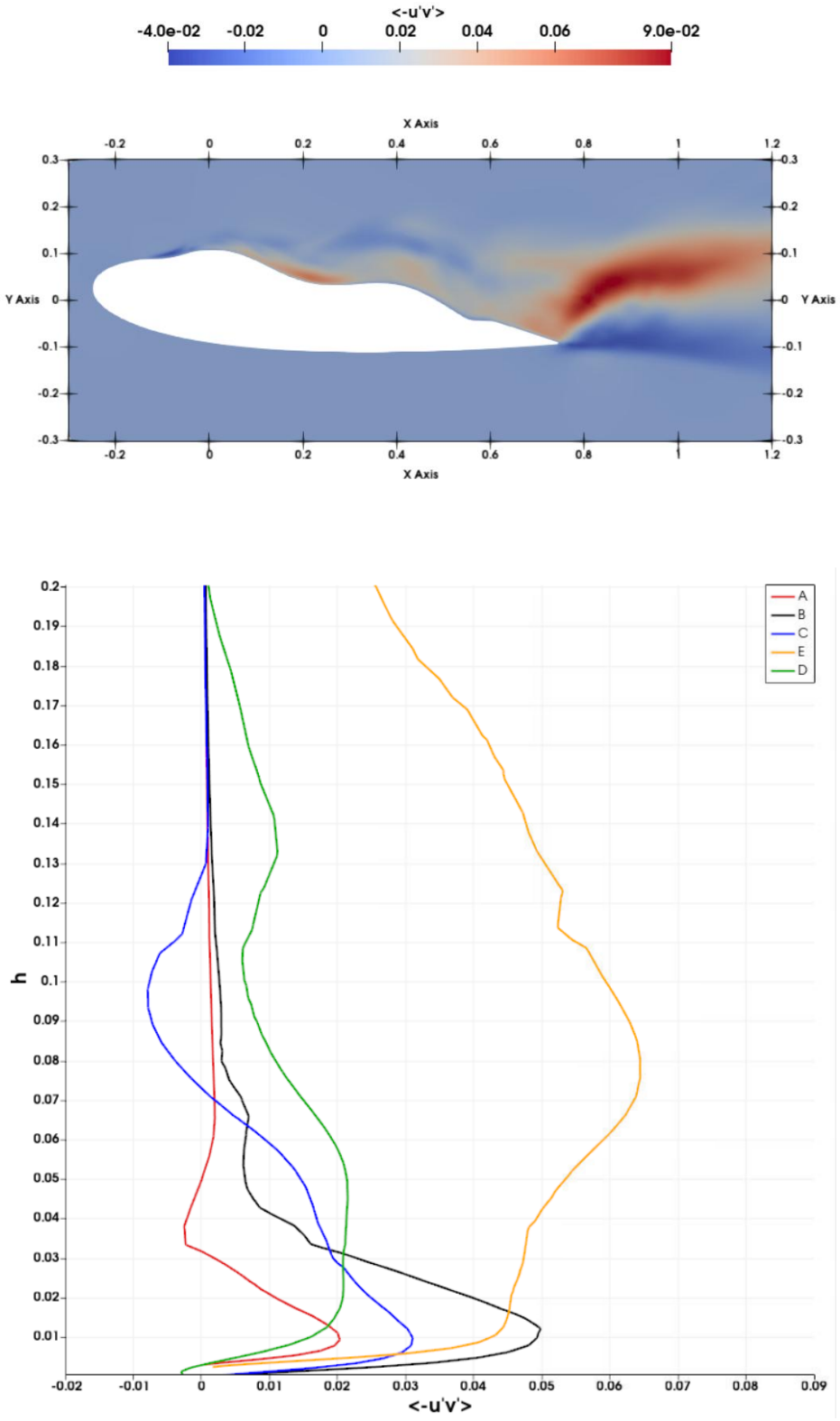

(c) Case 2

Figure 4-10- stress distribution and profiles at 7-degree angle of attack, with (a) representing the unactuated case, (b) showing Case 1 with a wave amplitude of 0.01, and (c) depicting Case 2 with a wave amplitude of 0.02. The colored lines represent Reynolds stress profiles along lines normal to the wall at various points (A: Red, B: Black, C: Blue, D: Green, E: Orange).

In the unactuated case, Figure 4-10-a, with an angle of attack of 7 degrees, the Reynolds stress distribution is intense in the separated region, indicating turbulent separation. The maximum Reynolds stress occurs along the line passing through point D with a value of 0.081 at a height of 0.085 from the boundary, suggesting a potential for reattachment as the turbulent energy is close to the surface.

For points A to C, the rate of increase in Reynolds stress is similar, indicating consistent trends in distribution across these regions, though the magnitudes differ. The sudden increase in Reynolds stresses at points D and E within the shear layer corresponds to low-velocity regions in the velocity vector field, suggesting that these areas of high turbulence are associated with recirculation zones where the flow decelerates significantly.

In Case 1, as shown in Figure 4-10-b, the Reynolds stress reaches its maximum value at a height of 0.01 from the surface across the entire airfoil, which is much closer to the wall compared to the unactuated case where it increased from point A to E. This indicates a very low level of separation and suggests that there are considerable velocity fluctuations relative to their average velocity values. Above point D, along the line passing through this point, there is a negative Reynolds stress of about -0.017 at a height of 0.11, indicating the emergence of slow streak areas on the suction surface. These slow streaks likely contribute to sweep and ejection events that help prevent flow separation by enhancing momentum transfer and maintaining flow attachment, thereby improving the overall aerodynamic performance.

In Case 2, with a larger wave amplitude in Figure 4-10-c, the Reynolds stress contour reveals the formation of two small bubbles at $x=-0.01$and $x=0.2$, indicating localized flow disturbances caused by the surface waves. Thin streaks of negative Reynolds stress are observed over the airfoil, suggesting regions of adverse momentum transfer and potential flow instability. The Reynolds stress profiles show that the maximum Reynolds stress occurs near the surface at a

height of about h=0.01, demonstrating the effect of the wave amplitude in concentrating turbulent energy close to the wall. The wake, formed due to flow separation at the trailing edge, is characterized by alternating vortices known as the von Kármán vortex street [113,114].

The positive Reynolds stress above the airfoil indicates momentum transport in the direction of the mean flow. In contrast, the negative Reynolds stress in the wake signifies a counter-gradient transport of momentum towards the vortex centers, enhancing mixing and energy dissipation. This complex momentum exchange is a hallmark of turbulent wakes.

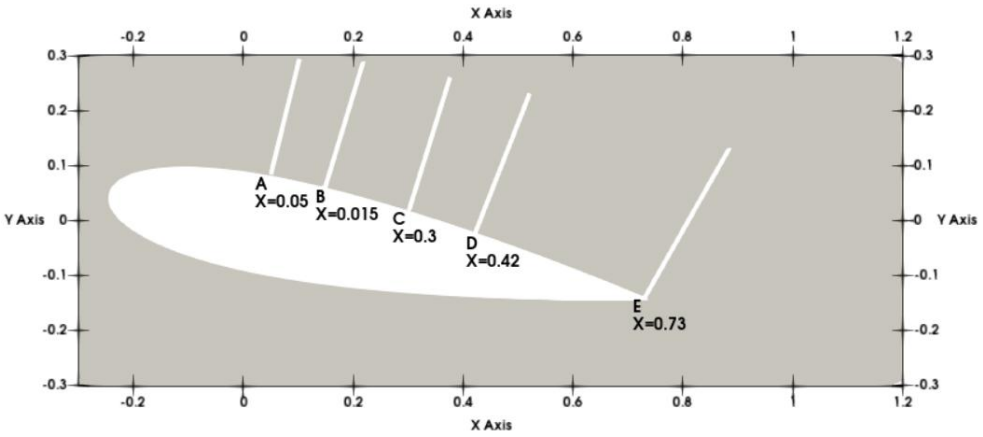

Figure 4-11- Diagram of the NACA airfoil with an 11-degree angle of attack, showing the locations of lines used for Reynolds stress profile analysis. The lines are positioned at specific x-coordinates along the airfoil surface.

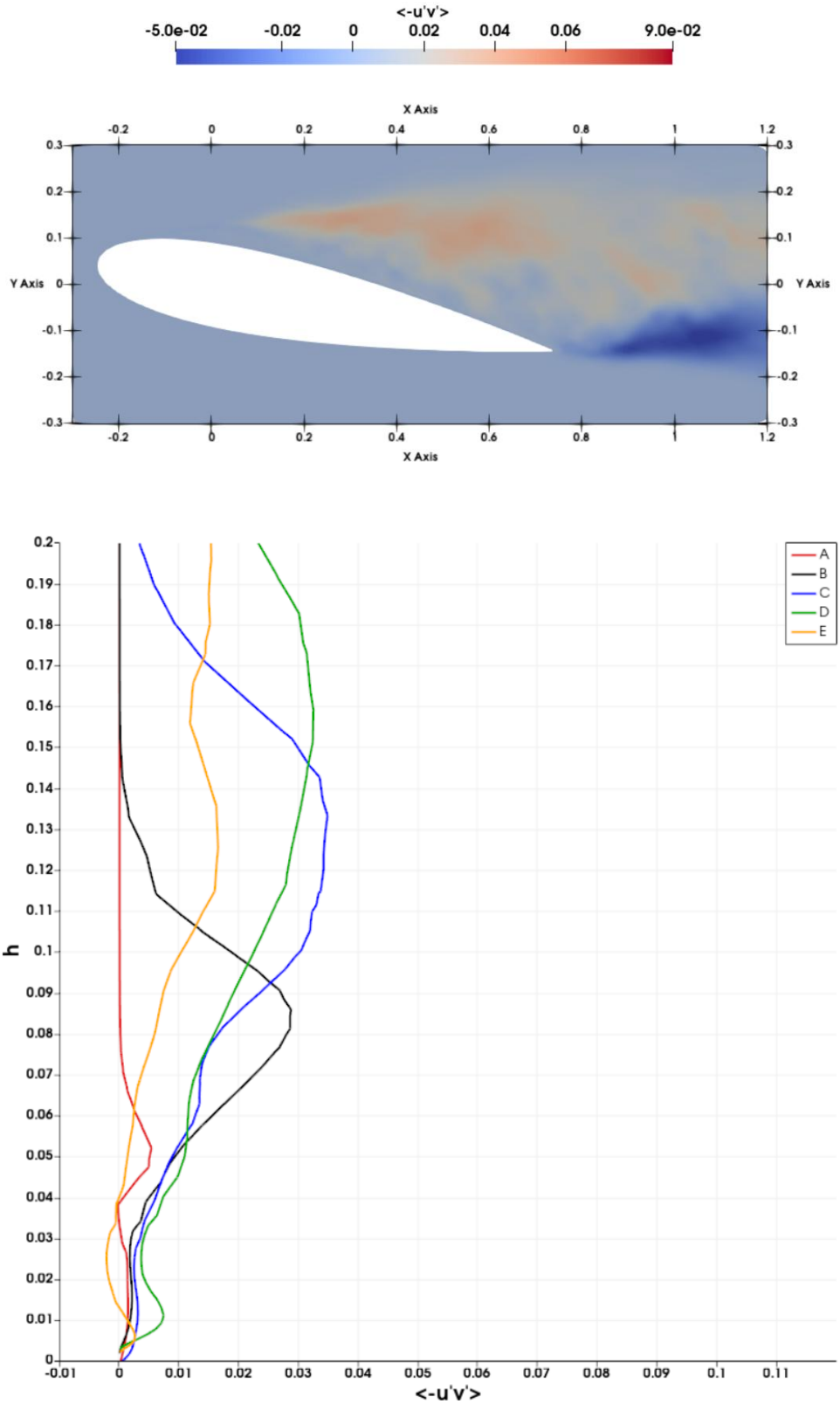

(a) Unactuated

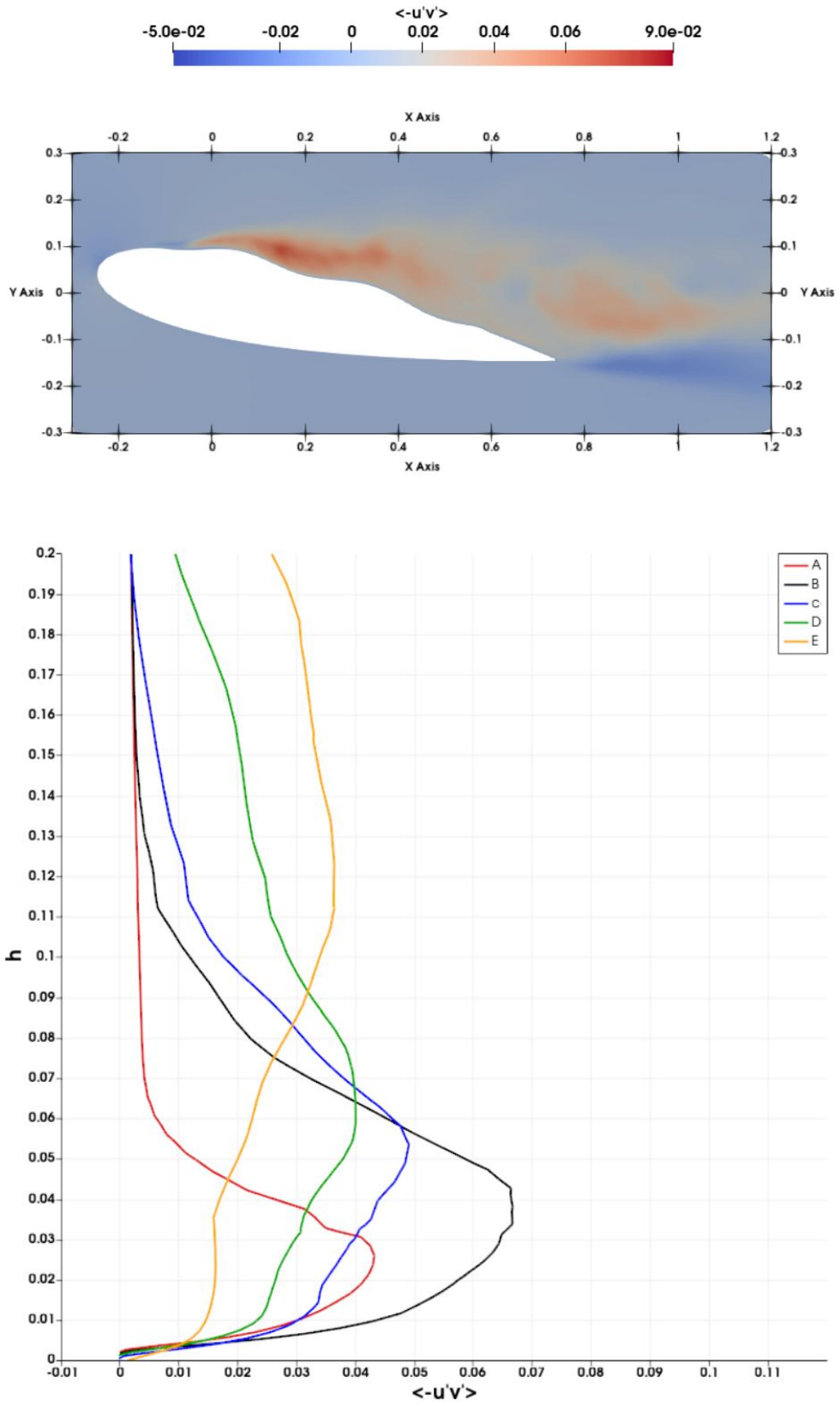

(b) Case 3

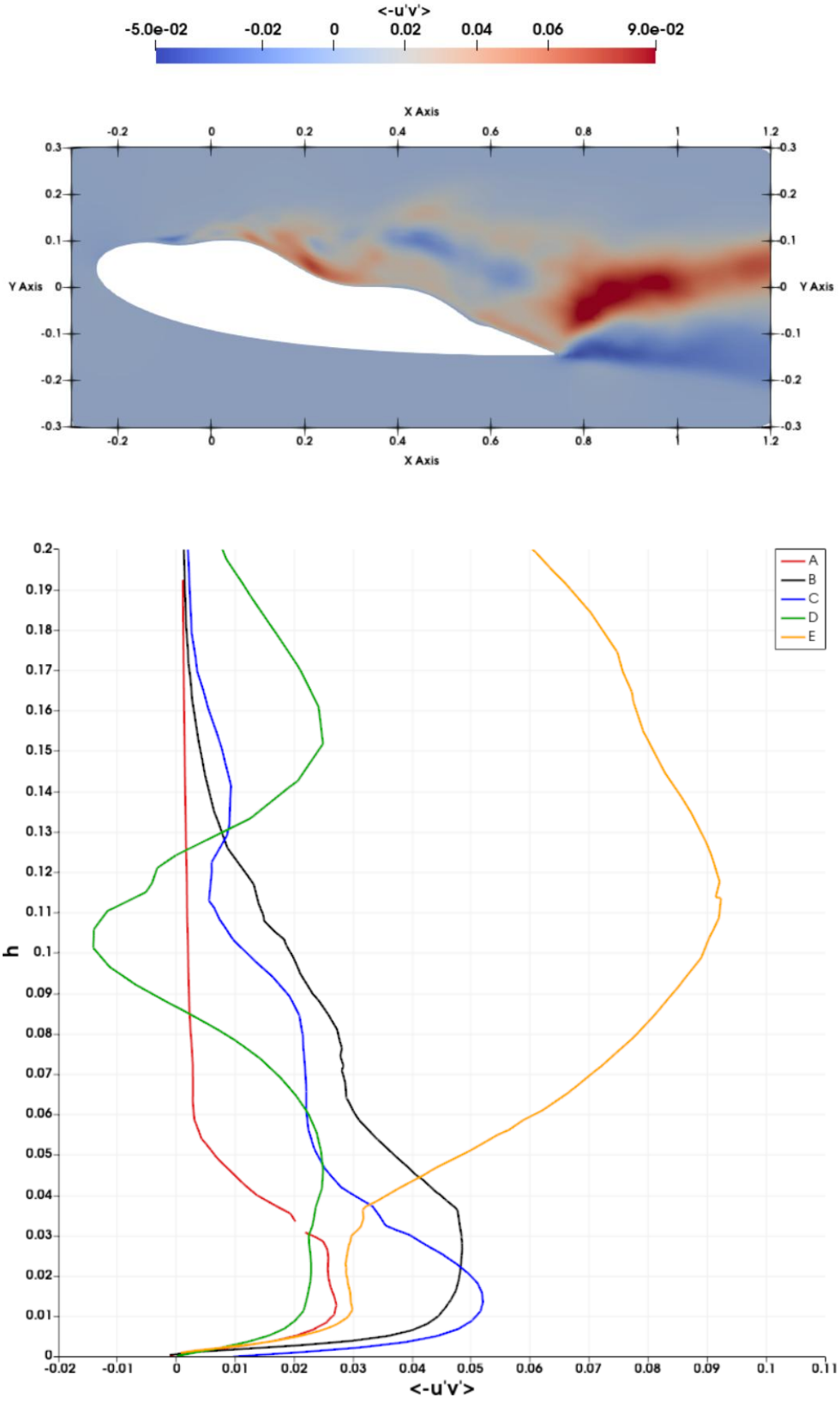

(c) Case 4

Figure 4-12- stress distribution and profiles at 11-degree AOA, with (a) representing the unactuated case, (b) showing Case 3, and (c) depicting Case 4. The colored lines represent Reynolds stress profiles along lines normal to the wall at various points (A: Red, B: Black, C: Blue, D: Green, E: Orange).

In Figure 4-12-a, in the unactuated case with an angle of attack of 11 degrees, the Reynolds stress is predominantly positive and located far from the airfoil surface. Up to a height of h=0.05, the Reynolds stress remains negligible (less than 0.01) almost for all of five points, showing weak turbulent activity near the wall.

The very strong negative Reynolds stress observed after the trailing edge is related to the flow jet emerging from the pressure surface, which features counter-rotating vortices that enhance mixing and momentum transfer back toward the wall. This suggests that the negative Reynolds stress is a result of the interaction between the pressure surface jet and the main flow, leading to recirculation zones with high turbulence levels. In Case 3, as seen in Figure 4-12-b with an amplitude of 0.01, the region of intense Reynolds stress moves closer to the surface near the leading edge where the flow is not yet separated, indicating improved boundary layer interaction due to the wavy surface.

The maximum Reynolds stress along the line passing through point B increases from 0.03 to 0.068 and is pulled down from a height of h=0.085 to h=0.032 compared to the unactuated baseline case. This shift suggests that the undulation of the surface enhances the roll-up of shear layers, which aids in delaying flow separation by concentrating turbulence closer to the wall. For other points, the maximum Reynolds stress also occurs nearer to the wall, demonstrating the effectiveness of the surface undulation in redistributing turbulent energy and promoting better flow attachment. As depicted in Figure 4-12-c, in Case 4, with a larger amplitude of 0.02, the region of high Reynolds stress moves even closer to the airfoil surface compared to the unactuated case, indicating enhanced turbulence interaction with the boundary layer.

A key difference from Case 3 is the appearance of negative Reynolds stress over the surface, which may be associated with the presence of low-momentum streaks. Near the trailing edge, there is a counterclockwise jet of flow with a very strong clockwise jet above it, indicating the

transfer of a high-turbulent shear layer and spanwise vortices generated by the wave moving downstream.

The maximum Reynolds stress occurs at point E near the trailing edge and is twice as strong as the stress at point C, reflecting the intensified roll-up of shear layers as the flow moves downstream. This suggests that the increased wave amplitude promotes stronger momentum transfer and vortex formation, which enhances mixing and potentially improves aerodynamic performance by reducing flow separation

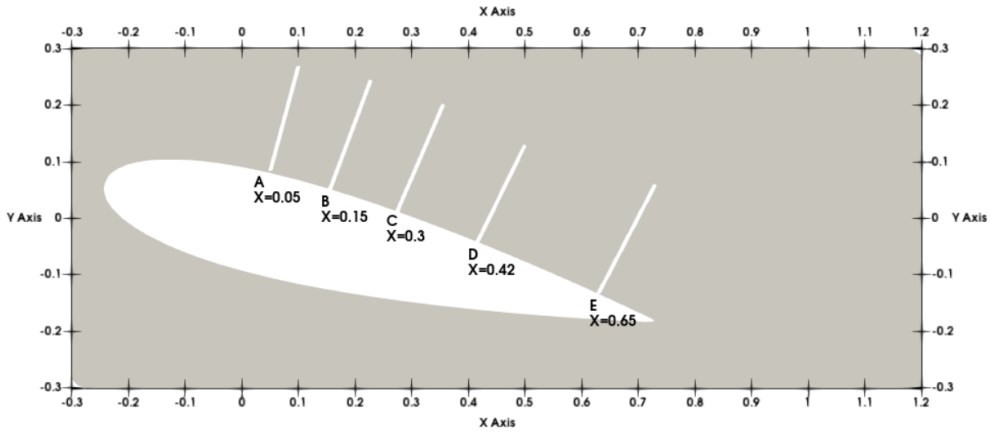

Figure 4-13- Diagram of the NACA airfoil with a 14-degree angle of attack, showing the locations of lines used for Reynolds stress profile analysis. The lines are positioned at specific x-coordinates along the airfoil surface.

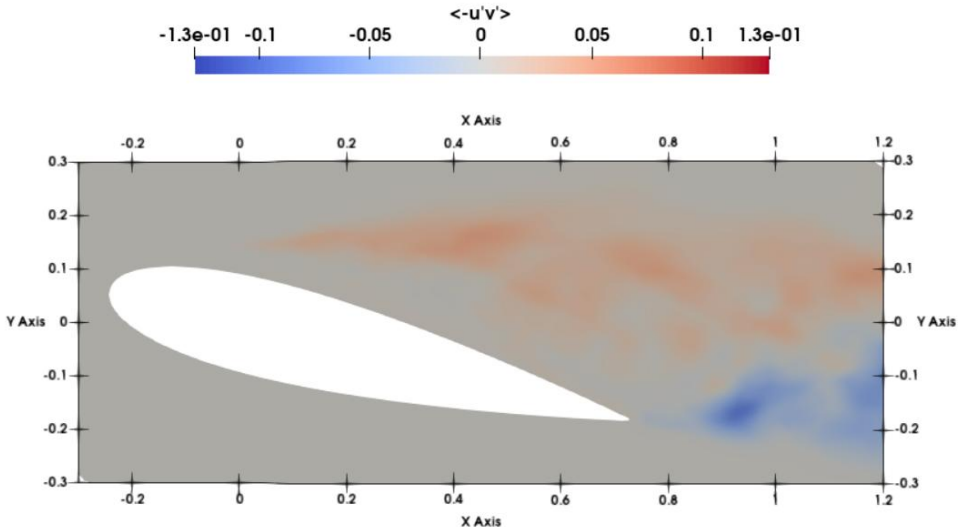

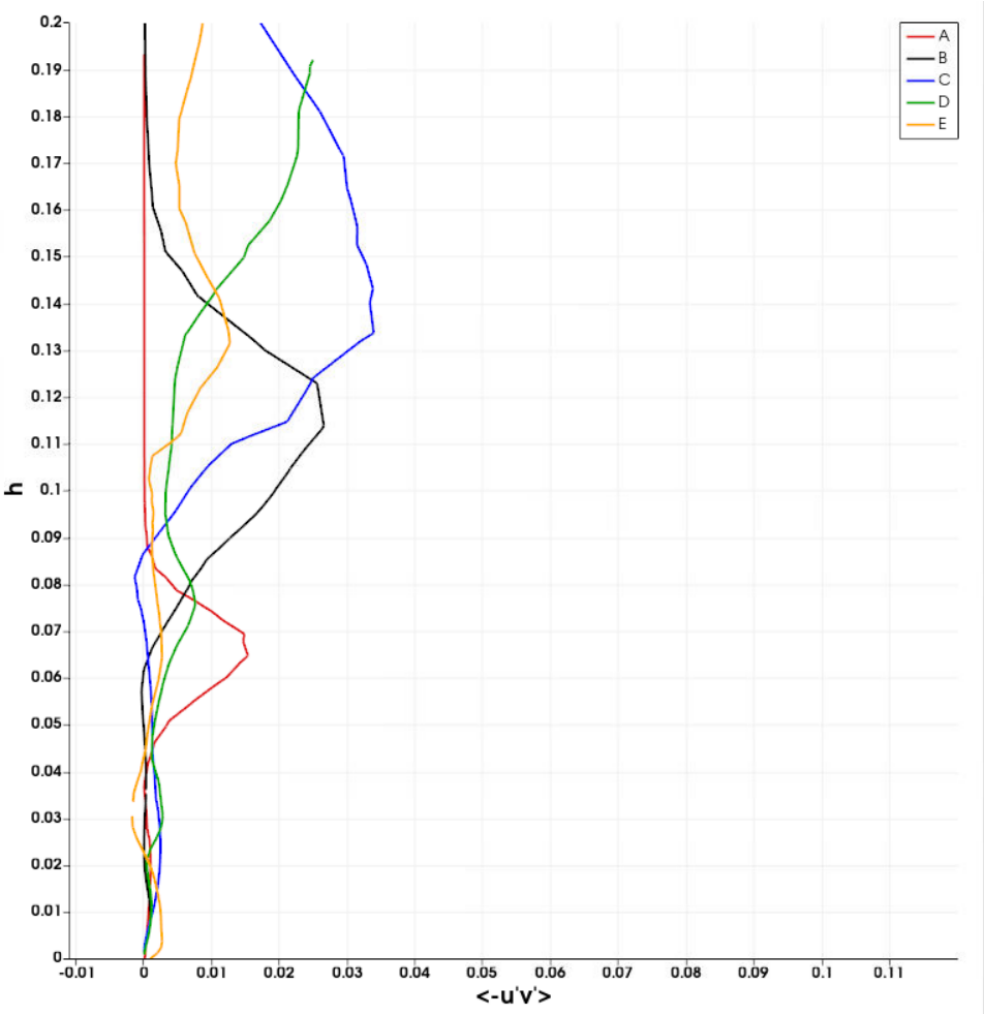

(a) Unactuated

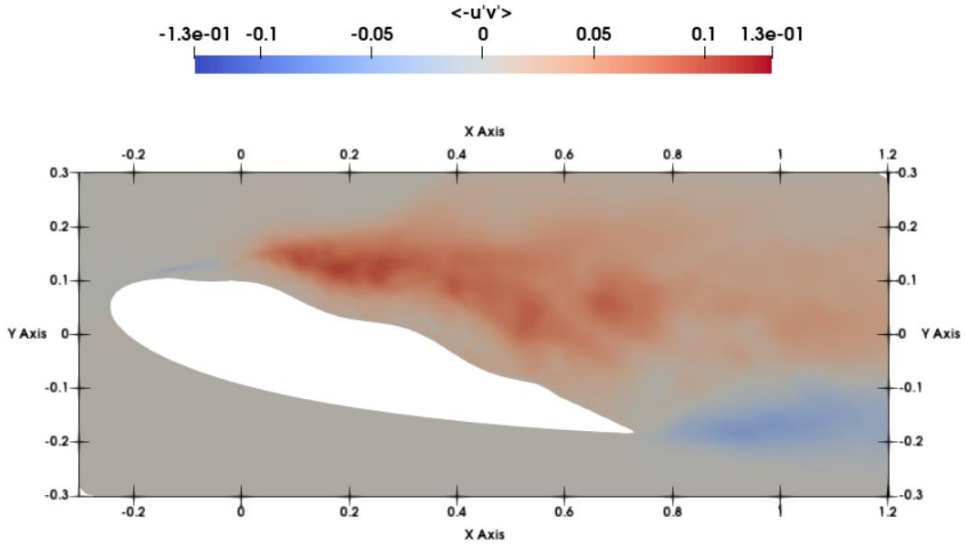

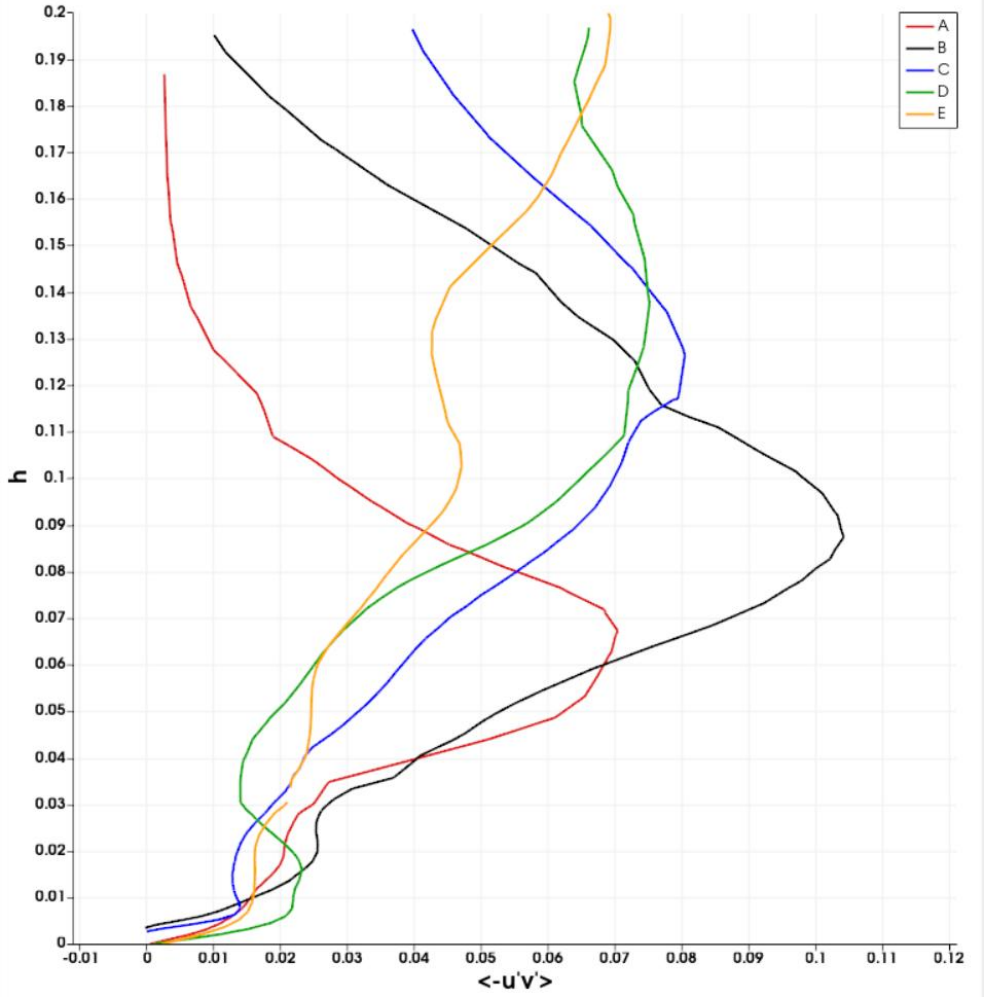

(b) Case 5

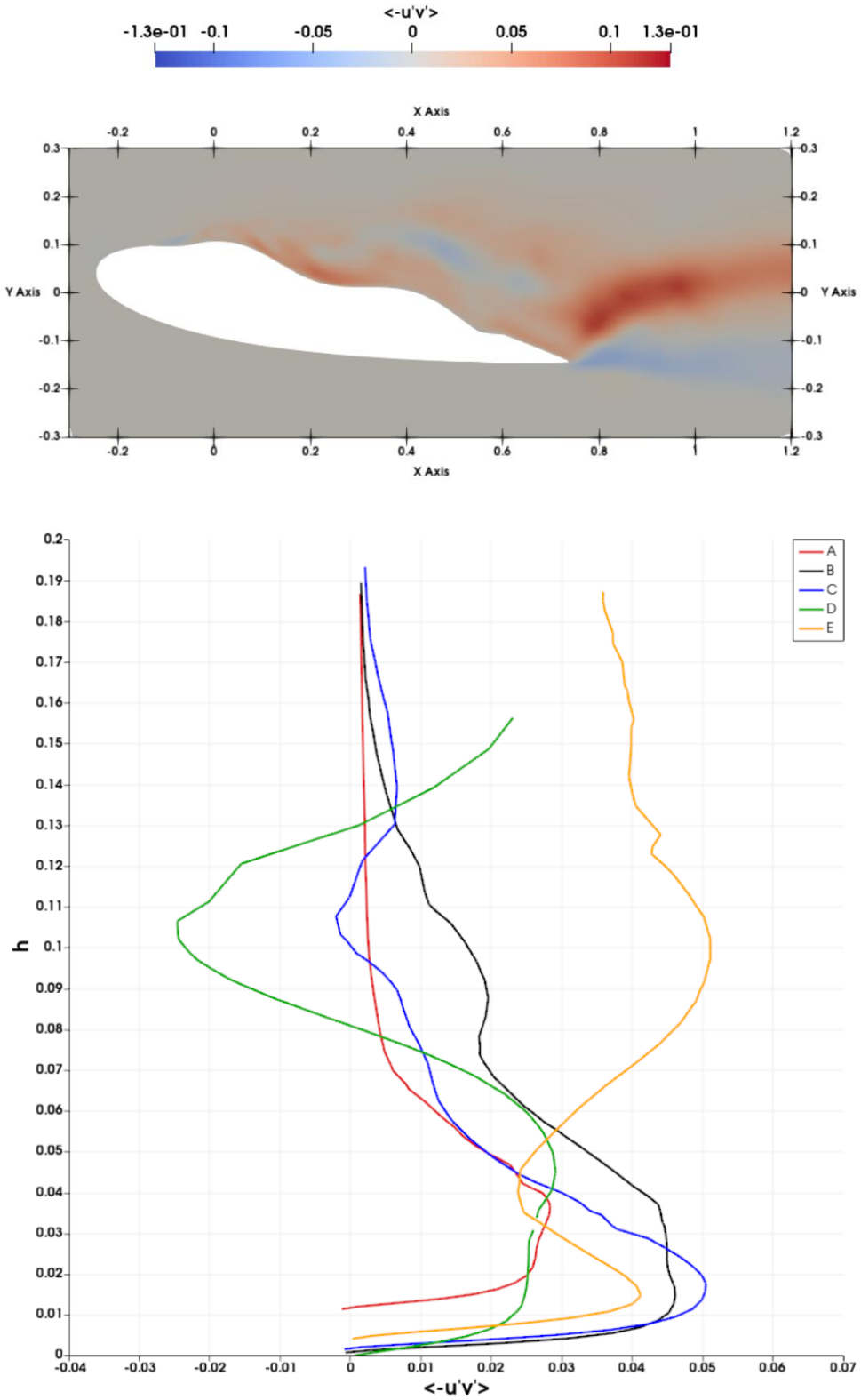

(c) Case 6

Figure 4-14- Reynolds stress distribution and profiles for NACA 0018 airfoil configurations at 14-degree AOA, with (a) representing the unactuated case, (b) showing Case 5, and (c) depicting Case 6. The colored lines represent Reynolds stress profiles along lines normal to the wall at various points (A: Red, B: Black, C: Blue, D: Green, E: Orange), showing turbulence intensity and distribution for each configuration.

The Reynolds stress contour in Figure 4-14 shows that positive Reynolds stress intensities are predominantly located away from the boundary layer, indicating that momentum transfer is more significant in the outer regions of the flow rather than near the wall. In contrast, the wake of the trailing edge exhibits negative Reynolds stress, which signifies that momentum is being extracted from the flow, likely due to recirculation zones that are characteristic of the wake region. The presence of negative Reynolds stress in the wake indicates that the turbulent structures are transferring momentum back towards the wall, contributing to the reverse flow seen in the wake. Analyzing the Reynolds stress profiles plotted along lines normal to the airfoil suction surface, the most intense turbulence is observed above point “B”, approximately 0.132 units away from the wall, where the Reynolds stress reaches 0.033. At the boundary points, the Reynolds stress is negligible, with values less than 0.1 which is in order of the airfoil thickness size, caused by full stalls happening there which reduces the order of magnitude of velocity and its fluctuations. In the Case 5 with a wave amplitude of 0.01, as shown in Figure 4-14-b, the contour plot shows that the region of intense Reynolds stress has moved closer to the airfoil surface compared to the unactuated case. This suggests that the introduction of traveling waves is influencing the flow dynamics, potentially helping to mitigate flow separation by bringing turbulence closer to the wall. The turbulence is not yet dominant enough to fully reattach the flow but is beginning to play a role in managing separation. In fully separated flows, turbulent mixing needs to occur within the buffer layer to overcome the adverse pressure gradient and reattach the flow. In Case 6, as shown in Figure 4-14-c, with a larger wave amplitude of 0.02, the Reynolds stress distribution moves even closer to the wall compared to both the unactuated case and Case 5. This closer proximity indicates improved separation control and enhanced flow stability due to the wave's influence on the boundary layer. The near-wall Reynolds stress values are three to four times greater than

in Case 5, highlighting the impact of the higher amplitude on energizing the flow. The contour plot shows that negative Reynolds stresses are pulled upward, indicating counter-gradient momentum transfer, which means momentum flows from lower to higher velocity regions. This is indicative of large coherent structures generated by the higher amplitude wave, enhancing mixing and potentially improving aerodynamic performance by reducing separation. Although the maximum Reynolds stress intensities are lower than in Case 5 due to mixing, they remain significantly larger than in the unactuated case, suggesting effective turbulence control that reduces drag and increases lift.

4.8 Flow structures and velocity vectors

In this section, we find that analyzing the velocity vector fluctuations (u', v') is essential for understanding the separation control mechanism, as it is more directly related to near-surface turbulent motions. These fluctuation velocity vectors provide insights into how turbulent energy is distributed and how flow control strategies impact the boundary layer's stability and attachment to the airfoil surface.

In the analysis of the airfoil at a 7-degree angle of attack, as depicted in Figure 4-15-a, the unactuated case reveals chaotic and disorganized velocity fluctuation vectors (u', v') at t=80s, indicating extensive flow separation with large regions of low momentum fluid detached from the surface, resulting in increased drag and reduced lift. In contrast, Figure 4-15-b shows the actuated Case 2 at t=65 seconds, where traveling wave actuation applied to the airfoil surface results in a more organized pattern in the velocity fluctuations. The traveling wave induces periodic undulations on the surface, creating disturbances that interact with the boundary layer flow and generate alternating regions of compression and expansion. At x=-0.06 and x=0.38**,** the fluctuations are pulled downward, creating sweep events responsible for eliminating separation by energizing the near-wall flow and maintaining attachment. At x=0.18 and x=0.64,

it exhibits upward ejection of low momentum fluid near the boundary layer, enhancing mixing and reducing the extent of separation. The vortices generated by the traveling wave enhance mixing within the boundary layer, transporting higher momentum fluid from the outer layer to the near-wall region, making the boundary layer less susceptible to separation.

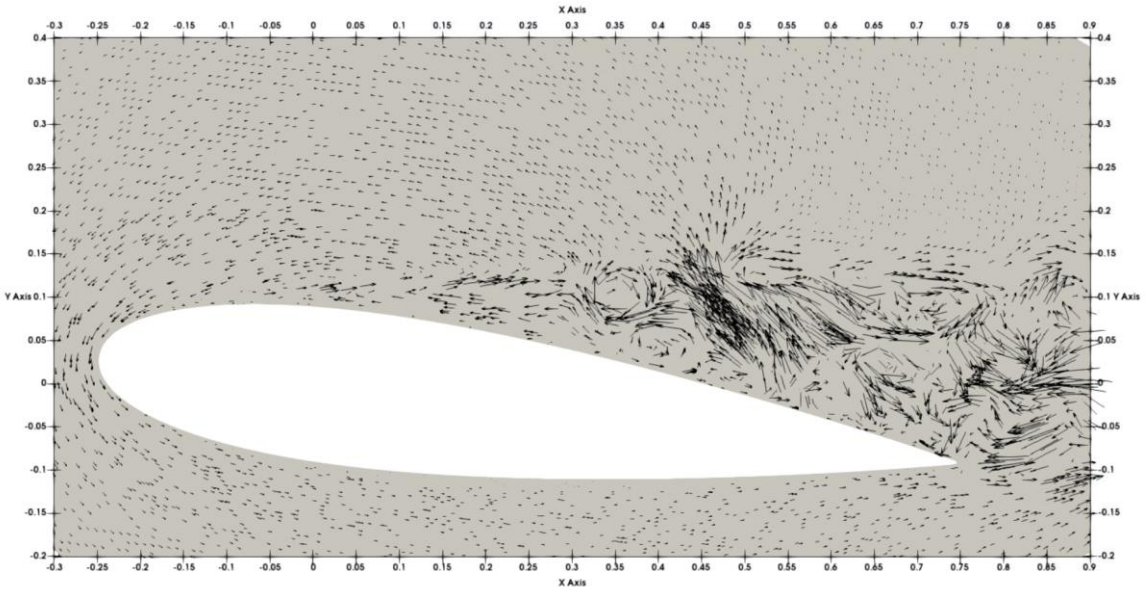

(a)

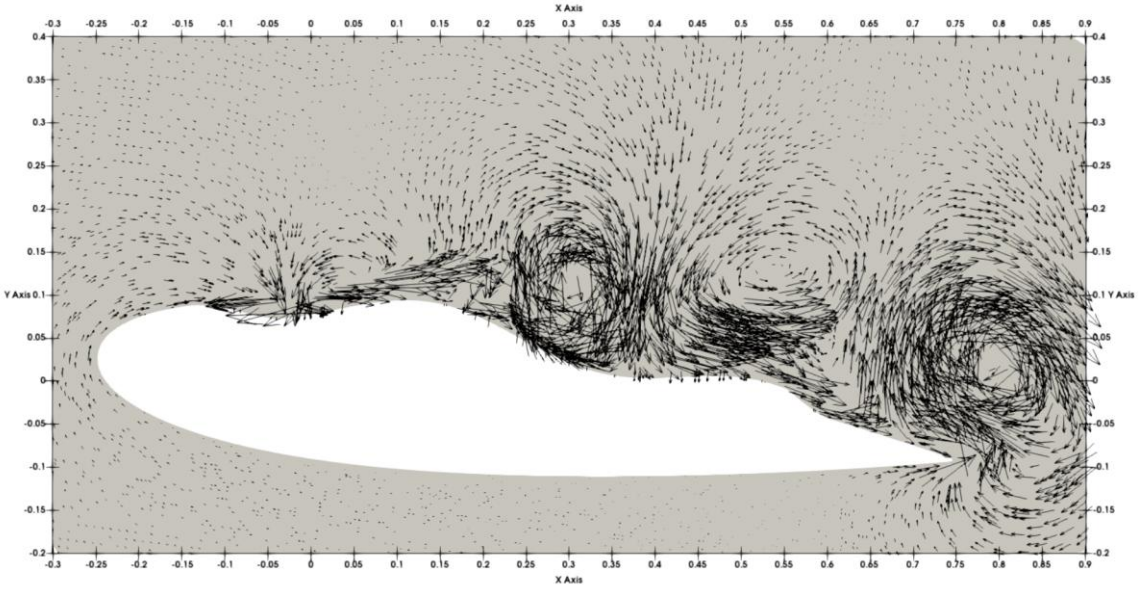

(b)

Figure 4-15- Vector plots of the fluctuating components (u', v') over a NACA 0018 airfoil (a) without

and (b) with traveling wave actuation at an angle of attack of 7°.

The velocity fluctuations (u', v') vector observed in Figure 4-16 airfoil is generated by the traveling wave actuation applied to the airfoil's surface at 11-degree angle of attack. As the wave propagates along the surface, it creates periodic undulations that interact with the boundary layer flow, disturbing it and generating alternating regions of compression and expansion. The periodic undulations cause fluid particles near the surface to oscillate, inducing momentum transfer within the boundary layer.

In Figure 4-17, the fluctuation vectors are depicted at 14-degree angle of attack. As expected, we see a chaotic motion over the entire suction surface when there is no travelling wave in Figure 4-17-a since we have a full stall condition at this angle of attack. In the actuated Case 6, Figure 4-17-b, where traveling wave actuation is applied to the airfoil's surface, the flow dynamics change significantly. The actuation induces large amplitude periodic undulations on the airfoil's surface, creating disturbances that pull the flow close to the boundary at x=0.35 which bring high momentum from the mainstream to the windward side of the wave at this point. Despite the existence of the crest wave the attached flow extends up to x=0.51. Near trailing edge around x=0.63, there is a strong vorticity that creates an upwash of low-momentum flow behind it and help the flow reattach in front of it. This mechanism demonstrates the effectiveness of the traveling wave in reducing the adverse pressure gradient and promoting boundary layer attachment even at such a high angle of attack. The interaction between the wave-induced disturbances and the boundary layer re-energizes the flow, limiting separation near the trailing edge and improving aerodynamic stability.

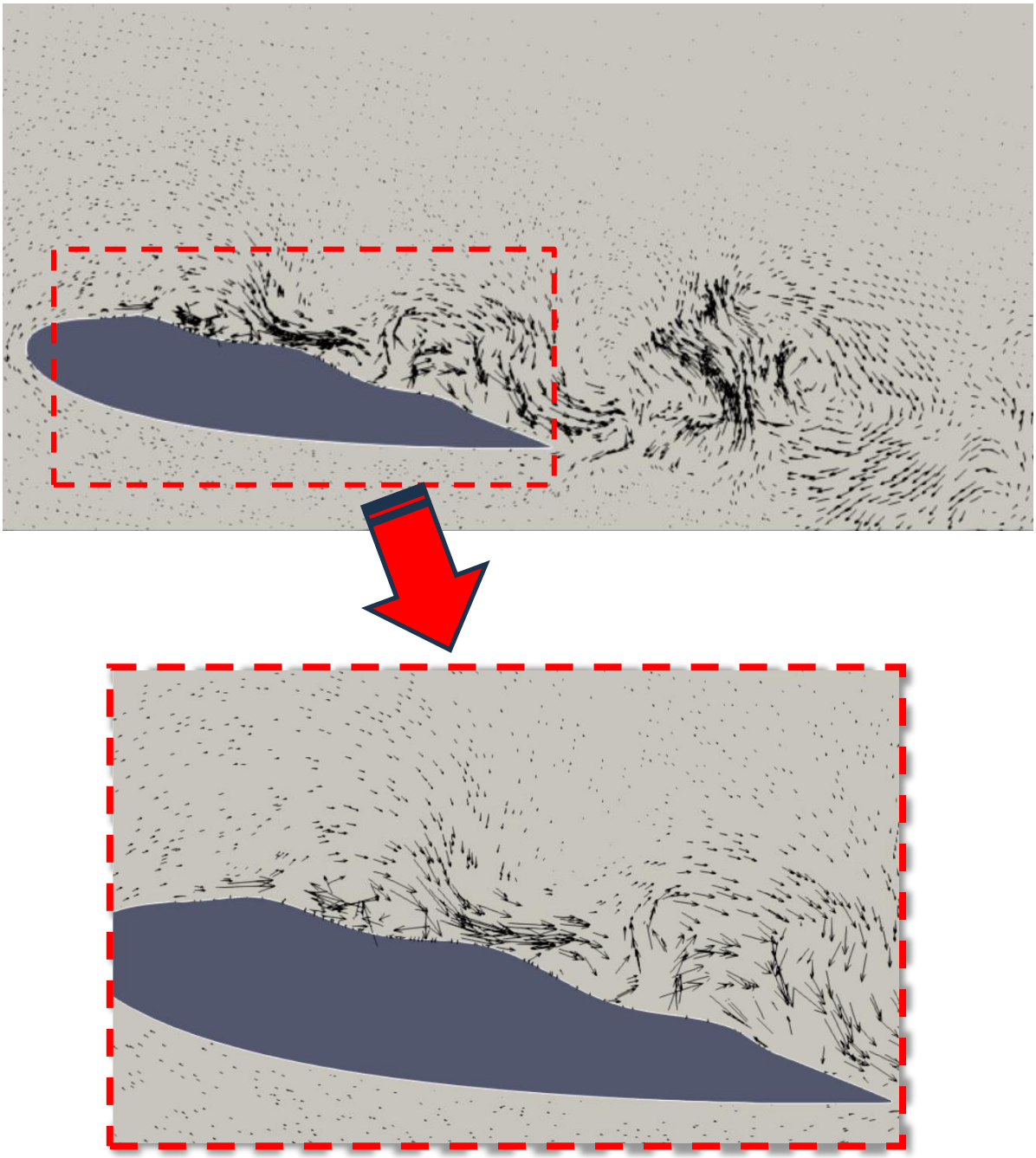

Figure 4-16- vector plots of the fluctuating components (u', v') over a NACA 0018 airfoil with traveling wave actuation at an angle of attack of 11°. The top image shows the overall flow field around the airfoil, indicating regions of significant downward velocity fluctuations (v') and circulatory patterns indicative of vortex generation near-boundary region. The bottom image provides a 2-x zoom near the boundary layer, highlighting the detailed interactions and momentum transfer induced by the traveling wave. These fluctuations contribute to maintaining attached flow, delaying separation, and enhancing aerodynamic performance.

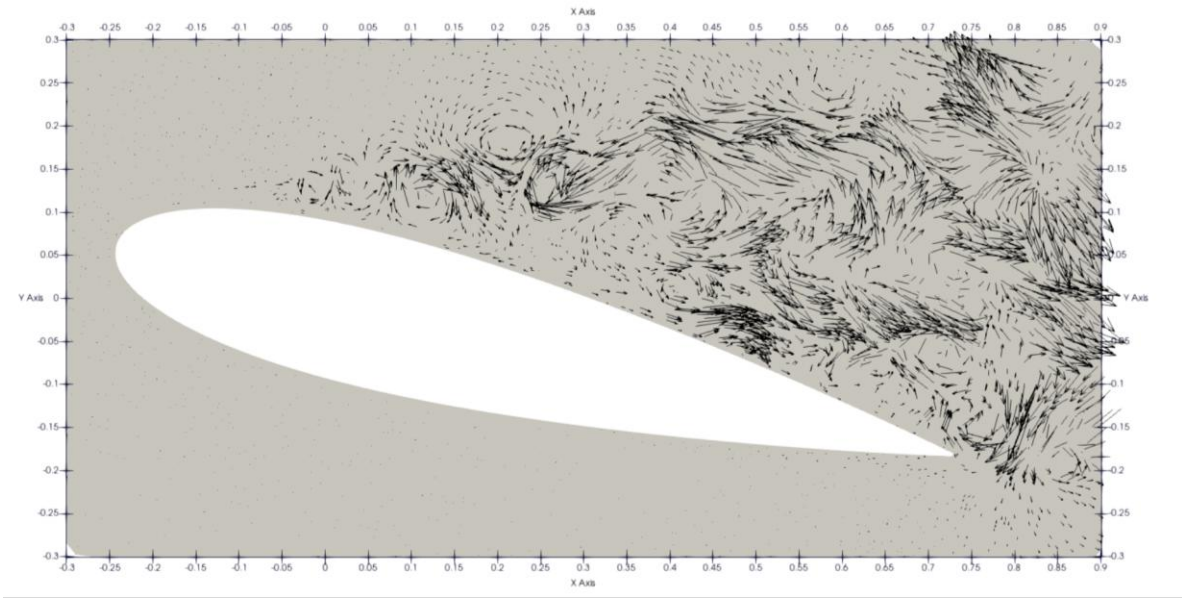

(a)

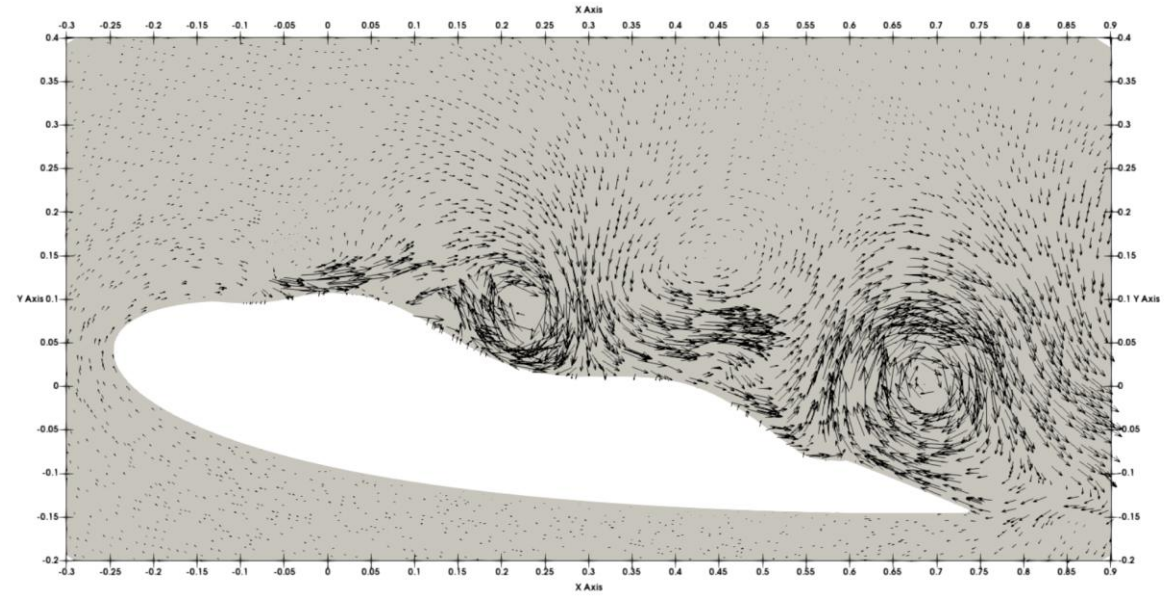

(b)

Figure 4-17- Vector plots of the fluctuating components (u', v') over a NACA 0018 airfoil (a) with and (b) without traveling wave actuation at an angle of attack of 14°. This figure shows that Case 6 was able to pull the flow structures from the suction surface high momentum area to the suction surface, However, it was not able to reattach the flow.

4.9 Large Coherent Structures (LCS) Investigation

In this section, we aim to reveal and analyze these large coherent structures, such as vortex pairs and horseshoe vortices, which are crucial in understanding how the traveling wave mechanism enhances flow control. By visualizing these structures, we can better comprehend how they facilitate momentum transfer from the main flow to the boundary layer, thereby maintaining flow attachment and improving the aerodynamic efficiency of the airfoil.

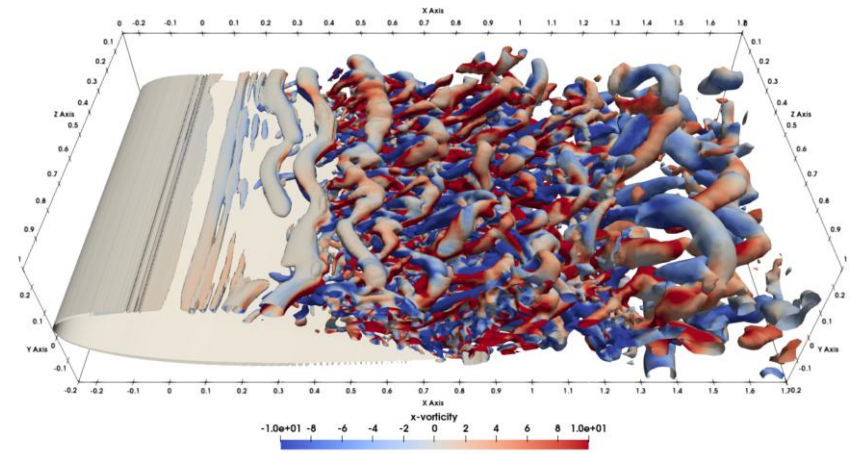

a-Unactuated

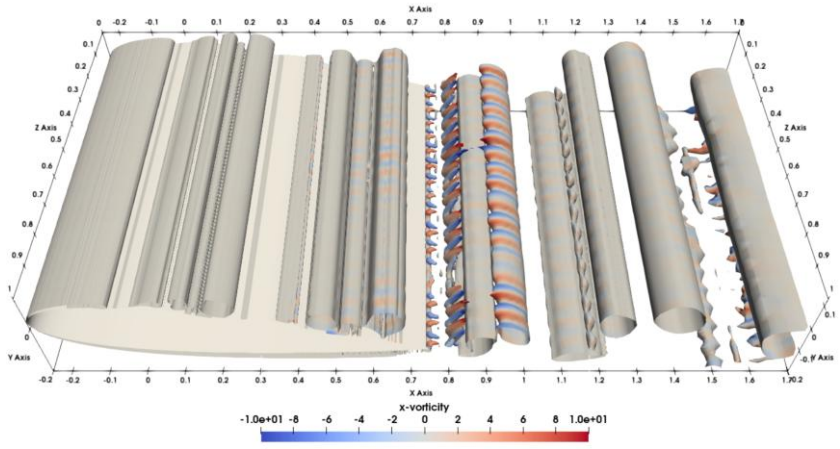

b-Case 1

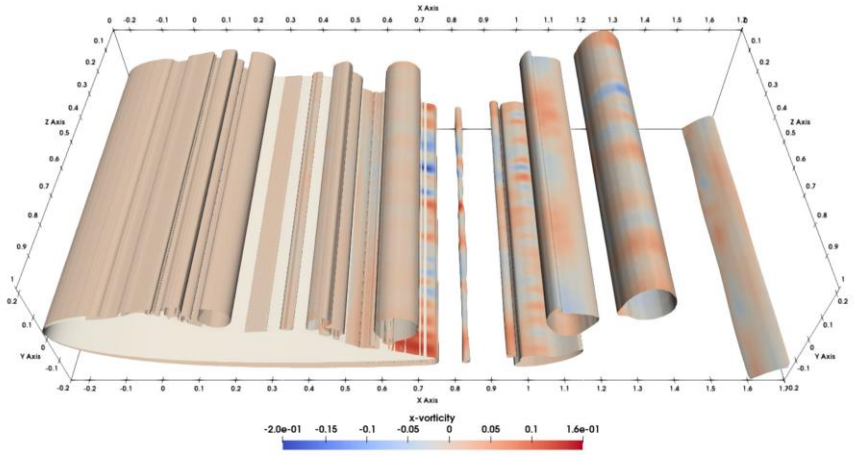

c-Case 2

Figure 4-18. LCS at a 7-degree angle of attack: (a) unactuated, showing early separation and chaotic vortices; (b) Case 1 with moderate TWM, displaying semi-laminar flow and organized vortex tubes; (c) Case 2 with higher TWM, featuring spanwise vortex tubes and re-laminarized flow, leading to improved stability and orderly downstream vortices.

In Figure 4-18, the LCS are depicted for Case 1 and Case 2, along with unactuated cases at the 7-degree angle of attack. In the unactuated case, Figure 4-18-a, flow separation begins at $x = 0.28$ and transitions to turbulence around $x = -0.1$, with spanwise vortices bending and numerous turbulent structures, such as horseshoe and hairpin vortices and vortex pairs [115], leading to significant drag and reduced lift. The turbulent boundary layer cannot withstand the adverse pressure gradient, resulting in chaotic flow separation, as seen in both the top view normal to the x-y surface and the 3D view. In contrast, the actuated Case 1, as shown in Figure 4-18-b, shows a semi-laminar flow without transient behavior or vortex bending. The traveling wave generates organized vortex tubes that extend to the trailing edge, eliminating flow separation. These vortex tubes enhance mixing within the boundary layer by pulling high-momentum fluid from the outer layer and ejecting low-momentum fluid, resulting in improved boundary layer stability and a more uniform Reynolds stress distribution. This enhanced mixing and reduced separation demonstrates the effectiveness of traveling wave actuation in increasing lift and reducing drag, as confirmed by the Q-criterion visualization and consistent

with Figure 4-7. For Case 2, as seen in Figure 4-18-c, which involves higher amplitude TWM, the majority of the observed structures consist of spanwise vortex tubes. This is supported by the x-vorticity color map, which predominantly displays a gray tone, indicating near-zero x-vorticity values. The presence of these spanwise structures suggests significant re-laminarization of the flow, as the actuation effectively dampens turbulent fluctuations and prevents the development of streamwise vortices. This re-laminarization stabilizes the boundary layer and enhances flow attachment over the airfoil surface. Consequently, the reduction in chaotic, high-energy structures allows for the formation of more orderly von Kármán vortices downstream of the trailing edge. This downstream vortex shedding points to a smoother flow transition beyond the airfoil, indicating successful flow control and reduced separation due to the higher amplitude traveling wave actuation.

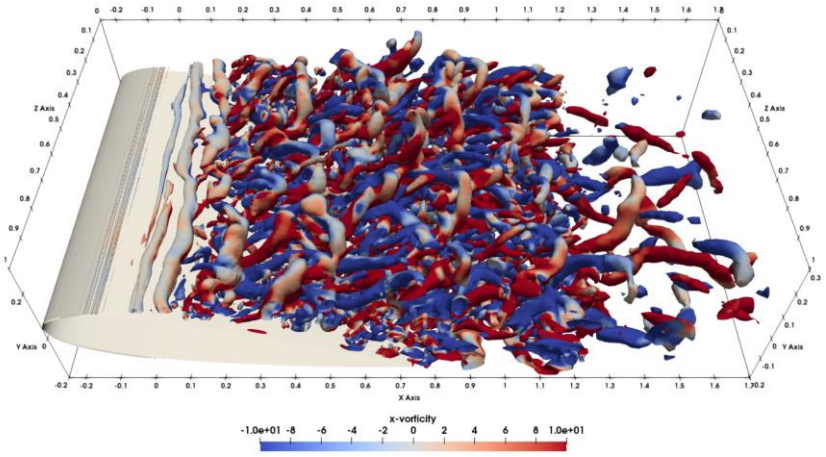

a-Unactuated

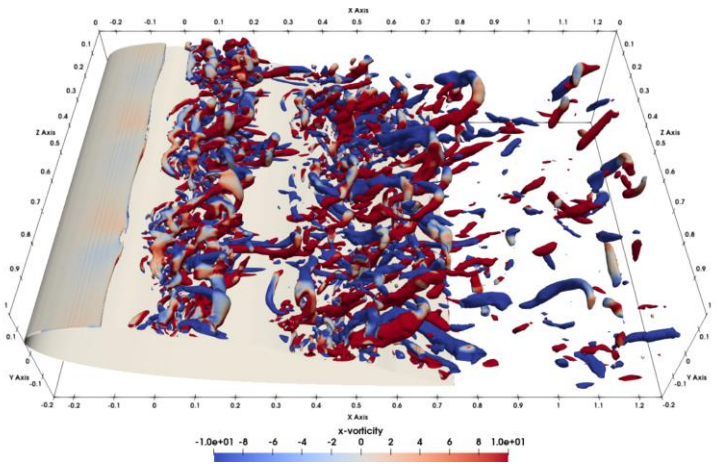

b-Case 3

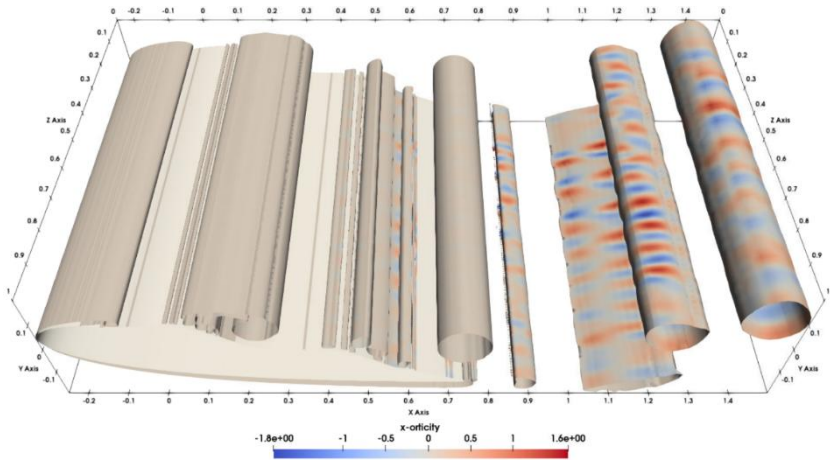

c-Case 4

Figure 4-19- Large coherent structures over the NACA 0018 airfoil at AOA=11 for (a) unactuated, (b) Case 3, and (c) Case 4. (a) The unactuated case shows laminar flow transitioning to chaotic 3D structures, leading to separation. (b) Case 3 displays early laminar separation transitioning to turbulence, with vortex pairs aiding boundary layer control. (c) Case 4 shows quasi-laminar flow across most of the surface, stabilized by high-amplitude TWM, with 3D structures appearing only near the trailing edge.

As show in Figure 4-19, at an 11-degree angle of attack, the flow dynamics differ significantly between the unactuated case and the actuated cases with varying amplitudes of traveling wave actuation (TWM). In the unactuated case, Figure 4-19-a, up to x=−0.14, the flow remains almost laminar but begins to exhibit three-dimensional characteristics after x=−0.03. This region is marked by 2D tube-like structures that evolve into horseshoe vortices, which then extend upstream and interact with each other, leading to a mixed and chaotic flow. In Case 3, as shown in Figure 4-19-b, the flow shows improvements in structure and control. From the leading edge to x=−0.05, a laminar separation is observed that gradually transitions to turbulence. The coherent structures in this initial region are less defined due to dominant shear stress over vorticity. Between x=−0.05 and x=0.18 in the wave trough, the flow transitions to fully turbulent behavior, characterized by large, disorganized structures. However, three notable vortex pairs stretch downstream, remaining close to the boundary and marking the end

of the windward face of the wave trough. Between x=0.18 and x=0.28 in the next wave crest, the presence of fewer large coherent structures suggests a quasi-laminar zone induced by TWM that prevents excessive vortex formation. From x=0.31 to the trailing edge, while the TWM influence diminishes and more chaotic structures begin to emerge, the pre-formed vortices continue to contribute to boundary layer control, helping maintain attachment longer than in the unactuated case. In Figure 4-19-c, the effect of TWM is even more pronounced. From the leading edge to the trailing edge, the flow displays mostly spanwise vortex tubes, and the x-vorticity contour appears solid gray, indicating near-zero rotation of vortices in the x-direction. This suggests a significant quasi-laminarization of the flow, with TWM effectively dampening turbulence across the surface. Signs of 3D structures become visible only close to the trailing edge, around x=0.57, showing how the high amplitude of the wave has been effective in maintaining flow stability and reducing separation over most of the surface. This case

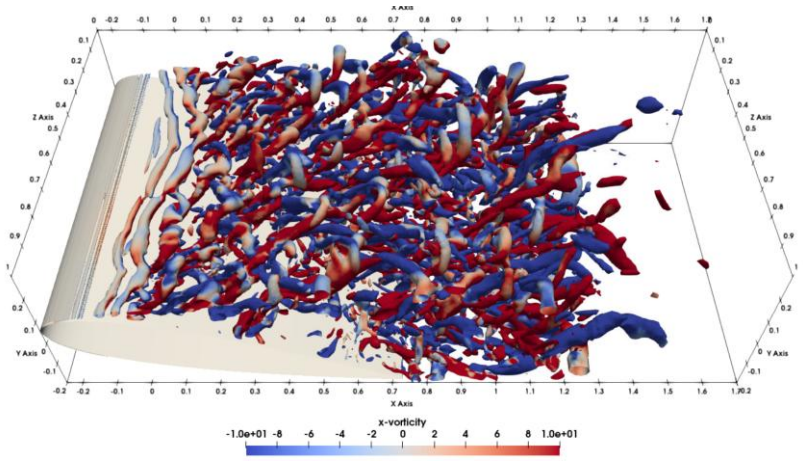

a-Unactuated

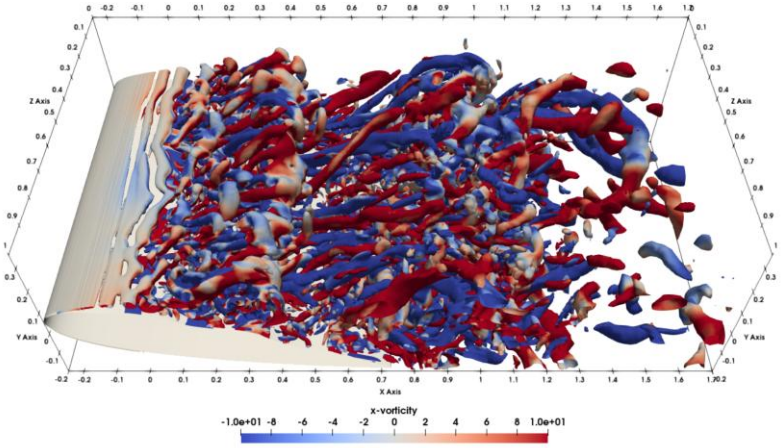

b-Case 5

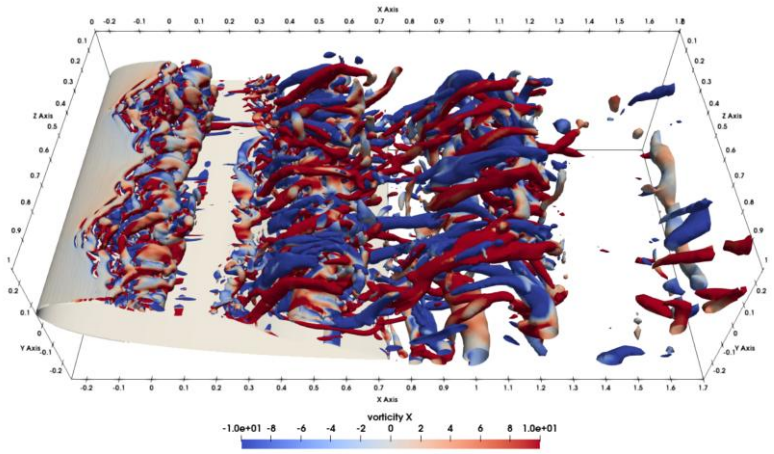

c-Case 6

Figure 4-20- Flow structures over the NACA 0018 airfoil at AOA=14 for (a) unactuated, (b) Case 5, and (c) Case 6. (a) The unactuated case shows an extended separation zone up to x=−0.2 and initial instabilities marked by bent vortex tubes, indicating high chaotic motion. (b) Case 5 displays large streamwise vortex legs extending downstream but positioned too far from the boundary, limiting effective momentum transfer and failing to reduce separation. (c) Case 6 demonstrates successful flow control with higher amplitude TWM, maintaining 2D structures up to x=1.6, enhancing boundary layer stability and reducing separation.

highlights the potential of high-amplitude TWM to create a more stable boundary layer and maintain attached flow, minimizing turbulent breakdown and improving overall aerodynamic performance. In Figure 4-20-a, at a14-angle of attack, the flow shows an extended separation zone stretching toward the leading edge up to x=−0.2, indicating near full stall due to the high angle of attack. Stronger, bent tube-like structures appear as initial instabilities near x=−0.16,

and there are fewer horseshoe and common vortex structures compared to AOA=11, signifying highly chaotic motion. In Case 5, see Figure 4-20-b, TWM with a=0.01was not successful in eliminating flow separation. Large streamwise vortex legs extend downstream but are situated too far from the boundary, indicating that the mainstream high momentum could not effectively reach the near-wall region to energize the boundary layer. While sweep events occur, their distance from the surface limits their ability to recover momentum close to the boundary, reducing the impact on flow reattachment and maintaining attachment. As a result, this configuration shows limited success in improving boundary layer control and reducing separation.

In successful Case 6, see Figure 4-20-c, TWM with a higher amplitude of a=0.02 was effective in maintaining flow attachment. The long counter-rotating vortex pairs are again seen structures beyond the leading edge, starting from x=0.26, indicating the integration of sweep and ejection events are being are happening after this point, facilitating better momentum transfer and effectively re-energizing the boundary layer. This results in improved flow control, reduced separation, and enhanced aerodynamic performance compared to the lower amplitude case.

4.10 Conclusion

This study provides an in-depth exploration of the effectiveness of Traveling Wave Modulation (TWM) as an active flow control strategy for enhancing the aerodynamic performance of a NACA 0018 airfoil at a low Reynolds number (Re=20,000). By examining the influence of TWM at three distinct angles of attack—7°, 11°, and 14°—the research underscores the profound impact of surface wave actuation on boundary layer dynamics, vortex behavior, and overall aerodynamic efficiency.

At a low angle of attack (7°), where the flow is on the verge of separation, the application of TWM proved highly effective in stabilizing the boundary layer. The traveling waves generated organized vortex structures that facilitated enhanced mixing of high-momentum fluid into the boundary layer. This prevented early separation and maintained flow attachment along the airfoil surface. The resulting smoother pressure recovery significantly improved aerodynamic performance, as evidenced by reduced drag and increased lift. The improved flow behavior demonstrated at this angle illustrates TWM's potential as a control mechanism for enhancing the efficiency of aerodynamic surfaces operating near pre-stall conditions.

For the moderate angle of attack (11°), where flow separation becomes more pronounced, TWM exhibited even greater influence. In unactuated cases, flow separation was extensive, leading to a significant drag penalty and diminished lift. However, the introduction of traveling waves disrupted the large separation bubbles typically seen at this angle. By inducing controlled instabilities and creating organized vortex structures, the traveling waves enabled the transfer of high-momentum fluid from the free-stream into the separated regions, thus mitigating the adverse pressure gradient responsible for flow detachment. This enhanced reattachment and allowed the boundary layer to remain stable over a greater portion of the airfoil's surface. The pressure recovery was more effective, and the resultant aerodynamic forces indicated a marked improvement in performance.

At a high angle of attack (14°), corresponding to post-stall conditions, the flow was characterized by extensive separation in the unactuated state, resulting in chaotic vortex shedding and significant performance losses. Although TWM did not completely eliminate flow separation at this challenging condition, it demonstrated considerable potential by altering the dynamics of the turbulent flow. The actuation brought turbulent energy closer to the surface, where it could contribute to boundary layer reattachment near the trailing edge. While the improvements were less dramatic than at lower angles of attack, the reduction in the size of the

separated region and the enhanced flow stability were notable. This outcome points to TWM's ability to manage even severe flow conditions effectively, albeit with limitations at very high angles of attack.

The findings of this study highlight the importance of wave parameters, including amplitude, frequency, and wavelength, in determining the efficacy of TWM. Higher amplitudes proved particularly effective in energizing the boundary layer and maintaining flow attachment, but they also introduced a trade-off by occasionally destabilizing the flow at higher angles of attack. Similarly, the optimal choice of wave frequency was shown to depend on the flow conditions, with higher frequencies benefiting flow control at lower angles while sometimes increasing turbulence in post-stall scenarios. Wavelengths that matched the natural flow instabilities demonstrated the greatest potential for reducing separation and improving lift and drag characteristics, as they maximized the interaction between the traveling waves and the boundary layer.

An important contribution of this research lies in the detailed examination of Reynolds stress distribution and its role in turbulent momentum transport. TWM consistently concentrated turbulent energy near the airfoil surface, reducing the extent of separation and stabilizing the boundary layer. The observed redistribution of Reynolds stresses emphasized the critical role of surface wave actuation in managing turbulent energy. Negative Reynolds stresses in certain regions highlighted counter-gradient momentum transfer, which contributed to enhancing flow attachment and mitigating separation. The study also provided a clear visualization of large coherent structures, demonstrating how TWM transforms chaotic vortices into organized patterns, such as vortex tubes and spanwise structures. These structures were instrumental in maintaining boundary layer stability and reducing drag.

This investigation underscores the significant aerodynamic improvements achievable with TWM. Across all angles of attack, the application of traveling waves led to better lift-to-drag ratios, highlighting the versatility of this method in addressing a wide range of flow conditions. Even under post-stall conditions, where traditional flow control methods often falter, TWM showed promise by re-laminarizing turbulent flows and extending flow attachment.

Future work should focus on refining the wave parameters for specific aerodynamic applications, particularly for scenarios involving higher Reynolds numbers and more complex flow regimes. Experimental validation of the findings presented in this study would provide a more comprehensive understanding of TWM's practical applications and its potential integration into real-world aerodynamic systems. Furthermore, the exploration of advanced materials and actuator technologies for implementing traveling waves could expand the feasibility and efficiency of this flow control strategy in various aerospace and engineering contexts.

5 Chapter 5: CFD-ML Integration for Accurate Drag and Lift Predictions over a Controlled NACA 0018 Airfoil at Reynolds number of 20,000

Abstract

In this study, the integration of machine learning (ML) techniques with Computational Fluid Dynamics (CFD) simulations is explored in order to predict drag and lift coefficients on a NACA-0018 airfoil subjected to traveling wave surface actuations. Firstly, for data generation, the effects of wave characteristics—including frequency, amplitude, and wavelength—on drag and lift were evaluated using advanced computational fluid dynamics (CFD) simulations. Then, for the prediction, Key ML models, including Gaussian Process Regression (GPR), Support Vector Machines (SVM), Decision Trees (DT), and Least Squares Boosting (LSBoost), were employed. Additionally, the Parrot Optimizer (PO) was utilized to optimize these models, improving their accuracy and reducing computational costs. The results indicate that the frequency had the strongest impact on drag and lift. Higher frequencies were found to decrease drag and enhance lift by postponing flow separation. Among the models, PO-GPR and PO-DT outperformed other methods in predicting aerodynamic forces. While machine learning models were more accurate in drag prediction, lift proved more challenging due to its sensitivity to fluid dynamic complexities.

Keywords: Flow Control, CFD integrated with Machine Learning, Drag and Lift Prediction, Travelling Wave Method

5.1 Introduction

The application of machine learning (ML) algorithms to optimize flow control processes over aerodynamic shapes has emerged as a transformative approach across diverse industries. These algorithms, leveraging vast datasets and complex numerical computations, offer innovative solutions that surpass traditional methods. In the aerospace industry, for instance, machine learning is employed to predict and manipulate airflow structures over wing surfaces, leading to improved lift and drag forces resulting in fuel efficiency and reduced emissions in aircrafts [116–118]. By analyzing vast amounts of flight data, machine learning models can identify patterns and optimize wing configurations, reducing drag and improving lift.

The advancements in high performance computing and experimental observation techniques and sophisticated tools have resulted in an explosion of data in the literature. The huge volume of data captured wither numerically or experimentally has motivated fluid mechanics researchers to employ ML in statistical analysis of fluid structures[119,120]. On the other hand, traditional numerical methods of processing and analyzing this data have utilized database clusters to handle the vast volumes of information in order to post-process results captured from simulation. However, these methods often require substantial domain expertise and complex algorithms, which can be limiting, complex and time-consuming [121]. For example, this study used numerical methods to simulate 3D turbulent fluid flow over a NACA 0018 airfoil with traveling wave actuators, the complexity of the task is immense, involving a fluid domain of 15 by 15 by 1 unit, meticulously divided into a structured mesh comprising 6 million cells. This granularity is essential to capture the detailed turbulent structures and interactions accurately. The simulations employ the Large Eddy Simulation (LES) approach, a high-fidelity method that resolves large-scale eddies while modeling smaller scales, ensuring precise representation of turbulence dynamics. The computational demands are staggering: each simulation case (to observe a steady result) requires 6 days of continuous computation on a

state-of-the-art high-performance computing cluster. This setup involves 32 MPI processes, with each process demanding 2 GB of memory, amounting to an enormous total of 64 GB of memory usage. The temporal resolution is equally demanding, with a minuscule time step of 0.0005 seconds necessary to capture the transient phenomena accurately over a simulated period of 80 seconds. This level of detail ensures that no subtle fluid dynamic behavior is overlooked, but it comes at the cost of extended computational time and resources. Such intensive computational requirements highlight the immense challenge of using traditional CFD methods for simulating complex, large-scale problems, pushing the limits of current computational capabilities and necessitating the use of cutting-edge hardware and parallel computing techniques. Therefore, CFD Simulations are recognized for their accuracy but are noted for being computationally expensive, memory-demanding, and time-consuming.

To address some of these challenges, advancements like morphing surfaces driven by traveling waves provide a promising alternative**.** These waves, by altering the shape and movement of the airfoil surface, directly influence aerodynamic forces like lift and drag. These kinds of waves mimic aquatic locomotion, causing shape changes and dynamic movements across the airfoil surface. This results in increased lift and delayed stalling, which is particularly useful in scenarios requiring sudden maneuvers, such as at high angles of attack. Thompson and Goza [104] employed travelling wave surface over a NACA0012 airfoil and demonstrated that optimal actuation for lift involved different spatial and temporal configurations compared to drag minimization. Similarly, morphing studies have shown that large reductions in flow separation can be realized and hence be responsible for increases in lift and reduction in drag [51,122]. Further, as proved by research of Aziz et. Al [123] combined morphing effects, like droop nose and trailing edges, could enhance the aerodynamics of an airfoil to a great extent and thus had great potential for morphing surfaces in all regimes to better aircraft efficiency.

While morphing surfaces show considerable promise in enhancing aerodynamic performance, optimizing their design and control remains a complex task. Machine Learning (ML) offers a powerful tool to address this challenge by automating and improving the process of identifying optimal configurations and actuation parameters for these surfaces. Machine Learning (ML) offers a successful approach to turbulent flow modeling by significantly reducing simulation times and computational costs. By training ML models on high-fidelity simulation data, it enables rapid and accurate predictions of complex flow behaviors, streamlining the exploration of different parameters [124,125]. ML methods have been also used in conjunction with computational fluid dynamics to optimize airfoil parameters and increase aerodynamic properties [126]. These methods have being employed to shape the optimal bidimensional airfoil, maximizing the lift-over-drag ratio [127]. Specifically, ML techniques are being applied to flow control over morphing airfoils. Haughn et al. [128] developed a closed-loop control system based on deep reinforcement learning for a morphing airfoil, which was designed with Macro Fiber Composites and piezoelectric flex sensors. This study reveals that deep learning techniques can effectively address typical challenges in achieving adequate modeling and control methods when using smart composite actuators in autonomous aerospace applications. In another related effort, a feedback control approach was utilized to improve lift and drag forces on the airfoil with the actuation profile optimized for drag minimization and lift maximization by Thompson and Goza [104] . They varied the speed of the morphing actuators and discussed its relations to flow structures over a NACA0012 airfoil. Liu et al. [129] also developed a new morphing control approach for an asymmetric deformable airfoil using deep reinforcement learning, achieving a performance improvement of 29.8%. Karbasian and van Rees developed a quick numerical design approach for morphing airfoils utilizing deep learning surrogate models, reducing the required number of flow solutions [130].

A surrogate-model approach is a computational technique used to approximate and predict the behavior of complex systems, which are typically expensive and time-consuming. It can be concluded that the prediction of the lift and drag coefficient of an airfoil like NACA 0018 using the deep learning method is a great leap in integrating machine learning with aerodynamics. Because it significantly improves the accuracy of simulations, which reduces the need for time-consuming, complicated traditional CFD methods while offering real-time visions for optimal airfoil design. Such an approach is more sophisticated for the test of influence on several factors like frequency, amplitude, wavelength, among others, because computational analytics has compatibility with the physical process. In other words, deep learning models can process large groups of datasets as well as non-linear relationships of wave parameters and fluid flow characteristics compared to the traditional methods which often require simplifying assumptions or are computationally intensive when analyzing this complex system of equations. In this study, we examined what the applicability of each machine learning methods is for improving the prediction of lift and drag coefficients over a NACA0018 airfoil at Reynolds number flow of 20,000. Specifically, we explored Gaussian Process Regression (GPR), a non-parametric Bayesian approach known for its effectiveness in handling data with uncertainty [131]. Additionally, a employed Support Vector Machines (SVM) is employed in this paper which is a widely-used method for regression and classification of large dataset [132]. To better interpret non-linear data, the Decision Tree (DT) algorithm has been incorporated [133]. Lastly, we employed Least Squares Boosting (LSBoost) to minimize prediction error (mean-square error) in noisy datasets [134]. Through this comparative analysis, we aim to identify the most robust and accurate machine learning model for predicting drag and lift coefficients in this turbulent flow.

5.2 Material and methods

5.2.1 Data

In this study, we carried out Finite-Volume Method (FVM) encompassed with Large Eddy Simulation method to model the behavior of the flow. The geometry of this problem is a 3D NACA-0018 airfoil located in the middle of an unconfined channel and is under affected of turbulent flow with the Reynolds number of $\mathrm{Re} = \frac{\mathrm{UL}}{\nu}$ = 20,000. The details of the sizes and flow conditions have been demonstrated in Figure 5-1. The computational domain dimensions were chosen to minimize blockage effects and ensure that boundary-induced disturbances, such as wall reflections, do not influence the flow around the airfoil. The main equations and concepts, including the Navier-Stokes equations and turbulence model are all set out in this section. The Navier-Stokes equations account for the conservation of momentum and describe the motion of fluid particles in vicinity of external forces. The general form of the Navier-Stokes equations [25] for an incompressible fluid is given by:

$$\frac{\partial \vec{u}}{\partial t} + (\vec{u}.\vec{\nabla})\vec{u} = -\frac{1}{\rho}\nabla\vec{\mathrm{p}} + \nu\nabla^2\vec{u} + \vec{f} \qquad \text{(Equation 5-1)}$$

where u, is the velocity field, ρ is the fluid density, and p is the pressure. The summation of body forces vectors is demonstrated by $\vec{f}$. These equations show momentum conservation, with the left side of the equation depicting acceleration (temporal and convective) and the right-side representing forces acting on the fluid.

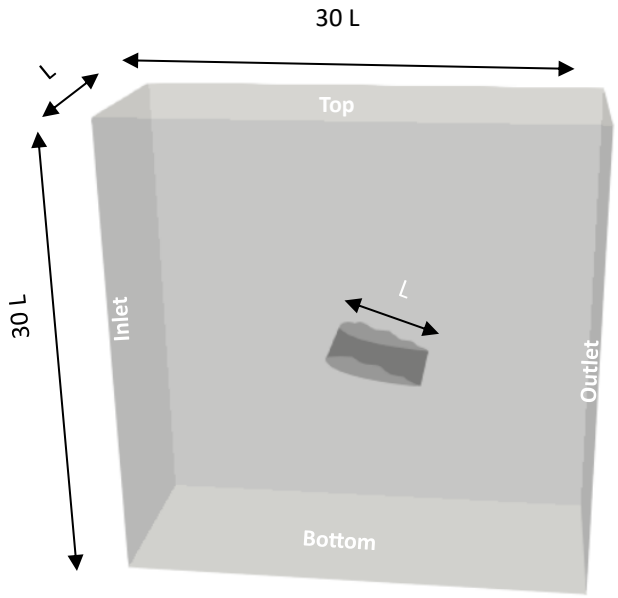

Velocity:

Airfoil: Moving wall

Front and **Back**: Cyclic

Inlet: Uniform velocity

Outlet: Zero gradient

Top and **Bottom**: Slip

Pressure:

Airfoil: Zero gradient

Front and **Back**: Cyclic

Inlet: Zero gradient

Outlet: Zero gradient

Top and **Bottom**: Zero gradient

Turbulent kinetic energy

Airfoil: Zero ($k = 1e - 8$)

Front and **Back**: Cyclic

Inlet: Zero ($k = 1e - 8$)

Outlet: Zero gradient

Top and **Bottom**: Zero gradient

Turbulent kinematic viscosity

Airfoil: Placeholder

Front and **Back**: Cyclic

Inlet: Placeholder

Outlet: Placeholder

Top and **Bottom**: Placeholder

Figure 5-1- The computational domain and boundary conditions. A placeholder namely calculated means the value is delivered from other fields

Due to the complexity in modeling the turbulent flow over airfoil it is characterized by chaotic fluid movements and is often modelled with statistical approaches. DNS (Direct Numerical Simulation) [135], RANS (Reynolds-Averaged Navier-Stokes) Models [136], ,LES (Large Eddy Simulation) [137], and many other methods [138,139]**.** LES showed accurate resolving transient, unpredictable flows that are generated by the morphing surface of airfoils. It provides a reliable representation of different scales of flow structures in near-boundary regions, flow separation, reattachment, and transition phenomena [25,54]. Following LES rules, the filtered Navier-Stokes equation for incompressible flow is expressed as

$$\frac{\partial \tilde{u}}{\partial t} + (\tilde{u}.\nabla)\tilde{u} = -\frac{1}{\rho}\nabla\tilde{p} + \nu\nabla^2\tilde{u} + \tilde{f} - \nabla.\tau \qquad \text{(Equation 5-2)}$$

Where $\tilde{u}$ and $\tilde{p}$ are the filtered velocity and pressure, respectively, and τ represents the subgrid-scale stress tensor, which is modeled to consider the effects of the smaller, unresolved scales on the resolved scales [137]. The sub-grid tensor is defined as a key component in LES that represents the effects of the unresolved small-scale eddies which are smaller than unit cell size. There are different models that model additional term of τ in filtered Navier-Stokes equation [140–142] among Which we chose dynamic one-equation SGS kinetic energy model [76]. This model dynamically adjusts the turbulence model coefficient k based on the local flow conditions, enhancing the accuracy of turbulence representation across different flow regimes. Also, by solving transport equation for the sub-grid kinetic energy, it properly captures the energy transfer between larger to smaller eddies. Following this sub-grid model, parameter τ is defined as:

$$\tau = 2\rho\left(\nu_{sgs} + \nu\right)\tilde{S}_{ij}] \qquad \text{(Equation 5-3)}$$

Where ν_{sgs} and $\tilde{S}_{ij}$ are respectively is the sub grid scale eddy viscosity and filtered strain tensor. The viscosity above is defined as:

$$\nu_{sgs} = C_k \Delta \sqrt{k_{sgs}} \qquad \text{(Equation 5-4)}$$

where C_k is a constant coefficient is dependent on the sub-grid model. The parameter shows the volume of a cube and called the grid characteristic length. To resolve k_{sgs}, the transport equation below is defined. The constants C_ε and C_k are reported by Kim and Menon's [77].

$$\frac{\partial k_{sgs}}{\partial t} + \bar{u}_j \frac{\partial k_{sgs}}{\partial x_j} = \nu_{sgs}\left[2\tilde{S}_{ij}\tilde{S}_{ij}\right] - \varepsilon + \frac{\partial}{\partial x_j}\left(\nu_{sgs}\frac{\partial k_{sgs}}{\partial x_j}\right)$$

$$\varepsilon = \frac{C_\varepsilon k_{sgs}^{\frac{3}{2}}}{\Delta} \qquad \text{(Equation 5-5)}$$

The airfoil is equipped by travelling wave morphing surface on the suction side with different wave parameters. The time derivation of sinusoidal motion of the wave is described as:

$$d(X,t) = a(x)\sin\left(\frac{2\pi}{\lambda}(X - \lambda f t)\right) \qquad \text{(Equation 5-6)}$$

Where d is the amount of surface normal displacement in chord-wise position X and time t, the amplitude, wavelength and frequency of the wave are also demonstrated by a , λ and f. The above parameters are dimensionless with Airfoil chord length of L, and Uniform Inlet velocity U. The frequency, wavelength and amplitude of the wave has altered to extract different datasets. The outcomes of these simulations are the drag and lift coefficients, which vary according to the wave parameters, with frequency ranging from 1 to 10, amplitude values of 0.001, 0.01, and wavelength varying between 0.3 and 1. All other properties of the fluid and airfoil are kept unchanged to isolate the effects of the wave parameters. The angle of attack is also kept as 15 degrees where the unactuated airfoil (without travelling wave) is in post-stall

condition [26]. This particular angle was chosen because, at 15 degrees, the airfoil experiences a post-stall condition, making it ideal for evaluating the effectiveness of traveling wave actuation in delaying or mitigating flow separation. Table 5-1 and Table 5-2 below show the input parameters, e.g. frequency, wavelength, and amplitude for 93 cases along with the output parameters which are drag and lift coefficients. Worth mentioning that all the parameters are dimensionless by implementing, uniform inlet velocity U, time t and chord length of airfoil L.

Table 5-1 showcase the dimensionless input and output parameters for 93 simulation cases. Input parameters, including frequency, wavelength, and amplitude, and output parameters, drag and lift coefficients

Frequency	Amplitude	Wavelength	Drag
1	0.001	0.3	0.17
1	0.002	0.3	0.168
1	0.002	0.5	0.17
1	0.002	1	0.168
1	0.003	0.3	0.175
1	0.003	0.5	0.176
1	0.003	1	0.174
1	0.004	0.3	0.174
1	0.004	0.5	0.177
1	0.004	1	0.174
1	0.01	0.3	0.1
1	0.01	0.5	0.138
1	0.01	1	0.159
1	0.02	0.3	0.102

Table 5-1- Continued

1	0.02	0.5	0.145
1	0.02	1	0.109
2	0.001	0.3	0.162
2	0.001	0.5	0.159
2	0.001	1	0.162
2	0.002	0.3	0.153
2	0.002	0.5	0.152
2	0.002	1	0.152
2	0.003	0.3	0.146
2	0.004	0.3	0.131
2	0.004	0.5	0.138
2	0.004	1	0.13
2	0.01	0.3	0.111
2	0.01	0.5	0.088
2	0.01	1	0.073
3	0.001	0.3	0.111
3	0.001	0.5	0.137
3	0.001	1	0.137
3	0.004	0.5	0.1
3	0.002	0.3	0.112
3	0.002	1	0.134
3	0.004	0.3	0.169
3	0.004	0.5	0.1

Table 5-1- Continued

3	0.02	0.3	0.112
4	0.001	0.3	0.131
4	0.001	0.5	0.171
4	0.001	1	0.17
4	0.002	0.3	0.107
4	0.003	0.3	0.0822
4	0.004	0.3	0.079
4	0.004	0.5	0.082
5	0.001	0.3	0.107
5	0.001	0.5	0.106
5	0.001	1	0.105
5	0.002	0.3	0.093
5	0.002	1	0.091
5	0.003	0.3	0.0878
5	0.003	0.5	0.0876
5	0.004	0.3	0.088
5	0.004	0.5	0.087
5	0.004	1	0.0847
5	0.01	0.3	0.103
5	0.01	0.5	0.086
5	0.01	1	0.0837
5	0.02	0.3	0.108
5	0.02	0.5	0.0907

Table 5-1- Continued

5	0.02	1	0.0837
6	0.001	0.3	0.097
6	0.002	0.3	0.091
6	0.004	0.3	0.091
6	0.001	0.5	0.089
6	0.002	0.5	0.085
6	0.004	0.5	0.085
6	0.001	1	0.126
6	0.002	1	0.118
6	0.004	1	0.138
6	0.01	0.5	0.142
6	0.02	0.5	0.142
6	0.01	1	0.131
6	0.02	1	0.126
8	0.001	0.3	0.117
8	0.002	1	0.084
8	0.002	0.3	0.087
8	0.004	0.3	0.0812
8	0.004	0.5	0.0817
8	0.004	1	0.082
8	0.01	0.3	0.103
8	0.01	0.5	0.099
8	0.01	1	0.105

Table 5-1- Continued

10	0.002	0.3	0.091
10	0.002	0.5	0.113
10	0.002	1	0.098
10	0.001	0.3	0.087
10	0.001	0.5	0.108
10	0.001	1	0.094
10	0.004	0.3	0.132
10	0.004	0.5	0.13
10	0.004	1	0.141

Table 5-2-showcase the dimensionless input and output parameters for 93 simulation cases. Input parameters, including frequency, wavelength, and amplitude, and output parameters, drag and lift coefficients

Frequency	Amplitude	wavelength	Lift
1	0.001	0.3	0.456
1	0.002	0.3	0.439
1	0.002	0.5	0.49
1	0.002	1	0.448
1	0.003	0.3	0.56
1	0.003	0.5	0.579
1	0.003	1	0.54
1	0.004	0.3	0.565
1	0.004	0.5	0.636
1	0.004	1	0.573

Table 5-2-Continued

1	0.01	0.3	0.973
1	0.01	0.5	0.85
1	0.01	1	0.78
1	0.02	0.3	0.932
1	0.02	0.5	0.73
1	0.02	1	0.843
2	0.001	0.3	0.541
2	0.001	0.5	0.421
2	0.001	1	0.411
2	0.002	0.3	0.646
2	0.002	0.5	0.661
2	0.002	1	0.644
2	0.003	0.3	0.739
2	0.003	0.5	0.705
2	0.003	1	0.696
2	0.004	0.3	0.826
2	0.01	0.3	0.522
2	0.01	0.5	0.572
2	0.01	1	0.599
3	0.001	0.3	0.449
3	0.001	0.5	0.416
3	0.001	1	0.36
3	0.004	0.5	0.944

Table 5-2-Continued

3	0.002	0.3	0.581
3	0.002	1	0.805
3	0.004	0.3	0.462
3	0.004	0.5	0.944
3	0.02	0.3	0.596
4	0.001	0.3	0.759
4	0.001	0.5	0.77
4	0.001	1	0.811
4	0.002	0.3	0.902
4	0.003	0.3	0.659
4	0.004	0.3	0.598
4	0.004	0.5	0.664
5	0.001	0.3	0.871
5	0.001	0.5	0.866
5	0.001	1	0.868
5	0.002	0.3	0.841
5	0.002	1	0.917
5	0.003	0.3	0.805
5	0.003	0.5	0.884
5	0.004	0.3	0.623
5	0.004	0.5	0.758
5	0.004	1	0.775
5	0.01	0.3	0.576

Table 5-2-Continued

5	0.01	0.5	0.582
5	0.01	1	0.551
5	0.02	0.3	0.472
5	0.02	0.5	0.546
5	0.02	1	0.541
6	0.001	0.3	0.907
6	0.002	0.3	0.95
6	0.004	0.3	0.761
6	0.001	0.5	0.913
6	0.002	0.5	0.97
6	0.004	0.5	0.975
6	0.001	1	0.856
6	0.002	1	0.881
6	0.004	1	0.903
6	0.01	0.5	0.712
6	0.02	0.5	0.7
6	0.01	1	0.727
6	0.02	1	0.791
8	0.001	0.3	0.829
8	0.002	1	0.932
8	0.002	0.3	0.925
8	0.004	0.3	0.955
8	0.004	0.5	0.944

Table 5-2-Continued

8	0.004	1	0.92
8	0.01	0.3	0.776
8	0.01	0.5	0.78
8	0.01	1	0.731
10	0.002	0.3	0.868
10	0.002	0.5	0.758
10	0.002	1	0.81
10	0.001	0.3	0.651
10	0.001	0.5	0.698
10	0.001	1	0.61
10	0.004	0.3	0.775
10	0.004	0.5	0.709
10	0.004	1	0.792

In this study, OpenFOAM 19.6 was utilized to solve the Navier stokes equation using Finite Volume Method. The Pressure-Implicit with splitting of operators has been used for pressure-velocity decoupling of N-S equation. The time derivative is discretized based on backward divergence. The standard second-order central differencing has been used to discretize the diffusive terms except for the kinetic energy k that is discretized using cell-Limited Gauss Linear [78]. Convection terms of N-S equation are also discretized using Gauss Linear-Upwind Stabilized Transport method via the function called Gauss limited Linear [79] in OpenFOAM and based on Total Variation Diminishing (TVD) [80].

Figure 5-2-a and Figure 5-2-b shows the vorticity magnitude contour of the flow over the airfoil in two different cases including (a) unactuated (when travelling wave surface is ignored) and (b) controlled one with travelling wave method. Figure 5-2-c also confirms the effectiveness of travelling wave in pressure recovery over the airfoil near leading edge. The contours show the success of travelling wave on substantial suppression of separation, characterized by large, chaotic vortex structures over the suction surface. This flow pattern in Figure 5-2-a shows a high degree of turbulency over the airfoil with a strong low-pressure detachment from the suction surface, which typically happens over the unactuated airfoil in stall angle of attack. As also shown in Figure 5-2-c, the pressure distribution over the suction surface is plateau, and has been stretched from the near-region of leading edge toward the trailing edge which is sign of a significant separation [54]. This large eddies and swirling flows over the suction surface implies inefficient aerodynamic forces. In contrast, Figure 5-2-b illustrates the airfoil with travelling wave with amplitude of $a = 0.005$, wavelength of $\lambda = 0.3$ and frequency of $f = 2$. As seen, implementing travelling wave over the suction surface reduced the size and power of turbulent structures which generates smoother flow pattern. The more streamlined flow which is shown in Figure 5-2-b enhance aerodynamic efficiency, meaning reducing drag and increasing lift. Also, the pressure curve in Figure 5-2-c shows a gradual decrease of pressure from the near-region of leading edge toward the trailing edge.

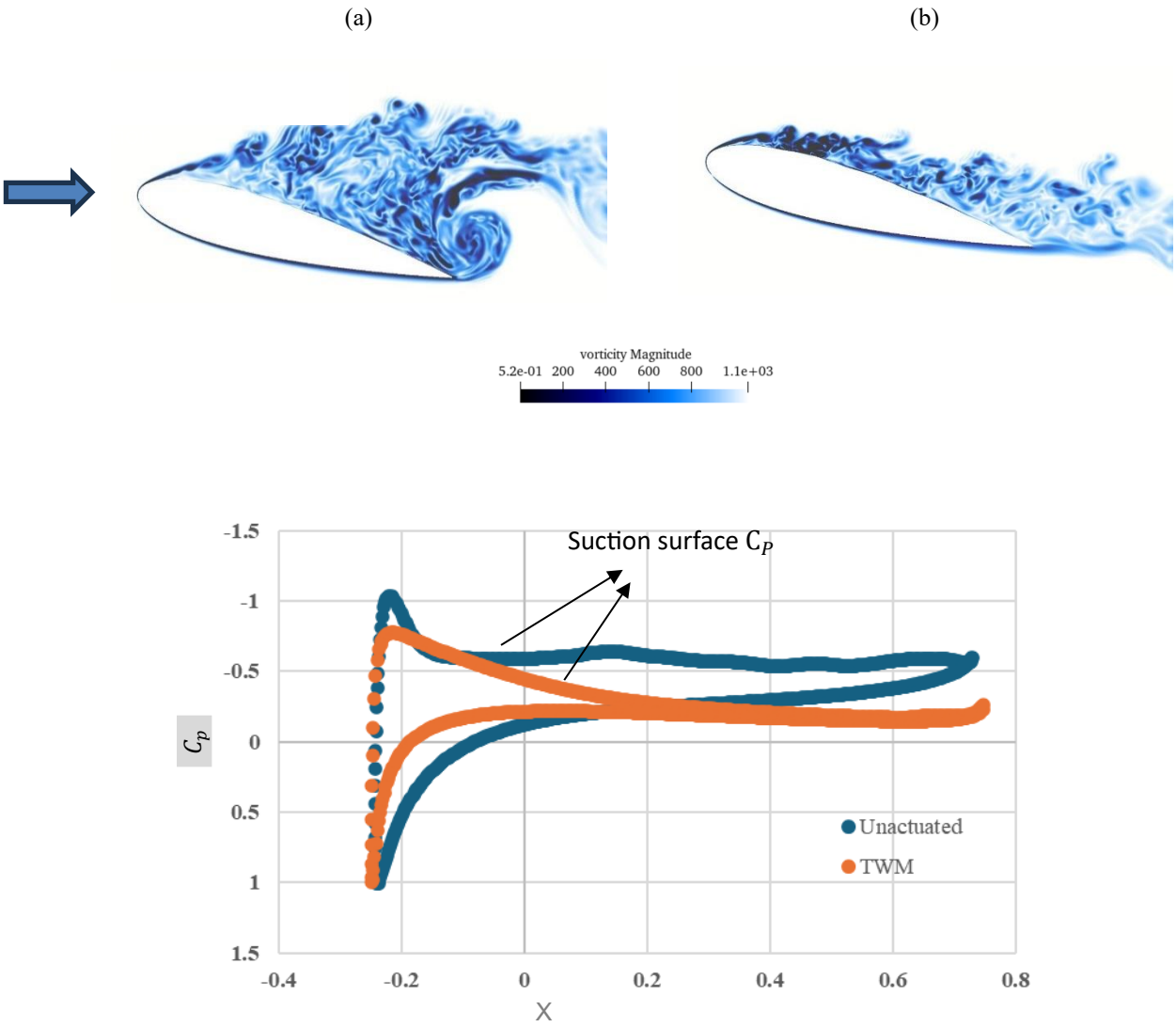

Figure 5-2- Comparison of vorticity magnitude over(a) an unactuated NACA0018 airfoil and (b) one with a traveling wave, (c) showing the pressure coefficient over the surface in turbulent flow at a Reynolds number of 20,000 and an angle of attack of 15 degrees.

5.2.2 Challenges and Computational time in CFD.

In OpenFOAM, the discretization of the time derivative with backward divergence requires the solver to compute large linear systems at every time step, dramatically increasing the computational cost. The discretization of the diffusional and convective items was used for calculation by the standard second-order central differencing and Gauss linear-upwind stabilized transport methods, the latter of which was supplemented with total variation diminishing properties to preserve solution boundedness and stability. This high degree of

detailed data analysis necessitates not just significant knowledge of fluid mechanics and numerical methods but also significant computational resources and constant adjustments to the calculation settings for each new parametric case, including simulations where the airfoil wave parametric vary. Nevertheless, while machine learning methods may make forecasts faster than such CFD methods after their initial training phase, they can even be generalized to new situations based on an accreditable dataset. Once trained with a sufficient and accurate dataset, the cost of training these models should not exceed the constant application of this CFD simulator. Furthermore, the most important factor in machine learning-based estimation validity is a detailed understanding of the training data's comprehensiveness and quality.

5.2.3 Machine Learning Models

In the following, we list a short definition of machine learning models used to enhance the accuracy of predicting the relationship between drag, lift, and wave parameters including wavelength, frequency and amplitude. While we avoid dip into the mathematical formulations and their parameters—since this work does not focus on developing or assessing these models—we aim to highlight their practical applications in our fluid dynamics problem with focus on flow control over an airfoil using the morphing surface.

5.2.3.1 Gaussian Process Regression (GPR)

Gaussian process regression is one of the Bayesian nonparametric methods, offering an approach to quantify uncertainties in predictions [143]. Its flexibility and non-parametric nature allow for effective handling of high-dimensional spaces through metamodels and sequential GPR (seqGPR), progressively refining predictions as more data becomes available. Key equations, e.g. the covariance function or kernel to measure similarity of any two elements,

are part of the GPR's mathematical foundation. The square exponential kernel is one of the most common used kernels [131,144]:

$$k(x, x') = \sigma_f^2 \exp\left(-\frac{(x - x')^2}{2l^2}\right) \quad \text{(Equation 5-7)}$$

Here x and x' are two points in the input space, σ_f^2 is the variance parameter (signal variance), and l is the length scale, dictating how quickly the correlation between points decreases with distance [144]. Another main equation in GPR is the prediction of a new point x_* is defined as:

$$y_*|x_*, X, y \sim \mathcal{N}(\mu_*, \sigma_*^2) \quad \text{(Equation 5-8)}$$

where $\mu_*$and σ_*^2 are the mean and variance of the predictive distribution of the new point, y_* trained on the training data X and the observations y.

5.2.3.2 Least Squares Boosting (LSBOOST)

LSBoost (Least Squares Boosting) is a powerful regression ensemble technique designed to reduce the mean-squared error (MSE) by iteratively fitting new models to the residuals of all previously combined models [134,145]. To correct the prediction based on a cumulative error made by an Ensemble up to this point, LSBoost introduces a new learner at each step. This strategy increases the accuracy of the prediction since it puts more concentration on cases which are difficult to anticipate. When the desired number of learner has been reached, this model is successfully finished. LSBoost's ability to adaptively improve the ensembles lies at the core of its effectiveness. It is particularly suited for performing complex regression tasks where accuracy of predictions is crucial [134]. Foe more technical details and parameters used in this model, one might see [146,147].

5.2.3.3 Support Vector Machines (SVM)

A wide range of frameworks have been reported in machine learning algorithms to address tasks such as classification, regression, and anomaly detection. Among these, Support Vector Machines (SVM) stand out as a powerful set of supervised learning methods [148]. . In 1995, Vapnik et al.'s [132] developed the details of *support-vector network*, providing a robust method to evaluate and model data points. In this study, SVMs are employed to model the nonlinear relationship between the traveling wave parameters (frequency, amplitude, and wavelength) and the resulting drag and lift coefficients.

The fundamental model of SVM relies on the construction of a model, which is profoundly dependent on subsets of training data, in particular those that are outside defined margins. This selective sensitivity ensures that the precise placement of training data points does not affect the cost function of a model. Either a 'soft margin' or a 'hard margin' approach may be used for this optimization [149]. The soft margin method allows for some misclassifications in order to achieve more flexibility of the model, whereas a harder margin approach applies stricter criteria and allows no error in classification error of the training database. The users of SVM believes a different approach using Kernel function as it generates higher dimensional space from single input data. It also empowers SVM to deal with more complex and nonlinear trends without any explicit computation of transforming space’s dimensions. Linear, polynomial, Basis Sigmoid, and Radial Basis Function (RBF) kernels [150,151] are the most shared functions among the users so far. In order to model turbulent flow, this study uses a hybrid function including polynomials and RBF. By combining the strengths of polynomial and RBF kernels, the hybrid function can effectively model both local and global patterns in the data, leading to improved prediction accuracy and generalization performance [152].

5.2.3.4 Decision tree

In order to increase the homogeneity of subsets regarding a target variable, an algorithm based on decision tree improves dataset division in a systematic way using conditions. In order to ensure efficient and reliable data separation, this process uses methods such as the Gini Index for Binary Classification and Rectification of Variables with Continuous Characteristics [153,154]. Its popularity in the machine learning era is attributed to its straightforwardness, interpretability, and versatility in handling different datasets. However, a significant challenge associated with decision trees is their susceptibility to overfitting, which might restrict their prediction accuracy. In the context of predicting drag and lift coefficients, overfitting can occur when a decision tree becomes overly complex and fits the training data too closely, leading to poor performance on unseen data.

To explain easily this method, decision trees are a methodology based on the treelike structure, in which each path from one root node contains a set of data dividing sequences that leads to a series of linear outcomes at leaf nodes. This model organizes knowledge by dividing data based on decision points, which are represented as nodes in the tree. Each node corresponds to a specific attribute or feature of the data, and the decision made at that node determines the next path to follow [133,155]. As the data progresses through these nodes, it is systematically evaluated, and the classification outcome is determined when the data reaches the leaf nodes. Leaf nodes represent the final classification, where each path through the tree ultimately leads to a specific category or decision.

5.2.3.5 Parrot optimizer (PO)

Parrot Optimizer (PO) is a novel swarm intelligence algorithm inspired by the behavior of domesticated Pyrrhura Molinae parrots introduced by Lian et al [156]. This optimizer mimics four key behaviors observed in these parrots: foraging, staying, communicating, and exhibiting fear of strangers to enhance the balance of exploration and exploitation while searching for optimal solutions. Foraging behavior allows solutions to explore the search space efficiently by making large and small jumps modeled using Lévy flight. The staying behavior helps maintain diversity within the population by randomly perching solutions in different areas. Communication behavior enables information sharing among solutions, fostering convergence towards the best solutions. The natural fear of strangers, a common trait among birds, ensures that solutions avoid suboptimal regions and reorient towards more promising areas, enhancing the overall search process. The Parrot Optimizer is distinguished by its unique integration of these behaviors, allowing each solution in the population to exhibit any behavior in each iteration randomly. The PO algorithm combines exploration and exploitation phases within each iteration, creating a more adaptive and robust search mechanism, while the traditional optimization algorithms separate these phases. This randomness in behavior enhances population diversity and mitigates the risk of the algorithm getting trapped in local optima. The algorithm can effectively navigate complex, high-dimensional optimization problems, balancing local and global search efforts [156] .

5.3 Model development.

In this study, four standalone models (GPR, SVM, DT, and LSB) predicted the collected data for drag and lift dataset. Also, novel hybrid models based on the PO algorithm (PO-GPR, PO-SVM, PO-DT, and PO-LSB) were employed to predict drag and lift, as shown in Figure 5-3.

The figure presents the framework for developing the proposed ML models in predicting aerodynamic drag and lift coefficients for a NACA 0018 airfoil. The predicting process includes data collection, processing, model development, and result analysis and visualization. The employed databases were created as described in section 2.1 that their aerodynamic features are frequency, amplitude, and wavelength of the traveling wave actuators. The subsequent step involves data preprocessing and model training using a 5-fold cross-validation method to provide a more reliable assessment of the machine learning model's performance [157]. The dataset is divided into five equal subsets, with each subgroup taking turns as the test set while the remaining subsets are used as training data. Then, data normalization is performed to standardize the features, followed by applying standalone (GPR, SVM, DT, LSB) and hybrid models (PO-GPR, PO-SVM, PO-DT, PO-LSB). The standalone models are selected for their various capabilities in handling non-linear relationships and regression tasks. Each model is initially trained using the prepared subsets of data. The PO algorithm is utilized to determine the optimal parameters for each standalone model. This optimization step is essential for improving model performance by fine-tuning hyperparameters, such as the kernel functions for GPR and SVM, or the number of learning cycles for LSB. The main parameters of the four models and their best values were obtained using PO, depicted in Table 5-3. In the last step, the models are evaluated using a range of statistical metrics, including Mean Absolute Error (MAE), Mean Squared Error (MSE), Root Mean Square Error (RMSE), and the coefficient of determination (R). Also, the results are visualized using scatter plots, Taylor diagrams, violin, and box plots.

In this paper, PO was utilized to obtain the optimal parameters for GPR, SVM, DT, and LSB, as these models rely on the value of their parameters. For instance, the main parameters of LSB are the number of ensembles learning cycles, the maximum number of depths, the minimum

number of leaf node observations, and the learning rate. The parameters of four models and their best value were obtained using PO, depicted in Table 5-3.

Table 5-3. The best solutions using PO in the fundamental parameters for different models.

Models	Parameters	Range
PO-GPR	Kernel function	{"exponential", "squared exponential", "rational quadratic"}
	Sigma	[1, 10]
	Basis function	{"none", "linear", "pureQuadratic"}
	Fitness method	{“exact GP”, “ Subset of data points approximation”, “Subset of regressors approximation”, “Fully independent conditional approximation”}
PO-SVM	Kernel function	{"RBF", "linear", "polynomial"}
	Epsilon	[0.001, 20]
	Kernel scale	[1, 10]
PO-DT	Minimum number of leaves	[1, 30]
	Maximum number of splits	[1, 100]
	Minimum size of parent	[1, 100]
PO-LSB	Maximum number of splits	[1, 100]
	Minimum size of leaves	[1, 30]
	Learning rate	(0, 1]
	Number of learning cycles	[2, 50]

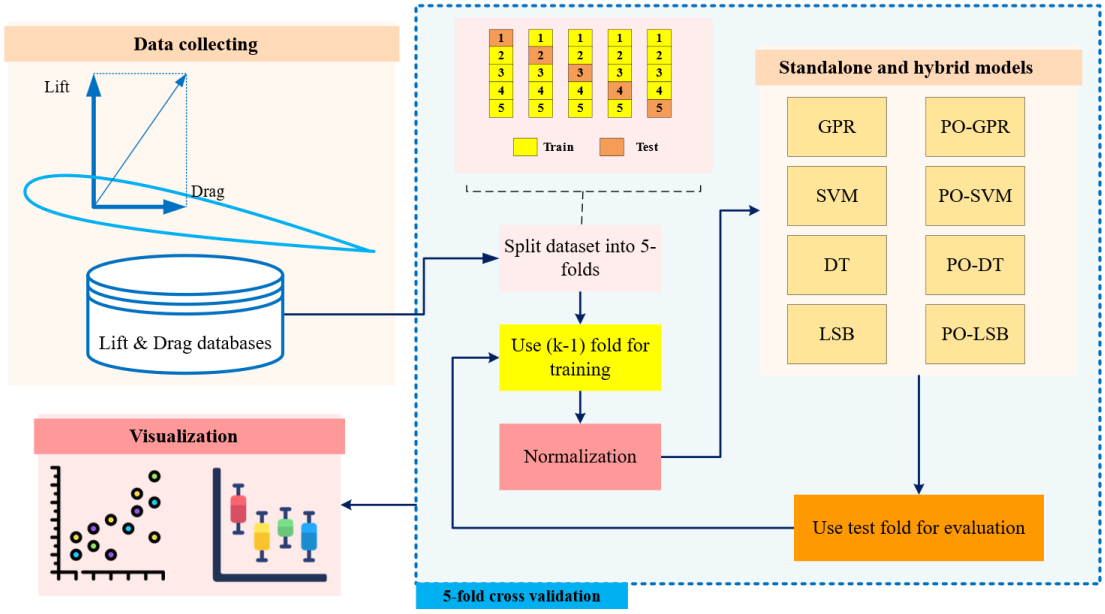

Figure 5-3. block Diagram for the proposed prediction model.

5.4 Results and discussion

The accuracy of the standalone and hybrid models for drag and lift prediction was evaluated using four statistical metrics: mean absolute error (MAE), root mean square error (RMSE), and coefficient of determination (R). The metrics calculated as follows:

$$MAE = \frac{\sum_{i=1}^{N}|Val_{p,i} - Val_{o,i}|}{N} \quad (9)$$

$$MSE = \frac{\sum_{i=1}^{N}(Val_{p,i} - Val_{o,i})^2}{N} \quad (10)$$

$$RMSE = \sqrt{\frac{\sum_{i=1}^{N}(Val_{p,i} - Val_{o,i})^2}{N}} \quad (11)$$

$$R = \frac{\sum_{i=1}^{N}(Val_{o,i} - \overline{Val_o}).(Val_{p,i} - \overline{Val_p})}{\sqrt{\sum_{i=1}^{N}(Val_{o,i} - \overline{Val_o})^2 . \sum_{i=1}^{N}(Val_{p,i} - \overline{Val_p})^2}} \quad (12)$$

Where $Val_{p,i}$ and $Val_{o,i}$ are the ith predicted and observed drag and lift values, respectively. $\overline{Val_o}$ and $\overline{Val_p}$ denoted the average value of observed and predicted drag and lift data,

respectively. The lowest values of MAE, MSE, RMSE, and the highest R indicate the better accuracy of any models that are used for the drag and lift estimation. Thus, comparing these metrics in Table 5-4 provides us with a comprehensive view of the minimum errors which are accompanied by the maximum R.

Table 5-4. Values of evaluation metrics for drag and lift prediction.

Output	Model	MAE	MSE	RMSE	R
Drag	**GPR**	0.0146	0.0004	0.0191	0.8079
	SVM	0.0134	0.0004	0.0191	0.8184
	DT	0.0134	0.0004	0.0191	0.8184
	LSB	0.0127	0.0003	0.0178	0.8408
	PO-GPR	0.0105	0.0002	0.0146	0.8947
	PO-SVM	0.0162	0.0004	0.0204	0.8195
	PO-DT	0.0124	0.0003	0.0164	0.8628
	PO-LSB	0.0143	0.0004	0.0211	0.8144
Lift	**GPR**	0.099	0.015	0.123	0.6481
	SVM	0.109	0.018	0.135	0.5645
	DT	0.109	0.018	0.135	0.5645
	LSB	0.073	0.012	0.111	0.7463
	PO-GPR	0.068	0.009	0.095	0.8112
	PO-SVM	0.08	0.01	0.1	0.7962
	PO-DT	0.078	0.011	0.107	0.7547
	PO-LSB	0.071	0.011	0.106	0.7962

Based on Table 5-4, For the drag coefficient section, the integration of PO by any methods

results in lowering the MAE and MSE which means the drags predicted by PO-ones are averagely closer to the observed values. In addition, the RMSE has been considerably decreased by adding the Parrot Optimizer to the models' algorithms which shows a decreased alterability in its prediction errors, making it the most consistent among the compared models. Also, the R factor is maximum for the PO-based models, which indicates a stronger correlation between the predicted and observed values. Particularly, PO-DT shows better performance than DT which means better match between observed and predicted drag values.

Similarly, for the lift coefficient, PO-optimized related numbers imply better performance than the case that pure models are utilized. The lowest values of MAE and RMSE confirm the PO-GPR accuracy and its superior consistency. Although the R in lift section is lower compared with the drag one, the PO-GPR stands out as the most effective model in improvement of the metrics.

Bringing PO into the discussion of the influence on these models, it can be argued that it indeed fine-tunes the predicting capabilities of the machine learning models used in fluid dynamics applications. It seems that PO-optimized models help to find the optimal parameter space and, perhaps, facilitate better feature selection, which results in more accurate and reliable predictions. However, not all models and output metrics show improvement, indicating that the influence of the Parrot Optimizer (PO) on the models is complex. While PO seems to fine-tune the predictive capabilities of the machine learning models by helping identify the optimal parameter space and potentially improving feature selection, the effectiveness of PO varies depending on the model. This suggests a nuanced interaction between the optimizer and the inherent strengths and limitations of each individual model. Particularly, the increase in RMSE for drag predictions for PO-SVM may entail a risk and hint that the PO may not be beneficial in all types of models, in all situations. Nonetheless, the overall effect of PO on the machine learning models appears to have improved their predictive accuracy. . Hence, the ability to

develop the aerodynamic characteristics with improved yet not perfect accuracy can tremendously benefit the domain of computational fluid dynamics.*Figure* 5-4 shows the correlation matrices of both drag and lift coefficients as the function of wave parameters, including frequency, amplitude and wavelength. These matrices give an insight about the percentage of the effects of each wave parameters on hydrodynamic forces. The negative values imply that a wave parameter causes an inverse effect, whereas the positive values indicate direct correlation.

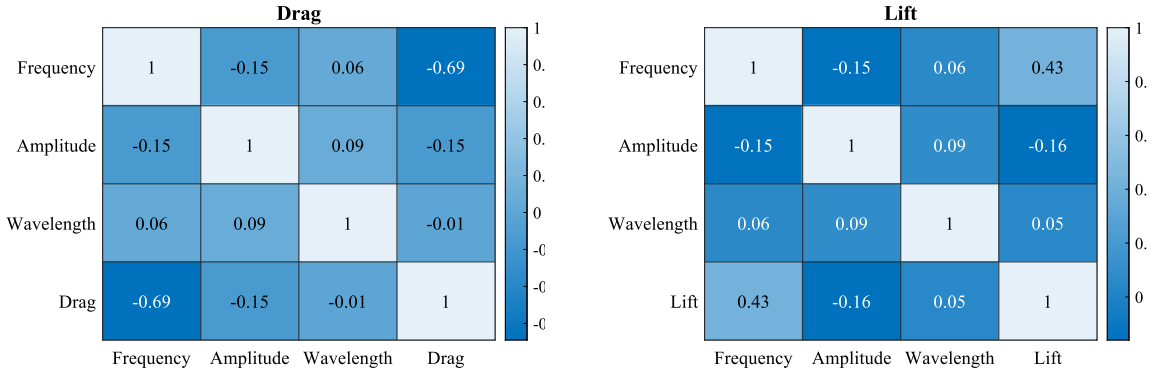

(a) (b)

Figure 5-4. correlation matrices for (a) drag and (b) lift coefficients indicating the correlation between input and output variables.

Figure 5-4-a is the drag matrix that shows a strong negative correlation (-0.69) between drag and frequency of the wave. This implies that increasing the frequency of the wave causes a decrease in drag coefficient. This type of correlation stems from the changes in the flow characteristics around the airfoil, such as reduced flow separation or a shift in the boundary layer behavior as the frequency increases [54]. In fact, frequency either postpones the flow separation or eliminates the strong flow recirculation over the airfoil which is the main reason of high drag pressure. Higher frequencies energize the boundary layer, promoting reattachment by preventing adverse pressure gradients from causing early separation. It is worth mentioning that frequency causes boundary layer to remain attached to the airfoil or to reattach quickly

after small separation. This matrix also demonstrates a weaker negative relationship between amplitude and drag coefficients equal to -0.15. The weaker negative effect of amplitude on drag change is attributed to the less contribution of amplitude enlargement in energy excitement over the airfoil [15]. While larger amplitude introduces more disturbances in the flow, without frequent input of energy (by increasing the frequency) does not always result in reattaching the flow to the airfoil surface. The wavelength effect on drag coefficient is almost negligible (-0.01). Unlike frequency, which represents the rate of momentum injection into the flow per unit time, wavelength affects the physical length of these oscillations. With longer wavelengths, any given point on the airfoil surface senses less frequent change in hydrodynamic forces over time, reducing the potential for these changes to consistently affect the boundary layer and, consequently, the drag [42]. Also, drag coefficient is sum of pressure and viscous drag applied all around the airfoil. Pressure drag is influenced by the large-scale flow separation whereas viscous drag (skin friction drag) is affected by the behavior of the boundary layer in each local point of the airfoil surface. Changes in wavelength decrease the skin friction drag whereas increases the pressure drag, peaking at the same wavelength [158].

Analyzing the lift matrix in Figure 5-4-b shows that there is a moderate positive correlation (0.43) between the lift coefficient and frequency of the wave. This value implies frequency increment leads to the lift enhancement over the NACA-0018 airfoil. Just like the drag coefficient, the lift enhancement is due to the energized boundary layer as the result of frequent oscillation of the suction surface. In fact, a greater portion of the airfoil surface experiences attached flow which enhances the lift coefficient. Amplitude and lift have a slightly negative correlation (-0.16), indicating that larger amplitude of the wave marginally reduces the lift coefficient. This relationship stems from increasing the flow instabilities due to the sharp steepness of the wave, leading to changes in pressure distribution over the airfoil. In fact, instabilities make small scale vortices over the airfoil which can be considered as the small

separations which generate downward forces, opposite to the positive lift direction. Finally, like the drag matrix, wavelength shows a very weak correlation with lift coefficient so that its value is 0.05.

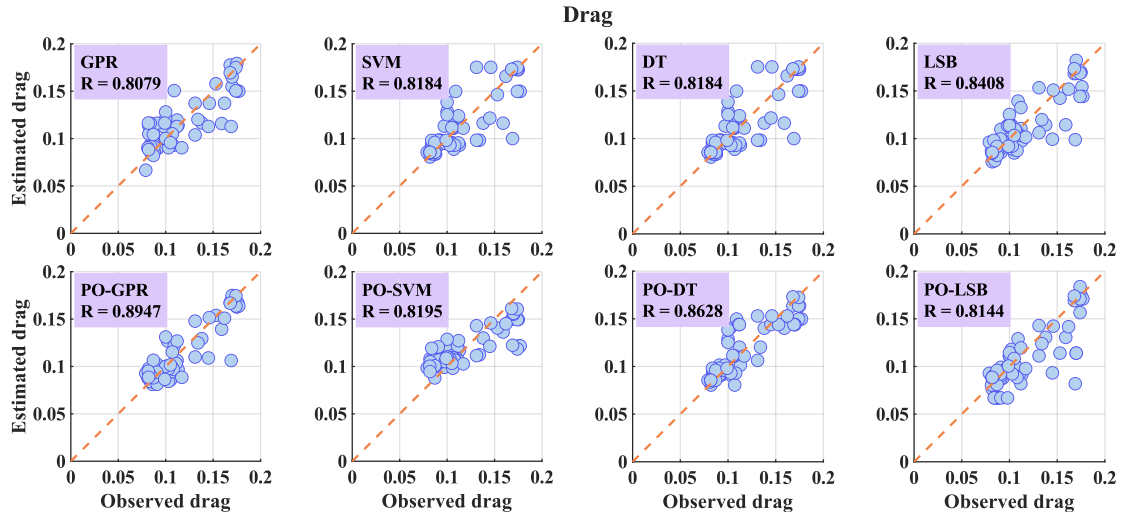

Figure 5-5 scatter plots of the observed and estimated drag using the standalone and hybrid machine learning models.

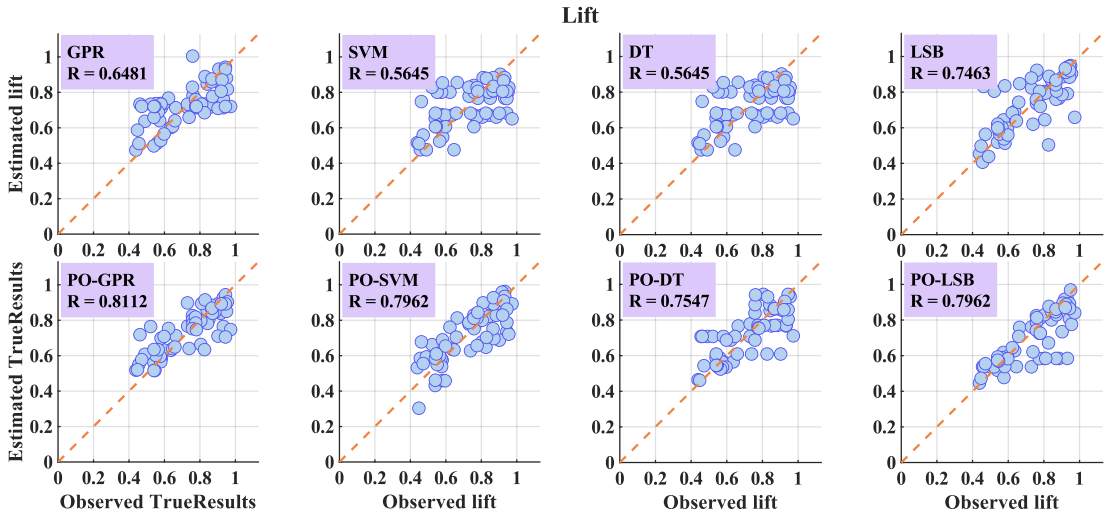

Figure 5-6. scatter plots of the observed and estimated lift using the standalone and hybrid machine learning models.

Figure 5-5 and Figure 5-6 compare observations and estimated drag and lift coefficients with different standalone and hybrid machine learning models. Focusing on these data and *R* value in each plot demonstrate the performance of each model. Considering scatter drag plots, as shown in Figure 5-5, a comparison between observed and estimated values from models

without PO (GPR, SVM, DT, LSB) and with PO (PO-GPR, PO-SVM, PO-DT, PO-LSB) has been demonstrated. The closer the blue points (the predicted values) are to the diagonal line, the more accurate the machine learning is. The PO-models lie tighter clustering around the diagonal line which shows their superior performance in prediction drag values. This plot again confirms a particular performance of the PO-GPR model, which aligns with the earlier observation in Table 5-4, with the highest R value.

For lift scatter plot, as shown in Figure 5-6, a similar pattern emerges. Comparing the standard machine learning models, the PO-enhanced ones show an improvement over them, particularly the PO-GPR model. Although the enhancement in R values for lift prediction is less remarkable than for drag, the improvement in prediction accuracy is still apparent for models employing PO.

In summary, to understand why the machine learning models are more effective for the drag than for the lift, it is necessary to consider that the angle of attack, the shape of the airfoil, and flow speed have a greater impact on lift than on drag. Compared with drag, the lift force is more sensitive to changes in these parameters. The lift amount is mainly the differences in pressure across the surface of the airfoil, which are strongly affected by flow separation and vortex formation. Thus, small changes in solid and fluid structures have a stronger impact on lift coefficient. In addition, non-linear dependency of the lift coefficients may be related to the measurement and simulation data used for training machine learning models. In other words, variabilities in wave parameters such as frequency, wavelength, and amplitude can generate small perturbations in the flow field, which in turn create additional sensitivity in the lift parameters. This variability makes it more difficult for any model, even when enhanced with optimization techniques like PO, to achieve a dramatic improvement in prediction accuracy.

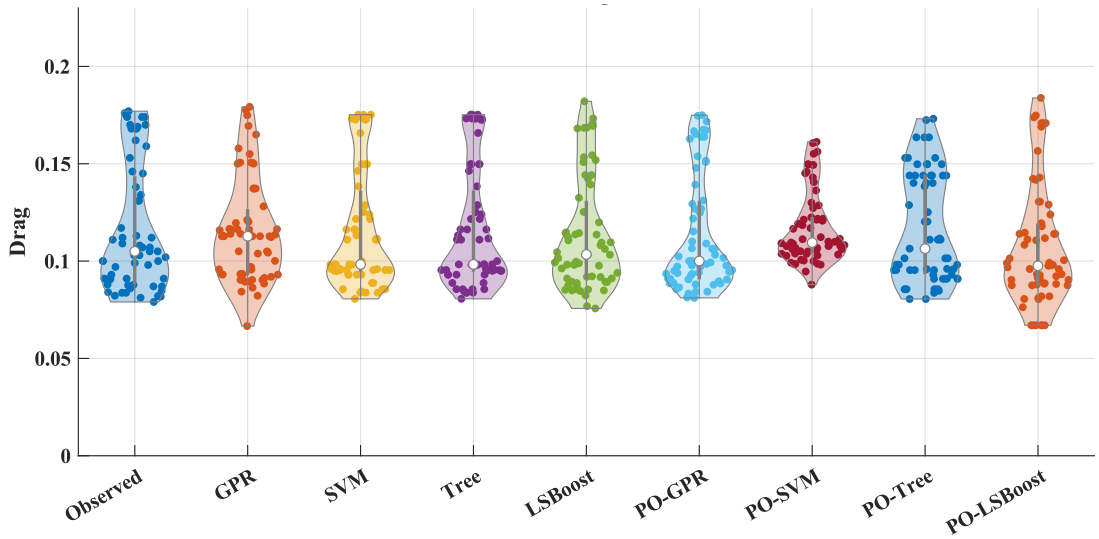

Figure 5-7 violin of the observed and estimated drag using the standalone and hybrid machine learning models.

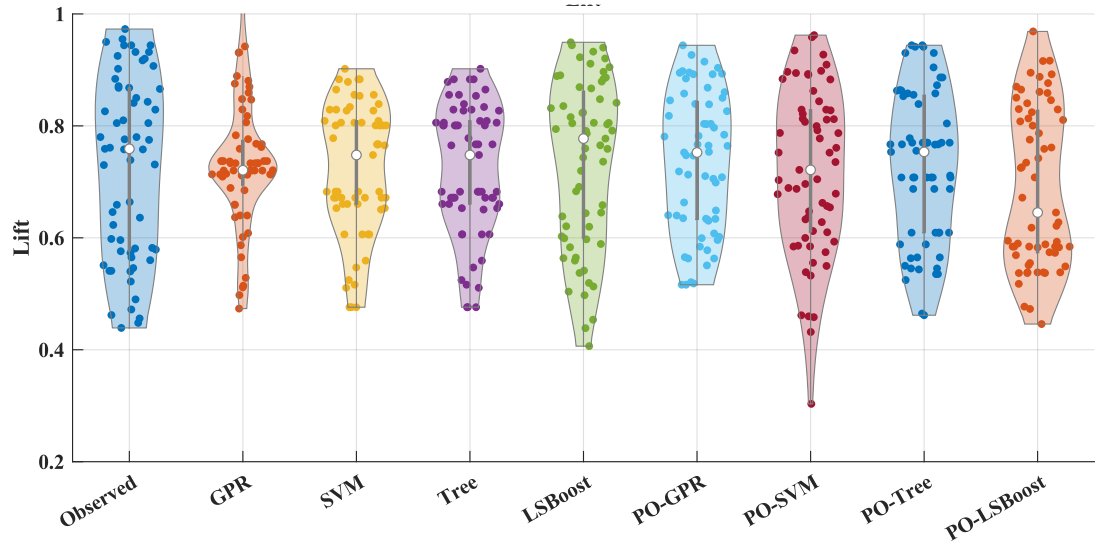

Figure 5-8. violin plots of the observed and estimated lift using the standalone and hybrid machine learning models.

The violin plots depicted in the Figure 5-7 and Figure 5-8 provide a detailed comparison of the distribution of predicted versus observed values for drag and lift coefficients across various machine learning models, both standalone and those enhanced with the Parrot Optimizer (PO). These visualizations allow for a nuanced assessment of each model's prediction accuracy, distribution width, and central tendency relative to the actual observed measurements.

In the drag prediction models, see Figure 5-7, the observed data's violin plot shows a compact and consistently shaped distribution, setting a benchmark for the machine learning models' predictive performances. Among the standalone models-GPR, SVM, DT, and LSB-none perfectly mirrors the observed distribution. For instance, the SVM model exhibits a slightly wider spread, suggesting some deviation in the accuracy and perhaps higher variability in predictions. On the other hand, the GPR model shows a more condensed distribution but still does not align perfectly with the observed data's central peak.

Upon introducing the Parrot Optimizer to these models, there is a visible shift towards narrower distributions that more closely approximate the observed data's shape and spread. Notably, PO-GPR and PO-DT display tighter distributions that are more aligned with the observed values. This indicates that the optimizer not only refines the accuracy of the predictions but also reduces the variability, making the predictions more consistent across different data points.

Turning to the lift prediction models, Figure 5-8, the observed lift's distribution is broader than that of drag, indicating inherent variability in lift measurements. This variability could stem from the complex interactions between the airfoil and fluid dynamics, which are more sensitive to changes in operational conditions than drag measurements. The standalone models for lift, such as GPR and DT, show broader distributions, reflecting challenges in accurately capturing these dynamics.

The application of PO to the lift models results in a noticeable improvement in prediction accuracy and consistency. The PO-enhanced models, particularly PO-GPR and PO-LSB, exhibit distributions that are significantly narrower and more closely resemble the observed lift distribution. This improvement suggests that PO effectively handles the modeling complexities associated with lift, possibly by optimizing parameters that are crucial for capturing the non-linear dynamics of lift generation.

These observations underscore the effectiveness of the Parrot Optimizer in enhancing the predictive performance of machine learning models used in fluid dynamics. By narrowing the distribution of predicted values and aligning them more closely with the observed data, PO demonstrates its capacity to fine-tune models to handle the intricate and sensitive nature of aerodynamic force predictions. This analysis not only highlights the optimizer's role in improving model reliability but also points towards its potential to facilitate more precise engineering designs and simulations in aerodynamics.

Figure 5-9 and Figure 5-10 show a box plot illustrating the similarities between observed and estimated drag and lift coefficients using different machine learning methods. The horizontal red line inside the box indicates the median of the values estimated by each model. It shows the tendency of the data, especially in skewed distributions, since it is not affected by extreme values. The top and bottom edges of blue box indicate the third quartile (Q3) and the first quartile (Q1), respectively. These quartiles are very useful in understanding distribution and skewness of data around the median. The Interquartile Range (IQR), which is the distance between Q1 and Q3, indicates the variability in the middle half of the data set. The narrower box suggests more consistent predictions than the wider ones. And Whiskers (Vertical dashed lines extending from the Box) provide an overall view about the range of data, excluding outliers which are shown in red lines. These are data points that lie beyond the whiskers, typically defined as being 1.5 times the IQR above the third quartile or below the first quartile. To determine which method has the best performance in comparison to the observed data in the box plot, we examine a few characteristics: the closeness of the median calculated by each model to that of observed one, the matching of IQR and presence of outliers.

or the drag plot shown in Figure 9, comparing the medians reveals that the PO-Tree method, with a median of 0.104, and the LSBoost method, with a median of 0.107, have the closest medians to the observed data's median of 0.105. This indicates that both methods produce drag

predictions that are more closely aligned with the actual observed values compared to the other models. . These two methods of PO-Tree and LSBoost not only have the closest medians, but also show the most similar compactness, notch, and IQR. The PO-Tree generates fewer outliers and a more compressed range, indicating it might be missing some of the variability in the observed data but is more stable in their predictions.

The observed box in the lift box plot, as shown in Figure 5-10, also demonstrates the actual distribution of the lift coefficient. The observed box has a median of 0.758, bottom edge of 0.575 and top edge of 0.868. This setup shows a relatively symmetric distribution with a insignificant skew towards higher values. Upon a close inspection, PO-tree results show the best similarities to the observed box plot. This performance is in terms of median alignments which is 0.755, overall distribution along with the notch shape, and capturing the outlier lift values.

Overall, in evaluating the machine learning models for prediction of drag and lift coefficient, The scatter plot and box plot reveal significant discrepancies despite the overall predictive ensemble predictivity. PO-Tree demonstrates optimal performance in the box plot analysis, meaning its capability to predict variations while considering the outliers. On the other hand, its performance in scatter plot analysis is less than that of PO-GPR, which claims the very highest R values, always corresponding to better correlation with the observed data. Therefore, the two models are inversely related – PO-Tree is less susceptible to exceptional outliers, whereas PO-GPR is most efficient in capturing complex linear correlations. Such a conclusion, in turn, argues for a highly appropriate approach to deciding on a predictive model. Hence, researchers using box plot analysis without evaluating the scatter plot might opt for the wrong model and vice versa.

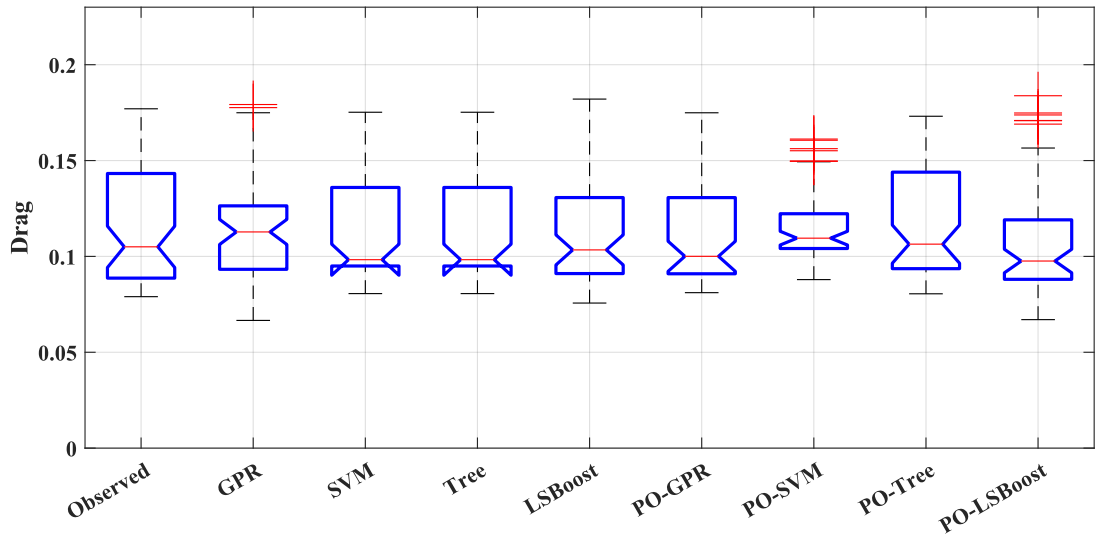

Figure 5-9. box plots of the observed and estimated drag using the standalone and hybrid machine learning models.

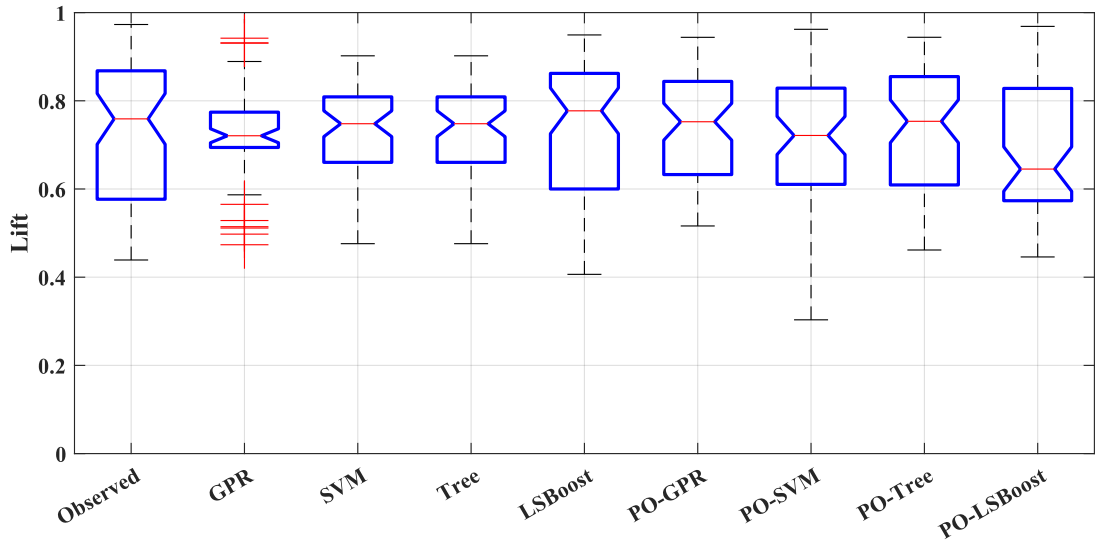

Figure 5-10. box plots of the observed and estimated lift using the standalone and hybrid machine learning models.

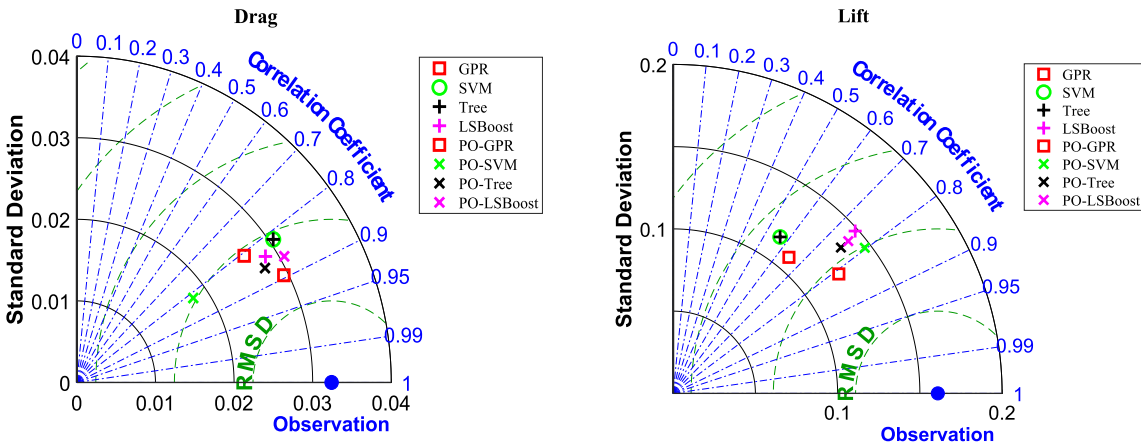

(a) (b)

Figure 5-11. Taylor diagrams of the observed and estimated (a) drag and (b) lift using the standalone and hybrid machine learning models.

Figure 5-11 shows the Taylor diagram of the results that graphically compares the accuracy of both standalone and hybrid machine learning models based on Standard Deviation (SD), correlation coefficient, and Root Mean Square Difference (RMSD) [159]. As illustrated in Figure 5-11-a, the black solid loops around the center point (0,0) demonstrate the standard deviation (SD) from the mean value of the data. The larger the radius of the loops, the more distributed the data is around the mean value. However, we are looking to choose a method that has the closest value to the observed data. Whereas PO-SVM shows the minimum SD (equals 0.017), it is more departed far from the SD for observed data which is 0.032. Thus, SDs for SVM (0.030), Tree (0.030), PO-LSBoost (0.030), and PO-GPR (0.029) are acceptable in comparison to that of observed data. The dashed green encircled the reference point depicts magnitude of the average error between observed and predicted values. Points lying on or close to a particular contour line have the same RMSD, indicating the level of error in the prediction relative to the observed data. Thus, in terms of RMSD, methods of PO-GPR, PO-Tree and PO-LSBoost are respectively the best prediction methods. To measure the accuracy of the methods in Taylor diagram in term of correlation coefficient, the angular position of the points relative to the reference point is considered. This ranges from 0 to 1 where 1 is observed data. The PO-

GPR gets the maximum value in this metric with the value of 0.9 which proves the best performance among the methods utilized in this research.

In lift diagram (Figure 5-11-b), SD for observed data gets the value of 0.160 which is closer to that of SVM (0.138) and LSBoost (0.145). In terms of RMSD, PO-GPR and PO-SVM show the best performance in generating the minimum errors compared to the observed data. They also showed the maximum correlation coefficients with the values of 0.80 for PO-SVM and 0.82 for PO-GPR. In conclusion, when identifying which models perform best overall against observed data, PO-GPR can be selected. The difference in metric of standard deviation for drag and lift in the case of using PO-SVM can be attributed to the inherent differences in the fluid dynamics of drag and lift forces, combined with the proficiencies and limits of the machine learning models. Learning the drag coefficients for PO-SVM is easier since drag is less variable and more predictable. In contrast, non-linear, complex and highly variable nature of lift forces makes a very large gap between the PO-SVM predictions and the observed data.

5.5 Limitations and recommendations

Certain constraints, e.g. a restricted set of parameters and concerns about model accuracy, are associated with this study. The range of the wave parameters used may affect the wider applicability of the results, and the model's lack of interpretation may hinder its practical application. In order to overcome these problems, subsequent research should broaden the range of parameters, gather more diverse data, investigate hybrid modeling approaches, perform sensitivity analyses, implement real time model monitoring systems and promote cross disciplinary cooperation so as to improve both accuracy and usability. Experimental validation should also be pursued to complement the numerical findings. Future experiments could involve fabricating the traveling wave mechanism using mechanical shafts to simulate the surface morphing. However, there are practical limitations to consider. The size of the airfoil

is constrained by the space required to house the wave-generating equipment, which could impact the experimental setup. Additionally, achieving the required wave frequencies in a wind tunnel to effectively control the flow poses a technical challenge. Addressing these limitations will be crucial for the successful experimental validation and practical implementation of the Traveling Wave Method.

5.6 Conclusion

This study has demonstrated the effectiveness of integrating machine learning techniques with computational fluid dynamics (CFD) methods to predict the drag and lift coefficients over a NACA-0018 airfoil subjected to travelling wave on the suction surface. A range of machine learning models have been implemented such as Gaussian Process Regression (GPR), Support Vector Machines (SVM), Decision Trees (DT), and Least Squares Boosting (LSBoost), and further optimized these models using the Parrot Optimizer (PO) to enhance prediction accuracy. The data set extracted from CFD simulation show that frequency had the strongest effect on both drag and lift coefficients, with higher frequencies generally reducing drag by energizing the boundary layer and postponing flow separation. The amplitude had a less pronounced negative effect on drag, while wavelength showed minimal impact. In the case of lift, frequency had a moderate positive correlation, suggesting that higher frequencies improve lift by promoting better flow attachment, while amplitude slightly reduced lift due to increased flow instability.

Through a comparison of evaluation metrics such as Mean Absolute Error (MAE), Root Mean Square Error (RMSE), and the coefficient of determination (R), we identified that the Parrot Optimizer significantly improved the performance of all models, particularly in terms of reducing the error for drag prediction. Among the models, the PO-GPR and PO-DT

configurations exhibited superior consistency and predictive accuracy, making them well-suited for capturing both local and global aerodynamic patterns.

While the machine learning models were effective in modeling drag, predicting lift proved to be more challenging due to its higher sensitivity to variations in wave parameters and fluid dynamics. The hybrid PO models still demonstrated improved accuracy for lift prediction but did not match the performance seen for drag. This highlights the complexity of modeling lift forces, which are influenced by non-linearities such as flow separation and vortex formation. Overall, this work illustrates the potential of machine learning models, particularly when optimized, to reduce computational costs and improve the accuracy of predictions in aerodynamic studies. By leveraging the power of machine learning, we can achieve faster, reliable solutions to problems that traditionally require significant computational resources. Future research could expand on this study by incorporating more extensive datasets, exploring additional wave parameters, and developing hybrid modeling frameworks to address the challenges in lift prediction more comprehensively. Moreover, integrating real-time optimization systems and cross-disciplinary approaches could further enhance the practical application of these methods in engineering design and simulation.

References

[1] Xiao T, Li Z, Deng S, Ang H, Zhou X. Numerical study on the flow characteristics of micro air vehicle wings at low Reynolds numbers. International Journal of Micro Air Vehicles 2016;8:29–40. https://doi.org/10.1177/1756829316638204.

[2] Li L. Experimental testing of low reynolds number airfoils for unmanned aerial vehicles. PhD Thesis. University of Toronto, 2013.

[3] Joshi SN, Gujarathi YS. A review on active and passive flow control techniques. International Journal on Recent Technologies in Mechanical and Electrical Engineering 2016;3:1–6.

[4] Jahanmiri M. Active flow control: a review 2010.

[5] Rosi GA, Zhu D, Gates ID, Wang J. Passive flow control devices—well design and physics of their different flow regimes: A review. Journal of Petroleum Science and Engineering 2022;218:110999.

[6] Kitsios V, Cordier L, Bonnet J-P, Ooi A, Soria J. On the coherent structures and stability properties of a leading-edge separated aerofoil with turbulent recirculation. Journal of Fluid Mechanics 2011;683:395–416.

[7] Altememe A, Myers OJ, Hall A. Preliminary design and computational fluid dynamic analysis of flapping wing of micro aerial vehicle for low Reynolds numbers regime. Int J Aeronaut Aerosp Eng 2019;1:36–45.

[8] Amiralaei MR, Alighanbari H, Hashemi SM. An investigation into the effects of unsteady parameters on the aerodynamics of a low Reynolds number pitching airfoil. Journal of Fluids and Structures 2010;26:979–93.

[9] Thake M, Packard N, Bonilla C, Bons J. Low Reynolds Number Laminar Airfoil with Active Flow Control. 5th Flow Control Conference, Chicago, Illinois: American Institute of Aeronautics and Astronautics; 2010. https://doi.org/10.2514/6.2010-4579.

[10] Fouatih OM, Medale M, Imine O, Imine B. Design optimization of the aerodynamic passive flow control on NACA 4415 airfoil using vortex generators. European Journal of Mechanics-B/Fluids 2016;56:82–96.

[11] Lee C, Hong G, Ha QP, Mallinson SG. A piezoelectrically actuated micro synthetic jet for active flow control. Sensors and Actuators A: Physical 2003;108:168–74.

[12] Genç MS, Koca K, Demir H, Açıkel HH. Traditional and new types of passive flow control techniques to pave the way for high maneuverability and low structural weight for UAVs and MAVs. Autonomous Vehicles 2020:131–60.

[13] Kral LD. Active flow control technology. ASME Fluids Engineering Technical Brief 2000:1–28.

[14] Collis SS, Joslin RD, Seifert A, Theofilis V. Issues in active flow control: theory, control, simulation, and experiment. Progress in Aerospace Sciences 2004;40:237–89.

[15] Akbarzadeh AM, Borazjani I. Controlling Flow Separation on a Thick Airfoil Using Backward Traveling Waves. AIAA Journal 2020;58:3799–807. https://doi.org/10.2514/1.J059428.

[16] Ogunka UE, Borazjani I. Effect of Wavelength on Traveling Wave Flow Control. AIAA SCITECH 2024 Forum, Orlando, FL: American Institute of Aeronautics and Astronautics; 2024. https://doi.org/10.2514/6.2024-0929.

[17] Li G, Wang J. Partial Oscillation Flow Control on Airfoil at Low Reynolds Numbers. Applied Sciences 2024;14:4762.

[18] Valdepeñas Pujol P. Active flow control on cambered airfoils at ultralow Reynolds using synthetic jets. B.S. thesis. Universitat Politècnica de Catalunya, 2017.

[19] Dai Q, Qi E, Huang S, Zhou Z, Wang Y. Research on Active Flow Control Method of NACA0012 Airfoil with Traveling Wave Structure. Journal of Applied Fluid Mechanics 2024;17:1293–305.
[20] Yao Y, Lu C, Si T, Zhu K. Experimental Investigation on the Drag Reduction Characteristics of Traveling Wavy Wall At High Reynolds Number in Wind Tunnel. J Hydrodyn 2010;22:719–24. https://doi.org/10.1016/S1001-6058(09)60108-6.
[21] Shen L, Zhang X, Yue DK, Triantafyllou MS. Turbulent flow over a flexible wall undergoing a streamwise travelling wave motion. Journal of Fluid Mechanics 2003;484:197–221.
[22] McLean D. Understanding aerodynamics: arguing from the real physics. John Wiley & Sons; 2012.
[23] Hassanalian M, Abdelkefi A. Classifications, applications, and design challenges of drones: A review. Progress in Aerospace Sciences 2017;91:99–131.
[24] Haider N, Shahzad A, Mumtaz Qadri MN, Ali Shah SI. Recent progress in flapping wings for micro aerial vehicle applications. Proceedings of the Institution of Mechanical Engineers, Part C: Journal of Mechanical Engineering Science 2021;235:245–64. https://doi.org/10.1177/0954406220917426.
[25] Jones G, Santer M, Papadakis G. Control of low Reynolds number flow around an airfoil using periodic surface morphing: A numerical study. Journal of Fluids and Structures 2018;76:95–115.
[26] Park YW, Lee S-G, Lee D-H, Hong S. Stall Control with Local Surface Buzzing on a NACA 0012 Airfoil. AIAA Journal 2001;39:1400–2. https://doi.org/10.2514/2.1460.
[27] Albers M, Meysonnat PS, Schröder W. Actively Reduced Airfoil Drag by Transversal Surface Waves. Flow Turbulence Combust 2019;102:865–86. https://doi.org/10.1007/s10494-018-9998-z.
[28] Calisch S, Gershenfeld N, Fan D, Jodin G, Triantafyllou M. Fabrication and characterization of folded foils supporting streamwise traveling waves. Journal of Fluids and Structures 2019;91:102563.
[29] Akbarzadeh A, Borazjani I, Ogunka U. The Role of Amplitude on Controlling Flow Separation Using Traveling Wave Morphing. AIAA Scitech 2021 Forum, VIRTUAL EVENT: American Institute of Aeronautics and Astronautics; 2021. https://doi.org/10.2514/6.2021-2005.
[30] Taneda S, Tomonari Y. An Experiment on the Flow around a Waving Plate. J Phys Soc Jpn 1974;36:1683–9. https://doi.org/10.1143/JPSJ.36.1683.
[31] Munday PM, Taira K. On the lock-on of vortex shedding to oscillatory actuation around a circular cylinder. Physics of Fluids 2013;25.
[32] Shyy W, Lian Y, Tang J, Viieru D, Liu H. Aerodynamics of low Reynolds number flyers. 2008.
[33] Sum Wu K, Nowak J, Breuer KS. Scaling of the performance of insect-inspired passive-pitching flapping wings. J R Soc Interface 2019;16:20190609. https://doi.org/10.1098/rsif.2019.0609.
[34] Uhlenbeck GE. The Mathematical Theory of Non-uniform Gases. By S. Chapman and T. G. Cowling. J Phys Chem 1941;45:876–7. https://doi.org/10.1021/j150410a017.
[35] Bhatnagar PL, Gross EP, Krook M. A Model for Collision Processes in Gases. I. Small Amplitude Processes in Charged and Neutral One-Component Systems. Phys Rev 1954;94:511–25. https://doi.org/10.1103/PhysRev.94.511.
[36] Afra B, Nazari M, Kayhani MH, Delouei AA, Ahmadi G. An immersed boundary-lattice Boltzmann method combined with a robust lattice spring model for solving flow–structure interaction problems. Applied Mathematical Modelling 2018;55:502–21.

[37] Wolfram S. Cellular automaton fluids 1: Basic theory. Lattice Gas Methods for Partial Differential Equations, CRC Press; 2019, p. 19–74.
[38] Afra B, Nazari M, Kayhani MH, Ahmadi G. Direct numerical simulation of freely falling particles by hybrid immersed boundary – Lattice Boltzmann – discrete element method. Particulate Science and Technology 2020;38:286–98. https://doi.org/10.1080/02726351.2018.1536092.
[39] Delouei AA, Nazari M, Kayhani MH, Kang SK, Succi S. Non-Newtonian particulate flow simulation: A direct-forcing immersed boundary–lattice Boltzmann approach. Physica A: Statistical Mechanics and Its Applications 2016;447:1–20.
[40] Mittal S, Tezduyar TE. Massively parallel finite element computation of incompressible flows involving fluid-body interactions. Computer Methods in Applied Mechanics and Engineering 1994;112:253–82.
[41] Gopalakrishnan Meena M, Taira K, Asai K. Airfoil-Wake Modification with Gurney Flap at Low Reynolds Number. AIAA Journal 2018;56:1348–59. https://doi.org/10.2514/1.J056260.
[42] V'Dovec T. Implementation of travelling waves on lifting surface for drag reduction. PhD Thesis. Massachusetts Institute of Technology, 2019.
[43] Li D, Zhao S, Da Ronch A, Xiang J, Drofelnik J, Li Y, et al. A review of modelling and analysis of morphing wings. Progress in Aerospace Sciences 2018;100:46–62.
[44] Chae EJ, Moosavian A, Pankonien AM, Inman DJ. A comparative study of a morphing wing. Smart Materials, Adaptive Structures and Intelligent Systems, vol. 58264, American Society of Mechanical Engineers; 2017, p. V002T03A020.
[45] Belobaba P, Cooper J, Langton R, Seabridge A. Morphing aerospace vehicles and structures. vol. 57. John Wiley & Sons; 2012.
[46] Vocke RD, Kothera CS, Woods BKS, Wereley NM. Development and Testing of a Span-Extending Morphing Wing. Journal of Intelligent Material Systems and Structures 2011;22:879–90. https://doi.org/10.1177/1045389X11411121.
[47] Kang W, Xu M, Yao W, Zhang J. Lock-in mechanism of flow over a low-Reynolds-number airfoil with morphing surface. Aerospace Science and Technology 2020;97:105647.
[48] Kumar RST, Sivakumar V, Ramakrishnananda B, Arjhun AK, Suriyapandiyan. Numerical investigation of two element camber morphing airfoil in low Reynolds number flows. Journal of Engineering Science and Technology 2017;12:1939–55.
[49] Bhayadia A, Olivett A, Singh T, Karami MA. Input shaping for travelling wave generation. Smart Materials and Structures 2022;31:055006.
[50] Olivett A, Corrao P, Karami MA. Flow control and separation delay in morphing wing aircraft using traveling wave actuation. Smart Materials and Structures 2021;30:025028.
[51] Olivett A, Corrao P, Karami MA. Flow control and separation delay in morphing wing aircraft using traveling wave actuation. Smart Materials and Structures 2021;30:025028.
[52] Shukla S, Thekkethil N, Sharma A, Agrawal A, Bhardwaj R. Hydrodynamics study on a traveling wave-based undulating surface of a hydrofoil in a free-stream flow. Phys Rev Fluids 2022;7:084703. https://doi.org/10.1103/PhysRevFluids.7.084703.
[53] Ogunka UE, Akbarzadeh A, Borazjani I. FLOW CONTROL with TRAVELING-WAVE SURFACE MORPHING at POST-STALL ANGLES of ATTACK. AIAA SCITECH 2022 Forum, San Diego, CA & Virtual: American Institute of Aeronautics and Astronautics; 2022. https://doi.org/10.2514/6.2022-1948.
[54] Akbarzadeh A, Borazjani I. A numerical study on controlling flow separation via surface morphing in the form of backward traveling waves. AIAA Aviation 2019

Forum, Dallas, Texas: American Institute of Aeronautics and Astronautics; 2019. https://doi.org/10.2514/6.2019-3589.
[55] Dehez B, Vloebergh C, Labrique F. Study and optimization of traveling wave generation in finite-length beams. Mathematics and Computers in Simulation 2010;81:290–301.
[56] Malladi VVS, Albakri M, Tarazaga PA. An experimental and theoretical study of two-dimensional traveling waves in plates. Journal of Intelligent Material Systems and Structures 2017;28:1803–15. https://doi.org/10.1177/1045389X16679284.
[57] Musgrave PF, Sriram Malladi VVN, Tarazaga PA. Generation of Traveling Waves in a 2D Plate for Future Drag Reduction Manipulation. In: Di Miao D, Tarazaga P, Castellini P, editors. Special Topics in Structural Dynamics, Volume 6, Cham: Springer International Publishing; 2016, p. 129–38. https://doi.org/10.1007/978-3-319-29910-5_13.
[58] Kendall J. Experimental study of laminar boundary layer receptivity to a traveling pressure field. 19th AIAA, Fluid Dynamics, Plasma Dynamics, and Lasers Conference, Honolulu,HI,U.S.A.: American Institute of Aeronautics and Astronautics; 1987. https://doi.org/10.2514/6.1987-1257.
[59] Wu JM, Wu JZ, Wu CJ, Vakili AD. Preliminary study of nonlinear flow over traveling wavy wall. Nonsteady Fluid Dynamics 1990:359–68.
[60] Akbarzadeh AM, Borazjani I. Reducing flow separation of an inclined plate via travelling waves. Journal of Fluid Mechanics 2019;880:831–63.
[61] Yang DI, Shen L. Direct-simulation-based study of turbulent flow over various waving boundaries. Journal of Fluid Mechanics 2010;650:131–80.
[62] Yang D, Shen L. Characteristics of coherent vortical structures in turbulent flows over progressive surface waves. Physics of Fluids 2009;21.
[63] Wu TY-T. Swimming of a waving plate. Journal of Fluid Mechanics 1961;10:321–44.
[64] Barrett DS, Triantafyllou MS, Yue DKP, Grosenbaugh MA, Wolfgang M. Drag reduction in fish-like locomotion. Journal of Fluid Mechanics 1999;392:183–212.
[65] Jeong J, Hussain F. On the identification of a vortex. Journal of Fluid Mechanics 1995;285:69–94.
[66] Guezennec YG. Stochastic estimation of coherent structures in turbulent boundary layers. Physics of Fluids A: Fluid Dynamics 1989;1:1054–60.
[67] Lu SS, Willmarth WW. Measurements of the structure of the Reynolds stress in a turbulent boundary layer. Journal of Fluid Mechanics 1973;60:481–511.
[68] Morrison JF, Tsai HM, Bradshaw P. Conditional-sampling schemes for turbulent flow, based on the variable-interval time averaging (VITA) algorithm. Experiments in Fluids 1988;7:173–86. https://doi.org/10.1007/BF02332982.
[69] Grmela M, Jou D, Casas-Vazquez J, Bousmina M, Lebon G. Ensemble averaging in turbulence modelling. Physics Letters A 2004;330:54–64.
[70] Hoepffner J, Fukagata K. Pumping or drag reduction? Journal of Fluid Mechanics 2009;635:171–87.
[71] Lu X-Y, Yin X-Z. Propulsive performance of a fish-like travelling wavy wall. Acta Mechanica 2005;175:197–215. https://doi.org/10.1007/s00707-004-0117-y.
[72] Chuijie W, Yanqiong X, Jiezhi W. “Fluid roller bearing” effect and flow control. Acta Mech Sinica 2003;19:476–84. https://doi.org/10.1007/BF02484582.
[73] Dong G-J, Lu X-Y. Numerical analysis on the propulsive performance and vortex shedding of fish-like travelling wavy plate. Int J Numer Meth Fluids 2005;48:1351–73. https://doi.org/10.1002/fld.984.
[74] Gad-el-Hak M. Control of low-speed airfoil aerodynamics. AIAA Journal 1990;28:1537–52. https://doi.org/10.2514/3.25250.

[75] Cant S. SB Pope, Turbulent Flows, Cambridge University Press, Cambridge, UK, 2000, 771 pp. Combustion and Flame 2001;125:1361–2.
[76] Yoshizawa A. Statistical theory for compressible turbulent shear flows, with the application to subgrid modeling. The Physics of Fluids 1986;29:2152–64.
[77] Kim W-W, Menon S. A new dynamic one-equation subgrid-scale model for large eddy simulations. 33rd Aerospace Sciences Meeting and Exhibit, Reno,NV,U.S.A.: American Institute of Aeronautics and Astronautics; 1995. https://doi.org/10.2514/6.1995-356.
[78] Darwish FMLMM. The finite volume method in computational fluid dynamics. 2016.
[79] Cao Y, Tamura T. Large-eddy simulations of flow past a square cylinder using structured and unstructured grids. Computers & Fluids 2016;137:36–54.
[80] Sweby PK. High Resolution Schemes Using Flux Limiters for Hyperbolic Conservation Laws. SIAM J Numer Anal 1984;21:995–1011. https://doi.org/10.1137/0721062.
[81] Cunha Galeazzo FC. Simulation of Turbulent Flows with and without Combustion with Emphasis on the Impact of Coherent Structures on the Turbulent Mixing. KIT Scientific Publishing; 2016.
[82] Winslow J, Otsuka H, Govindarajan B, Chopra I. Basic Understanding of Airfoil Characteristics at Low Reynolds Numbers (104–105). Journal of Aircraft 2018;55:1050–61. https://doi.org/10.2514/1.C034415.
[83] Feng L-H, Jukes TN, Choi K-S, Wang J-J. Flow control over a NACA 0012 airfoil using dielectric-barrier-discharge plasma actuator with a Gurney flap. Exp Fluids 2012;52:1533–46. https://doi.org/10.1007/s00348-012-1263-y.
[84] Anyoji M, Okamoto M, Hidaka H, Kondo K, Oyama A, Nagai H, et al. Control surface effectiveness of low Reynolds number flight vehicles. Journal of Fluid Science and Technology 2014;9:JFST0072–JFST0072.
[85] Tuck A, Soria J. Separation control on a NACA 0015 airfoil using a 2D micro ZNMF jet. Aircraft Engineering and Aerospace Technology 2008;80:175–80.
[86] You D, Ham F, Moin P. Discrete conservation principles in large-eddy simulation with application to separation control over an airfoil. Physics of Fluids 2008;20.
[87] Kuhn S, Wagner C, Rudolf Von Rohr P. Influence of wavy surfaces on coherent structures in a turbulent flow. Exp Fluids 2007;43:251–9. https://doi.org/10.1007/s00348-007-0262-x.
[88] Wang L-H, Xu C-X, Sung HJ, Huang W-X. Wall-attached structures over a traveling wavy boundary: Turbulent velocity fluctuations. Phys Rev Fluids 2021;6:034611. https://doi.org/10.1103/PhysRevFluids.6.034611.
[89] Robinson SK. Coherent Motions in the Turbulent Boundary Layer. Annu Rev Fluid Mech 1991;23:601–39. https://doi.org/10.1146/annurev.fl.23.010191.003125.
[90] Yang Z, Wu J-Z. Drag reduction by axisymmetric traveling wavy wall. Zhongguo Kexue Jishu Daxue Xuebao(Journal of University of Science and Technology of China) 2005;35:471–9.
[91] Shi Y, Xia Z, Chen S. A new identification method in sampled quadrant analysis for wall-bounded turbulence. Physics of Fluids 2016;28.
[92] Holst D, Church B, Wegner F, Pechlivanoglou G, Nayeri CN, Paschereit CO. Experimental analysis of a NACA 0021 airfoil under dynamic angle of attack variation and low Reynolds numbers. Journal of Engineering for Gas Turbines and Power 2019;141:031020.
[93] Truong VK. An analytical model for airfoil aerodynamic characteristics over the entire 360° angle of attack range. Journal of Renewable and Sustainable Energy 2020;12.

[94] Elsakka MM, Ingham DB, Ma L, Pourkashanian M. CFD analysis of the angle of attack for a vertical axis wind turbine blade. Energy Conversion and Management 2019;182:154–65.
[95] Du Y, Symeonidis V, Karniadakis GE. Drag reduction in wall-bounded turbulence via a transverse travelling wave. Journal of Fluid Mechanics 2002;457:1–34.
[96] Anderson J. EBOOK: Fundamentals of Aerodynamics (SI units). McGraw hill; 2011.
[97] Geissler W, van der Wall BG. Dynamic stall control on flapping wing airfoils. Aerospace Science and Technology 2017;62:1–10.
[98] Goodarzi M, Rahimi M, Fereidouni R. Investigation of active flow control over NACA0015 airfoil via blowing. International Journal of Aerospace Sciences 2012;1:57–63.
[99] Kornilov V. Combined Blowing/Suction Flow Control on Low-Speed Airfoils. Flow Turbulence Combust 2021;106:81–108. https://doi.org/10.1007/s10494-020-00157-7.
[100] Tousi NM, Coma M, Bergadà JM, Pons-Prats J, Mellibovsky F, Bugeda G. Active flow control optimisation on SD7003 airfoil at pre and post-stall angles of attack using synthetic jets. Applied Mathematical Modelling 2021;98:435–64.
[101] Fish FE, Lauder GV. PASSIVE AND ACTIVE FLOW CONTROL BY SWIMMING FISHES AND MAMMALS. Annu Rev Fluid Mech 2006;38:193–224. https://doi.org/10.1146/annurev.fluid.38.050304.092201.
[102] Amitay M, Glezer A. Controlled transients of flow reattachment over stalled airfoils. International Journal of Heat and Fluid Flow 2002;23:690–9.
[103] Seifert A, Pack LG. Oscillatory Control of Separation at High Reynolds Numbers. AIAA Journal 1999;37:1062–71. https://doi.org/10.2514/2.834.
[104] Thompson E, Goza A. Optimal surface morphing using adjoint optimization. AIAA SCITECH 2023 Forum, National Harbor, MD & Online: American Institute of Aeronautics and Astronautics; 2023. https://doi.org/10.2514/6.2023-0460.
[105] Xia Y, Dai Y, Huang G, Yang C. Stall flutter mitigation of an airfoil by active surface morphing. Physics of Fluids 2024;36.
[106] Ogunka UE, Akbarzadeh AM, Borazjani I. Mechanisms of Morphing Wall Flow Control by Traveling Waves over an Airfoil. AIAA Journal 2023;61:1687–707. https://doi.org/10.2514/1.J062449.
[107] Wu C-J, Wang L, Wu J-Z. Suppression of the von Kármán vortex street behind a circular cylinder by a travelling wave generated by a flexible surface. Journal of Fluid Mechanics 2007;574:365–91.
[108] Olivett A, Bhayadia A, Karami MA. Traveling Waves for Flow Control in Viscoelastic Morphing Skin. Smart Materials, Adaptive Structures and Intelligent Systems, vol. 85499, American Society of Mechanical Engineers; 2021, p. V001T01A013.
[109] Tang F, Yan ZL, Wang XH. Experimental research on lift up and drag reduction effect of streamwise travelling wave wall. Key Engineering Materials 2011;483:721–6.
[110] Zhang L, Lv M, Zhao X, Fan H, Xie T, Shan X, et al. Achieving travelling wave drag reduction by micro piezoelectric actuator. International Journal of Mechanical Sciences 2024;275:109326.
[111] Germano M, Piomelli U, Moin P, Cabot WH. A dynamic subgrid-scale eddy viscosity model. Physics of Fluids A: Fluid Dynamics 1991;3:1760–5.
[112] Sheldahl RE, Klimas PC. Aerodynamic characteristics of seven symmetrical airfoil sections through 180-degree angle of attack for use in aerodynamic analysis of vertical axis wind turbines. Sandia National Lab.(SNL-NM), Albuquerque, NM (United States); 1981.

[113] Damiola L, Siddiqui MF, Runacres MC, De Troyer T. Influence of free-stream turbulence intensity on static and dynamic stall of a NACA 0018 aerofoil. Journal of Wind Engineering and Industrial Aerodynamics 2023;232:105270.
[114] Lesovoy I, Efrati R, Stalnov O. Experimental investigation of instantaneous lift on NACA 0018 airfoil section due to a non-harmonic pitching motion. Journal of Fluids and Structures 2024;125:104003.
[115] Hussain AF. Coherent structures and turbulence. Journal of Fluid Mechanics 1986;173:303–56.
[116] Brunton SL. Machine Learning of Dynamics with Applications to Flow Control and Aerodynamic Optimization. In: Braza M, Hourigan K, Triantafyllou M, editors. Advances in Critical Flow Dynamics Involving Moving/Deformable Structures with Design Applications, vol. 147, Cham: Springer International Publishing; 2021, p. 327–35. https://doi.org/10.1007/978-3-030-55594-8_28.
[117] Li J, Du X, Martins JR. Machine learning in aerodynamic shape optimization. Progress in Aerospace Sciences 2022;134:100849.
[118] Yan X, Zhu J, Kuang M, Wang X. Aerodynamic shape optimization using a novel optimizer based on machine learning techniques. Aerospace Science and Technology 2019;86:826–35.
[119] Sharma P, Chung WT, Akoush B, Ihme M. A review of physics-informed machine learning in fluid mechanics. Energies 2023;16:2343.
[120] Buzzicotti M. Data reconstruction for complex flows using AI: Recent progress, obstacles, and perspectives. Europhysics Letters 2023;142:23001.
[121] Brunton SL, Noack BR, Koumoutsakos P. Machine Learning for Fluid Mechanics. Annu Rev Fluid Mech 2020;52:477–508. https://doi.org/10.1146/annurev-fluid-010719-060214.
[122] Ogunka UE, Akbarzadeh AM, Borazjani I. Mechanisms of Morphing Wall Flow Control by Traveling Waves over an Airfoil. AIAA Journal 2023;61:1687–707. https://doi.org/10.2514/1.J062449.
[123] Aziz MA, Mansour M, Iskander D, Hany A. Combined droop nose and trailing-edges morphing effects on airfoils aerodynamics. SN Appl Sci 2019;1:1033. https://doi.org/10.1007/s42452-019-0796-6.
[124] Tracey BD, Duraisamy K, Alonso JJ. A Machine Learning Strategy to Assist Turbulence Model Development. 53rd AIAA Aerospace Sciences Meeting, Kissimmee, Florida: American Institute of Aeronautics and Astronautics; 2015. https://doi.org/10.2514/6.2015-1287.
[125] Zhang ZJ, Duraisamy K. Machine Learning Methods for Data-Driven Turbulence Modeling. 22nd AIAA Computational Fluid Dynamics Conference, Dallas, TX: American Institute of Aeronautics and Astronautics; 2015. https://doi.org/10.2514/6.2015-2460.
[126] Zhao P, Gao X, Zhao B, Liu H, Wu J, Deng Z. Machine learning assisted prediction of airfoil lift-to-drag characteristics for Mars helicopter. Aerospace 2023;10:614.
[127] Areias P, Correia R, Melicio R. Airfoil Analysis and Optimization Using a Petrov–Galerkin Finite Element and Machine Learning. Aerospace 2023;10:638.
[128] Haughn KPT, Gamble LL, Inman DJ. Deep reinforcement learning achieves multifunctional morphing airfoil control. Journal of Composite Materials 2023;57:721–36. https://doi.org/10.1177/00219983221137644.
[129] Lu K, Fu Q, Cao R, Peng J, Wang Q. Asymmetric Airfoil Morphing via Deep Reinforcement Learning. Biomimetics 2022;7:188.
[130] Karbasian H, Van Rees WM. A Deep-Learning Surrogate Model Approach for Optimization of Morphing Airfoils. AIAA SCITECH 2023 Forum, National Harbor,

MD & Online: American Institute of Aeronautics and Astronautics; 2023. https://doi.org/10.2514/6.2023-1619.
[131] Alghamdi AS, Polat K, Alghoson A, Alshdadi AA, Abd El-Latif AA. Gaussian process regression (GPR) based non-invasive continuous blood pressure prediction method from cuff oscillometric signals. Applied Acoustics 2020;164:107256.
[132] Cortes C, Vapnik V. Support-vector networks. Mach Learn 1995;20:273–97. https://doi.org/10.1007/BF00994018.
[133] Song Y-Y, Ying LU. Decision tree methods: applications for classification and prediction. Shanghai Archives of Psychiatry 2015;27:130.
[134] Zhang Y, Xu X. Solid particle erosion rate predictions through LSBoost. Powder Technology 2021;388:517–25.
[135] Moin P, Mahesh K. DIRECT NUMERICAL SIMULATION: A Tool in Turbulence Research. Annu Rev Fluid Mech 1998;30:539–78. https://doi.org/10.1146/annurev.fluid.30.1.539.
[136] Alfonsi G. Reynolds-averaged Navier–Stokes equations for turbulence modeling 2009.
[137] Lesieur M, Métais O, Comte P. Large-eddy simulations of turbulence. Cambridge university press; 2005.
[138] Reynolds WC. Computation of Turbulent Flows. Annu Rev Fluid Mech 1976;8:183–208. https://doi.org/10.1146/annurev.fl.08.010176.001151.
[139] Piquet J. Turbulent flows: models and physics. Springer Science & Business Media; 2013.
[140] Fureby C, Tabor G, Weller HG, Gosman A. A comparative study of subgrid scale models in homogeneous isotropic turbulence. Physics of Fluids 1997;9:1416–29.
[141] Ma J, Wang F, Tang X. Comparison of Several Subgrid-Scale Models for Large-Eddy Simulation of Turbulent Flows in Water Turbine. In: Xu J, Wu Y, Zhang Y, Zhang J, editors. Fluid Machinery and Fluid Mechanics, Berlin, Heidelberg: Springer Berlin Heidelberg; 2009, p. 328–34. https://doi.org/10.1007/978-3-540-89749-1_51.
[142] Aubard G, Stefanin Volpiani P, Gloerfelt X, Robinet J-C. Comparison of Subgrid-scale Viscosity Models and Selective Filtering Strategy for Large-eddy Simulations. Flow Turbulence Combust 2013;91:497–518. https://doi.org/10.1007/s10494-013-9485-5.
[143] Naslidnyk M, Kanagawa M, Karvonen T, Mahsereci M. Comparing Scale Parameter Estimators for Gaussian Process Regression: Cross Validation and Maximum Likelihood 2023.
[144] Aigrain S, Foreman-Mackey D. Gaussian Process Regression for Astronomical Time Series. Annu Rev Astron Astrophys 2023;61:329–71. https://doi.org/10.1146/annurev-astro-052920-103508.
[145] Zhang Y, Xu X. Modulus of elasticity predictions through LSBoost for concrete of normal and high strength. Materials Chemistry and Physics 2022;283:126007.
[146] Hastie T, Friedman J, Tibshirani R. The Elements of Statistical Learning. New York, NY: Springer New York; 2001. https://doi.org/10.1007/978-0-387-21606-5.
[147] Breiman L. Random forests. Machine Learning 2001;45:5–32.
[148] Salima O, Asri N, Hamid HJ. Machine learning techniques for anomaly detection: an overview 2013.
[149] Liu Y, Zhang HH, Wu Y. Hard or Soft Classification? Large-Margin Unified Machines. Journal of the American Statistical Association 2011;106:166–77. https://doi.org/10.1198/jasa.2011.tm10319.
[150] Patle A, Chouhan DS. SVM kernel functions for classification. 2013 International conference on advances in technology and engineering (ICATE), IEEE; 2013, p. 1–9.
[151] Panja S, Chatterjee A, Yasmin G. Kernel Functions of SVM: A Comparison and Optimal Solution. In: Luhach AK, Singh D, Hsiung P-A, Hawari KBG, Lingras P,

Singh PK, editors. Advanced Informatics for Computing Research, vol. 955, Singapore: Springer Singapore; 2019, p. 88–97. https://doi.org/10.1007/978-981-13-3140-4_9.
[152] Wang K, Band SS, Ameri R, Biyari M, Hai T, Hsu C-C, et al. Performance improvement of machine learning models via wavelet theory in estimating monthly river streamflow. Engineering Applications of Computational Fluid Mechanics 2022;16:1833–48. https://doi.org/10.1080/19942060.2022.2119281.
[153] Tangirala S. Evaluating the impact of GINI index and information gain on classification using decision tree classifier algorithm. International Journal of Advanced Computer Science and Applications 2020;11:612–9.
[154] Daniya T, Geetha M, Kumar KS. Classification and regression trees with gini index. Advances in Mathematics: Scientific Journal 2020;9:8237–47.
[155] Charbuty B, Abdulazeez A. Classification based on decision tree algorithm for machine learning. Journal of Applied Science and Technology Trends 2021;2:20–8.
[156] Lian J, Hui G, Ma L, Zhu T, Wu X, Heidari AA, et al. Parrot optimizer: Algorithm and applications to medical problems. Computers in Biology and Medicine 2024:108064.
[157] Krstajic D, Buturovic LJ, Leahy DE, Thomas S. Cross-validation pitfalls when selecting and assessing regression and classification models. J Cheminform 2014;6:10. https://doi.org/10.1186/1758-2946-6-10.
[158] Mamori H, Fujimura M, Udagawa S, Iwamoto K, Murata A, Kawaguchi Y, et al. Effect of wavelength of sinusoidal wavy wall surface on drag and heat transfer at turbulent thermal boundary layer flow. Journal of Thermal Science and Technology 2018;13:JTST0023–JTST0023.
[159] Taylor KE. Summarizing multiple aspects of model performance in a single diagram. J Geophys Res 2001;106:7183–92. https://doi.org/10.1029/2000JD900719.

6 Conclusions and Future Studies Recommendations

This study investigated the impact of traveling wave modulation (TWM) as an active flow control technique to enhance the aerodynamic performance of a NACA 0018 airfoil at low Reynolds numbers (Re = 1,000 and 20,000). The primary goal was to understand the effects of TWM parameters, including wavelength, amplitude, and frequency, on aerodynamic forces such as lift and drag. Additionally, this research integrated machine learning (ML) techniques to optimize wave configurations, reducing computational costs while maintaining high accuracy in predicting aerodynamic performance.

Chapter 2 introduced the immersed boundary lattice Boltzmann method (IB-LBM) as a preliminary study at Re = 1,000 to establish baseline aerodynamic trends. The results demonstrated that backward traveling waves effectively increased the lift-to-drag ratio by stabilizing the flow and delaying separation. In contrast, forward traveling waves were found to reduce aerodynamic efficiency by inducing reverse flow. The analysis showed that for wavelengths between 0.1 and 0.4, the lift-to-drag ratio improved by approximately 12%, rising from 3.21 to 3.55, compared to the unactuated airfoil at 2.83. The study also indicated that an optimal frequency of 1.5 and amplitude of 0.003 led to a fourfold increase in lift coefficient when compared to low-frequency cases.

Chapter 3 extended the investigation to Re = 20,000 using large eddy simulations (LES) to explore TWM's influence on turbulent boundary layer dynamics. The analysis identified a significant enhancement in aerodynamic efficiency, particularly with wavelengths of 0.3, amplitude of 0.003, and frequency of 1.0, which resulted in a maximum lift-to-drag ratio of 5.47, a substantial increase compared to the unactuated case at 2.91. The study further revealed that at 11° angle of attack, the suction peak decreased from -2.15 (unactuated) to -1.27 (actuated), leading to a notable reduction in separation bubble size. These results confirmed

that TWM effectively stabilizes boundary layer fluctuations, delaying separation and improving overall aerodynamic performance. The findings also showed that at higher amplitudes (a = 0.02), the surface waves-maintained flow attachment at 14° angle of attack, a condition where conventional airfoils often suffer from severe flow separation.

Chapter 4 focused on further evaluating the effects of different wave configurations across multiple angles of attack. The study demonstrated that at higher angles, TWM significantly improved flow reattachment, particularly at AOA = 14°, where backward traveling waves delayed separation and sustained aerodynamic efficiency. The findings were further validated through Q-criterion analysis and Reynolds stress decomposition, providing insight into how traveling waves influence vortex dynamics and turbulence intensity. The results highlighted that wave-induced boundary layer energization played a crucial role in improving aerodynamic stability in turbulent flow conditions.

Chapter 5 introduced CFD-ML integration, where machine learning models were trained on 93 CFD simulation cases to predict aerodynamic forces efficiently. The study employed Gaussian Process Regression (GPR), Support Vector Machines (SVM), and Decision Trees (DT) to analyze the relationship between TWM parameters and aerodynamic coefficients. The machine learning models successfully predicted lift and drag values while optimizing wave configurations to enhance performance. At 11° AOA, the optimized wave configuration resulted in a 40% reduction in drag and a 20% increase in lift, reinforcing the effectiveness of ML in identifying high-performance configurations. The study also demonstrated that ML-based surrogate models could replace additional CFD simulations, significantly reducing computational costs while maintaining accuracy.

A comparative analysis with previous studies at higher Reynolds numbers, including the work of Akbarzadeh et al. at Re = 50,000, revealed notable differences in the effects of TWM across

different flow regimes. While Akbarzadeh et al. reported a 38.3% increase in lift and a 68.4% reduction in drag, leading to a lift-to-drag ratio of 10.62, the current study at Re = 20,000 demonstrated a stronger relative effect, emphasizing that TWM is particularly effective at lower Reynolds numbers where laminar separation bubbles dominate the flow dynamics.

The findings of this research have significant implications for the design of micro air vehicles (MAVs) and unmanned aerial vehicles (UAVs), where improving aerodynamic efficiency is crucial for enhancing flight stability and endurance. The study has established that TWM is a viable active flow control strategy that can be optimized through data-driven approaches, offering a novel method for enhancing airfoil performance in low-Re applications.

Future research should focus on experimental validation using piezoelectric actuators to generate traveling waves and verify numerical predictions. Additionally, extending the analysis to three-dimensional traveling waves, such as spanwise and diagonal wave patterns, could provide further insight into complex flow interactions. The integration of CFD-ML techniques should also be expanded by incorporating additional parameters, including angle of attack variations and turbulence intensity effects, to refine predictive capabilities. Moreover, conducting a linear stability analysis could enhance the understanding of boundary layer transition mechanisms under TWM. By combining computational fluid dynamics with machine learning-driven optimization, this study provides a scalable and efficient framework for future aerodynamic research. The findings contribute to advancing active flow control techniques and demonstrate the potential of data-driven modeling in optimizing aerodynamic performance in practical engineering applications.

Based on the findings and objectives of this study, the following areas are recommended for future research to further enhance the understanding and application of traveling wave surface morphing (TWM):

- **Experimental Validation Using Piezoelectric Actuators:**

  Future studies should conduct experimental validation using piezoelectric actuators to generate traveling waves. This approach would allow for precise control of wave parameters, enabling direct comparison with numerical results and providing insights into the practical feasibility and efficiency of TWM in real-world applications.

- **Investigation of 3D Traveling Wave Configurations:**

  Extending the current research to three-dimensional traveling wave patterns, such as spanwise or diagonal waves, could reveal additional mechanisms for controlling flow structures. These configurations may improve flow control performance, particularly in mitigating three-dimensional flow phenomena like wingtip vortices and crossflow instabilities.

- **Integration of CFD and Machine Learning with Additional Inputs:**

  Further integration of CFD and machine learning techniques should include more comprehensive input parameters, such as angle of attack (AOA), Reynolds number, and flow conditions. This would enable the development of more robust and versatile predictive models, optimizing TWM performance across a broader range of scenarios.

- **Instability Analysis of Traveling Wave Actuation:**

  A detailed instability analysis of traveling wave actuation should be performed to better understand its impact on boundary layer stability and the onset of flow disturbances. This would provide valuable insights into the limits of TWM effectiveness and help refine its implementation in applications requiring high levels of stability.

These future works aim to address key limitations and expand the applicability of TWM in both research and practical aerodynamic systems.